Multifunctional Nanocomposites and Particulate Composites with Nanocomposite Binders for Deformation and Damage Sensing

Engin Cem Sengezer

Dissertation submitted to the Faculty of the
Virginia Polytechnic Institute and State University
in partial fulfillment of the requirements for the degree of

Doctor of Philosophy
in
Aerospace Engineering

Gary D. Seidel, Chair
Mayuresh Patil
Michael Philen
Scott W. Case

July 21, 2017
Blacksburg, Virginia

Keywords: Carbon Nanotube, Alignment, Dielectrophoresis, Raman Spectroscopy, Nanocomposites, Particulate Composites, Energetics, Piezoresistivity, Strain Sensing, Damage Sensing, Digital Image Correlation, Instrumented Charpy Impact

Multifunctional Nanocomposites and Particulate Composites with Nanocomposite Binders for Deformation and Damage Sensing

Engin Cem Sengezer

ABSTRACT

At present, structural health monitoring (SHM) efforts focus primarily on the sensors and sensing systems for detecting instances and locations of damage through techniques such as X-ray, micro CT, acoustic emission, infrared thermography, lamb wave etc., which only detect cracks at relatively large length scales and rely heavily on sensors and sensing systems which are external to the material system. As an alternative to conventional commercially available SHM techniques, the current work explores processing-structure-property relationships starting from carbon nanotube (CNT) based nanocomposites to particulate composites with nanocomposite binder/matrix materials, i.e. hybrid particulate composites to investigate deformation and damage sensing capabilities of inherently sensing materials and structures through their piezoresistive (coupled electro-mechanical) response. Initial efforts focused on controlling the dispersion of CNTs and orientation of CNT filaments within nanocomposites under dielectrophoresis to guide design and fabrication process of nanocomposites by tuning CNT concentration, applied AC electric field intensity, frequency and exposure time. It is observed that a combination of exposure time to AC electric field and the AC field frequency are the key drivers of filament width and spacing and that the network for filament formation is much more efficient for pristine CNTs than for acid treated functionalized CNTs. With the knowledge obtained from controlling the morphological features, AC field-induced long range alignment of CNTs within bulk nanocomposites was scaled up to form structural test coupons. The morphology, electrical and mechanical properties of the coupons were investigated. The anisotropic piezoresistive response both for parallel and transverse to CNT alignment direction within bulk composite coupons under various loading conditions was obtained. It is observed that control of the CNT network allows for the establishment of percolation paths and piezoresistive response well below the nominal percolation threshold

observed for random, so called well-dispersed CNT network distributions. The potential for use of such bulk nanocomposites in SHM applications to detect strain and microdamage accumulation is further demonstrated, underscoring the importance of microscale CNT distribution/orientation and network formation/disruption in governing the piezoresistive sensitivities. Finally, what may be the first experimental study in the literature is conducted for real-time embedded microscale strain and damage sensing in energetic materials by distributing the CNT sensing network throughout the binder phase of inert and mock energetic composites through piezoresistive response for SHM in energetic materials. The incorporation of CNTs into inert and mock energetic composites revealed promising self-diagnostic functionalities for in situ real-time SHM applications under quasi-static and low velocity impact loading for solid rocket propellants, detonators and munitions to reduce the stochastic nature of safety characterization and help in designing insult tolerant energetic materials.

This work received support from Virginia Tech's Institute for Critical Technology and Applied Science, Air Force Office of Scientific Research (grant FA9550-12-1-0205) in the Multi-Scale Structural Mechanics and Prognosis Program and (grant FA9550-16-1-0198) in the Dynamic Materials and Interactions Program.

Multifunctional Nanocomposites and Particulate Composites with Nanocomposite Binders for Deformation and Damage Sensing

Engin Cem Sengezer

GENERAL AUDIENCE ABSTRACT

At present, structural health monitoring (SHM) efforts focus primarily on the sensors and sensing systems for detecting instances and locations of damage, which only detect cracks at relatively large length scales and rely heavily on sensors and sensing systems which are external to the material system. As an alternative to conventional commercially available SHM techniques, the current work explores the incorporation of carbon nanotubes (CNTs) into nanocomposites and particulate composites to investigate deformation and damage sensing capabilities of inherently sensing materials and structures through their coupled electromechanical response. Initial efforts focused on controlling the dispersion of CNTs and orientation of CNT filaments within nanocomposites to guide design and fabrication process of nanocomposites. With the knowledge obtained from controlling the morphological features, long range alignment of CNTs within bulk nanocomposites was scaled up to form structural test coupons. The potential for use of such bulk nanocomposites in SHM applications to detect strain and microdamage accumulation is further demonstrated. Finally, what may be the first experimental study in the literature is conducted for real-time embedded deformation and damage sensing in inert and mock energetic composites to reduce the stochastic nature of safety characterization and help in designing insult tolerant solid rocket propellants, detonators and munitions.

DEDICATED TO MY PARENTS

Sevim and Iskender

Sengezer

Acknowledgments

I am grateful to Dr. Gary Seidel, my advisor and mentor, who gave me an opportunity to be a part of his research group. He helped me develop both personally and professionally. I sincerely thank him for his constant support and guidance, his ability to understand me at the personal level, his efforts to shape and build my professional interaction skills, providing me challenges to push myself harder and teaching me how to pay attention to key details, which enabled me to reach my goals in my graduate studies.

I also thank my committee members Dr. Mayuresh Patil who helped me gain insight on how to scale-up nanocomposites into structural test coupons, Dr. Michael Philen who allowed me to use any equipment in Aerospace Structures Lab, and Dr. Scott Case who provided great support to conduct my research at a higher level.

I would like to acknowledge my colleagues, Dr. Francis Avilés, Dr. Andrés Oliva-Avilés, Dr. Jandro Abot, Dr. Adarsh Chaurasia, Dr. Xiang Ren, Dr. Yumeng Li, Naveen Prakash, Krishna Talamadupula, Stefan Povolny , Ryan Seifert, and Skylar Stephens, for their support and brainstorming discussions. I also would like to acknowledge undergraduate students Peter Freshwater, Jimmy Congleton, Kris Tan, Samantha Rocker, and Wade Pearrell with whom I had the opportunity to collaborate and mentor.

I would like to thank Dr. Robert Bodnar and Mr. Charles Farley in the Department of Geosciences who assisted with the Raman analyses, Dr. Mike Gregg and Dr. Michael Butler for providing me access to use the Instron Tensile Frame in the Frith Freshman Design

Laboratory at Virginia Tech, Dr. Kevin Edgar and Dr. Richey Davis for providing me access to use rotary evaporator, Dr. Judy Riffle for showing me some tricks related to solvent evaporation, Dr. Todd Lowe and Dr. Lin Ma for allowing me to use high speed Photron camera, Mr. Mac McCord for his assistance with strain gauge placement and data recording, Mr. David Gilham for providing me a differential voltage probe, Mr. Mark Montgomery for his valuable advice related to electrical measurements, Mr. Todd Rumbaugh from Hadland Imaging for providing me high intensity LED source for high speed recordings, and Mr. Richard Prevost from LaVision for teaching me how to use digital image correlation systems. I also would like to acknowledge Dr. Yavuz Yaman, Dr. Altan Kayran, Dr. Guclu Seber, Dr. Melin Sahin, and Dr. Demirkan Coker for their great support in my transition to graduate school.

On a personal note, I would like express my deepest gratitude, appreciation, and love to my parents, Sevim and Iskender Sengezer, for supporting me at every stage of my life. I also would like express my gratitude to my aunt Selma Totu for extending her best wishes throughout my graduate studies. Last but not least, many thanks to Andrea Rolong for bearing with me and standing by me for the last two years.

Contents

List of Figures

List of Tables

Chapter 1

Introduction

1.1 CNT alignment and the multi-CNT-filament formation via dielectrophoresis

Nanocomposite materials are being designed by dispersing various nanomaterials, including zero dimensional [1] (nanospheres, nanoparticles, embedded clusters), one dimensional [2] (nanowires, nanotubes), two dimensional [3] (nanoplates, nanoscalecoatings), and three dimensional [4] (embedded networks, continuous nanoporous phase) nanoobjects, into a matrix material. Of particular interest to the present work are carbon nanotubes (CNTs). CNTs are currently being used for various applications, such as field effect transistors [5, 6], electrochemical capacitors [7], memory storage devices [8], sensors [9–12], actuators [13, 14], and field emission sources [11, 15, 16]. CNT-nanocomposites are known for their multifunctionality due to the unique combinations of excellent mechanical, electrical, and thermal properties [17], and sensing [18–20] and actuating [21–25] capabilities. Critical to tailoring these functionalities is the degree to which alignment of CNTs within the matrix material can be achieved, thereby leading to significant improvements in thermal, electrical, and mechanical properties, and their sensing and actuating functionalities in the alignment direction. Fab-

rication processes for obtaining microscale alignment of CNTs in nanocomposites include application of acoustic wave [26–28], shear-induced [29, 30], mechanically stretching [31], magnetic field [32–35], and electric field [36–45] alignment of CNTs in the polymeric matrices. Acoustic radiation and acoustic streaming have been shown to lead to some alignment of CNTs, but waviness was a problem [26]. Efforts to use surface acoustic waves in the alignment of CNTs have not significantly improved the mechanical and electrical properties of nanocomposites [27, 28]. One of the easier alignment approaches to implement in large scale nanocomposite material production is the imposition of external mechanical loads and the resulting shear flow for the alignment of the nanotubes. However, the biggest drawback of this technique is that it decreases electric and dielectric properties in the shear direction, as well as in the transverse direction, and requires high CNT concentration to achieve significant mechanical reinforcement [30]. Magnetic field alignment of CNTs typically requires high magnetic fields of more than 9 T (fields as high as 166 T have also been reported [46]) to overcome the viscous forces of the polymer [47, 48]. Shaver et al. [46] measured dynamic linear dichroism of aligned SWNT suspensions of aqueous surfactant solutions of sodium dodecylbenzene sulfonate (SDBS) in pulsed high magnetic fields. Steinert et al. [33] aligned 0.5, 1 and 3 wt% SWNTs in polyethylene terephthalate (PET) matrix with a magnetic field of 9.4 T. Addition of 0.5 and 1 wt% of randomly oriented SWNTs resulted in seven orders of magnitude increase in conductivity compared to the pure PET material. Magnetic field-induced alignment with 3 wt% SWNTs results in two orders of magnitude improvement in electrical conductivity in the alignment direction over the randomly oriented value. Choi et al. [48] aligned 3 wt% purified SWNTs (Carbon Nanotechnologies) in epoxy medium with high magnetic fields of 15T and 25T for 4 h of exposure time. Addition of 3 wt% of randomly oriented SWNTs resulted in an increase in conductivity of six orders of magnitude compared to the neat epoxy at room temperature. Such large increases even before alignment are expected as 3 wt% SWNTS is noted to be above the typical values reported for the percolation threshold in SWNT-epoxy nanocomposites (i.e. on the order of 0.1) [49–55]. For the 25 T magnetic field aligned samples, an additional 35% increase in electrical conductivity over

the randomly oriented value was obtained in the alignment direction at room temperature. For the 15 T magnetic field aligned samples, 70% increase has been observed in electrical conductivity obtained in the alignment direction compared to the electrical conductivity in the transverse direction. Indeed, aligning CNTs using electric fields has been widely used, since it allows one to enhance the mechanical properties and to manipulate the electrical and dielectric properties of the nanocomposite by varying the magnitude, frequency and time of the application of AC electric fields [36, 42, 56–58]. Zhu et al. [42] applied an AC electric field of 28 $V_{RMS}\ mm^{-1}$ with frequency of 2 kHz for 10 min of exposure time during fabrication on 0.5 wt% MWNT suspension of epoxy, and observed an increase in storage modulus parallel to the applied AC electric field compared to nanocomposites produced with no electric field. However, the (longitudinal) conductivity parallel to electric field was on the order of 10^{-11} S cm^{-1} at 1 kHz for 0.5 wt% of pristine MWNT-epoxy nanocomposites, which was two orders of magnitude higher than that of randomly oriented with no electric field case. Ma et al. [57] produced 0.1 wt% aligned oxidized (COOH-acid treated) MWNT/PMMA composites with AC electric field of 5 $V_{RMS}\ mm^{-1}$ with frequency of 500 Hz for 180 min of exposure time. It was observed that the longitudinal conductivity of as-produced sample was on the order of 10^{-8} S cm^{-1}, which was 10 orders of magnitude higher than that of pure PMMA. Moreover, the tangential G-band ratio of 90°/0° of oxidized MWNT/PMMA composites was 0.77 which was not an indicator of good alignment. It has further been observed that by controlling the magnitude, frequency and time of the application of AC electric fields it is possible to achieve not only alignment, but also controlled agglomeration of nanotubes into aligned CNT filaments [57]. This leads to still further enhancement of the electrical properties in the alignment direction compared to the well dispersed, aligned CNT case, as well as over the well-dispersed randomly oriented case. Here we report on how varying parameters such as CNT type, applied AC electric field intensity, frequency and exposure time can lead to repeatable microscale filament structures characterized by parameters such as filament width and filament spacing in order to be able to guide design.

The alignment of CNTs and formation of filament structures stems from the dielectrophoresis

phenomenon which has been investigated by many researchers [59–63]. Although a parallel electrode setup, as applied in this work, creates a globally uniform electric field, local gradients in the electric field due to the difference in the dielectric permittivity of CNTs and acrylate solution result in a locally nonuniform electric field. Non-uniform electric fields induce electric dipoles in CNTs, and results in dielectrophoresis (DEP) i.e., in forces and torques being applied to the CNTs. The polarized CNT subjected to DEP causes the CNT in the nanocomposite solution to both rotate into alignment with the local electric field direction by overcoming the viscous torque arising from the medium as shown in Fig. 1.1 [61], and to coalesce into filament structures (i.e., to agglomerate into thick chains, or filaments, of CNT-rich regions). Furthermore, the magnitude of the dielectrophoretic forces and torques on the CNTs is affected by the CNT geometry, the electric field frequency which affects conductivities and permittivities of both the medium and the particle, and the electric field magnitude [59–65]. The force and torque exerted on a CNT bundle can be given as [61]

$$F_{DEP} = \frac{\pi r^2 l}{2} \varepsilon_m Re(K) \nabla E \tag{1.1}$$

$$\Gamma_{DEP} = \frac{\pi r^2 l}{2} \varepsilon_m \frac{(\varepsilon_p - \varepsilon_m)^2}{[\varepsilon_p + (\varepsilon_p - \varepsilon_m) L_{II}](\varepsilon_p + \varepsilon_m)} E^2 \sin(2\theta) \tag{1.2}$$

where

$$K = \frac{(\varepsilon_p^* - \varepsilon_m^*)}{\varepsilon_m^* + (\varepsilon_p^* - \varepsilon_m^*) L_{II}}$$

$$\varepsilon_{m,p}^* = \varepsilon_{m,p} + \frac{\sigma_{m,p}}{i\omega}$$

where r and l are the radius and length of a CNT bundle, E is the applied local electric field, θ is the angle between the axis of the CNT bundle and the applied local electric field, E. L_{II} is the depolarization factor (on the order of 10^{-5} for CNTs). $\varepsilon_{m,p}$ and $\sigma_{m,p}$ are the permittivities and the conductivities of both the medium and the particle, respectively. F_{DEP} and Γ_{DEP} are the force and the torque on a dipole, respectively. While these equations are gen-

erally accepted as adequately describing how individual particles/CNTs respond under the influence of dielectrophoresis, it is difficult to extend such a model to complex multiparticle interactions believed to be responsible for the formation of aligned CNT filaments. As such, here a phenomenological approach to understand the CNT alignment and the multi-CNT-filament formation was explored by varying the applied electric field magnitude, frequency and exposure time.

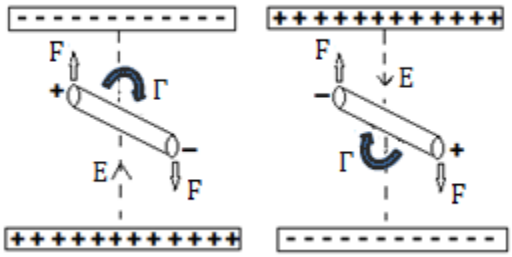

Figure 1.1: Rotational motion of ellipsoidal CNT bundle under AC electric field.

1.2 Piezoresistivity Characteristics of CNT-Polymer Nanocomposites

As an alternative to conventional commercially available metallic strain gauges, carbon nanotube (CNT)-polymer nanocomposites are currently being considered for structural health monitoring (SHM) applications wherein they can provide in situ, real-time situational awareness of current structural state. SHM capabilities of CNT nanocomposites in the form of strain sensing which correlates measurable changes in the macroscale sensing properties, i.e. electrical resistance, to deformation have been investigated under both quasi-static monotonic and cyclic loading using strain-sensing patches [66–73], thin films [36, 74–81] and structural composites with embedded nanocomposite strain [82–97] and damage [82, 83, 85, 86, 88–94, 96–100] sensing. Much of the exploration of the coupled deformation-resistance, or piezoresistive, response has focused on nanocomposites fabricated by doping polymers

with randomly oriented, well-dispersed CNTs [66–73, 75–80, 82–90, 98–100]. The effective change in the macroscale piezoresistivity of CNT-polymer nanocomposites is believed to be attributed in large part to the rearrangement, i.e. either disruption or formation, of conductive networks of CNTs within the matrix material [38, 96, 101–104] and the associated electron hopping in neigh-

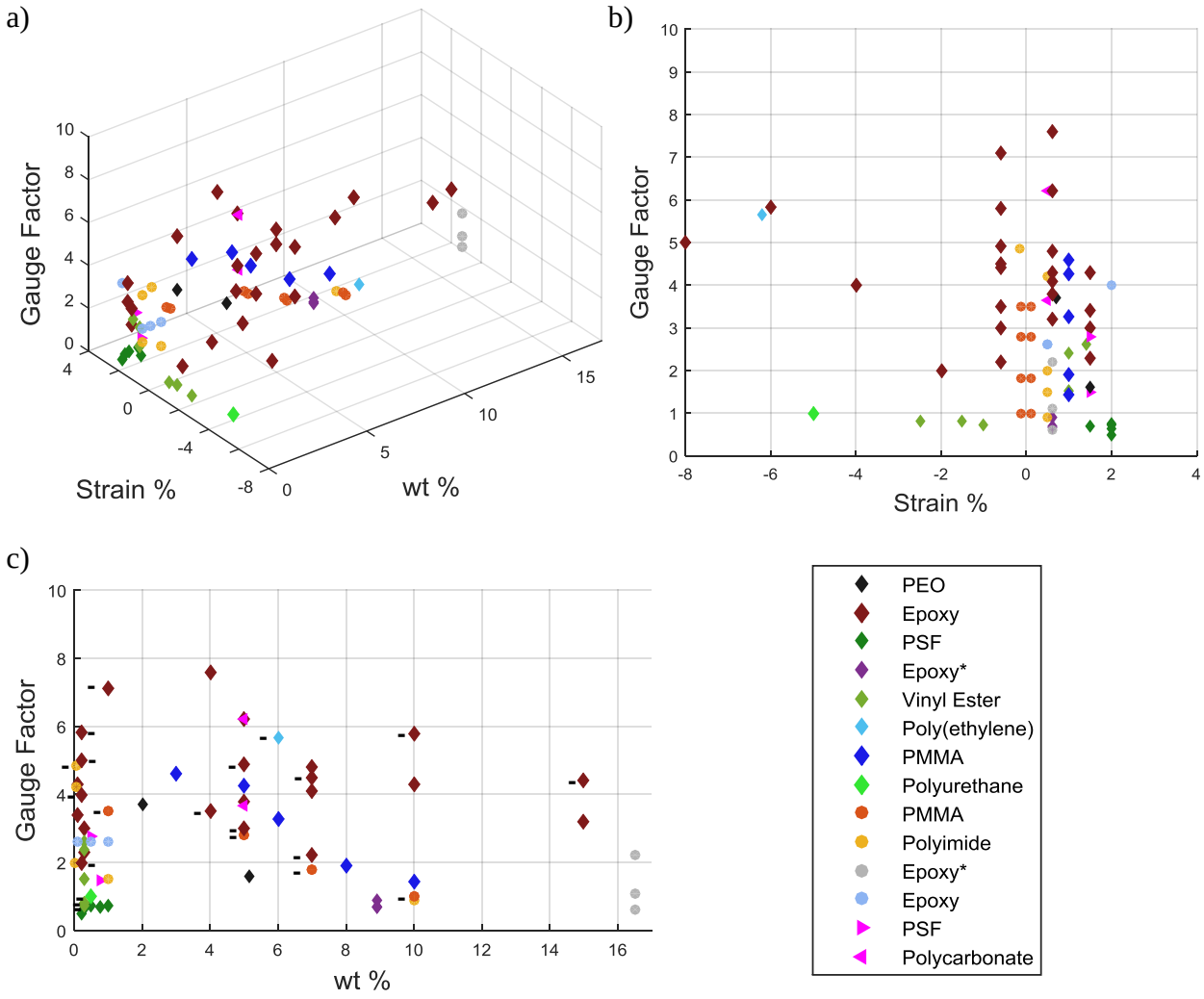

Figure 1.2: Piezoresistive sensitivity of CNT-polymer nanocomposites with varying weight concentrations (*vol%) under tension and compression as found in the literature (randomly oriented MWCNTs and SWCNTs denoted by ◊ and ∘,respectively, aligned MWCNTS denoted by ▷ ,◁ and − in figure c corresponds to compressive strain data)

boring CNTs, i.e. tunneling resistance change [105–120] rather than the intrinsic individ-

ual CNT piezoresistivity, i.e. CNT resistance change under deformation [121–126]. The piezoresistive sensitivity of randomly oriented, well dispersed CNT-polymer nanocomposites as found in the literature is denoted with the $\Diamond$ and $\circ$ symbols in Fig. 1.2 [36, 68, 69, 71, 72, 74, 75, 79, 80, 84, 88, 127–134]. The obtained gauge factor data, the metric used to assess the degree of piezoresistive sensitivity, is plotted in terms of measured strain and CNT weight concentration embedded into different polymer systems. The large variation in Fig. 1.2 stems from differences in the processing-structure-property-relationships associated with the randomness in CNT orientation and microscale dispersion. In order to better understand the structure-property relationship, and perhaps produce larger or perhaps controlled gauge factors, other efforts have focused on producing microscale CNT alignment within the matrix [31, 35, 36, 103, 107, 117–120, 129]. The corresponding experimental piezoresistive sensitivity of aligned CNT-polymer nanocomposites is denoted with the $\triangleright$,$\triangleleft$ symbols in Fig. 1.2, and are observed to be on the same order as those of randomly oriented samples. This stems from the fact that the optimum concentration of CNTs used in these experimental studies for both the randomly oriented and aligned CNT piezoresistivity were either near or above percolation threshold for electrical conductivity of CNT-polymer nanocomposites.

Vecitis et al. [135] provided a summary of literature for DC or AC electric field aligned carbon nanotube studies and their experimental conditions. To illustrate, Park et al. [39] investigated morphological, electrical and dielectric properties of aligned 0.03 wt% SWCNT/UDMA /HDDMA nanocomposites under AC electric field ranging from 1.5 to 38 V_{RMS}/mm with a frequency ranging from 10^{-3} to 10^{5} Hz for exposure times ranging from 1 to 60 min. However, the electrode spacing studied was 2.3 mm; therefore there was no structural test coupon fabrication under dielectrophoresis suitable for mechanical testing. Zhu et al. [42] applied an AC electric field of 28.28 V_{RMS}/mm with frequency of 2 kHz for 10 min of exposure time with an electrode separation of 25 mm during fabrication on 0.5 wt% MWNT suspension of epoxy. UV light was used for 10 min to cure each layer of suspension within nanocomposites which consisted of five layers. An increase in storage modulus parallel to the applied AC electric field was observed compared to nanocomposites produced with no elec-

tric field. However, the longitudinal conductivity parallel to electric field was on the order of 10^{-11} S/cm at 1 kHz for 0.5 wt% of pristine MWNT-epoxy nanocomposites, which was two and three orders of magnitude higher than that of randomly oriented with no electric field case and pure epoxy, respectively. In addition, no piezoresistive testing of the as-produced specimens was reported. Minaie et al. [43] aligned 4.5 wt% functionalized carbon nanofibers (CNFs) in epoxy resin using AC electric field of 22.27 V_{RMS}/mm with a frequency of 2 kHz and with an electrode separation of 31.75 mm. Samples were fabricated by maintaining the electric field within temperature controlled oven at 100 ^{o}C followed by a constant ramp (3 ^{o}C/min) to 177 ^{o}C. The electrical field was maintained for almost an hour to make sure the resin gelled. Compressive strength and modulus of aligned samples were improved around 8% and 19%, respectively compared to the neat composites. Electrical properties were also enhanced four orders of magnitude in the alignment direction with respect to the neat composites. In addition, again no piezoresistive testing was reported. Kim et al. [44] studied the alignment of MWCNTs within a bulk epoxy matrix under DC electric field during composite curing. The applied voltage ranged from 100 V/cm to 200 V/cm at an elevated temperature of 100 ^{o}C during curing with an electrode spacing of 50 mm. Nanocomposite specimens were machined to 20 mm long x 3 mm wide x 1 mm thick for electrical conductivity, tensile and storage modulus measurements, and to 45 mm wide x 43.2 mm high x 5 mm thick samples for compact tension testing to obtain fracture toughness for aligned specimens. Elastic modulus and fracture toughness of aligned 0.3 wt% MWCNT-epoxy composites were increased by 40% and 50%, respectively compared to the neat epoxy samples. In addition, no piezoresistive response of electric field-aligned CNT bulk nanocomposites was presented. Sun et al. [45] studied an array of interdigitated parallel wire electrodes with a spacing of 1 cm to fabricate aligned 0.05 wt% MWCNTs within epoxy film created by an electric field approach for large-scale production (15 cm (length) x 15 cm (width) x 0.4 mm (thickness)). AC voltage of 5 kV (with an electric field of 176.75 V_{RMS}/mm) at a frequency of 4 kHz for 10 min was applied to tungsten wire electrodes resulting in an aligned MWCNT/epoxy film which was cured by UV light irradiation at room temperature for 30 min. For electri-

cal resistivity measurements, the large MWCNT/epoxy film was cut into square specimens with dimensions of 1 cm x 1 cm. Three orders of magnitude enhancement for the aligned film coupons was obtained compared to randomly-oriented film coupons. The approach was promising, however, there was no fully continuous alignment of CNTs within large-scale film due to interdigitated parallel wire electrodes, and no piezoresistive testing was reported.

One of the pioneering works on piezoresistive characterization of aligned CNT thin films fabricated under AC electric field with electrode spacing of 30 mm was studied by Oliva-Aviles et al. [36]. Aviles et al. [36] first identified the percolation concentration for MWCNT/polysulfone films containing randomly oriented, well-dispersed MWCNTs to be 0.1wt%, and subsequently produced thin films containing 0.5 and 0.75 wt% of AC electric field aligned MWCNTs in polysulfone which were assessed in terms of piezoresistive sensitivity. Applied AC electric field was 7 V/mm with frequency of 60 Hz for 3 min of exposure time during fabrication. The thin films were rescaled from ASTM D638 Type IV as 25 mm long, with 3 mm central width and 200 μm thickness. The measured gauge factor in the alignment direction for 0.5 wt% of AC electric field aligned MWCNTs in polysulfone thin films was 2.78 ± 0.42 (at strain of 1.5%), which could not be compared with 0.5 wt% randomly oriented samples due to high initial resistance and minuscule changes in resistance of 0.5 wt% randomly oriented samples which could not be sufficiently distinguished from baseline values. For the 0.75 wt% of AC electric field aligned MWCNTs in polysulfone thin films, they observed the gauge factor in the alignment direction to be 1.49 ± 0.30 (at strain of 1.5%), which was as much as a 2 fold increase in gauge factor for the randomly oriented samples at that same concentration and strain. Another demonstration of dielectorphoretically aligned film testing was provided by H. Meeuw et al. [136] who fabricated AC-field induced aligned 0.02 and 0.03 wt% MWCNT-epoxy films. Applied AC electric field with 30 mm electrode spacing was 60 V/mm at a frequency of 50 Hz during 15 hours of curing the epoxy at 35^{o}C. The nanocomposite strain sensing patches were mounted on epoxy substrate and their piezoresistive characterization was carried out by unidirectional monotonic quasi-static tensile loading. Linear piezoresistive response was observed up to higher strain levels of 4% at failure. It

should be noted that MWCNTs were aligned to a certain degree that unfortunately was not quantified, and that the CNTs did not coalesce into continuous CNT filament structures due to inefficient input parameters for dielectrophoretic alignment.

Moving away from assessing dielectrophoretically aligned piezorestivity in films, others [31, 35, 129] focused on different CNT alignment techniques to investigate piezoresistive response of aligned CNT nanocomposites or films. Parmar et al. [129] studied the anisotropic piezoresistivity of 5 wt% MWCNT/polycarbonate composites with MWCNTs partially aligned through the use of an injection molding process. The samples were fabricated by aligning MWCNTs either parallel (represented as in-flow direction) to pulling direction or transversely (represented as cross-flow direction) to the tensile loading direction. It was observed that the piezoresistive sensitivity in the in-flow direction was increased in comparison to that of the samples prepared with randomly oriented CNTs, i.e. gauge factors of 3.65 compared to 2.62 (at strain of 0.5%), respectively. In addition, it was noted that the samples which were aligned transverse to the loading direction (cross-flow) exhibited higher piezoresistive sensitivity than those aligned parallel to the loading direction (in-flow) by as much as 70%. Liu et al. [31] studied the piezoresistivity of spray coated mechanically stretched SWCNT thin films of different draw ratios λ. It should be noted that SWCNT thin films were nearly bucky papers which were well above percolation It was observed that the piezoresistive sensitivity of thin films of relatively small draw ratio ($\lambda < 2$), leading to a partial SWCNT alignment, was on the order of 2 and was believed to be largely governed by quantum tunneling conduction between neighboring CNTs. In contrast, stretching of thin films to relatively higher draw ratio ($\lambda > 2$), resulted in not only an increase in the degree of SWCNT alignment, but also in severe CNT network disruption with in situ developed micro-crack damage, leading to a nonlinear response with higher piezoresistive sensitivity, e.g., on the order of 6. The investigation of the anisotropic piezoresistive response by Miao et al. [35] focused on CNT films attached to a PVC bar loaded under in-plane straining. MWCNTs were decorated with iron oxide nanoparticles and spray deposited onto polyethylene terephthalate substrate in conjunction with an applied magnetic field to produce an aligned CNT network. CNT-

iron oxide nanoparticles films were aligned both parallel and transversely to the applied strain direction. Under the low spraying volume of 2 mL, and corresponding low density CNT network, it was similarly found that the CNT-iron oxide nanoparticles network aligned transversely to the applied strain direction exhibited higher piezoresistive sensitivity than both the randomly oriented CNT network and the CNT network aligned parallel to the applied strain, with gauge factor values of 4.5, 2.4, and 2.1 (at strain of 8%), respectively. It was postulated that the differences in gauge factors between the three cases could be attributed to the differences in the degree of tube-tube contact within each network. In fact, increasing the spray volume thereby leading to an increased density of CNT network diminished the difference in piezoresistive sensitivity between both aligned and randomly oriented samples, implying that there may be an optimum degree of tube-tube contact governing piezoresistive sensitivity.

In most cases, including those mentioned above, the optimum concentration of CNTs producing sufficient numbers of tube-tube contacts, but not too many so as to saturate the piezoresistive response, seems to be near or just above the percolation threshold for electrical conductivity of the CNT doped polymer matrices to maximize piezoresistive response. There are little to no results in the open literature exploring the AC field-induced long range alignment of CNTs within bulk composites corresponding to a structural test coupon which investigates the morphology, electrical and mechanical properties and coupled electro-mechanical response both for parallel and transverse to CNT alignment direction within bulk composite under quasi-static monotonic and cyclic loading for CNT loadings well below percolation threshold. Of particular interest to the present work is capturing the anisotropic piezoresistive response in the axial and transverse directions in aligned CNT-polymer nanocomposites at a CNT concentration well below the nominal percolation threshold, underscoring the importance of microscale CNT distribution and network formation/disruption in governing the piezoresistive sensitivity. In this study, the electrical conductivity, the polarized Raman spectroscopy and the piezoresistive behavior of randomly oriented, well dispersed and long range electric field aligned single-wall nanotubes (SWCNTs) in a photopolymerizable

monomer blend (urethane dimethacrylate (UDMA) and 1,6-hexanediol dimethacrylate (HDDMA)) were quantitatively and qualitatively evaluated. Specifically, the axial and transverse piezoresistive responses of 0.03wt% aligned SWCNT-acrylate polymer nanocomposites were investigated under quasi-static monotonic and cyclic tensile loading to further demonstrate the potential for use of such bulk nanocomposites in SHM applications through correlation of changes in strain with changes in resistivity.

1.3 Polymer Bonded Explosives

Polymer bonded explosives (PBXs) are particulate composite explosive materials consisting of explosive materials/crystals embedded in a polymer binder which provides structural integrity and a degree of tolerance to accidental external stimuli. Typical explosive materials include orthorhombic or monoclinic crystals of HMX (cyclotetramethylene-tetranitramine), RDX (trinitroperhydro-triazine), TATB (triamino- trinitrobenzene), PETN (pentaerythritol-tetranitrate). Common binder materials include epoxy, estane (thermoplastic polyurethane), HTPB (Hydroxyl-terminated polybutadiene), Viton-A (fluoropolymer binder), Kel-F (poly(chlorotrifluoroethylene-covinylidene fluoride), PDMS (Polydimethylsiloxane). Binder weight concentrations range from 2 to 40% [137], corresponding to volume fractions of 20 to 40% [138]. PBXs can be in obtained in pressed or cast forms. Pressed PBXs are formed by consolidating binder coated crystals (molding powder) under vacuum and heat at a specific geometry, which enables higher crystal fill-fraction, but can result in crystal-crystal friction and crystal fracture during processing. Cast PBXs, having relatively lower crystal fill-fraction, are processed by curing crystal-binder mixtures. With less particle-particle interactions, they are less sensitive to mechanical insult, but do typically incur some void formation during processing. Young's moduli of high explosive crystals are on the order of 5-30 GPa [139–141] while the surrounding polymer binders can have a range of properties such as low modulus-low strength-high ductility or relatively high modulus-high strength-more brittle behavior depending on the applications such as detonators, solid

rocket propellants or munitions.

A concern with PBXs is damage incurred due to low velocity impact associated with incidental loadings during transportation and handling or tool drop during manufacturing or machining. Such instances can lead to inadvertant ignition due to development of localized regions of high temperature known as 'hot spots' at the microscale [142]. As such, the characterization of the mechanical properties of PBXs has drawn great interest of many researchers for the safety and stability of the energetic materials. Quasi-static compressive loading via Brazilian disk tests, in which tensile stresses result from compression loads, were used by Palmer [141], Rae [143, 144] and Chen [145] to demonstrate that the mechanical properties of as produced energetics were largely influenced by the binder despite its low concentration within the energetic. Palmer et al. [141] studied various explosive compositions based on TATB, PETN and HMX with different crystal sizes (coarse fillers with a median of 150 μm and 400 μm and fine fillers with a median of $\sim$10 μm) with different binders using the Brazilian disk test to obtain tensile strength of as produced PBXs. It was observed that the predominant failure mechanisms for rubbery elastomer binders were debonding and micro void expansion within the binder which they referred to as cavitation, and rare crystal fracture. Moreover, higher strength was observed for the compositions with micronized crystals compared to coarser crystals contaning the same binder. Rae et al. [143, 144] employed the Brazilian disk test under quasi-static loading and found that fracture paths tend to avoid regions of fine filler-binder but instead tend to initiate along straight edges of large explosive fillers for PBX 9501 which consists of HMX explosive crystals with a bimodal size distribution of 45 μm and 150-300 μm surrounded by plasticized polyurethane binder of estane. They also suggested that large particles in close proximity where no binder infused led to potential failure at contact points, underscoring the importance of the microstructure on the failure of PBXs. Effects of particle size were also studied by Skidmore [146] and Drodge and Williamson [147]. Skidmore et al. [146] found that processing as-received HMX powder into molding powder and hydrostatic pressing to fabricate PBXs changed the particle size distribution and its morphology. They reported that as-received HMX particles were initially

234 μm and 5 μm for dry blend coarse and fine classes, respectively. However, the maxima were 177 μm for the molding powder, and 147 μm for the consolidated piece. An additional peak was observed at 17 μm both for the molding powder and pressed piece, which was an indication of breakup of coarse particles during processing of HMX powder. Drodge and Williamson [147] investigated RDX-HTPB energetics with coarse ($\sim$250 μm), fine ($\sim$30 μm) and a mixture of coarse and fine particles in the ratio 70:30, respectively. RDX particles volume fractions in cast RDX-HTPB composites were 54% for fine RDX, 60% for coarse RDX and 67% for bimodal RDX in order to prevent particle-particle interactions. It was found out that coarse particle filled composites had lower mechanical strength among all as-produced samples.

Due to concerns with safety, cost and availability, other efforts have studied ammonium perchlorate [148] (AP, NH_4ClO4) as virtually inert energetic crystal without being metalized, the most extensively used solid oxidizer which was introduced in the late 1940's in solid rocket propellants [149–154], or of sugar [138, 155] which is a monoclinic crystalline solid similar in geometry and mechanical properties to actual explosive crystals. AP and sugar crystals are embedded in the same binder materials and using the same processing methods as actual explosives to produce energetic composite simulants. Balzer et al. [148] studied mechanical properties of AP embedded PBXs and AP based propellants to investigate the microstructure effect on ignition mechanisms under quasi-static and dynamic loading. Cast cured AP embedded PBXs (CTX-1) were fabricated with AP/Al/RDX/TNT/binder composition of 40.5/23.8/15/14.1/7.1% with an average AP particle size $\sim$400 μm. Cast cured AP based propellants were fabricated either with AP/HMX/binder (CCP) composition of 80/5/15% with an average AP particle size $\sim$400 μm or with AP/HTPB (CPX 372) ratio of 66/33 containing a range of different average AP particle size $\sim$3 μm, $\sim$8 μm, $\sim$30 μm and 200–300 μm. It was found that all cast cured AP-HTPB propellants (even with different average particle sizes) reached larger strains with smaller stresses compared to cast cured CTX-1 and CCP materials. Therefore, the mechanical behavior of AP embedded PBXs and AP based propellants were different under quasi-static loading at a strain rate of 10^{-2} s^{-1},

indicating the effect of binder, composition and the microstructure. Under dynamic loading, drop-weight experiments at an estimated strain rate of ∼5 x 10^3 s^{-1} showed CTX-1 and CCP compositions had many ignition sites within ∼400 μs at a strain of ∼2.3 mm/mm, whereas AP/HTPB compositions with average particle size ∼3 μm, ∼8 μm and ∼30 μm had one or two ignition sites at later stages (∼700 μs) during impact loading with strain levels of 3-4 mm/mm. Hopkinson bar experiments at applied strain rates of ∼6 x 10^3 s^{-1} showed that bulk heating was varying at different deformation levels for the various compositions. To illustrate, CCP propellants deformed plastically to larger strains of ∼0.6 mm/mm at higher stress levels ∼20 MPa compared to CTX-1 (which deformed plastically at a strain of ∼0.4 mm/mm and stress of ∼15 MPa), resulting in more energy dissipation as heat which created many ignition sites leading to rapid deflagration. However, AP/HTPB propellants had lower strain of ∼0.3 mm/mm and stress levels ∼8 MPa than CCP propellants, leading to rare ignition sites at a later time. These observations indicated the connection between the mechanical and ignition properties to design safer AP-based compositions. Sivior et al. [138] studied mock energetics using 66% caster sugar crystals, with a mean particle size of ∼270 μm embedded into HTPB binder using quasi-static loading and X-ray tomography to investigate the key failure mechanism at room temperature. Recovered specimens from the quasi-static compression revealed the effects of debonding of sugar crystals from the binder with a color change due to increased number of scattering points developed during interfacial failure. X-ray tomography scans showed no obvious change in the sugar crystals shape or their size, such that there was virtually no crystal fracture. Debonding was observed taking place throughout the specimen which supported the observations from the recovered specimens from the quasi-static experiments. It was found that interfacial failure between crystals and binder was the key failure mechanism during room temperature deformation. This failure mechanism was also observed in scanning electron micrographs of fracture surface of specimens in Brazillian disk tests conducted by Palmer [141] and by Rae [143, 144].

While such mechanical characterizations generally operate on the macroscale and measure

macroscopic variables, it is the microscale complexity which leads to inadvertent detonation under mechanical insult and results in the large stochasticity in the characterization of the safety and stability of energetic materials. What would be beneficial is a way to monitor in situ microstructural changes in real-time during a mechanical insult event via structural health monitoring (SHM). At present SHM efforts focus primarily on the sensors and sensing systems for detecting instances and locations of damage through techniques such as X-ray [156], micro CT [157], acoustic emission [158], infrared thermography [159], ultrasonic inspection [160], lamb wave [161] etc., which only detect cracks at relatively large length scales above 100 μm and rely heavily on sensors and sensing systems which are external to the material system. Distributing a sensing network of CNTs throughout the binder phase of energetic composites in an effort to establish real-time embedded sensing of strain and damage in energetic materials through piezoresistive response for SHM in energetic materials may be invaluable in reducing the stochastic nature of safety characterization and may help in designing insult tolerant energetic materials. This work describes the electro-mechanical characterization of MWCNT embedded AP inert hybrid energetics and sugar mock hybrid energetics to provide basis to explore in situ detection of strain and damage state as a proof of concept demonstration for nanocomposite bonded energetics under quasi-static and low velocity impact loading.

Chapter 2

Phenomenological Characterization of Fabrication of Aligned Pristine-SWNT and COOH-SWNT Nanocomposites via Dielectrophoresis under AC Electric Field

Dielectrophoresis under the application of AC electric fields is one of the primary fabrication techniques (DEPFT) for obtaining aligned carbon nanotube (CNT)-polymer nanocomposites, and is used here to generate data sets from which DEPFT fabrication models in terms of CNT dispersion and orientation distribution can be developed. While the general understanding of how CNTs form aligned filaments under the influence of dielectrophoretic forces and moments is well established, detailed multi-CNT-filament formation predictions of microstructure evolution from a random dispersion into a more ordered structure remain intractable. As such, effort here is focused towards the development of phenomenological fabrication models for controlling local CNT dispersion and orientation as a function of

applied electric field magnitude, frequency, and exposure time. In this study, 0.03 wt% single-wall nanotubes (SWNTs) and acid treated functionalized SWNTs (COOH-SWNTs) were dispersed in a photopolymerizable monomer blend (urethane dimethacrylate (UDMA) and 1,6-hexanediol dimethacrylate (HDDMA)). Ultrasonication techniques were used to obtain the two different acrylate solutions i.e., 0.03% SWNTs/ UDMA/ HDDMA(9/1) solution and a 0.03% COOH-SWNTs/UDMA/HDDMA(9/1) solution, consisting of randomly oriented, well dispersed SWNTs. Pristine SWNTs and acid treated SWNTs solutions were then subjected to controlled AC electric fields in order to explore the formation of aligned SWNT-filaments. To assess key morphological features of the as-produced SWNT-acrylate and SWNT-COOH-acrylate nanocomposite samples, such as SWNT distribution and filament thicknesses, transmission optical microscopy has been used to observe the SWNT alignment and filament formation obtained by digitally mapping individual overlapping images. The acquisition of a large field of view with high magnification allows statistically meaningful distribution functions for morphological features to be constructed. Measurements of the as-produced nanocomposite electrical properties in the SWNT alignment direction and transverse to it were used as a macroscale measure to confirm alignment and contiguity of the SWNT-filament structure, with polarized Raman spectroscopy used to assess the degree of SWNT alignment at the local microscale level. It is observed that a combination of exposure time to AC electric field, and its frequency, is the key driver of filament width and spacing and that in general, the COOH-SWNTs align to a greater extent than the pristine SWNTs, though they do not form filaments that are as thick and contiguous for the exposure times studied.

2.1 Experimental Details

In the present study, the medium in which CNTs have been dispersed and aligned is a blend of two different photopolymerizable monomers which consisted of urethane dimethacrylate (UDMA) and 1,6-hexanediol dimethacrylate (HDDMA), following a procedure similar to one

reported by Banda and Ounaies [58] and expanding on the parametric studies therein. The monomers, the Camphorquinone, the photoinitiator, and N,N-dimethylaminoethyl methacrylate, the accelerator, were obtained from Esstech. The pristine CG200 single-wall nanotubes (SWNTs) (SouthWest Nano Technologies) used had a carbon content of 91.7%, and a T1 (which is an estimate of SWNT content by weight as a percentage of total carbon) of 80.7%. The acid treated SWNTs (COOH-SWNTs) (NanoLab) were reported to have a purity of more than 95%. Neat polymer samples were prepared from the photopolymerizable monomers with a ratio of 9 to 1 (UDMA/HDDMA (9/1)) to obtain the precursor acrylate solution, with the ratio likewise maintained in the preparation of nanocomposite samples. In preparing nanocomposite samples, 0.03 wt% of either SWNTs or COOH-SWNTs was added first to the lower viscosity HDDMA. To obtain a more uniformly dispersed aligned filament structure, the SWNTs and COOH-SWNTs were dispersed using a QsonicaSonicator 4000 operating at 20 kHz and amplitude of 10% with a 3/16 Microtip probe. About 0.03 wt% SWNTs-HDDMA and COOH-SWNTs-HDDMA mixtures were subjected to ultrasonication for 1.5 h. The choice to disperse SWNTs or COOH-SWNTs in HDDMA was due to the fact that HDDMA had lower viscosity compared to UDMA, leading to easier separation of SWNTs or COOH-SWNTs from each other. The UDMA was then added to the predispersed SWNT-HDDMA solution and resonicated for an additional 2.5 h with the same settings to obtain a homogeneous SWNTs or COOH-SWNTs distribution in the acrylate solution. A stirring plate with magnetic stir bar was used at 200 rpm to mix 0.3 wt% photoinitiator and 0.4% accelerator added into the SWNT-acrylate solution to obtain the photocurable/polymerizable nanocomposite acrylate solutions, i.e., the 0.03% SWNTs/UDMA/HDDMA (9/1) solution and the 0.03% COOH-SWNTs/UDMA/HDDMA (9/1) solution.

The prepared nanocomposite solutions were subsequently poured into a teflon mold between a pair of parallel aluminum electrodes (10 mm high by 20 mm wide by 1 mm thick) spaced 6.3 mm apart as shown in Fig. 2.1a and b. A combination of Agilent 33522A Arbitrary Waveform Generator and Trek Model 10/10B-HS-L-CE High Voltage Amplifier was used to obtain AC high voltages as indicated in Table 2.1. To prevent potentially damaging current during the

formation of the conductive filament paths, one of the aluminum electrodes was covered by a 0.7 mm thick insulating polycarbonate film (dielectric constant of 3). To calculate the voltage required to obtain the desired electric field with the addition of the polycarbonate film, the electrodes with the nanocomposite solution and the insulating film were considered as a set capacitors in series with the voltage drop across the polycarbonate film determined as:

$$V_{pc} = \frac{Vapp}{\frac{k_{pc}}{k_{nc}}\frac{d_{nc}}{d_{pc}} + 1} \tag{2.1}$$

where V_{pc} is the voltage drop across the polycarbonate film, V_{App} is the applied AC high voltage across the electrodes, k_{pc} and k_{nc} are the dielectric constants of the polycarbonate film and nanocomposite acrylate solution, respectively, and d_{pc} (0.7 mm) and d_{nc} (5.6 mm) are the corresponding widths. The applied electric field to the electrodes with an insulator was adjusted for frequencies of 1 and 10 kHz as shown in Table 2.1 in order to maintain the effective electric field acting on nanocomposite solution at 200 $V_{RMS}\ mm^{-1}$ as shown in Fig. 2.1c, $(V_{RMS-App} - V_{RMS-pc})/d_{nc}$, the value needed to manipulate pristine SWNTs in the nanocomposite solution. The change in dielectric constant of nanocomposite liquid solution vs. frequency reported in Table 2.1 was obtained using an Agilent E4980A Precision LCR Meter.

Table 2.1: Dielectric constant of pristine SWNTs nanocomposite liquid solution vs. frequency.

Frequency	Nanocomposite acrylate solution (k_{nc})	Electrodes (V_{App})	Decrease in V_{App} due to polycarbonate film (V_{pc})
1kHz	14.67	1805	684.75
10 kHz	14.01	1775	654.24

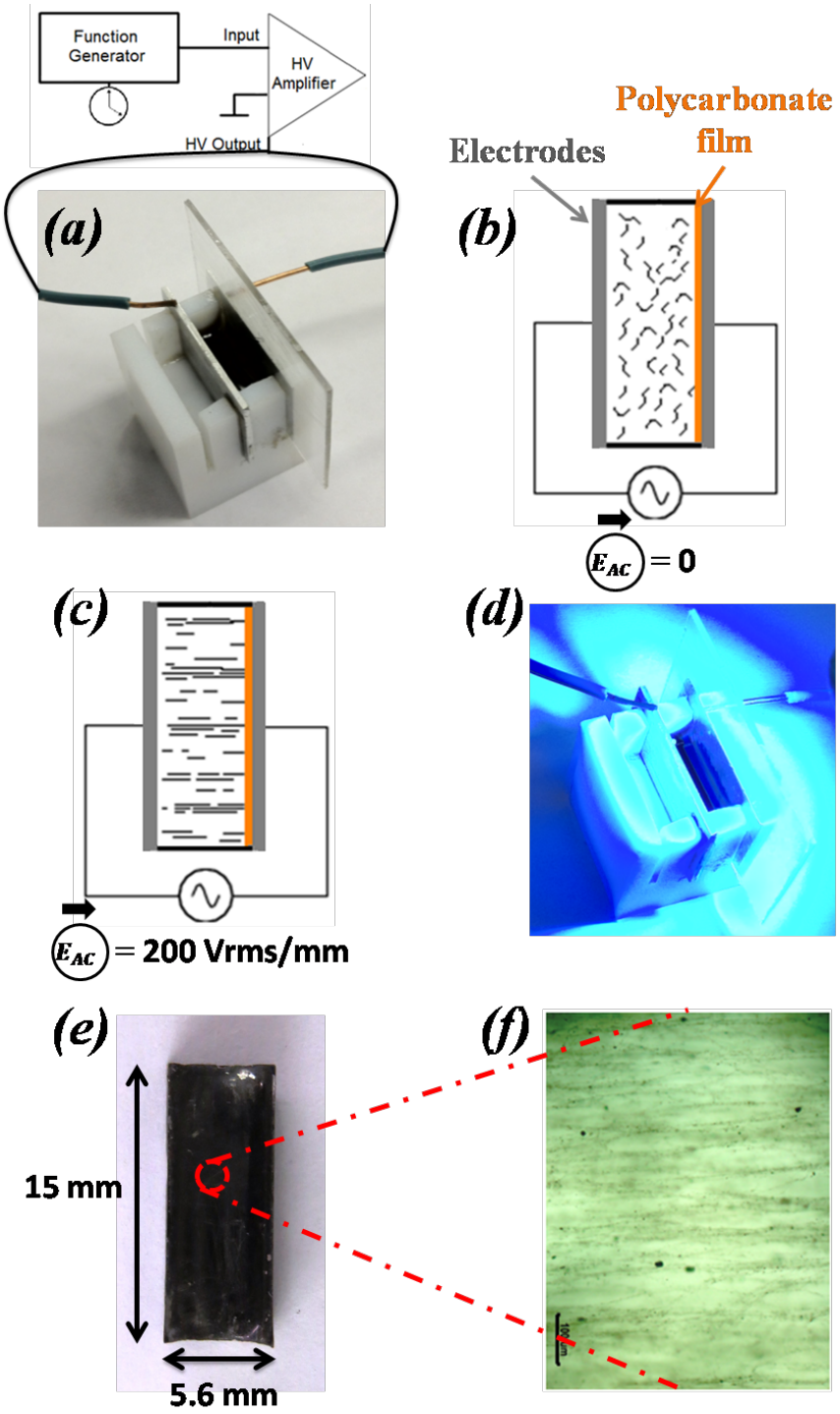

Figure 2.1: Demonstration of AC electric field fabrication of aligned pristine SWNT-filaments nanocomposites with a transmission optical microscopy image of the resulting pristine.

The AC electric field was maintained for 10, 20, or 30 min before applying the curing light for 2 min using a Demetron Optilux 501 Halogen Curing Light to cure the samples as shown in Fig. 2.1d. The electric field was maintained during the curing process in order to lock the pristine SWNTs or COOH-SWNTs into their structural configuration while forming solid test coupons for characterization purposes. The as-produced pristine SWNT-acrylate and COOH-SWNT-acrylate nanocomposite samples were first investigated using a Hirox high magnification (350-7,000x) optical microscope under transmission mode combined with digitally mapping of individual overlapping images to assess pristine SWNT and COOH-SWNT distribution and variations in formed filament width as a function of the AC electric field exposure time over a large specimen area ($\sim 6mm$ x $0.5mm$). The electrical properties of the as-produced pristine SWNTs-acrylate and COOH-SWNTs-acrylate nanocomposite samples were measured using an Agilent E4980A Precision LCR Meter. Raman spectroscopic analysis were obtained using a JY Horiba LabRam HR800 high resolution, 800-mm focal length spectrometer, with a 600 grooves mm^{-1} gratings, with Andor electronically cooled CCD detection system equipped with a 1,024 x 256 pixels front illuminated chip. The slit width and the confocal aperture were set to 150 and 400 μm, respectively. The Excitation energy was provided by a 109 mW, 785 nm (red) laser with a laser power setting of 25% and focused onto the sample through a 40x objective lens. SWNT Raman spectroscopy includes two major features, which are the radial breathing mode (RBM) and tangential G-band mode [162–164]. The tangential G-band spectra were obtained as a function of the angle between the polarization direction of incident light and SWNT filaments alignment axis. Rotating the stage by 15° intervals starting from 0°, where the polarization direction of incident light is parallel to alignment axis, and 90°, where it is perpendicular to the alignment axis. The tangential G-band intensities were recorded for each angle to assess the degree of the alignment for both pristine SWNT and COOH-SWNT-acrylate polymer nanocomposite samples.

2.2 Results and Discussion

Considerable effort was devoted towards the development of phenomenological fabrication models characterizing SWNT alignment as a function of applied electric field magnitude, frequency, and exposure time. To have an appreciation for the relative time scales associated with alignment of the SWNTs vs. the grouping of the SWNTs into aligned filaments, the rotation of ellipsoidal SWNT bundle under dielectrophoresis (DEP) was observed experimentally. Figure 2.2 shows rotation of an ellipsoidal SWNT bundle in the direction of electric field under AC electric field of 200 $V_{RMS}\ mm^{-1}$ with a frequency of 1 kHz as a function of time. For this particular case, it took 2 s for the SWNT bundle to rotate from its initial position into alignment with the electric field direction. Thus, it is expected that the majority of the exposure time is associated with filament width control rather than alignment, such that these two variables (frequency and time) will be correlated in the phenomenological model.

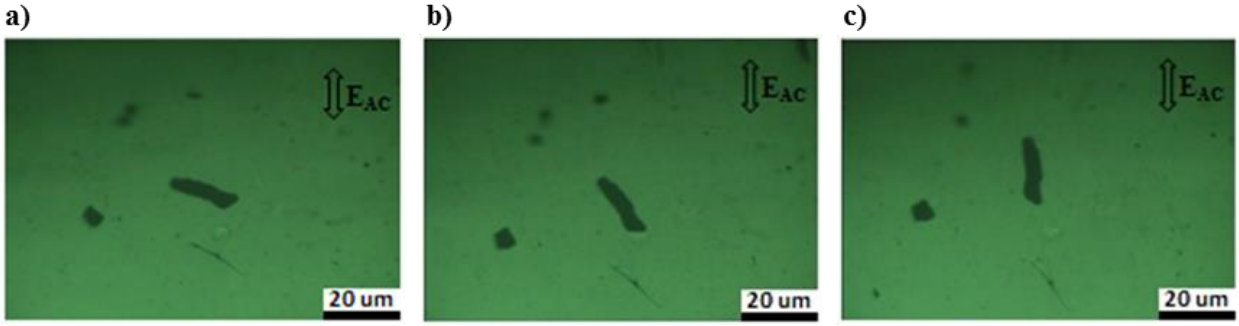

Figure 2.2: Rotation of an ellipsoidal SWNT bundle under AC electric field (EAC) of 200 $V_{RMS}\ mm^{-1}$ with a frequency of 1 kHz: (a) t=0 s, (b) t=1 s, (c) t=2 s.

Initial characterization of pristine SWNTs and COOH-SWNTs alignment and filament formation fabricated with AC electric field strength of 200 $V_{RMS}\ mm^{-1}$ for different frequencies was obtained using transmission optical microscopy combined with digital mapping of individual overlapping images. Figures 2.3 and 2.4 provide digitally mapped wide area high magnification (350x) transmission optical microscopy images of both the well-dispersed (no

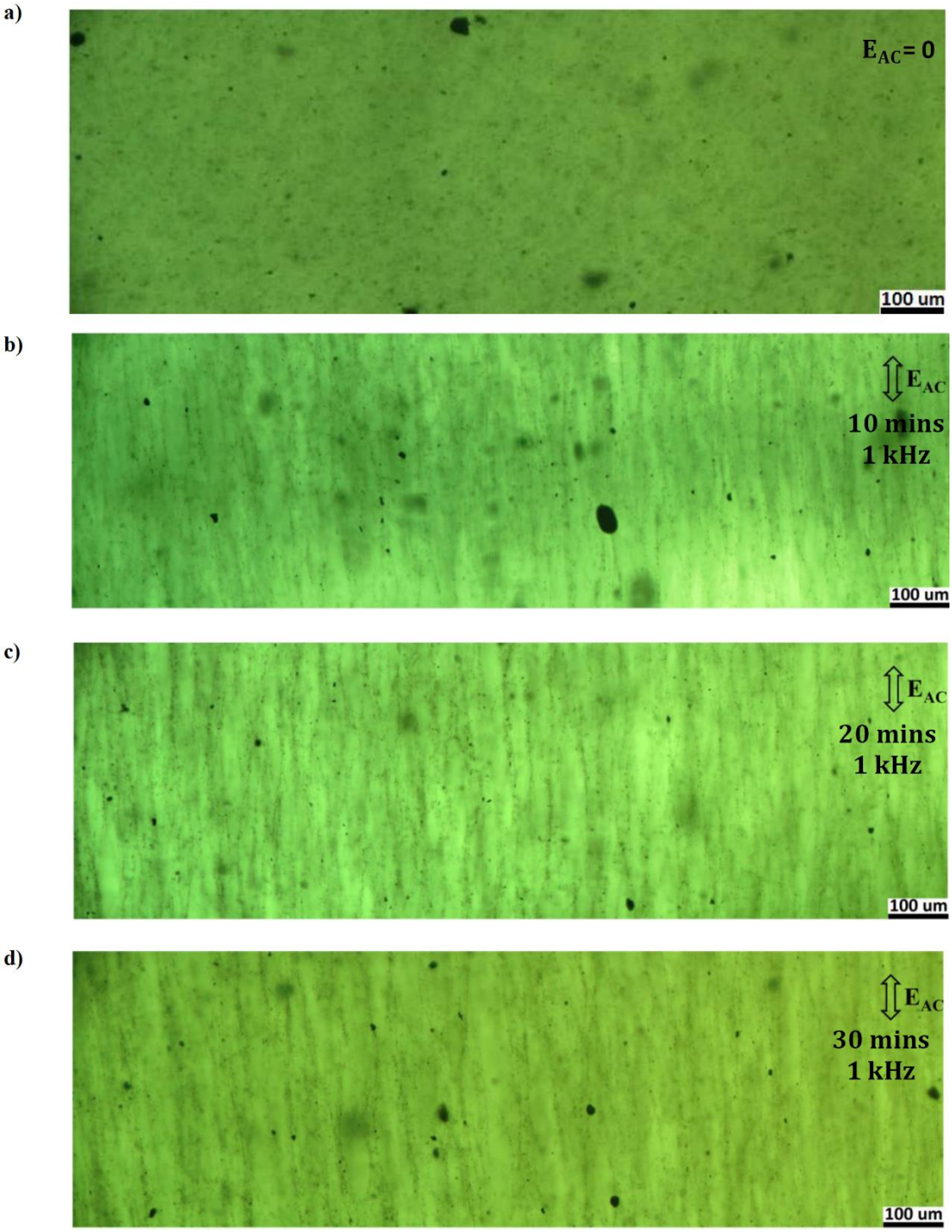

Figure 2.3: Transmission optical microscope panoramic images of 0.03 wt% pristine SWNT-acrylate polymer nanocomposite a) well dispersed pristine SWNTs under zero AC electric field, and aligned CNT-filament formation under AC electric field of 200 $V_{RMS}\ mm^{-1}$ with 1 kHz for three different exposure time to the AC electric field (E_{AC}) during fabrication: b) 10 minutes, c) 20 minutes, d) 30 minutes.

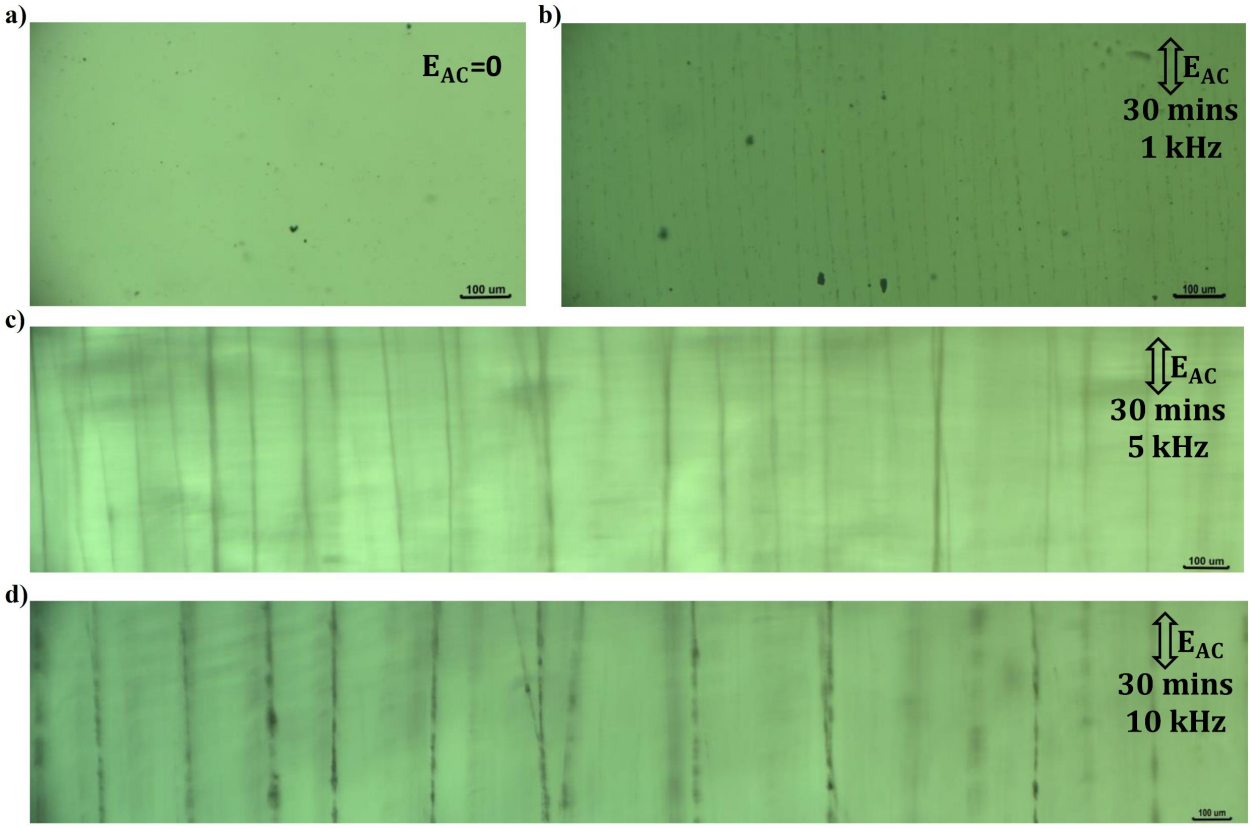

Figure 2.4: Transmission optical microscope panoramic images of 0.03 wt% COOH-SWNT-acrylate polymer nanocomposite (a) well dispersed COOH-SWNTs under zero AC electric field, and aligned CNT-filament formation under AC electric field of 200 $V_{RMS}\ mm^{-1}$ with 30 min exposure time to the AC electric field (E_{AC}) during fabrication for three different AC electric field frequency during fabrication: (b) 1 kHz, (c) 5 kHz, (d) 10 kHz.

electric field) and aligned SWNT cured nanocomposites at various exposure times for pristine and functionalized SWNTs, respectively. Figure 2.3a demonstrates that for the well-dispersed pristine SWNTs there is initially no perceivable alignment and only a few sizable agglomerations of SWNTs. In Fig. 2.3b–d it is observed that filament width varies with exposure time. For the well-dispersed functionalized SWNT nanocomposite shown in Fig. 2.4a, it is observed that there is again no visible alignment in the absence of the electric field, and that there are much fewer and smaller SWNT agglomerations visible. The acid treated functionalized SWNTs contain -COOH groups, which results in improved interaction with -C=O groups [22, 165] in the UDMA chain [166]. Thus, much better dispersion is obtained

with very few agglomerations using functionalized SWNTs in acrylate solution compared to pristine SWNTs. With application of the electric field, functionalized SWNT filaments form (Fig. 2.4b–d); however they are strikingly different from the pristine case in terms of width, number, and recognizable continuity of the filaments. It is noted that pristine SWNT filaments have more metal impurities compared to functionalized SWNT filaments as the acid treatment used in functionalizing the SWNTs has been noted to remove metal catalysts [167–170]. Moreover, it has been observed [171–173] that gold nanowires and rods can be aligned using AC electric fields. This implies that residual metal impurities in the pristine SWNT samples can contribute to the formation of SWNT filaments. Thus, not only do the functionalized samples have to overcome better dispersion and integration with the polymer matrix which lead to thinner and noncontinuous filaments, but they lack the assistance provided by the residual metal catalyst in the pristine samples which results in wider filament formation shown in Fig. 2.7a and b and higher conductivities in the axial and transverse directions shown in Fig. 2.10a and b. To quantify the observations made in Figs. 2.3 and 2.4, the filament width and spacing were examined both horizontally and vertically. Over a wide field of view, width and spacing measurements were made spanning the horizontal and vertical image range, with many filaments having multiple measurements along their length and spacing. It is noted that data sets for filament width and spacing distributions are measured at a specified depth of field and that multiple depths of field settings are used in order to demonstrate that these distributions are not strongly sensitive to the overall thickness of the samples. Figure 2.5 shows how the samples were analyzed to obtain statistically meaningful distribution functions for filament width and spacing as a function of frequency and exposure time to the AC electric field. Figure 2.5 shows transmission optical microscope panoramic images of filaments in the 0.03 wt% COOH-SWNT-acrylate polymer nanocomposite aligned CNT-filament. The sample was exposed to an AC electric field (E_{AC}) of 200 $V_{RMS}\ mm^{-1}$ with a frequency of 5 and 1 kHz, each after 30 min of exposure time during fabrication. The measurements for the pristine SWNT acrylate nanocomposite samples were taken using the same methodology.

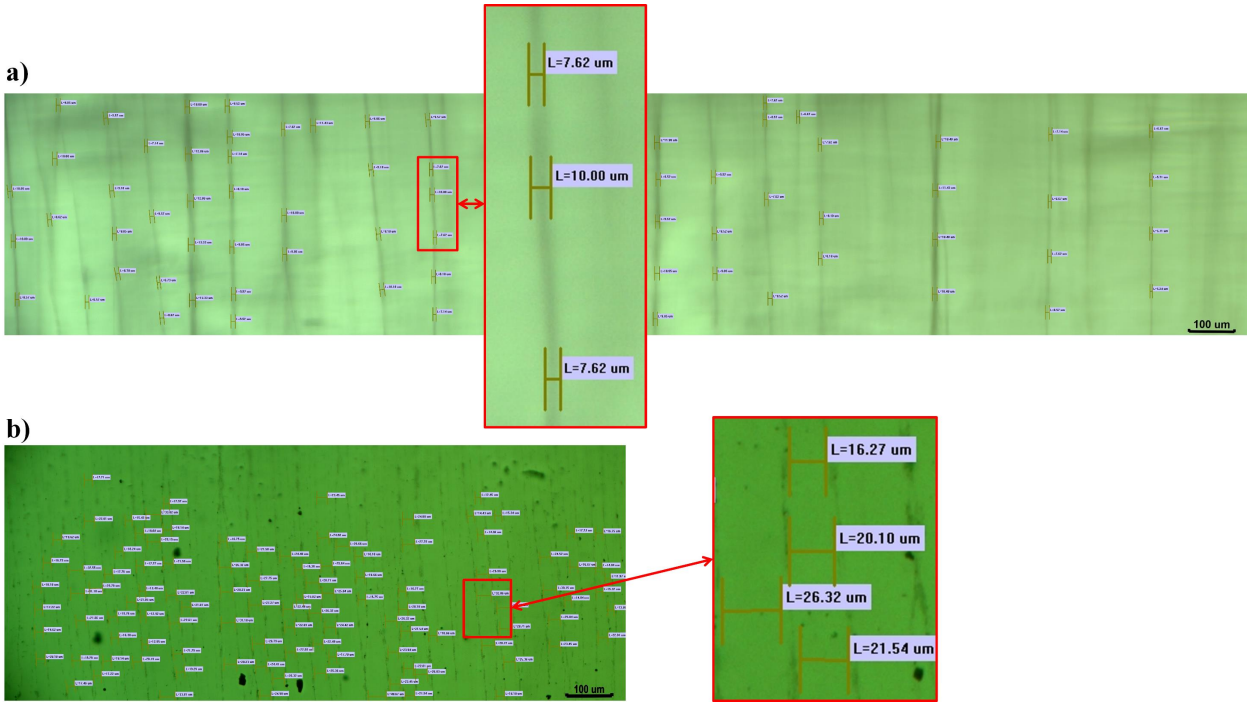

Figure 2.5: (a) Filament width and (b) spacing between filaments (micrometer, μm) shown in transmission optical microscope panoramic images of 0.03 wt% COOH-SWNT-acrylate polymer nanocomposite aligned CNT-filament formation under AC electric field (E_{AC}) of 200 $V_{RMS}\ mm^{-1}$ with (a) 5 kHz (b) 1 kHz for 30 min of exposure time during fabrication [100 measurements for width and 86 measurements for spacing].

Fig. 2.6 provides width distributions for the cases studied. Increasing duration of exposure to AC electric field results in an increase in filament width for a frequency of 1 kHz, as the width distribution shifts to greater average width in Fig. 2.6a. For the frequency of 10 kHz shown in Fig. 2.6b, the filament width distribution shifts further to the right, which indicates that an increase in AC field frequency causes wider filament formation. Similar behavior was observed in Fig. 2.6c and d for the COOH-SWNT acrylate nanocomposite samples. Thus, an increase in both of the exposure time and the frequency leads to more extensive agglomeration of SWNTs to form the aligned filaments during fabrication and results in an increase in width of aligned filaments. Exposure time to AC electric field results in an increase in filament width and an increase in spacing between filaments, consistent with geometric and conservation of mass constraints. Spacing distribution between filaments is

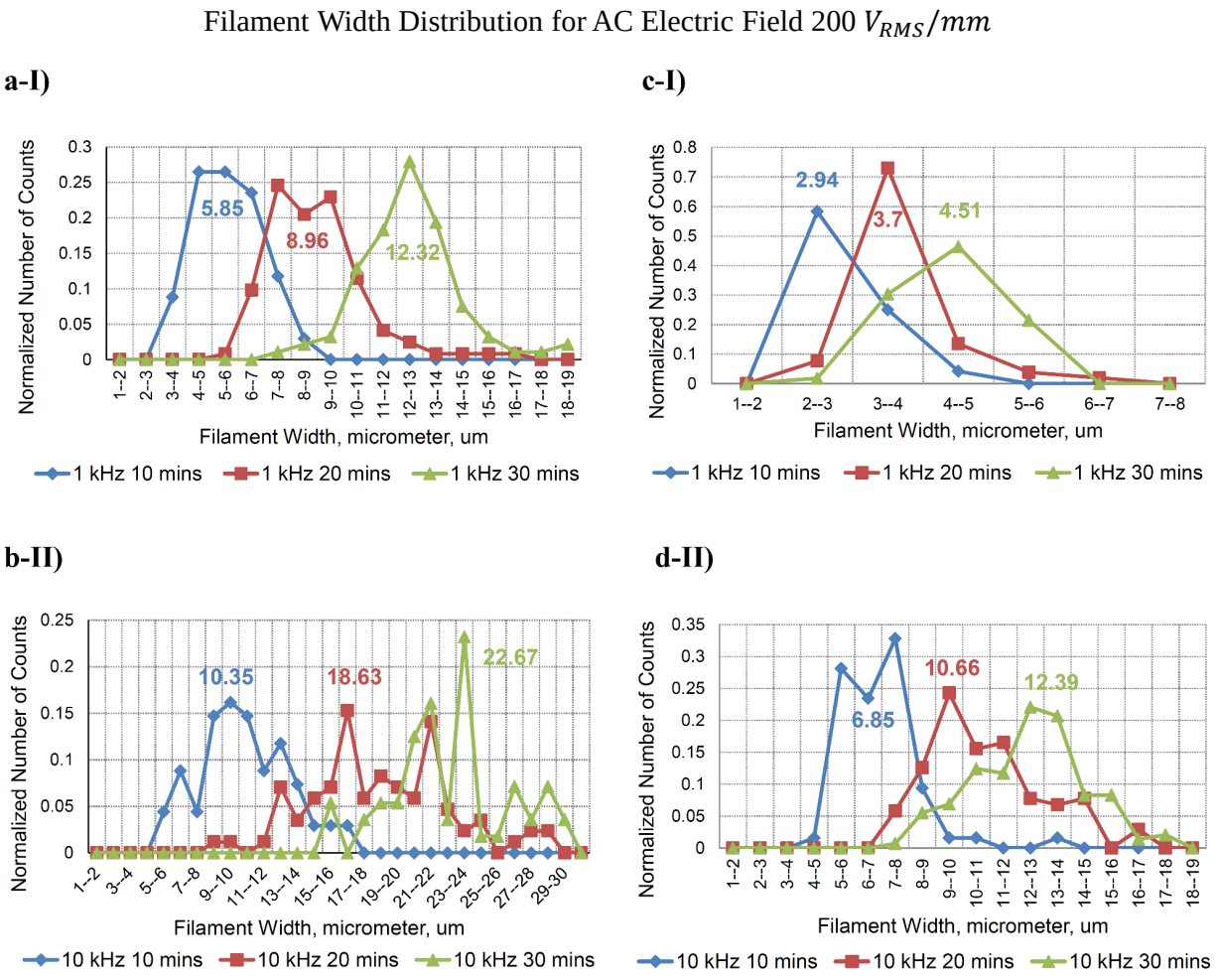

Figure 2.6: Assessment of 0.03 wt% (a) (b) pristine SWNT and (c) (d) COOH-SWNT-acrylate polymer nanocomposite aligned CNT-filament formation under AC electric field of 200 $V_{RMS}\ mm^{-1}$, filament width distributions as a function of frequency and exposure time to the AC electric field during fabrication by counting the filaments width normalized data. (I) 1 kHz, (II) 10 kHz Normalized number of counts is defined as the number of times a given width/spacing measurement was obtained divided by the total number of measurements of the width/spacing made on a particular sample, i.e. such that the sum of all normalized counts for sample is 1.

similar to the width distribution for the cases studied. Considering the frequency of 1 kHz for pristine SWNTs acrylate nanocomposite, the spacing distribution shifts to increased filament width as exposure time to AC electric field increases. For the frequency of 10 kHz for pristine SWNTs acrylate nanocomposite sample, the spacing distribution shifts to

even greater widths, proving that an increase in AC field frequency causes larger spacing between filaments due to wider filament formation, i.e., the number of SWNTs forming individual filaments is increasing. Similar behavior was observed for the COOH-SWNT acrylate nanocomposites. For each case approximately 80 width and spacing measurements were taken and used to construct average values and standard deviations. These data are used to create the filament width and the spacing formation functions of exposure time to the AC electric field with different frequencies.

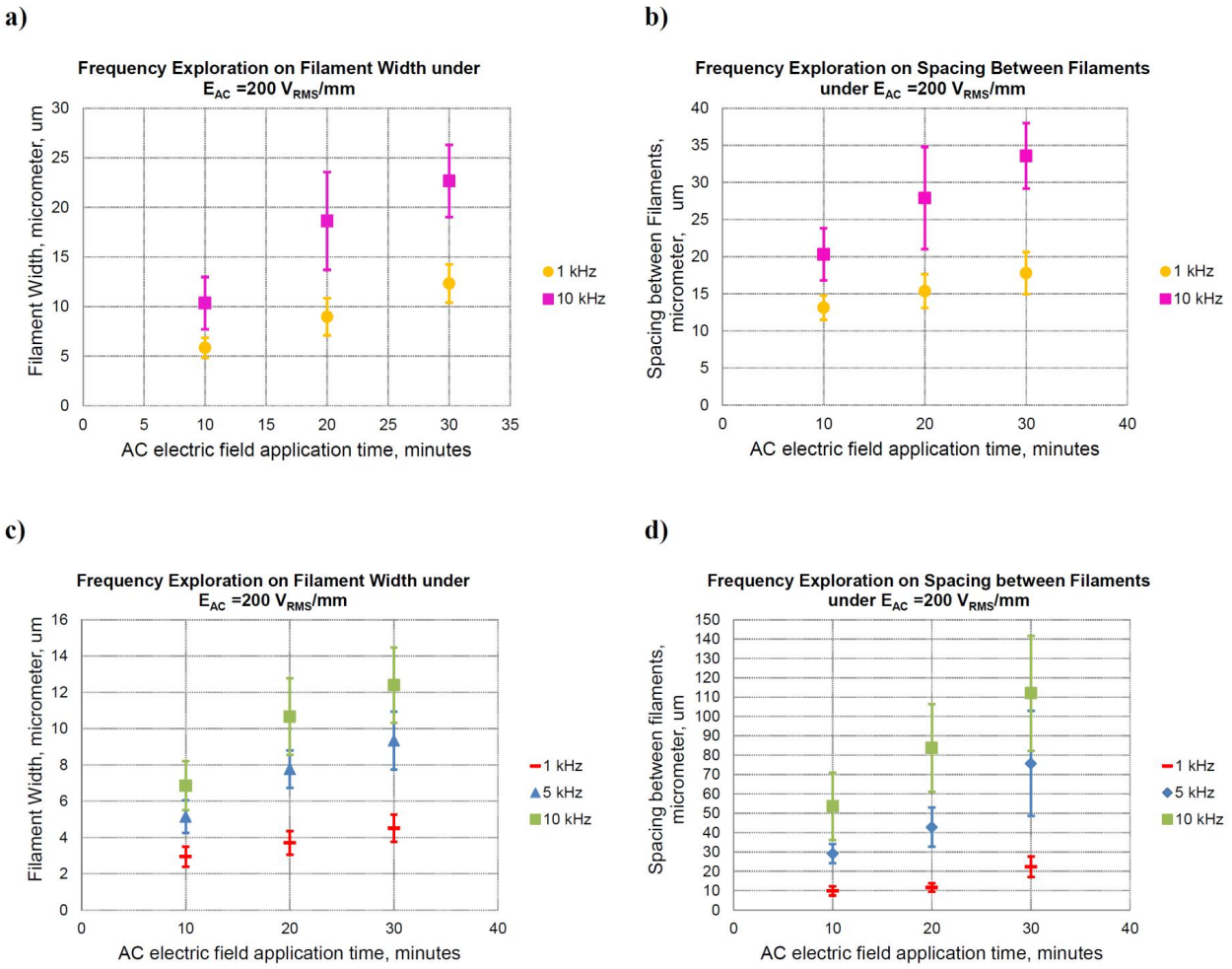

Figure 2.7: Assessment of 0.03 wt% (a) (b) pristine SWNT and (c) (d) COOH-SWNT-acrylate polymer nanocomposite aligned CNT-filament formation under AC electric field of 200 $V_{RMS}\ mm^{-1}$. (a) and (c) Measurement of filament width and (b) and (d) spacing between the filaments as a function of frequency and exposure time to the AC electric field during fabrication.

Fig. 2.7a shows that the filament width of 0.03 wt% pristine SWNT-acrylate polymer nanocomposites increases as exposure time to AC electric field and frequency increase. The spacing between the filaments of 0.03 wt% pristine SWNT-acrylate polymer nanocomposites in Fig. 2.7b increases as exposure time to AC electric field and frequency increase. Moreover, it is found that the filament width in Fig. 2.7c and the spacing between the filaments in Fig. 2.7d of 0.03 wt% COOH-SWNT-acrylate polymer nanocomposites all increase with increasing exposure time to AC electric field and increasing frequency. Comparatively, the aligned pristine SWCT-filaments were wider compared to the aligned COOH-SWNT-filaments. This indicates that the network for filament formation is more efficient for pristine SWNT-acrylate solution than that of the COOH-SWNT-acrylate solution, due to either one of two possible effects. First, the CNT geometry affects the magnitude of the dielectrophoretic forces and torques on the CNTs. Thus, local CNT dispersion (agglomeration) plays a crucial role. Under DEP, the local gradients in electric field between two neighboring CNTs leads to additional polarization and they are thus attracted to one another as time and frequency increase, leading to multi-CNT-filament formation [64] [55]. The few sizable agglomerations of SWNTs for the well-dispersed pristine SWNTs in Fig. 2.3 a compared to much fewer and smaller SWNT agglomerations for the well-dispersed functionalized SWNTs visible in Fig. 2.4 a suggests that the pristine SWNTs become additionally polarized and attracted to each other more rapidly to create the network for filament formation. Secondly, movement of COOH-SWNTs becomes restricted due to the interaction of hydrogen bonding between carboxyl group -COOH of COOH-SWNTs and the carbonyl groups -C=O [22, 174] of UDMA and HDDMA chains, which makes it more difficult to form the network for filament formation for COOH-SWNT-acrylate solution than for the pristine SWNT- acrylate solution. Multivariable polynomial fits to the data in Fig. 2.7 were obtained for the filament width and the spacing between filaments as functions of exposure time to the AC electric field and field frequency which are provided in Table 2.2 where W, S, t and ω represent the filament width, spacing between the filaments, exposure time to the AC electric field and its frequency, respectively. The correlation coefficients of the multivariable fit for filament

width and spacing between the filaments of pristine SWNT-acrylate nanocomposites are 0.9958 and 0.9994, respectively and are 0.9963 and 0.9950, respectively, for COOH-SWNT-acrylate nanocomposites. These fits were used in conjunction with triangle-based cubic interpolation [175] to obtain a surface plot relative to the fitted data as shown in Fig. 2.8. Within the range of the data set, the surface plot gives an indication of how one could tune fabrication parameters to obtain desired filament width and spacing.

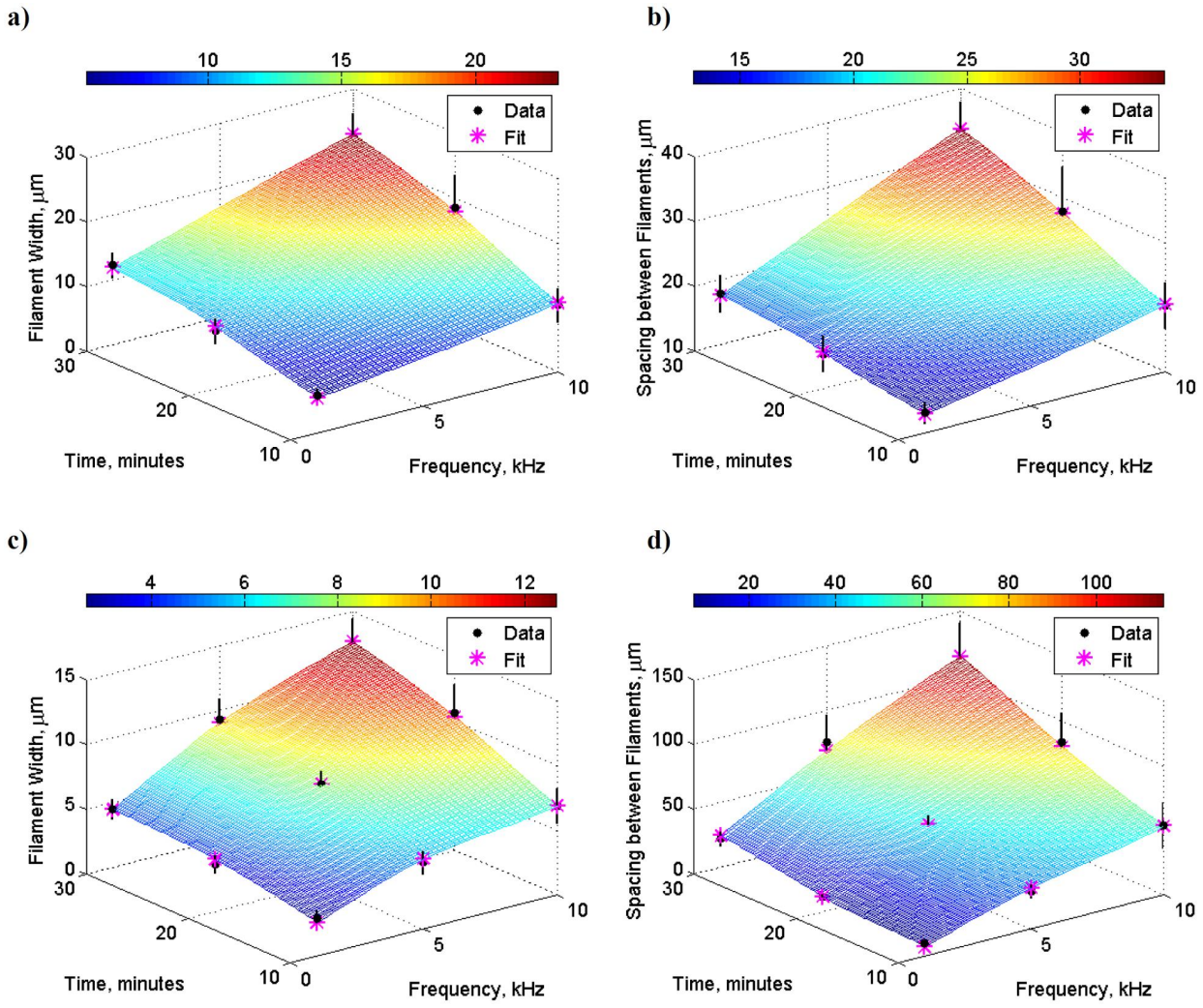

Figure 2.8: Multivariable polynomial fit for 0.03 wt% (ab) pristine SWNT and (cd) COOH-SWNT-acrylate polymer nanocomposite aligned CNT-filament formation under AC electric field of 200 $V_{RMS}\ mm^{-1}$. (a) and (c) Measurement of filament width and (b) and (d) spacing between the filaments as a function of frequency and exposure time to the AC electric field during fabrication.

Table 2.2: Filament width and the spacing formation functions of various exposure times to AC field (t, minutes) and frequency (ω , kHz), where R is correlation coefficient.

0.03 wt% pristine SWNT-acrylate polymer nanocomposites		
Filament Width Curve Fitting		
$W = -0.4270 - 0.3829\,\omega + 0.6900\,t + 0.0325\,\omega t + 0.0583\,\omega^2 - 0.0100\,t^2$	&	$R = 0.9958$
Spacing between the Filaments Curve Fitting		
$S = 5.0970 + 4.5986\,\omega + 0.3606\,t + 0.0479\,\omega t - 0.3856\,\omega^2 - 0.0044\,t^2$	&	$R = 0.9994$
0.03 wt% COOH-SWNT-acrylate polymer nanocomposites		
Filament Width Curve Fitting		
$W = -0.5980 + 0.7658\,\omega + 0.2774\,t + 0.0217\,\omega t - 0.0459\,\omega^2 - 0.0051\,t^2$	&	$R = 0.9963$
Spacing between the Filaments Curve Fitting		
$S = 7.0544 + 4.9083\,\omega - 1.1317\,t + 0.2494\,\omega t - 0.2080\,\omega^2 + 0.0439\,t^2$	&	$R = 0.9950$

Fig. 2.9 shows the tangential G-band spectra of 0.03 wt% pristine SWNT and COOH-SWNT-acrylate polymer nanocomposite aligned under AC electric field (E_{AC}) of $200 V_{RMS}/mm$ with frequencies of 1 and 10 kHz, respectively, after 20 min of exposure to the alignment field during fabrication. The tangential G-band intensity decreases as the angle between the polarization direction of incident light and SWNT filaments alignment axis increases. As expected, a maximum is observed at 0 when the polarization direction of incident light is parallel to alignment axis and a minimum is observed at 90° when the polarization direction of incident light is perpendicular to alignment axis [162, 163, 174, 176, 177]. To assess the alignment for both pristine and COOH-SWNT-acrylate polymer nanocomposites, the tangential G-band intensity ratios of different polarization angles of 15° intervals from 90° to 0° are listed in Table 2.3. Table 2.3 indicates that an increase in frequency during fabrication leads to better alignment because the tangential G-band ratio of 90°/0° decreases as frequency during fabrication increases. An increase in exposure time to AC field during fabrication also leads to a decrease in the tangential G-band ratio of 90°/0° for the three

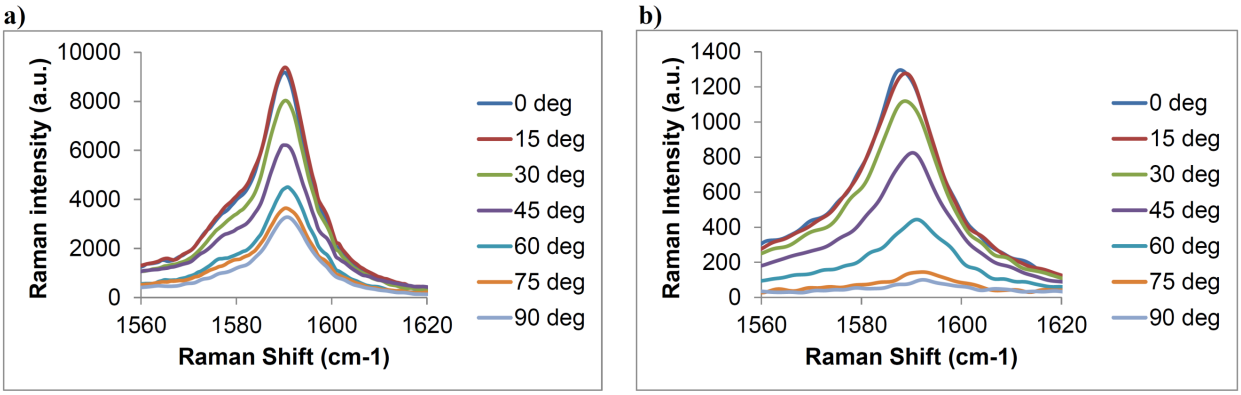

Figure 2.9: Raman spectra of the G-band of aligned 0.03 wt% (a) pristine SWNT and (b) COOH-SWNT-acrylate polymer nanocomposite under AC electric field (EAC) of 200 V_{RMS} mm^{-1} with (a) 1 kHz and (b) 10 kHz for 20 min of exposure time during fabrication at different polarizer angles, ranging from 0° to 90°.

Table 2.3: Raman tangential G-band intensity ratio for different polarizer angles for both pristine SWNT and COOH-SWNT-acrylate polymer nanocomposite.

Tangential G-band intensity ratio	10 kHz; 20 min COOH-SWNT	5 kHz; 20 min COOH-SWNT	1 kHz; 20 min COOH-SWNT	1 kHz; 30 min COOH-SWNT	1 kHz; 10 min COOH-SWNT	1 kHz; 20 min SWNT	10 kHz; 20 min SWNT
15o/0°	0.961 ± 0.024	0.888 ± 0.057	1.134 ± 0.024	1.027 ± 0.085	1.005 ± 0.024	1.025 ± 0.014	–
30°/0°	0.743 ± 0.120	0.872 ± 0.084	0.956 ± 0.024	0.756 ± 0.018	0.907 ± 0.034	0.941 ± 0.046	–
45°/0°	0.583 ± 0.053	0.647 ± 0.173	0.737 ± 0.053	0.611 ± 0.055	0.791 ± 0.029	0.770 ± 0.073	0.527 ± 0.042
60°/0°	0.356 ± 0.014	0.394 ± 0.103	0.559 ± 0.014	0.457 ± 0.032	0.640 ± 0.020	0.636 ± 0.106	–
75°/0°	0.208 ± 0.096	0.316 ± 0.104	0.463 ± 0.096	0.386 ± 0.028	0.511 ± 0.006	0.525 ± 0.092	–
90°/0°	0.176 ± 0.098	0.243 ± 0.117	0.410 ± 0.098	0.389 ± 0.013	0.449 ± 0.012	0.439 ± 0.067	0.296 ± 0.041

Polarized Raman spectroscopy was performed on both aligned SWNTs filaments and between filaments. The spot size was 1.7 μm

different exposure times provided. It was observed [57] that the tangential G-band ratio of 90°/0° of 0.1 wt% aligned oxidized (COOH-acid treated) MWNT/PMMA composites with AC electric field of 5 $V_{RMS}\ mm^{-1}$ with frequency of 500 Hz for 180 min of exposure time was 0.77. However, the tangential G-band ratio of 90°/0° of 0.03 wt% of COOH-SWNT-acrylate polymer nanocomposites with AC electric field of 200 $V_{RMS}\ mm^{-1}$ with frequency of 10 kHz for 20 min of exposure time is 0.176. Moreover, the tangential G-band ratio of 90°/0° of pristine SWNT-acrylate polymer nanocomposite is higher than that of COOH-SWNT-acrylate polymer nanocomposite, which indicates that the alignment of COOH-SWNT filaments is slightly better than for pristine SWNT filaments. Comparing additional ratios relative to the 0° data demonstrates the relative magnitude of misalignment within the sample.

The degree of alignment achieved within the nanocomposite samples is also assessed in the AC electrical conductivity measurements provided in Fig. 2.10 for the 0.03 wt% pristine SWNT and COOH-SWNT along with the neat polymer conductivity. The improvements in electrical conductivity are obtained at a concentration below percolation threshold. As expected, conductivity in the alignment direction for both SWNT and COOH-SWNT nanocomposites is a few orders of magnitude higher than that of both nanocomposites with well-dispersed, but randomly oriented, pristine SWNTs or COOH-SWNTs, which in turn are a few orders larger than the neat polymer. The increases in conductivity can be attributed to the formation of pristine SWNT or COOH-SWNT filaments. As observed in Fig. 2.10a, addition of 0.03 wt% of randomly oriented and well-dispersed pristine SWNTs resulted in an increase of two orders of magnitude compared to the neat acrylate polymer. It is noted [42] that the (longitudinal) conductivity parallel to electric field at 1 kHz for an AC electric field of 28 $V_{RMS}\ mm^{-1}$ with frequency of 2 kHz for 10 min of exposure time during fabrication on 0.5 wt% MWNT suspension of epoxy was on the order of 10^{-11} S cm^{-1}, which was three orders of magnitude higher than that of pure epoxy. However, aligning 0.03 wt% pristine SWNTs for 30 min exposure time to AC electric field at 1 and 10 kHz results in four and five orders of magnitude increase in the electrical conductivity in the alignment direction compared

to the neat acrylate polymer, respectively. Comparatively, as observed in Fig. 2.10c, the conductivity in the alignment direction for COOH-SWNTs-acrylate nanocomposites results in 2.8 and 3.3 orders of magnitude increase in the electrical conductivity in the alignment

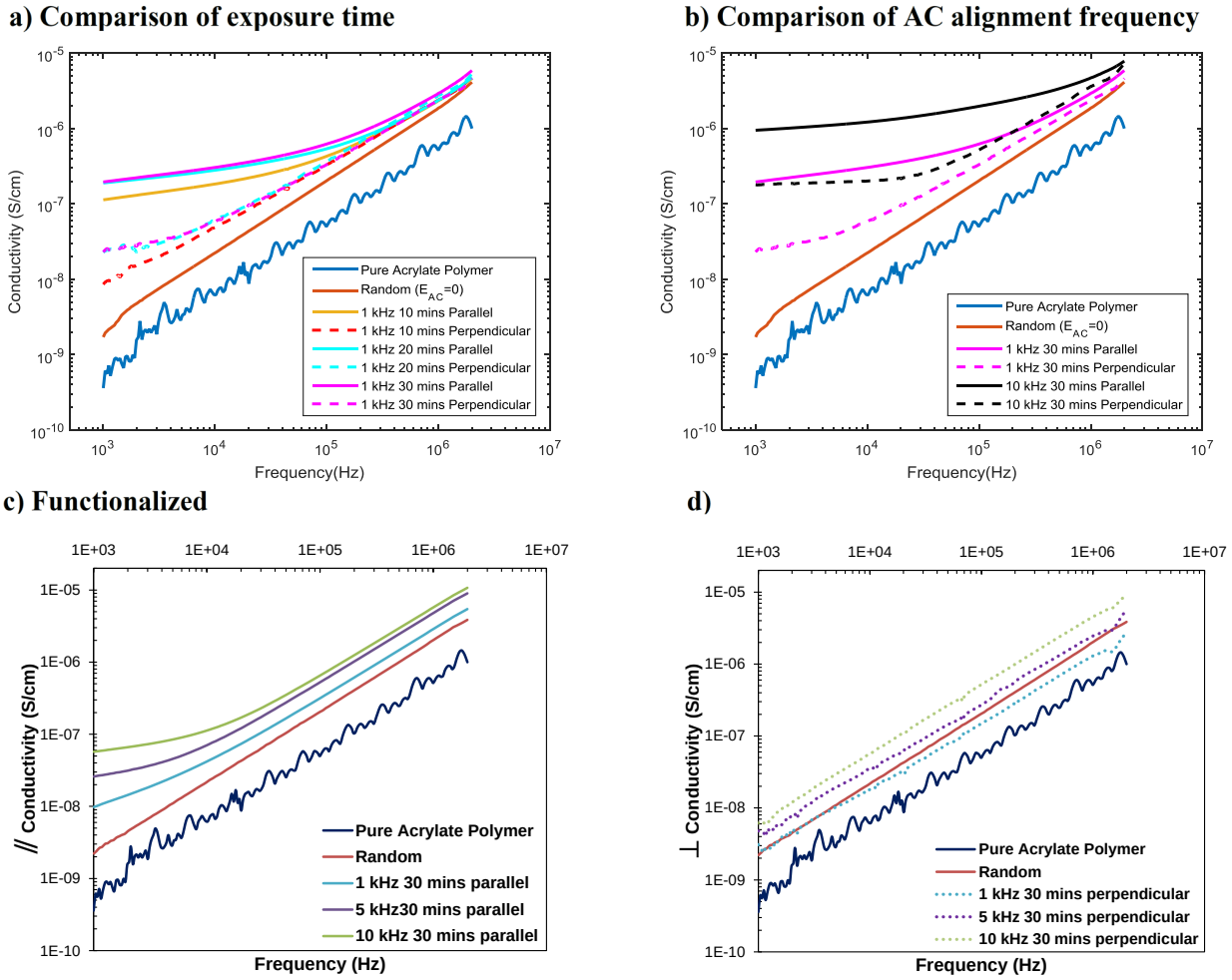

Figure 2.10: Assessment of 0.03 wt% (a) (b) SWNT (c) (d) COOH-SWNT-acrylate polymer nanocomposite aligned CNT-filament formation under AC electric field of 200 $V_{RMS}\ mm^{-1}$: Changes in nanocomposite conductivity at various measurement frequencies associated with microstructural evolution of SWNT filaments. The cases considered include pure polymer, well-dispersed randomly oriented SWNTs (random) and aligned CNT filament microstructures formed under (a) AC field frequencies of 1 and 10 kHz for varying degrees of AC field exposure times and (b) AC field frequencies of 1 and 10 kHz for 30 min of AC field exposure time (c) (d) AC field frequencies of 1, 5, and 10 kHz for 30 min of AC field exposure time. Conductivities are provided in both the CNT filament alignment direction (denoted by parallel) and the transverse direction (perpendicular).

direction compared to the neat acrylate polymer for as-produced solid test coupons after 30 min of exposure to AC electric field at 1 and 10 kHz, respectively. Thus, increases in exposure time to AC field and the frequency during fabrication led to wider aligned filaments and an increase in electrical properties in the alignment direction for both 0.03 wt% pristine SWNT and COOH-SWNT-acrylate polymer nanocomposites. However, thinner filaments or breaks in the COOH-SWNT filaments observed using optical microscopy results in a decrease in the conductivity in the alignment direction as compared to the pristine SWNT-acrylate polymer nanocomposites. Unexpectedly, the conductivity relative to nanocomposites with randomly oriented well-dispersed SWNTs also increases in the transverse direction for both 0.03 wt% pristine SWNT and COOH-SWNT-acrylate polymer nanocomposites. It would be expected that conductivity in the transverse direction would be less than that in the randomly well-dispersed sample, but here it is higher for both acrylate polymer nanocomposites. This is due to the network of pristine SWNT or COOH-SWNT filaments that have bridges from one to the other in the transverse direction. The other ratios relative to the 0° in Table 2.3 indicate that there are small degrees of misalignment in high aspect ratio CNT filaments leading to a network of SWNT filaments that have bridges from one to the other in the transverse direction. The Raman spectroscopy results are well-correlated with electrical conductivity results. Increases in exposure time to AC field and the frequency during fabrication led to an increase in electrical properties both in the alignment direction and in transverse direction for both 0.03 wt% pristine SWNT and COOH-SWNT-acrylate polymer nanocomposites.

Chapter 3

Piezoresistivity Characteristics of Aligned Carbon Nanotube-Polymer Nanocomposites

Dielectrophoresis under the application of AC electric fields is one of the primary fabrication techniques for obtaining aligned carbon nanotube (CNT)-polymer nanocomposites, and is used here to generate long range alignment of CNTs at the structural level. The degree of alignment of CNTs within this long range architecture is observed via polarized Raman spectroscopy so that its influence on the electrical conductivity and piezoresistive response in both the alignment and transverse to alignment directions can be assessed. Nanocomposite samples consisting of randomly oriented, well dispersed single-wall carbon nanotubes (SWCNTs) and of long range electric field aligned SWCNTs in a photopolymerizable monomer blend (urethane dimethacrylate (UDMA) and 1,6-hexanediol dimethacrylate (HDDMA)) are quantitatively and qualitatively evaluated. Piezoresistive sensitivities in form of gauge factors were measured for randomly oriented, well dispersed specimens with 0.03, 0.1 and 0.5 wt% SWCNTs and compared with gauge factors in both the axial and transverse to SWCNT alignment directions for electric field aligned 0.03 wt% specimens under both quasi-static

monotonic and cyclic tensile loading. Gauge factors in the axial direction were observed to be on the order of 2, while gauge factors in the transverse direction demonstrated a 5 fold increase with values on the order of 10 for aligned specimens. Based on Raman analysis, it is believed the higher sensitivity of the transverse direction is related to architectural evolution of misaligned bridging structures which connect alignment structures under load due to Poisson's contraction.

3.1 Experimental Details

3.1.1 Materials

In the present study, SWCNTs have been dispersed and aligned in a blend of two different photopolymerizable monomers which consisted of urethane dimethacrylate (UDMA) and 1,6-hexanediol dimethacrylate (HDDMA). The monomers, the camphorquinone photoinitiator, and the N,N-dimethyl-aminoet hylmethacrylate accelerator, were obtained from Esstech. The pristine SWCNTs, grown by chemical vapor deposition, were obtained from NanoLab and were reported to have a purity of more than 95%, ∼1.5 nm diameter and average lengths between 1-5 μm.

3.1.2 Preparation of SWCNT-Acrylate Nanocomposites

Following the same procedures outlined in [37,38], neat polymer samples were prepared from the photopolymerizable monomers with a ratio of 9 to 1 (UDMA/HDDMA (9/1)) to obtain the precursor acrylate solution, with this ratio likewise maintained in the preparation of nanocomposite samples having concentrations of 0.03, 0.1 and 0.5 wt% SWCNTs relative to the entire SWCNT-acrylate solution. In preparing nanocomposite samples, varying weight concentrations of SWCNTs were added first to the lower viscosity HDDMA (compared to UDMA). SWCNTs were dispersed using a bath sonication for 1.5 hours with a Qsonica

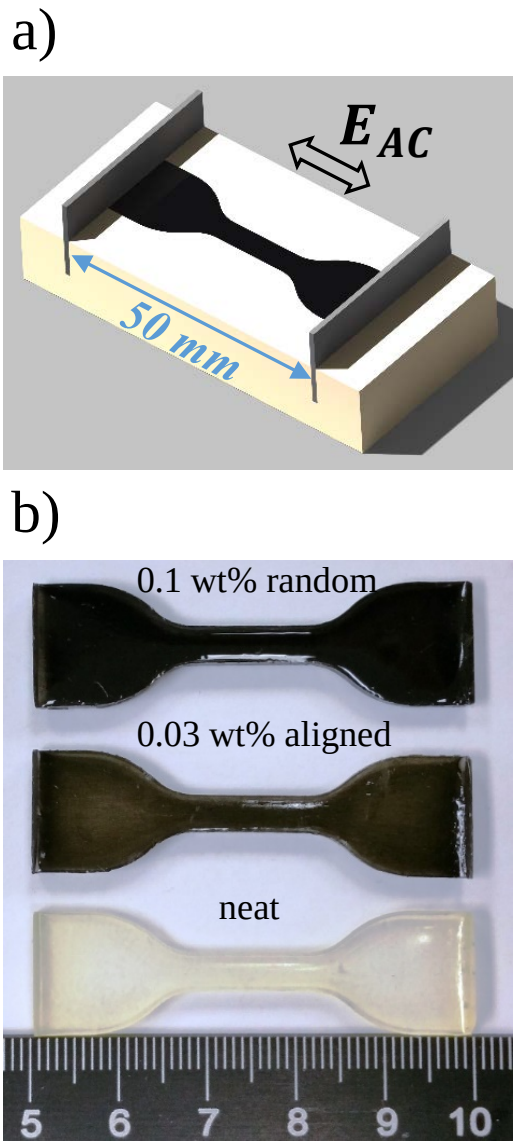

Figure 3.1: a) Demonstration of AC electric field fabrication of aligned 0.03 wt% SWCNT-acrylate nanocomposite, b) As-produced neat acrylate, 0.03 wt% SWCNT-acrylate nanocomposite and 0.1 wt% of randomly oriented acrylate nanocomposite specimens

Sonicator 4000 operating at 20 kHz and amplitude of 25% to obtain a more uniform initial dispersion of SWCNTs. The UDMA was then added to the predispersed SWCNT-HDDMA solution and resonicated for an additional 2.5 hours with the same settings to obtain a homogeneous SWCNT distribution within the acrylate solution. A stirring plate with magnetic stir bar was used at 200 rpm to mix 0.3 wt% photoinitiator and 0.4 wt% accelerator

added into SWCNT-acrylate solution to obtain photocurable/ polymerizable nanocomposite acrylate solution. The prepared nanocomposite solutions were heated to 65 ^{o}C and then subsequently poured into a dog-bone shaped Teflon mold between a pair of parallel aluminum electrodes with a spacing of 50 mm. Nanocomposite samples with well-dispersed, randomly oriented SWCNTs at concentrations of 0.03, 0.1 and 0.5 wt% were cured with no electric field applied using a Demetron Optilux 501 Halogen Curing Light with an output wavelength range of 400-505 nm (nanometers) for 2 minutes. In Sengezer et al. [37], a phenomenological approach to understanding the CNT alignment and the multi-CNT-filament formation under dielectrophoresis was explored by tuning the applied electric field magnitude, frequency and exposure time. It was observed that a combination of exposure time to AC electric field and its frequency were the key drivers of creating a network for filament formation. Moreover, it was also observed that the network filament formation was much more efficient for pristine SWCNT-acrylate solution than that of COOH functionalized SWCNTs. For this study, a combination of Agilent 33522A Waveform Generator and Trek Model 10/10B-HS-L-CE High Voltage Amplifier was used to obtain AC field-induced alignment within a dog-bone shaped Teflon mold between a pair of parallel aluminum electrodes as illustrated in Fig. 3.1 a. The electric field applied to the electrodes was 40 V_{RMS}/mm at a frequency of 5 kHz for 2 min exposure time leading to long range alignment and formation of SWCNT filaments in 0.03 wt% nanocomposite acrylate solutions before applying the curing light under the same electric field settings. The electric field was maintained during the curing process in order to lock the pristine SWCNTs into their structural configuration while forming the solid aligned bulk dog-bone SWCNT-acrylate nanocomposite samples. The neat acrylate and SWCNT-nanocomposite specimens shown in Fig. 3.1 b with a gage length of 11 mm for tensile loading have dimensions 50 x 4.2 x 1.7 mm (L x W x t) rescaled from ASTM standard D638 for specimen type IV, where the loading is exerted in longitudinal direction of 28 mm for the distance between the grips.

3.1.3 Morphological Characterization

The as-produced neat and SWCNT-acrylate nanocomposite samples were firstly investigated using a Hirox high magnification (350-7000x) optical microscope under transmission mode combined with digital mapping of individual overlapping images to assess SWCNT aligned filament structure. Raman spectroscopy data on SWNT alignment was obtained using a JY Horiba LabRam HR800 high resolution, 800 mm focal length spectrometer, with 600 $grooves/mm$ gratings, along with an Andor electronically cooled CCD detection system equipped with a 1024x256 pixels front illuminated chip. The slit width and the confocal aperture were set to 150 μm and 400 μm, respectively. The excitation energy was provided by a 109 mW, 785 nm (red) laser with a laser power setting of 25% which was focused onto the sample through a 40x objective lens. The tangential G-band spectra were obtained as a function of the angle between the polarization direction of incident light and the SWCNT filament alignment axis by rotating the stage about the selected spot by 15° intervals starting from 0°, where the polarization direction of incident light is parallel to alignment axis, and 90°, where it is perpendicular to the alignment axis. The tangential G-band intensities were recorded for each angle to assess the degree of the alignment for SWCNT-acrylate polymer nanocomposite samples at the local microscale level. A NeoScope JCM-5000 Benchtop SEM and a LEO (Zeiss) 1550, high-performance Schottky field-emission scanning electron microscope were used to conduct fracture surface topography characterization of neat and SWCNT-acrylate nanocomposites after mechanical testing.

3.1.4 Electrical and Piezoresistivite Characterization

The electrical properties and piezoresistive behavior of the as-produced pristine SWNT-acrylate nanocomposite samples were obtained using an Agilent E4980A Precision LCR Meter via a two terminal method (i.e., volume resistivity test) by applying 1 V at 10 kHz; the latter in conjunction with an Instron 5967 Dual Column testing system and LabVIEW for LCR meter data acquisition. Neat acrylate and nanocomposite samples with

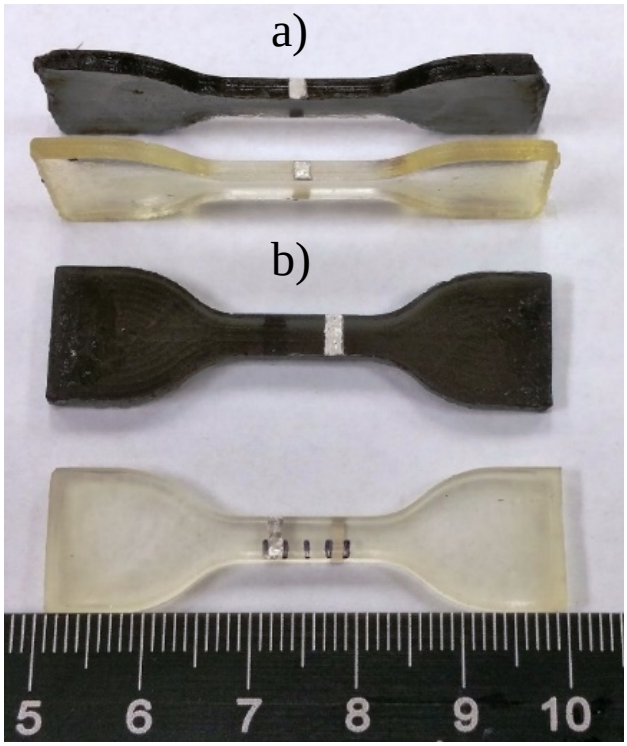

Figure 3.2: a) Electrode set-up for transverse piezoresistive response under tensile loading and b) electrode set-up for axial piezoresistive response under tensile loading

well-dispersed, randomly oriented SWCNTs at concentrations of 0.03, 0.1 and 0.5 wt% were tested for piezoresistivity measurements under quasi-static monotonic loading. Aligned 0.03 wt% SWCNT-acrylate nanocomposite samples were tested under quasi-static monotonic and tension-tension cyclic loading for axial and transverse piezoresistivity measurements. Average resistance readings over eight data points were obtained from LCR meter readings and correlated to applied strain from crosshead displacement during mechanical loading. The electrode placements for measuring piezoresistive response through instanteous resistance change ($\Delta R/R_0$, where R_0 is initial resistance) as the specimens undergo deformation are shown in Fig. 3.2. 8331 Silver conductive epoxy was used to construct electrodes. For axial piezoresistive response (response governed by the axial loading direction), the conductive epoxy electrodes were cemented on top and bottom of the gauge section at distance 4 mm apart on alternate sides of the sample to obtain volume piezoresistivity, mixed mode (where both transverse and axial strains are detectable due to Poisson's effect), measurements. For

transverse piezoresistive response (response governed by Poisson's contraction direction), the electrodes were placed on alternating sides of gage section along thickness at distance 4.2 mm apart. Tensile tests were carried out in accordance with ASTM D638 under the aforementioned rescaling of specimen dimensions. The quasi-static monotonic and tension-tension cyclic loadings were implemented at constant crosshead displacement rates of 2 mm/min corresponding to a strain rate of 0.0012 s^{-1}. The axial piezoresistive sensitivity was quantified by $k_{axial} = \frac{\Delta R/R_0}{\varepsilon_{axial}}$; whereas, the transverse piezoresistive sensitivity was quantified by $k_{transverse} = \frac{\Delta R/R_0}{\varepsilon_{transverse}}$, where $\varepsilon_{transverse}$ was calculated with the obtained Poisson's ratio of aligned 0.03 wt% SWCNT-acrylate nanocomposite samples.

3.2 Results and Discussion

3.2.1 Microstructure

Initial characterization of randomly dispersed SWCNTs and of SWCNTs alignment and filament formation fabricated with AC electric field was obtained using transmission optical microscopy combined with digital mapping of individual overlapping images. Fig. 3.3 provides digitally mapped wide area high magnification (350X) transmission optical microscopy images of both the well-dispersed (no electric field) and aligned SWCNT nanocomposites within the gage section. Fig. 3.3a demonstrates that for the well-dispersed 0.03 wt% SWCNTs there is initially no perceivable alignment or filament structures and only a few sizable agglomerations of SWCNTs. In Fig. 3.3b, long range alignment and filament formation from one edge to the other edge of the specimen fabricated with AC electric field is observed at the same concentration of 0.03 wt% SWCNTs. In Sengezer et al. [37], filament width distributions were examined as a function of frequecy and exposure time to the AC electric field during fabrication. It was observed that the filament width was $\sim$ 22 μm for the samples exposed to an AC electric field of 200 V_{RMS}/mm with a frequency of 10 kHz after 30 min of exposure time at ambient temperature during fabrication. Here, filament width is similar

with an AC electric field of 40 V_{RMS}/mm with a frequency of 5 kHz after 2 min of exposure time during fabrication after the solution was heated to 65 ^{o}C.

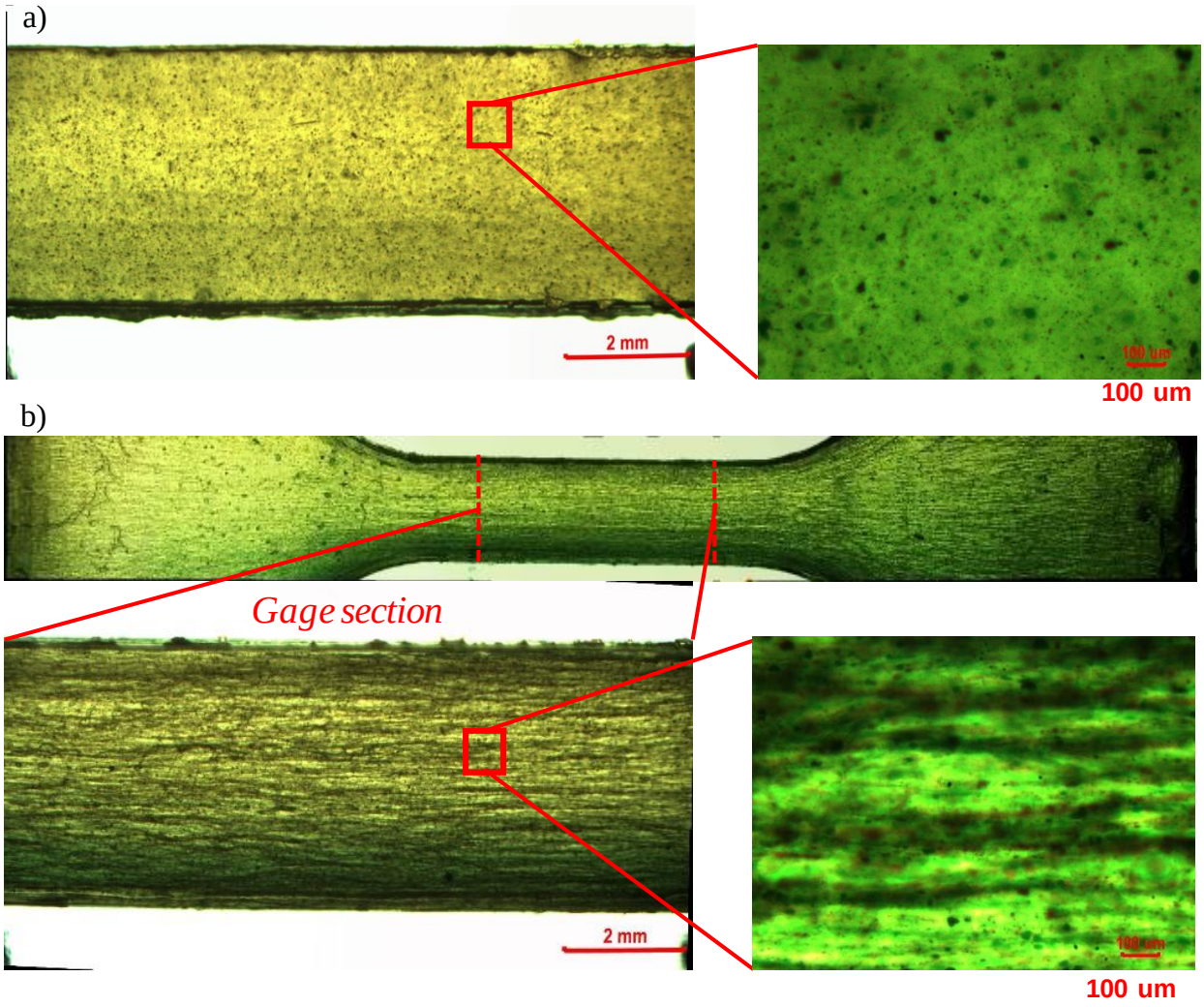

Figure 3.3: Transmission optical microscope panoramic images of 0.03 wt% SWCNT-acrylate polymer nanocomposite a) well dispersed SWCNTs under zero AC electric field, and b) aligned SWCNT-filament formation under AC electric field.*

*0.1wt% was too high of a concentration to be observed with transmission optical microscopy.

3.2.2 Fracture Surface Topography

In order to assess key morphological features of as produced neat acrylate and SWCNT-acrylate nanocomposites, their fracture surface topography after monotonic tensile loading has been investigated through a combination of SEM and FE-SEM. Fig. 3.4 provides the SEM micrographs of the neat acrylate fracture surface where regular fractured paths of river

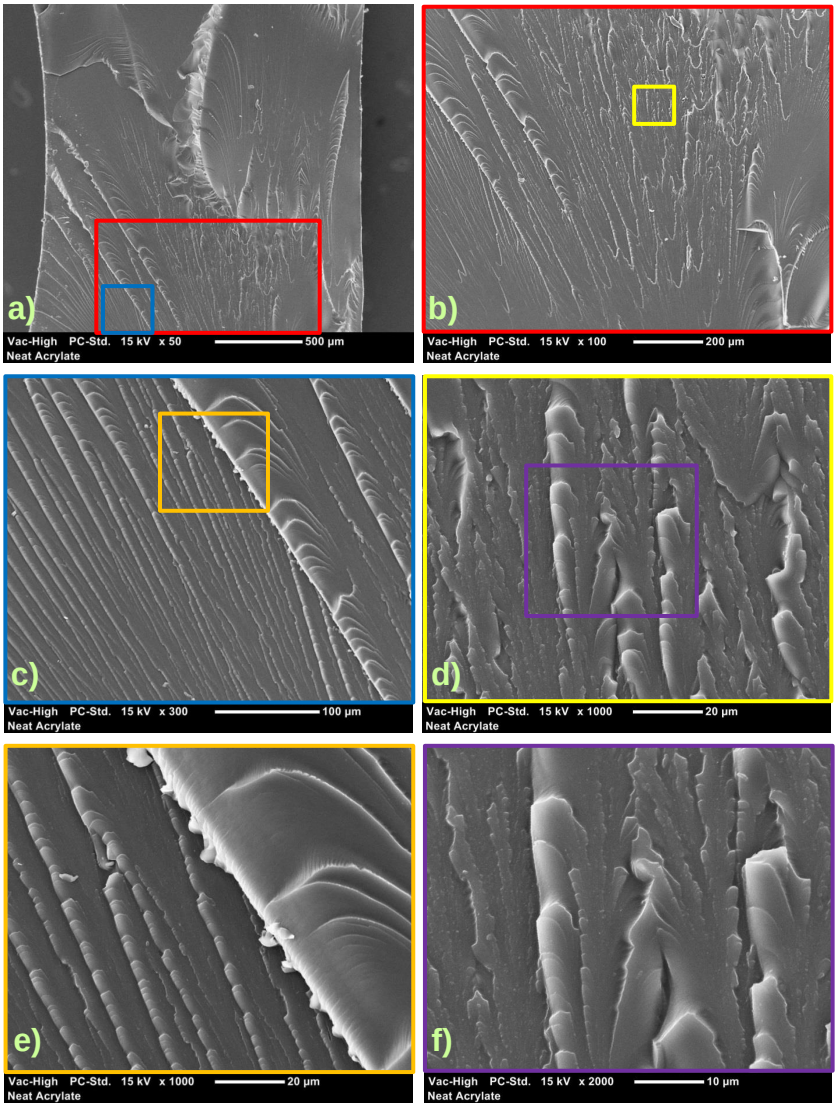

Figure 3.4: Fracture surface of neat acrylate (top view) - color frames represent the micrographs zoomed in to show higher resolutions within the original micrographs

line patterns in Fig. 3.4b-f can be observed, indicating brittle fracture. Fig. 3.5 provides the FE-SEM micrographs of randomly oriented, well dispersed 0.03 wt% SWCNT-acrylate nanocomposites where the fracture surface is relatively smooth with the introduction of slight tortuosity, and the cracks become more random compared to neat acrylate sample. On further zooming in on white cloud-like structures in Fig. 3.5a, it is observed that SWCNTs are bundled/agglomerated in collections (local nanotube networks) with a size range between 1-10 μm as shown in Fig. 3.5b-e. Intermittent radial cracks observed around local nanotube networks acting as microscopic stress concentrations, which induces an additional disturbance in the matrix stress, will have a significant effect in the measured mechnical properties of these nanocomposites. In comparison, Fig. 3.6 shows FE-SEM images of the microstructure of a fracture surface of an aligned 0.03 wt% acrylate polymer nanocomposite also tested until failure under monotonic tensile loading. The fracture surface of the aligned 0.03 wt% acrylate nanocomposite shows considerably different fractographic features compared to neat acrylate and randomly oriented, well dispersed 0.03 wt% SWCNT-acrylate nanocomposite. As can be seen in Fig. 3.6a, the patterns and branches become more sophisticated and there appears to be multiple cracking patterns, which provides a resistance towards crack initiation and propagation compared to the river line patterns of neat acrylate associated with a continuous tear and to slight tortuosity of randomly oriented SWCNT-acrylate nanocomposites. The fracture surface is rather rough, and the occurrence of microcracking and crack path deflection, which are some of the characteristic features of overall toughening, can be observed in Fig. 3.6a, c and e. A zigzag propagation path of the crack through matrix obstructed by aligned SWCNT regions can be clearly seen in Fig. 3.6 c which leads to an improvement of resistance to crack propagation in acrylate polymer matrix. Another key feature observed is that of individual transverse SWCNT bridging within single SWCNT filament which can be observed in Fig. 3.6b, d and f. In fact, some degree of CNT pull-out is evident in Fig. 3.6 e, g, h where individual SWCNTs were observed protruding from the crack surface.

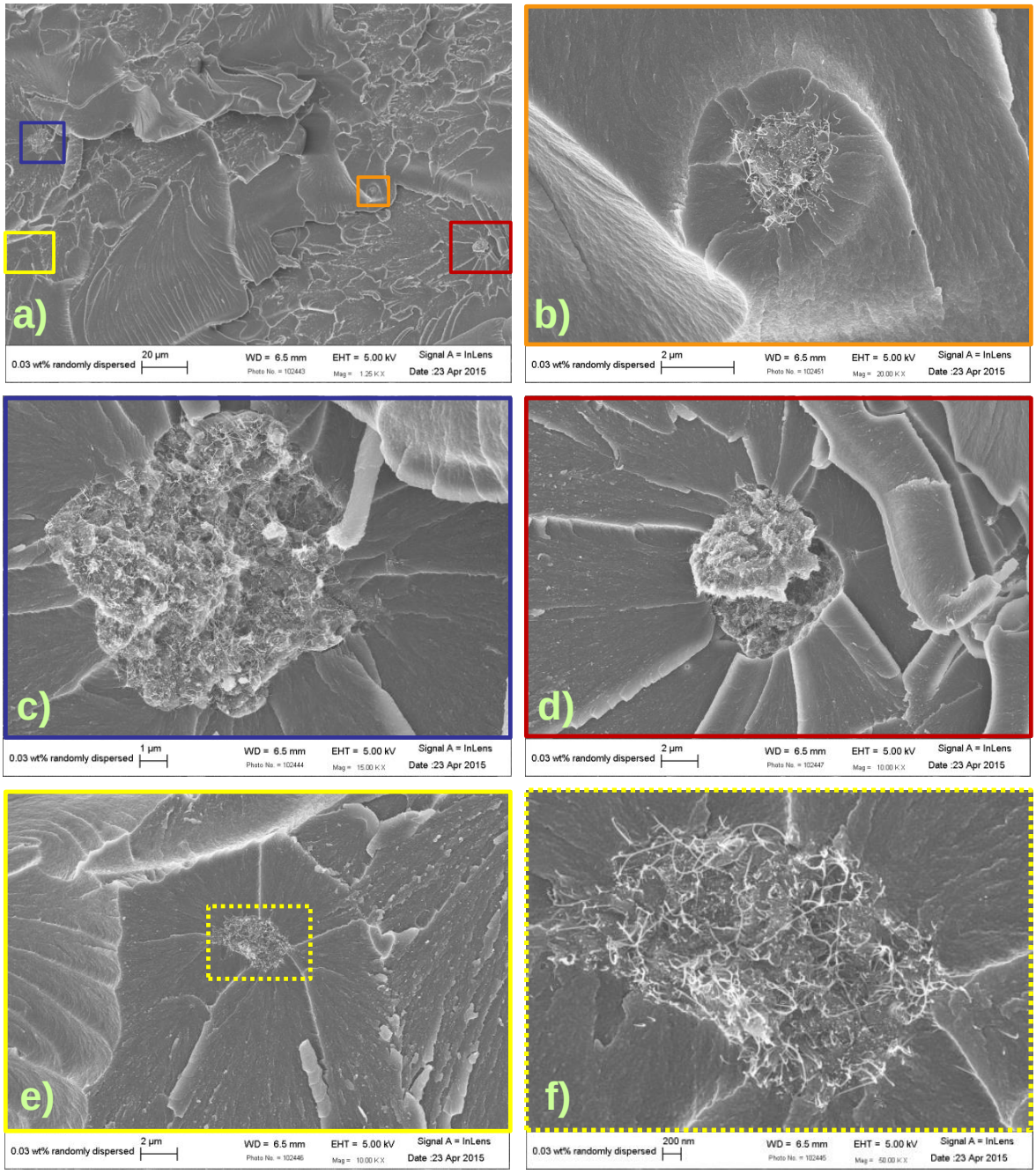

Figure 3.5: Fracture surface of randomly oriented, well dispersed 0.03 wt% SWCNT-acrylate nanocomposite (top view) - color frames represent the micrographs zoomed in to show higher resolutions within the original micrographs

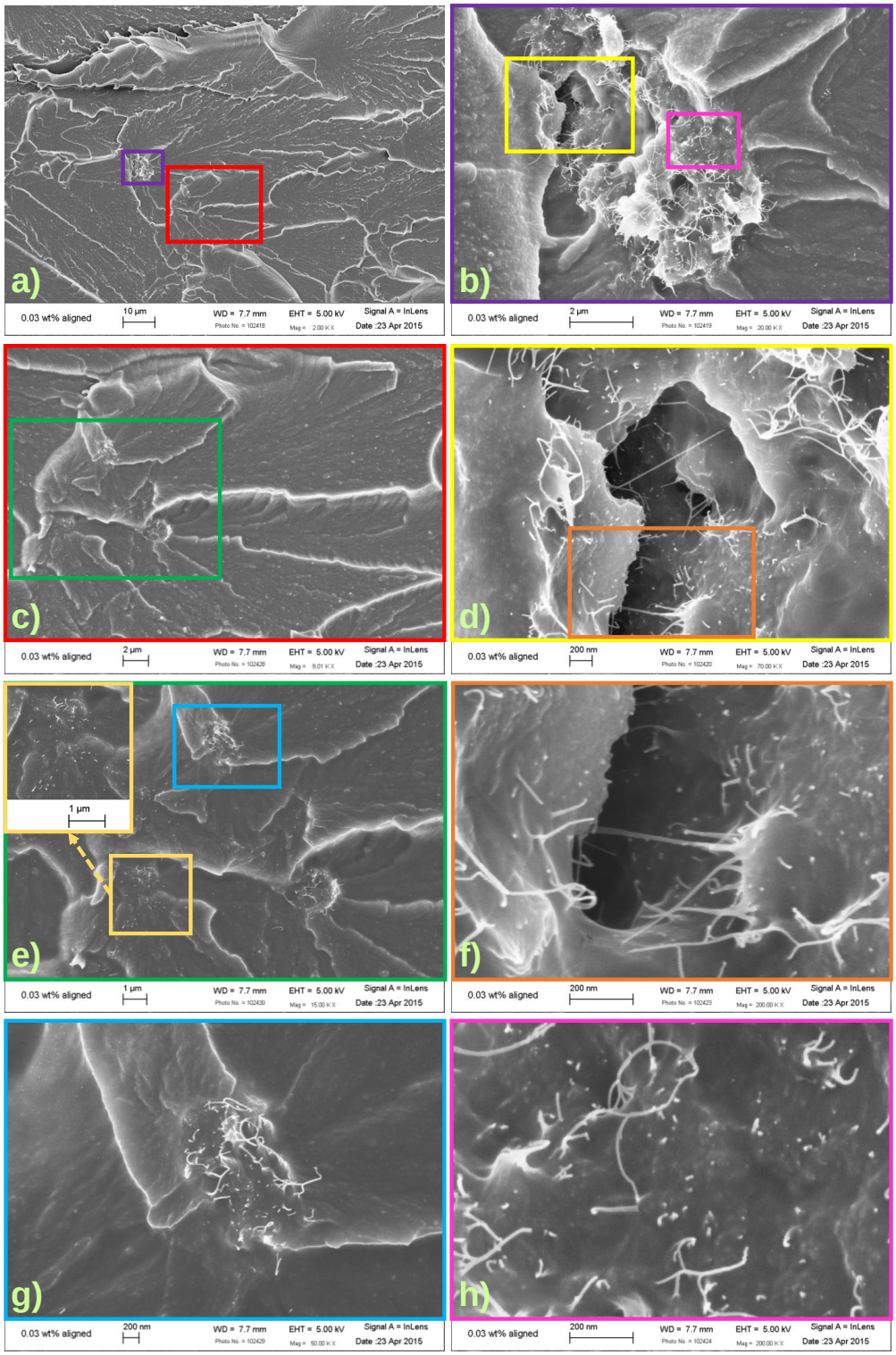

Figure 3.6: Fracture surface of aligned 0.03 wt% SWCNT-acrylate nanocomposite (top view) - color frames represent the micrographs zoomed in to show higher resolutions within the original micrographs

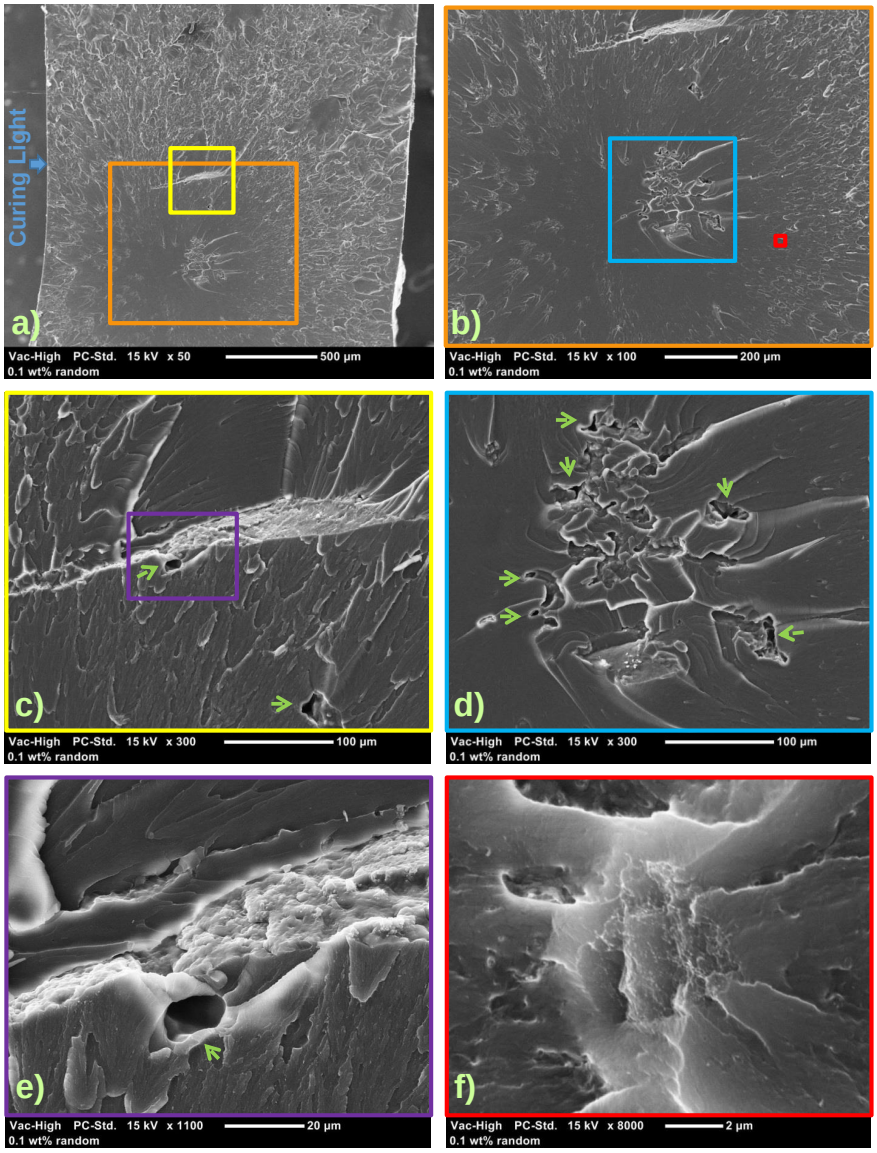

Figure 3.7: Fracture surface of randomly oriented 0.1 wt% SWCNT-acrylate nanocomposite (top view) - color frames represent the micrographs zoomed in to show higher resolutions within the original micrographs

Increasing SWCNT content throughout the acrylate matrix adversely affected the curing of the nanocomposites as can be seen in the as-produced samples. Curing light exposure during the fabrication of as-produced randomly oriented 0.1 and 0.5 wt% SWCNT-acrylate nanocomposites diminished significantly due to lack of transparency with the increased

weight concentration. This resulted in void formation throughout the acrylate matrix, which was observed to have a significant impact on the measured mechanical properties of these

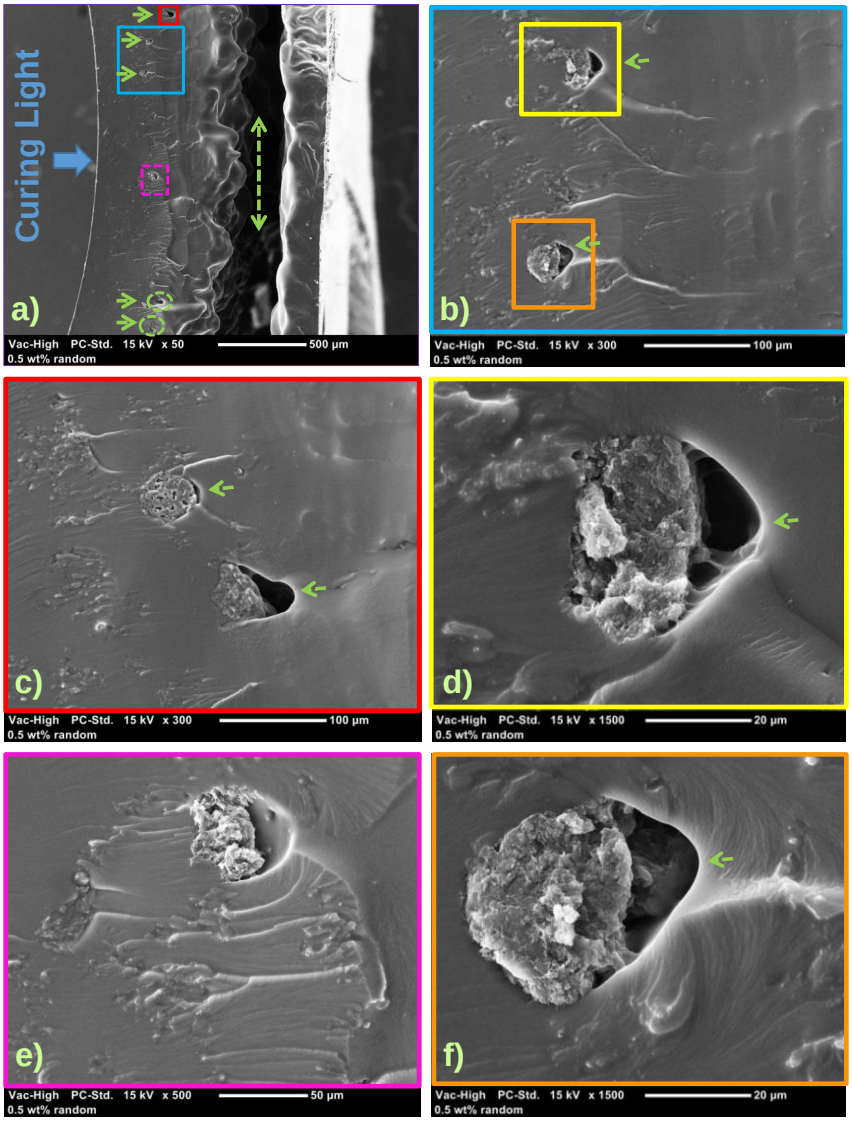

Figure 3.8: Fracture surface of randomly oriented, well dispersed 0.5 wt% SWCNT-acrylate nanocomposite (top view) - color frames represent the micrographs zoomed in to show higher resolutions within the original micrographs.**

nanocomposites. Figure 3.7 shows the SEM micrographs of randomly oriented, well dispersed 0.1 wt% SWCNT-acrylate nanocomposites. The fracture surface includes formations of void

**These samples were cured 30 seconds more from bottom after unmounting from the teflon mold.

region where the crack initiation occurred as shown in Fig. 3.7 a and b. On further zooming in Fig. 3.7 a and b, the formation of voids was marked with arrows in Fig. 3.7 c, d and e. These void formations tend to degrade the mechanical properties of as-produced 0.1 wt% SWCNT-acrylate nanocomposites. Figure 3.8 provides the SEM images of the microstructure of a fracture surface of randomly oriented 0.5 wt% SWCNT-acrylate nanocomposite where the fracture surface includes visible large SWCNT agglomeration with a size of ~ 20 μm. On further zooming in Fig. 3.8 a, the void formation around SWCNT agglomeration was marked with arrows in the micrographs of Fig. 3.8 b, c, d and f, indicating SWCNT agglomeration blocks curing light irradiation/penetration opposite the curing direction resulting in uncured polymer sagging. The dark region or layer marked with vertical dashed arrow opposite the curing direction at a depth of ~ 750 μm m in Fig. 3.8 a demonstrates the validity of the hypothesis that the increased SWCNT concentration throughout the acrylate matrix has an adverse effect in curing the nanocomposites. All of these led to a reduction in mechanical properties of the as-produced specimens, which will be discussed in the mechanical testing section.

3.2.3 Raman Analysis

Polarized Raman spectroscopy was used to assess the degree of SWCNT alignment at the local microscale level with a spot size of 1.7 μm. Figure 3.9 shows the tangential G-band spectra of 0.03 wt% pristine SWCNT-acrylate polymer dog-bone nanocomposite aligned under AC electric field (E_{AC}) of 40 V_{RMS}/mm with a frequency of 5 kHz after 2 min of exposure to the alignment field during fabrication. The tangential G-band intensity decreases as the angle between the polarization direction of incident light and SWCNT filaments alignment axis increases. As expected, a maximum is observed at 0° when the polarization direction of incident light is parallel to alignment axis and a minimum is observed at 90° when the polarization direction of incident light is perpendicular to alignment axis [162,178]. In an effort to quantify the quality of the alignment for pristine SWCNT-acrylate polymer

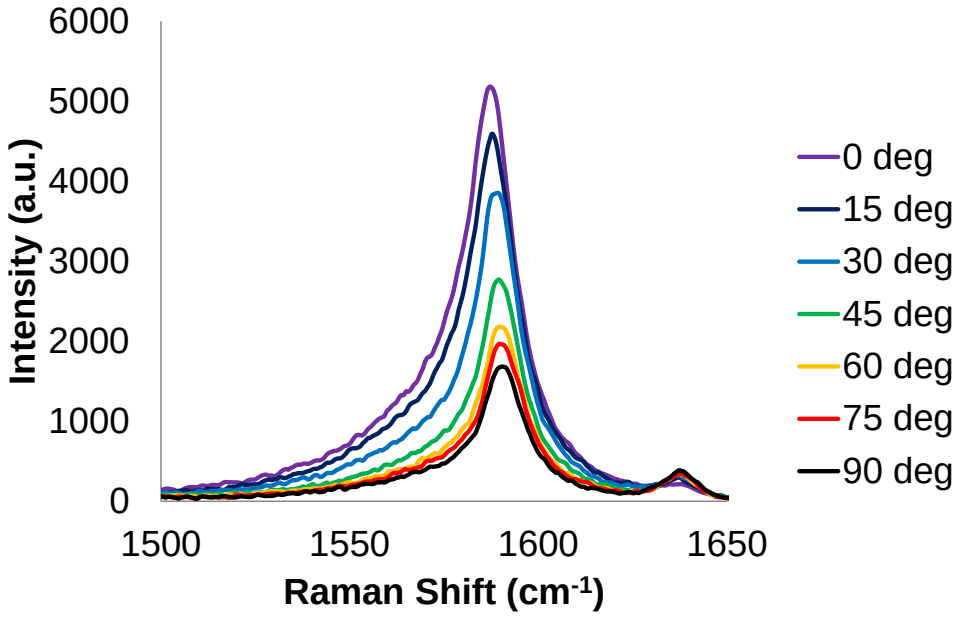

Figure 3.9: Raman spectra of the G-band of aligned 0.03 wt% pristine SWCNT-acrylate polymer nanocomposite dog-bone specimens under AC electric field (E_{AC}) of 40 V_{RMS}/mm with 5 kHz for 2 min of exposure time during fabrication at different polarizer angles, ranging from 0° to 90°.

Table 3.1: Raman tangential G-band intensity ratio for different polarizer angles for pristine SWCNT-acrylate polymer dog-bone nanocomposite. *Polarized Raman spectroscopy was performed on both aligned SWCNTs filaments and between filaments. The spot size was 1.7 μm

Tangential G-band intensity ratio	15°/0°	30°/0°	45°/0°	60°/0°	75°/0°	90°/0°
Average	0.8992 ±0.017	0.8035 ±0.019	0.6731 ±0.033	0.5725 ±0.036	0.5038 ±0.044	0.4543 ±0.044

nanocomposites, the tangential G-band intensity ratios of different polarization angles of 15° intervals from 90° to 0° are listed in Table 3.1. From Table 3.1, it is observed that the there is good alignment between +/− 30 degrees, and that a noticeable degree of misalignment in the transverse direction remains, which is believed to correspond to transverse bridging between the aligned filament structures as observed in the microscale images provided in Fig. 3.3 and Fig. 3.6.

3.2.4 Electrical Properties

The electrical properties of as-produced neat acrylate polymer and SWCNT-acrylate polymer nanocomposite dog-bone samples were measured using an Agilent Technologies E4980A Precision LCR Meter. Fig. 3.10 shows the log-log scale plot of the frequency dependence of the real part of AC electrical conductivity for as-produced samples. It is to be noted that the data presented in Fig. 3.10 have error bars asscociated with each data point calculated by testing six different samples. The conductivity of neat acrylate polymer samples is plotted to provide a baseline measurement from which to assess the effect of SWCNT concentration and orientation on the electrical conductivity. For the neat acrylate polymer samples, the acrylate polymer is expected to have low conductivity and thus displays a strong insulator-like behavior, i.e. frequency dependence as a function of input frequency measurement (1 kHz - 2 MHz). The conductivity increases from $\sim$ 3.3E-10 S/cm at relatively low frequency (1 kHz) to $\sim$ 5.6E-7 S/cm at higher frequency (2 MHz). On addition of highly conductive SWCNTs, the conductivity of randomly oriented, well-dispersed SWCNT-acrylate polymer samples is observed to increase from that of the baseline neat acrylate polymer samples. As an example, at 1 kHz input measurement frequency, the conductivities of the neat, 0.03 and 0.1 wt% SWCNT-acrylate polymer samples are observed to be about 3.3E-10 S/cm, 4.6E-10 S/cm and 5.3E-8 S/cm, respectively. The increase in effective conductivity can be attributed to formation of conductive pathways of nanotube network within the acrylate polymer as SWCNT weight concentration is increased. Large dependence of conductivity on measurement frequency is still observed for the randomly oriented, well-dispersed 0.03 and 0.1 wt% SWCNT-acrylate polymer samples, indicating that the as-produced SWCNT-acrylate polymer samples are still below percolation threshold, thus continuing to act like an insulator rather than a conductor. In contrast, the effective conductivity of randomly oriented, well-dispersed 0.5 wt% SWCNT-acrylate polymer samples demonstrated four orders of magnitude increase in conductivity at a measurement frequency of 1 kHz as compared to neat acrylate polymer corresponding to a value of 2.4E-6 S/cm. In addition, the conductivity of randomly oriented, well-dispersed 0.5 wt% SWCNT-acrylate polymer samples was observed to

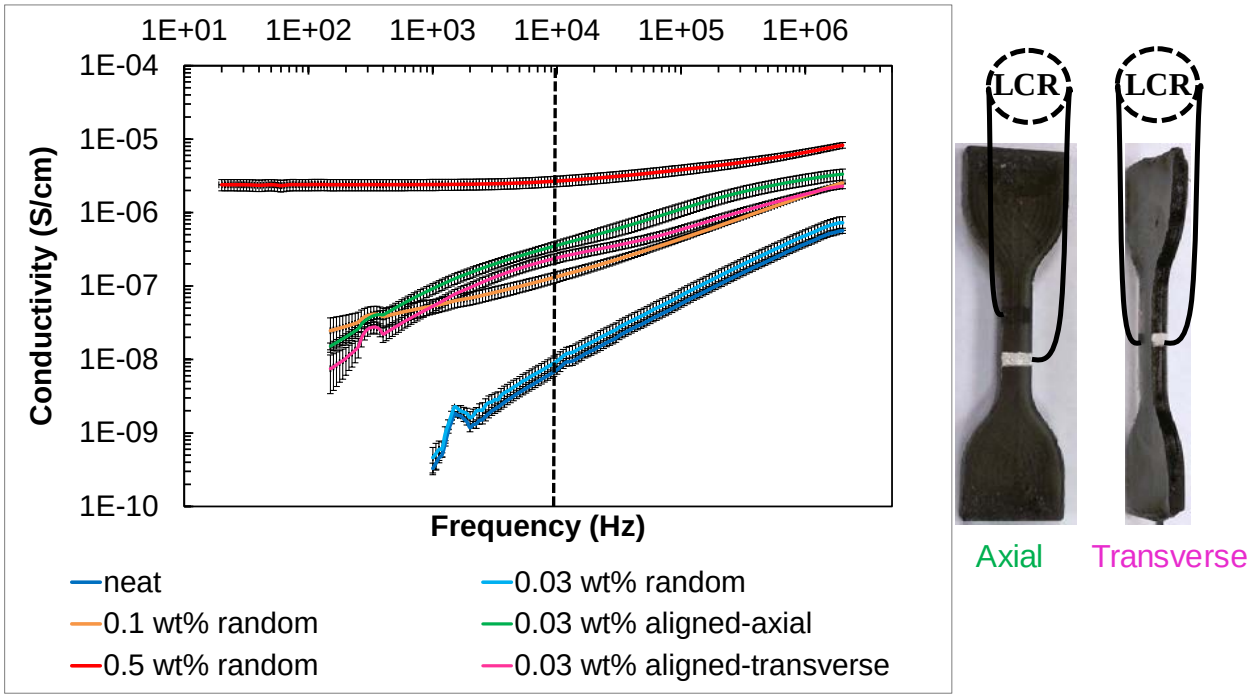

Figure 3.10: Assessment of electrical conductivity of neat, randomly oriented, well-dispersed and aligned SWCNT-acrylate polymer samples at various measurement frequencies. Inset shows the conductive epoxy electrodes cemented on the gage section of the dog-bone specimens to obtain volume conductivity measurements. Axial electrode set-up is a mixed mode measurement. The marked frequency (10kHz) indicates the frequency at which the resistance measurements were made during piezoresistive testing.

be less frequency dependent as a function of input frequency measurement (20 Hz - 2 MHz) as compared to the neat and other randomly oriented SWCNT weight concentration cases, which is an indication of transitioning towards percolation leading to a more conductive behavior. The degree of alignment achieved within the dog-bone specimens is also assessed for the 0.03wt% SWCNTs. The improvements in electrical conductivity are obtained at a concentration below percolation threshold. As expected, the effective conductivity measured with the axial electrode set-up for aligned 0.03wt% SWCNT-acrylate samples is observed to be ∼9.2E-8 S/cm at 1 kHz input measurement frequency, which is higher than that of both 0.03 and 0.1 wt% nanocomposites with well-dispersed, but randomly oriented SWCNTs which were 4.6E-10 S/cm, 5.3E-8 S/cm, respectively. The increases in conductivity can be attributed to the formation of SWCNT filaments in the alignment direction. It is also noted

that the effective conductivity in the transverse direction to the alignment measured with transverse electrode set-up for 0.03 wt% SWCNTs-acrylate nanocomposites is observed to be 5.3E-8 S/cm at 1 kHz input measurement frequency, which shows a two order of magnitude increase compared to 0.03 wt% randomly oriented, well-dispersed SWCNTs acrylate samples. The increases in conductivity in the transverse direction to the alignment can be attributed to small degrees of misalignment in high aspect ratio CNT filaments leading to a network of SWCNT filaments that have bridges from one to the other in the transverse direction, which is supported by Raman observertions in Table 3.1 and microscale images provided in Fig. 3.3 and Fig. 3.6.

3.2.5 Mechanical Properties of SWCNT-Acrylate Nanocomposites

Tensile tests were conducted to evaluate the mechanical properties of as-produced neat acrylate polymer and SWCNT-acrylate polymer nanocomposite dog-bone samples. Fig. 3.11a shows the typical stress-strain behaviour of the as-produced samples in order to compare the results of mechanical testing. Fig. 3.11b shows various aligned 0.03 wt% SWCNT acrylate nanocomposites stress-strain response to ensure consistency of the experiments. As can be seen in Fig. 3.11, there are some differences between SWCNT doped nanocomposites as compared to neat acrylate polymer sample. The resulting values for tensile modulus, tensile strength and fracture strain for the investigated samples are provided in Fig. 3.12. The average modulus value for the neat acrylate polymer was measured to be 678.45 ± 76.89 MPa. In brief, it was found that incorporating randomly oriented 0.03 wt% SWCNTs has no significant effect on elastic modulus of the acrylate polymer studied herein. However, increasing SWCNT content within acrylate matrix was found to significantly decrease the elastic modulus due to a) void formation, b) increased size and c) number of agglomerates throughout the acrylate matrix as shown in Fig. 3.7 and Fig. 3.8. The elastic moduli of the nanocomposites with 0.1 and 0.5 wt% were found to be 366.70 ± 58.15 MPa and 268.04 ± 94.28 MPa.

On the other hand, the nanocomposites with aligned SWCNTs have about 16% higher elastic modulus values (787.76 ± 151.25 MPa) than the neat acrylate samples. Moreover, the average tensile strength for neat acrylate polymer was measured to be 67.24±3.43 MPa. Incorporation of randomly oriented SWCNT into acrylate polymer was found to lead to a negative effect on tensile strength. For instance, the nanocomposites with 0.03 wt% SWCNT have about 21% lower strength (52.82 ± 3.57 MPa) than the neat acrylate samples. This reduction might be explained by the dispersion state of untreated (pristine) SWCNTs within the acrylate matrix. Having some visible small agglomerated zones as shown in Fig. 3.3a and Fig. 3.5 leads to stress concentration due to stiffness mismatch between SWCNT agglomeration and surrounding acrylate matrix. Moreover, the nanocomposites with 0.1 wt% and 0.5 wt% SWCNT have about 37% and 76% lower strength (41.99±9.18 MPa and 15.85±4.09 MPa, respectively) than the neat acrylate samples. It is believed that increasing SWCNT content within acrylate matrix diminished the transparency throughout the acrylate matrix leading to a reduction of curing light exposure during sample fabrication introducing voids and/or poorly cured regions. Furthermore, increasing randomly oriented SWCNT content within acrylate matrix led to relatively larger agglomerations and also void formation located near or around SWCNT agglomerations as shown in Fig. 3.7 and Fig. 3.8, which reduced the mechanical strength of the resulting nanocomposites. On the other hand, aligning 0.03 wt% SWCNTs within acrylate matrix had a substantial effect on the ten-

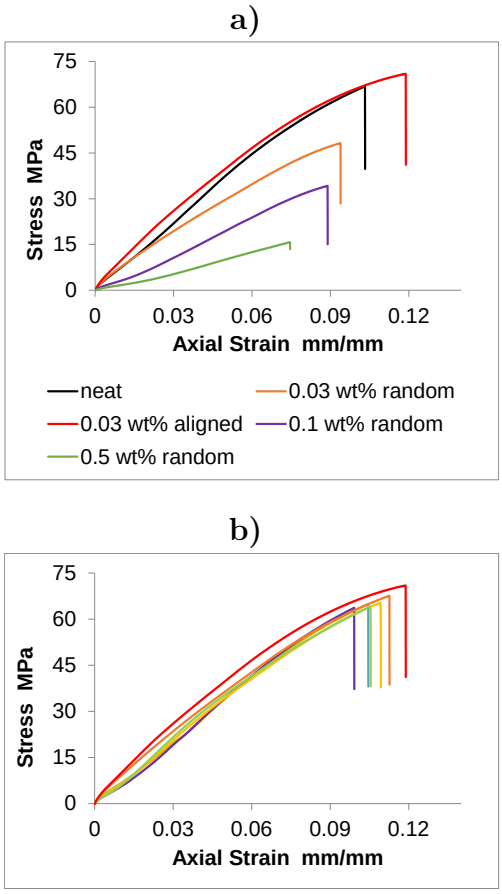

Figure 3.11: Stress-strain curves for a) neat acrylate and SWCNT-acrylate nanocomposites b) 0.03 wt% aligned SWCNT-acrylate nanocomposites

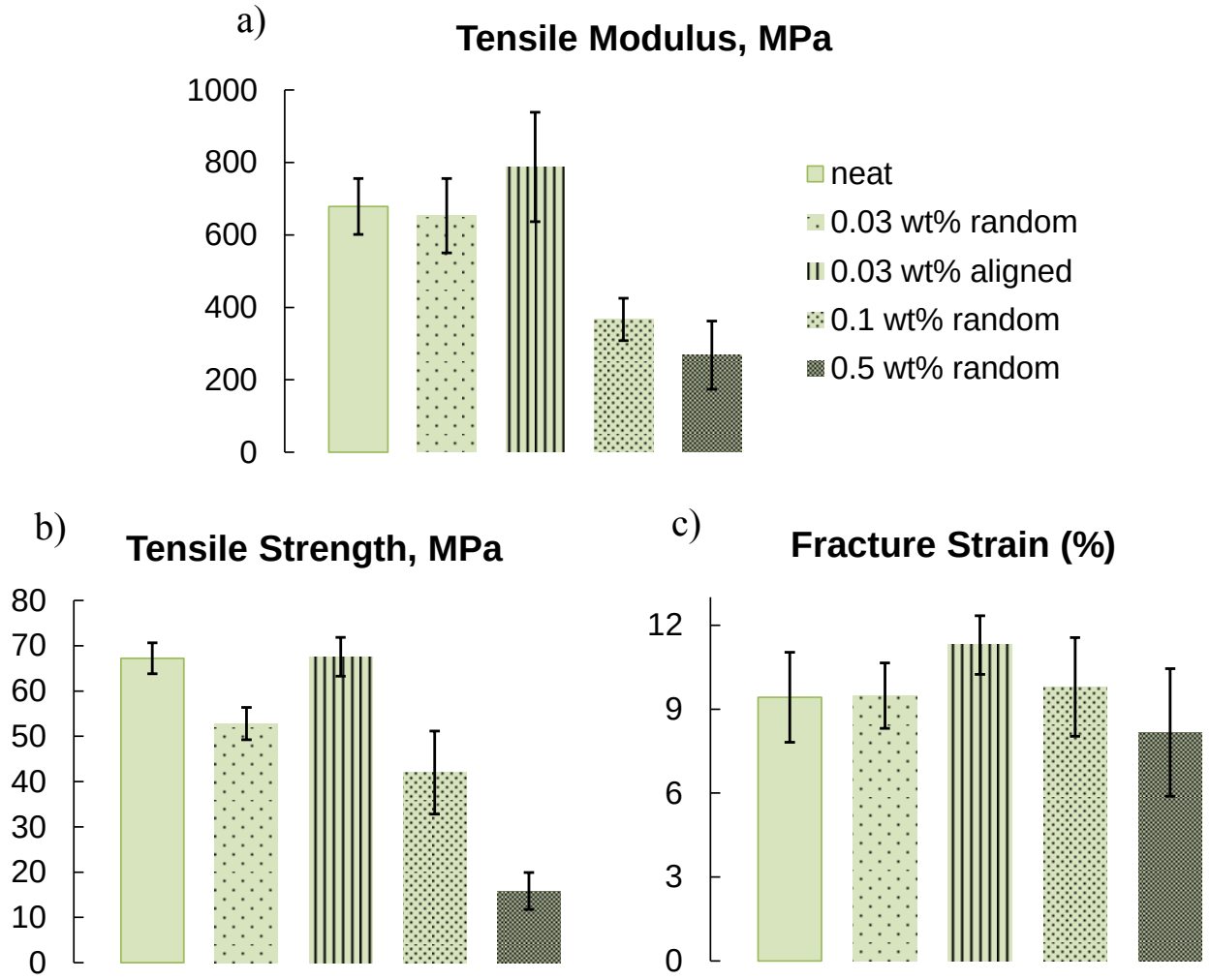

Figure 3.12: The resulting mechanical properties: a) Tensile modulus, b) Tensile strength and c) Fracture Strain

sile strength. Aligned 0.03 wt% SWCNT-acrylate nanocomposites have about 28% higher strength (67.57 ± 4.28 MPa) than those of randomly oriented 0.03 wt%. Furthermore, the average fracture strains for neat acrylate polymer, randomly oriented 0.03, 0.1 and 0.5 wt% SWCNT-acrylate samples were measured to be $9.42 \pm 1.61\%$, $9.48 \pm 1.17\%$, $9.80 \pm 1.76\%$ and $8.17 \pm 2.28\%$ respectively. On the other hand, aligning 0.03 wt% SWCNTs within acrylate matrix lead to improved fracture strain as $11.29 \pm 1.05\%$. For instance, the nanocomposites with aligned 0.03 wt% SWCNTs have about 19.81% and 19.07% of higher values than the neat acrylate samples and the ones with randomly oriented 0.03wt%.

In order to obtain transverse strain values for as-produced aligned acrylate nanocomposites, Poisson's ratios of aligned 0.03 wt% SWCNT-acrylate dog-bone samples were determined from the tensile experiments and found to be 0.358 ± 0.015. This value was determined from transverse strain (measured from the applied strain gauge) vs axial strain (measured from applied strain gauge) plots for three samples as shown in Fig. 3.13.

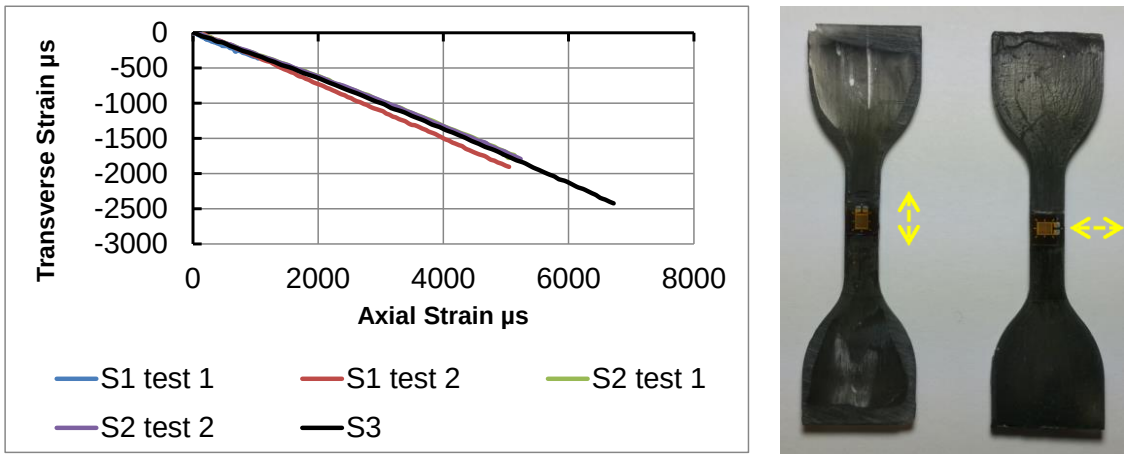

Figure 3.13: a) Transverse vs axial strain used to determine Poisson's ratio from the negative of the slope of the curves of aligned 0.03 wt% SWCNTs-acrylate nanocomposites (0.358 ± 0.015) where S1, S2, S3 correspond to different samples. b) Embedded strain gauges on each side of specimen indicating simultaneously measured axial and transverse strain

Cyclic tests were also performed with the same configurations as quasi-static monotonic loading. Aligned 0.03 wt% SWCNTs-acrylate nanocomposites were tested using tensile loading-unloading cycles strained between 6% and 10% tensile strain, i.e the specimens were strained up to 10% and then unloaded back to 6% tensile strain which was repeated until the sample failed. Figure 3.14 shows the stress response as a function of the number of cycles, measured at a constant strain amplitude of 10% until failure. The stress measured at 10% strain on each cycle is highest on the initial cycle and diminishes in subsequent cycles until the sample fails. Therefore, the observed response in strain-controlled cyclic loading in Fig. 3.14 is due to a combination of viscoelastic response and microdamage accumulation. All samples subjected to cyclic loading demonstrated the hysteresis loops in the induced stress-strain response, which represents the energy dissipation mechanisms associated with

the material's viscoelastic nature. Moreover, as the hysteresis loops are shifting, and as the samples cycled to failure, there is believed to be some accumulation of microdamage as well, though it is not possible to discern its relative contribution from the experimental results obtained.

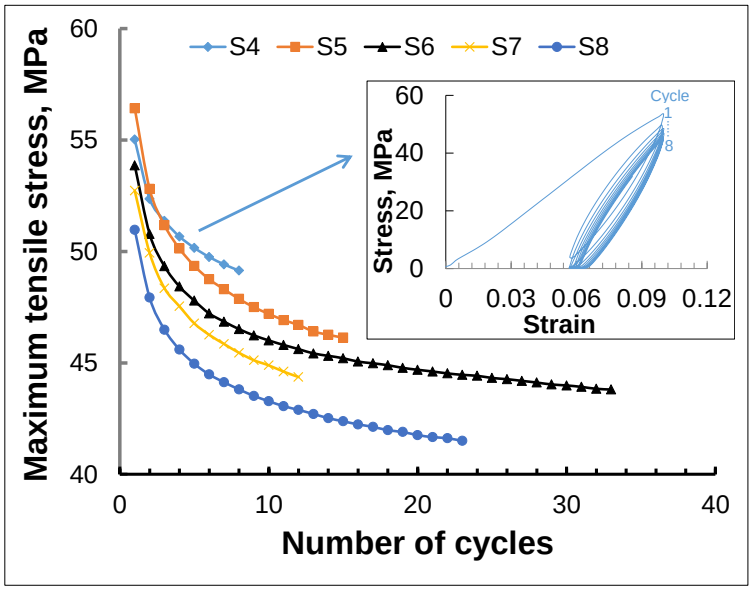

Figure 3.14: Measured tensile stress response at a strain amplitude of 10% with respect to number of cycles at a test displacement rate of 2 mm/min

3.2.6 Piezoresistive Testing of SWCNT-Acrylate Nanocomposites

In the present study, the piezoresistive response is obtained for randomly oriented, well dispersed 0.03, 0.1 and 0.5 wt% SWCNTs specimens under quasi-static monotonic loading, and for electric field aligned 0.03 wt% SWCNTs under quasi-static monotonic and cyclic tensile loading both in the axial and transverse to SWCNT alignment directions. Neat acrylate polymer samples were also tested to provide a baseline measurement from which to assess the effect of SWCNT concentration and orientation on the piezoresistivity. For the neat acrylate polymer samples, no piezoresistive response is observed in Fig. 3.15 as would be expected given the strong insulator like behavior demonstrated by the neat system in Fig. 3.10. Incorporating randomly oriented, well dispersed 0.03 wt% SWCNTs has also no significant

effect on the piezoresistive response. This is due to the fact that there is no conductive pathways formation with the addition of 0.03 wt% SWCNTs as shown in microscopy images in Fig. 3.3 and supported by electrical conductivity response in Fig. 3.10. However, increasing the randomly oriented SWCNT content to 0.1 and 0.5 wt% within arylate polymer was found to lead to a measurable piezoresistive response for these concentrations which have a sufficiently formed conductive pathways of nanotube network such that under tension, the network is disrupted leading to increased resistance and therefore positive normalized relative resistance change. Table 3.2 presents the average gauge factors of randomly oriented, well-dispersed nanocomposites with various levels of tensile strain. For instance, the gauge

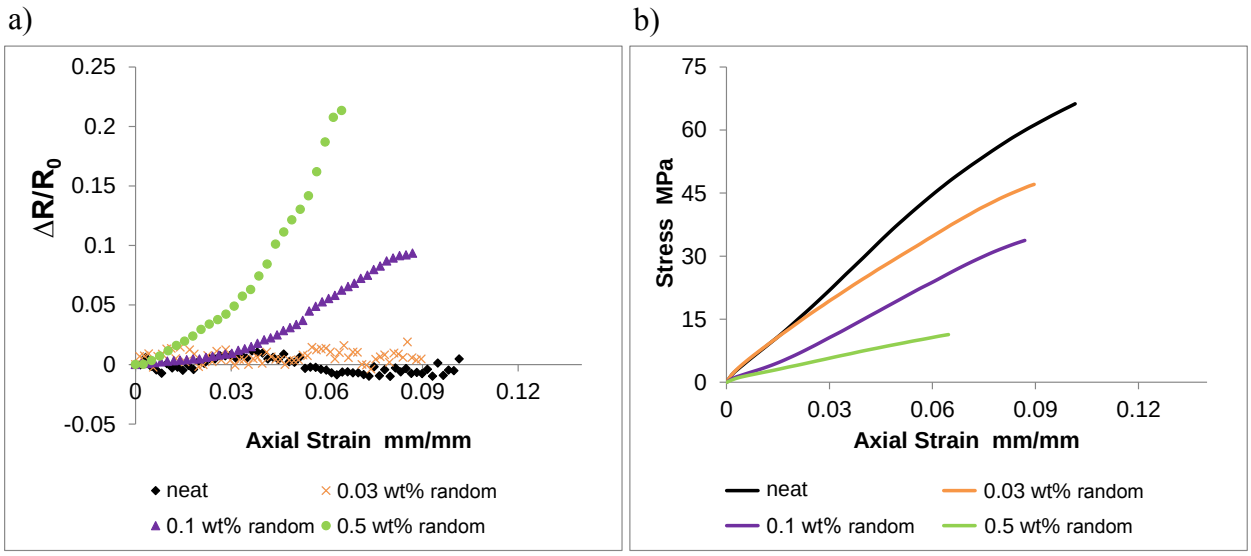

Figure 3.15: a) Piezoresistive response and b) corresponding stress-strain response of neat ($R_0 = 1.106\ G\Omega$), randomly oriented 0.03 wt% ($R_0 = 0.831\ G\Omega$), 0.1 wt% ($R_0 = 55.93\ M\Omega$) and 0.5 wt% ($R_0 = 3.51\ M\Omega$) SWCNTs-acrylate nanocomposites under monotonic loading

Table 3.2: Measured gauge factors for randomly oriented, well dispersed SWCNTs-acrylate nanocomposites

$\boldsymbol{k = \frac{\Delta R/R_0}{\varepsilon}}$	$\varepsilon = 1\%$	$\varepsilon = 3\%$	$\varepsilon = 5\%$	$\varepsilon = 7\%$	$\varepsilon = 9\%$
0.1 wt%	0.273 ± 0.059	0.336 ± 0.056	0.51 ± 0.18	0.68 ± 0.21	0.91 ± 0.41
0.5 wt%	1.08 ± 0.16	1.53 ± 0.35	2.33 ± 0.76	2.66 ± 0.79	–

factor of nanocomposites with 0.5 wt% SWCNTs was found to be on the order of 2 corresponding to ∼4 fold increase relative to the nanocomposites with 0.1 wt% SWCNTs.

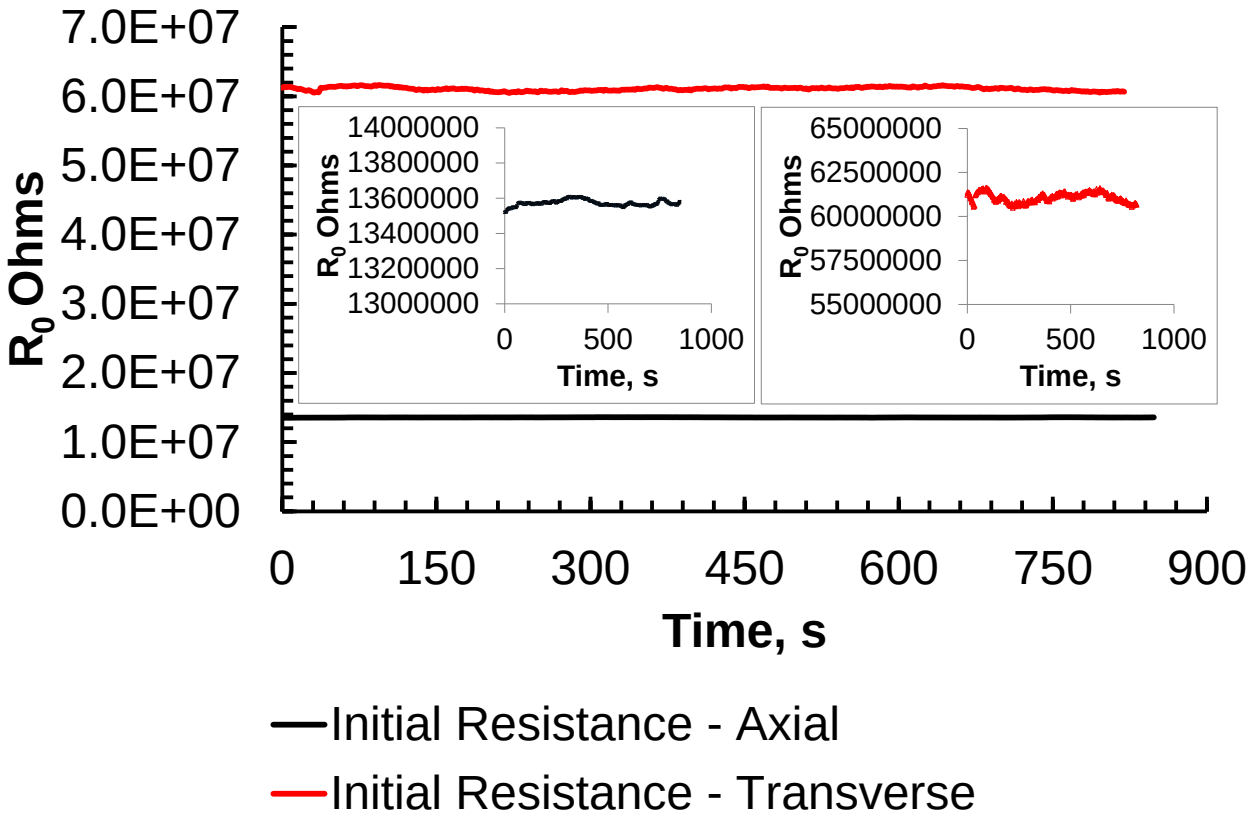

Figure 3.16: Typical initial resistance data under zero-load conditions for axial and transverse piezoresistivity response of aligned 0.03 wt% SWCNTs-acrylate nanocomposites

Aligned 0.03 wt% SWCNT-acrylate polymer nanocomposites piezoresistivity both in the axial and transverse to SWCNT alignment directions are quantitatively and qualitatively evaluated. Axial piezoresistive measurements represent the response in the alignment direction with the applied tensile strain, whereas transverse piezoresistive measurements represent the response in the transverse direction to the alignment with the transverse strain driven by the applied tensile strain, calculated with the Poisson's ratio of aligned 0.03 wt% SWCNT-acrylate dog-bone samples found experimentally from Fig. 3.13. Figure 3.16 shows the typical initial resistance data under zero-load conditions for axial and transverse piezoresistivity response for aligned 0.03 wt% SWCNT-acrylate nanocomposites. The typical initial

resistance data for axial and transverse direction under zero loading exhibits no significant deviation with time. It is to be noted that the initial resistance values for randomly oriented SWCNTs-acrylate dog-bone samples also did not drift under zero loading.

Figure 3.17 provides the typical axial and transverse piezoresistive response for aligned 0.03 wt% SWCNTs-acrylate nanocomposites which were quasi-statically loaded in axial tension until failure. Despite noting that the axial piezoresistive measurements are mixed mode setup, it is clear that the normalized resistance change for axial piezoresistive response increases with the tensile strain applied to the specimen, which is an indication that the response is axial dominated. However, the resistance decreases in the transverse direction due to Poisson's contraction driven by the applied axial strain, which is an indication that the response is transverse dominated. During loading of the specimens, the resistance-strain responses for axial piezoresistivity and for transverse piezoresistivity of aligned 0.03 wt% nanocomposites are substantially different. The anisotropy in transverse and axial sensitivity is evident from the change in slope between the axial and transverse piezoresistive responses in Fig. 3.17a.

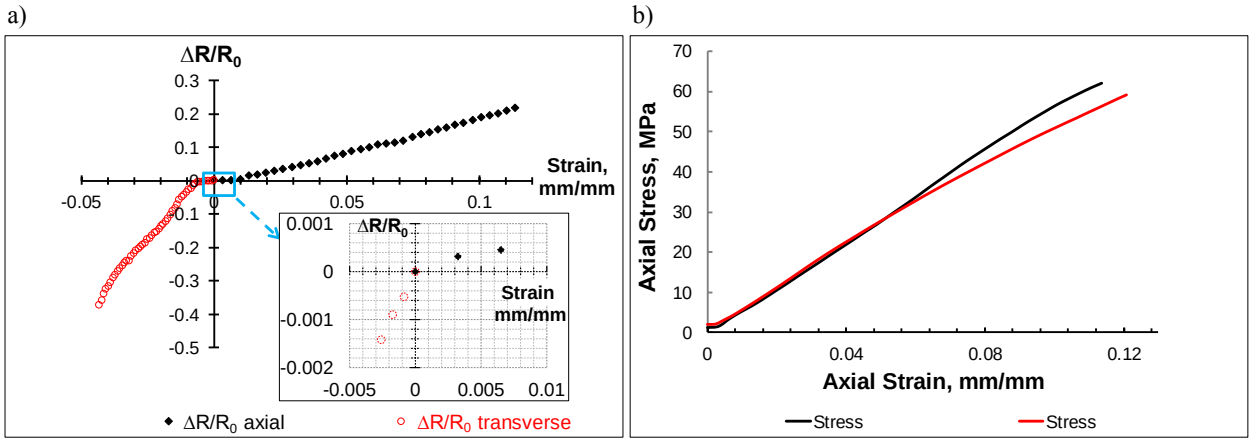

Figure 3.17: a) Axial ($R_0 = 13.58\ M\Omega$) and transverse ($R_0 = 31.11\ M\Omega$) piezoresistive response and b) corresponding stress-strain response of aligned 0.03 wt% SWCNTs-acrylate nanocomposites under quasi-static monotonic loading

Indeed, the transverse piezoresistive response sensitivity surpasses the axial piezoresistive

response, as shown in Table 3.3. The transverse piezoresistive sensitivity of aligned 0.03 wt% SWCNT nanocomposites demonstrates a 5 fold increase in gauge factor compared to the axial sensitivity. Table 3.3 provides the average gauge factors of aligned 0.03 wt% SWCNTs-acrylate polymer for both axial and transverse piezoresistivity measurements with various tensile strains. The axial piezoresistive sensitivity of aligned 0.03wt% nanocomposites results in an order of magnitude increase compared to randomly oriented, well dispersed 0.03 wt% nanocomposites fabricated in the absence of electric field. Moreover, the axial piezoresistive

Table 3.3: Measured gauge factors for aligned 0.03 wt% SWCNTs-acrylate nanocomposites for the axial and transverse piezoresistive response

Axial Strain	$\varepsilon = 1\%$	$\varepsilon = 3\%$	$\varepsilon = 5\%$	$\varepsilon = 7\%$	$\varepsilon = 9\%$
$\boldsymbol{k_{axial} = \frac{\Delta R/R_0}{\varepsilon_{axial}}}$	0.74 ± 0.44	1.19 ± 0.39	1.56 ± 0.32	1.84 ± 0.42	2.13 ± 0.54
Transverse Strain		$\varepsilon = -1\%$	$\varepsilon = -1.8\%$	$\varepsilon = -2.5\%$	$\varepsilon = -3.2\%$
$\boldsymbol{k_{transverse} = \frac{\Delta R/R_0}{\varepsilon_{transverse}}}$		4.73 ± 1.38	7.50 ± 1.95	9.77 ± 2.29	10.54 ± 2.48

sensitivity of the aligned 0.03 wt% nanocomposites is about three times higher than the values obtained for randomly oriented, well dispersed 0.1 wt% nanocomposites, as provided in Table 3.2 and 3.3. Thus, SWCNT filament formation due to alignment inside acrylate polymer increases sensitivity in piezoresistive response in axial direction. It is further observed that the piezoresistive sensitivity in axial direction driven by the applied tensile strain increases nonlinearly, gradually increasing its slope until failure, as shown in Fig. 3.17a and Table 3.3. Stretching of the SWCNT filaments and disruption of axial conduction paths along with geometric effect nominally lead to increases in the normalized resistance change whereas stretching induced increases in alignment correspond to increases in conductivity. The net effect of the former is larger than the latter, though latter results in appreciable nonlinear effect on the increase in the normalized resistance change with applied strain. However, once the alignment increases are completed, the resistance increases due to filament stretching dominated by a decrease in the number of conductive pathways in the axial

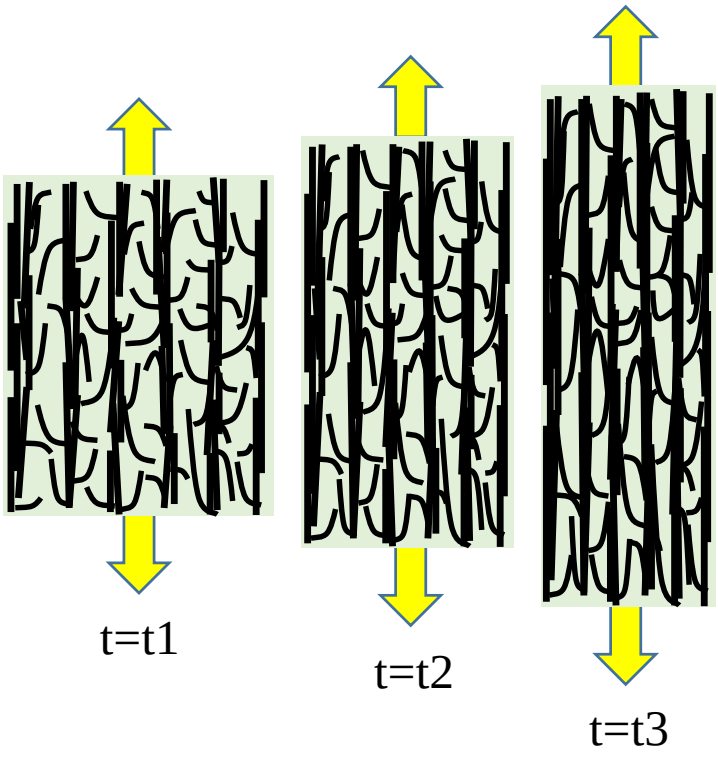

Figure 3.18: Representation of the dimensional change in gauge section due to Poisson's contraction of aligned 0.03 wt% SWCNTs-acrylate nanocomposites under tensile loading

direction driven by the applied tensile strain and microscale damage initiation. It is also suspected that the mixed mode measurement, where the active transverse strain leading to a reduction in electrical resistivity, in the axial electrode setup to obtain volume piezoresistivity may also lead to the nonlinear gradual increase in the axial piezoresistivity. On the other hand, the nonlinearity in piezoresistive response for transverse measurements is more visible compared to axial response. The change in transverse piezoresistive response is again attributed to the rearrangement of the aligned SWCNT network, in this case due to Poisson's contraction associated with the applied axial strain. The dimensional change due to Poisson's contraction causes some of the misaligned SWCNT filament branches, shown in Fig. 3.3b qualitatively and in Table 3.1 quantitatively, to come closer to each other in the transverse direction to form conductive paths between the filaments through the gage section, represented in Fig. 3.18, resulting in increased effective conductivity or decreased re-

sistance. It is also to be noted that the formation of conductive paths establishes significant transitioning towards percolation in the transverse direction, which results in substantially larger gauge factors.

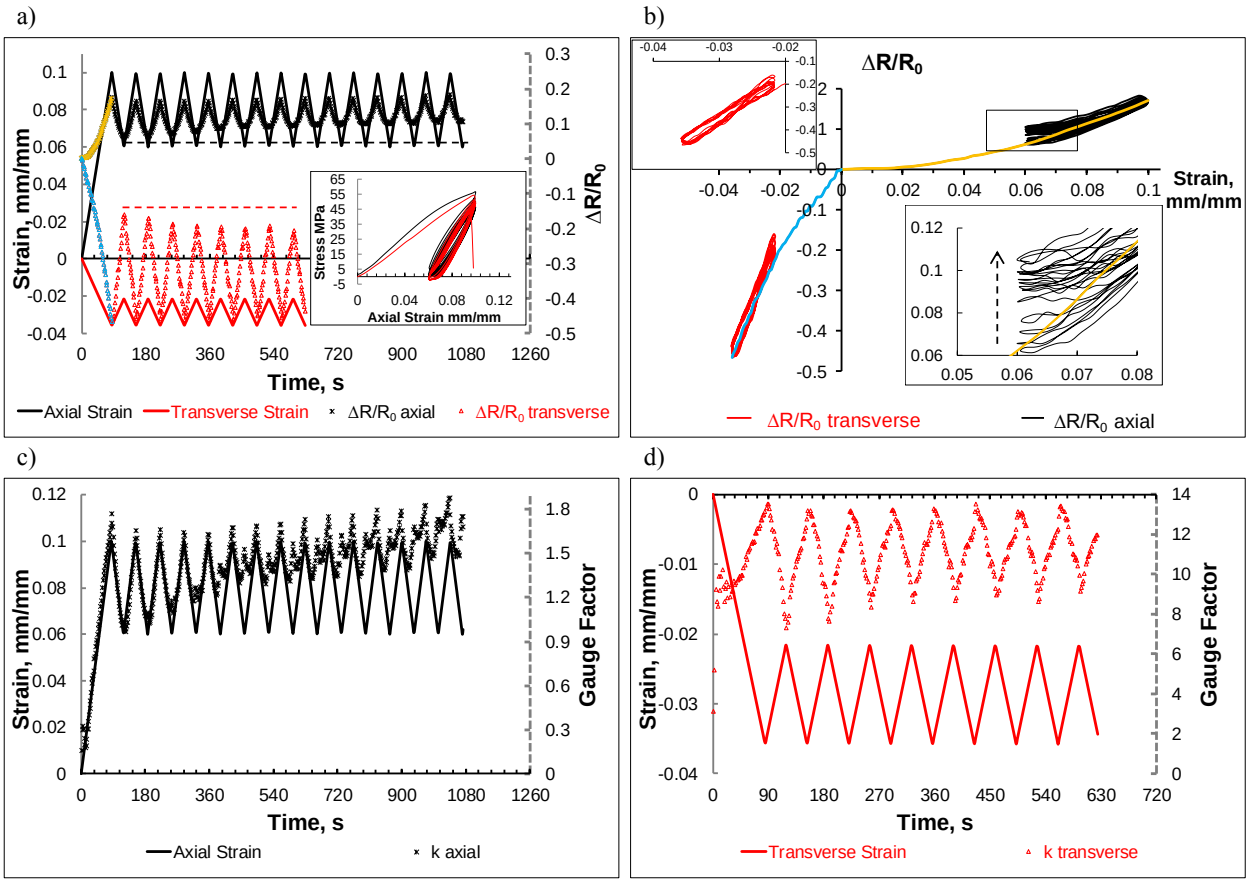

Figure 3.19: Axial ($R_0 = 17.96\ M\Omega$) and transverse ($R_0 = 39.98\ M\Omega$) piezoresistive response of aligned 0.03 wt% SWCNTs-acrylate nanocomposites under cyclic loading: a) as a function of time, b) correlated to strain, c) axial and d) transverse gauge factors correlated to strain as a funtion of time - blue and yellow curves represent $\Delta R/R_0$ curves for 1^{st} cycle of loading

Figure 3.19 shows a typical axial and transverse piezoresistive response of aligned 0.03 wt% SWCNTs-acrylate nanocomposites tested using tensile loading-unloading cycles strained between 6% and 10% tensile strain. The specimens were strained up to 10% and then unloaded back to 6% tensile strain. The axial and transverse piezoresistive response of aligned nanocomposites as a function of time and correlated to strain is shown in Fig. 3.19a and

3.19b, respectively. In Fig. 3.19a, the axial piezoresistive response follows the applied tensile strain without any lag in the loading and unloading stages. It is also clear that the piezoresistive response does not make the same peak values in the loading stages which is an indication of microdamage accumulation. Fig. 3.19b demonstrates the hystheresis and the upward shift of the hystheresis loops in the axial piezoresistive response. It is further observed that there is a permanent and larger resistance change after each subsequent cycle in the unloaded state shown in Fig. 3.19b, as $\Delta R/R_0$ doesn't return to its initial value after each subsequent cycles, supporting the belief of increased disruption of conductive network, i.e. loss of contacts among nanotubes, at the microscale in the axial deformation, which is also an indication of microdamage accumulation. Moreover, the transverse response also follows the transverse strain without having any lag both in loading and unloading stage as shown in Fig. 3.19a. The asymmetry between axial and transverse response still exists with each cycle, indicating the enhanced sensitivity in transverse direction compared to the axial direction with the applied tensile strain, as shown in Fig. 3.19a and 3.19b. The effective gauge factors observed for both axial and transverse piezoresistive response are highly dependent on the applied strain, as shown in Fig. 3.19c and 3.19d. Moreover, the amplified gauge factor response in Fig. 3.19c and 3.19d also corroborates the microdamage sensing.

Figure 3.20 shows the typical axial piezoresistive response of aligned 0.03 wt% SWCNTs-acrylate nanocomposites tested using tensile loading-unloading cycles under stress control. The specimens were cycled between 0 to 40 MPa, 60 % of respective tensile strength, as shown in Fig. 3.20a. An increasing strain at every load cycle, ratcheting strain accumulation, which is a characteristic of a viscoelastic response, becomes smaller for the subsequent cycles. The axial piezoresistive response of aligned nanocomposites as a function of time and correlated to stress and strain is shown in Fig. 3.20b and 3.20d, respectively. The axial piezoresistive response still follows the applied tensile strain without any lag in the loading and unloading stages as shown in Fig. 3.20c and 3.20d. Even though the strain starts to stabilize after 10th cycle, it is to be noted that the normalized resistance change in Fig. 3.20d doesn't return to the same peak in the unloading stages indicating microdamage accumulation. Figure 3.21

shows the typical transverse piezoresistive response of aligned 0.03 wt% SWCNTs-acrylate nanocomposites tested under stress control with the same settings, as shown in Fig. 3.21a.

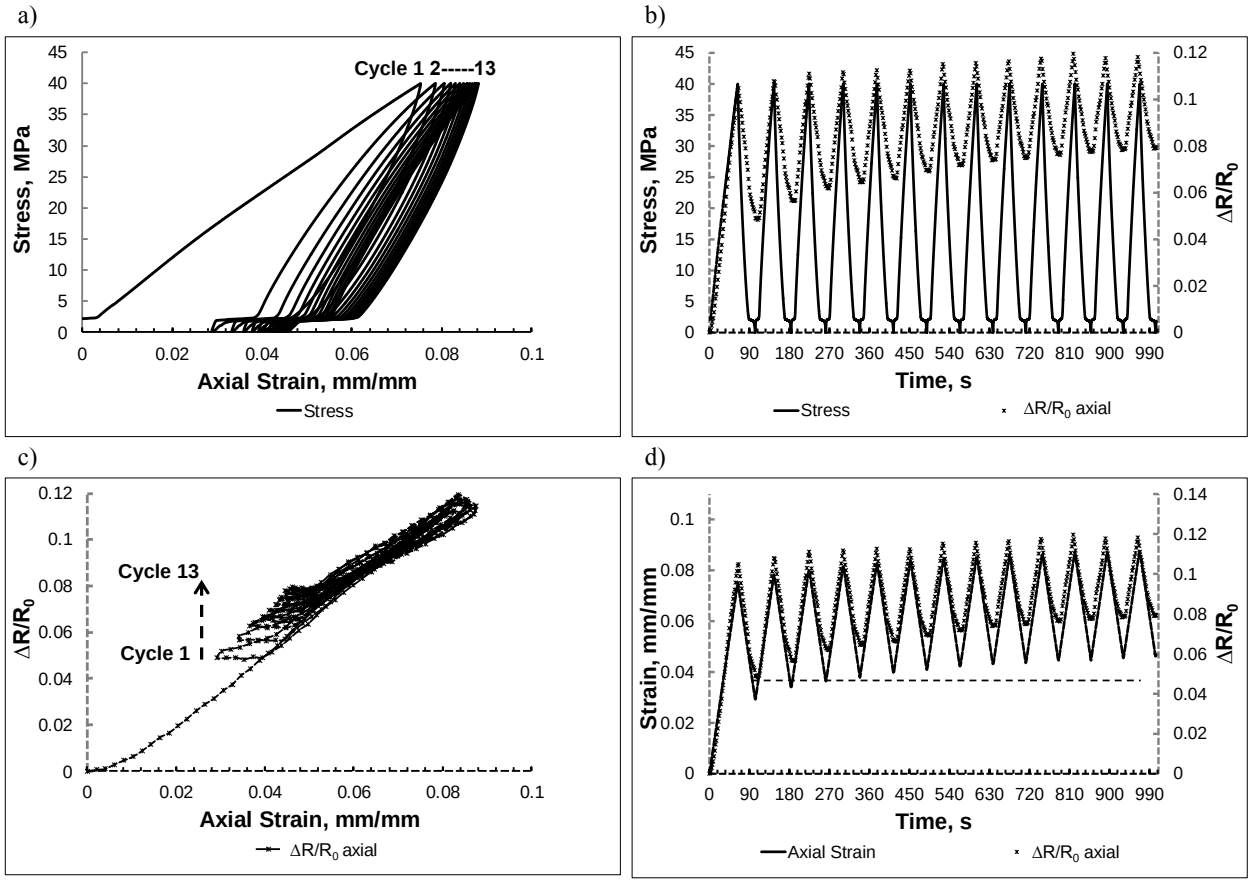

Figure 3.20: a) Stress-strain response, b) stress and axial piezoresistive response as a function of time, c) axial piezoresistive response as a function of axial strain and d) strain and axial piezoresistive response as a function of time of aligned 0.03 wt% SWCNTs-acrylate nanocomposites under cyclic loading ($R_0 = 19.81\ M\Omega$)

The transverse piezoresistive response of aligned nanocomposites as a function of time and correlated to stress and transverse strain is shown in Fig. 3.21b and 3.21d, respectively. The transverse piezoresistive response, the normalized resistance change in transverse direction, still follows the transverse strain without any lag in the loading and unloading stages as shown in Fig. 3.21c and 3.21d. It is to be noted that microdamage accumulation in transverse response cannot be separated from the viscoelastic response given the short number of cycles

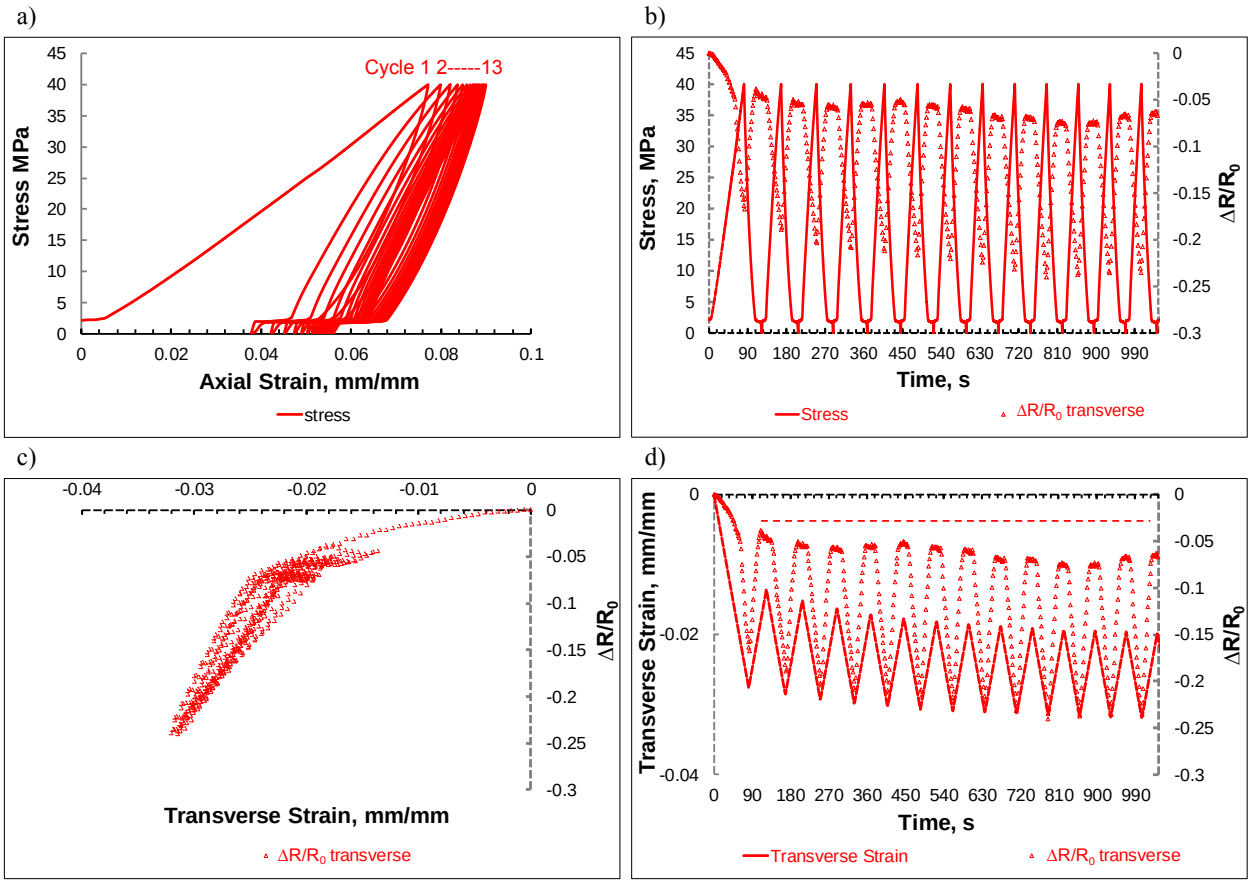

Figure 3.21: a) Stress-strain response, b) stress and transverse piezoresistive response as a function of time, c) transverse piezoresistive response as a function of transverse strain and d) transverse strain and transverse piezoresistive response as a function of time of aligned 0.03 wt% SWCNTs-acrylate nanocomposites under cyclic loading ($R_0 = 60.66\ M\Omega$)

under stress control. In short, the improvements in axial and transverse piezoresistive response for sensing strain and damage accumulation under monotonic and cyclic loading in viscoelastic materials are obtained at a concentration below percolation threshold for electric field aligned specimens with SWCNTs loading as low as 0.03 wt%, with noted asymmetry and anisotropy such that the transverse response yields larger sensitivity than the axial response.

Chapter 4

Structural Health Monitoring of Nanocomposite Bonded Energetic Materials through Piezoresistive Response

The application of in situ structural health monitoring in polymer bonded explosive materials through the introduction of carbon nanotubes into the binder phase is investigated through piezoresistive response under quasi-static and low velocity impact loading in order to provide the basis for deformation and damage sensing for real-time self-diagnostic functionalities in energetic materials. The experimental effort herein is focused on inert energetics using 70 wt% ammonium perchlorate (AP) and mock energetics using 70 wt% sugar crystals embedded into epoxy binder having concentrations of 0.1 and 0.5 wt% MWCNTs relative to the entire hybrids. Electrical conductivity, mechanical properties and piezoresistive sensitivities of inert and mock energetics are quantitatively and qualitatively evaluated. Electrical conductivity was improved ∼3 and ∼5 orders of magnitude for 0.1 and 0.5 wt% MWCNTs inert hybrid energetics and mock hybrid energetics from that of the baseline neat inert energetics

and neat mock energetics, respectively. Incorporating MWCNTs into local binder improved tensile modulus of AP inert hybrid energetics and sugar mock hybrid energetics, ∼15% and ∼70% respectively, and tensile strength of sugar mock hybrid energetics ∼40% compared to neat inert energetics and neat mock energetics. Significant piezoresistive response was obtained both for MWCNT AP inert hybrid energetics and MWCNT sugar mock hybrid energetics, demonstrating the electro-mechanical characterization of inert and mock energetic materials which provides proof of concept for strain and damage sensing under quasi-static and low velocity impact loading for real-time structural health monitoring in energetics.

4.1 Experimental Details

4.1.1 Materials

In the present study, the medium in which MWCNTs have been dispersed is epoxy (West System 105/206). The epoxy system was selected as the binder for its general coating and bonding applications along with its low viscosity. The pristine MWCNTs (PD15L1-5), grown by chemical vapor deposition, were obtained from NanoLab and were reported to have a purity of more than 95%, ∼15 nm outer diameter and average lengths between 1-5 μm. AP (NH_4ClO4), as a virtually inert energetic crystal without being metalized, and granulated sugar, as a mock material, were used as inert and mock forms in place of actual energetic composites/materials/compositions.

4.1.2 Preparation of Mock MWCNT-Epoxy Hybrid Composites

AP-epoxy inert energetic and sugar-epoxy mock energetic samples were prepared with a weight ratio of 70/30 (corresponding to 59 vol% NH_4ClO4 and 64 vol% granulated sugar, respectively) to obtain the neat (i.e. no MWCNTs) AP-epoxy and neat sugar-epoxy mixture. The 70/30 ratio was maintained in the preparation of hybrid binder samples with the

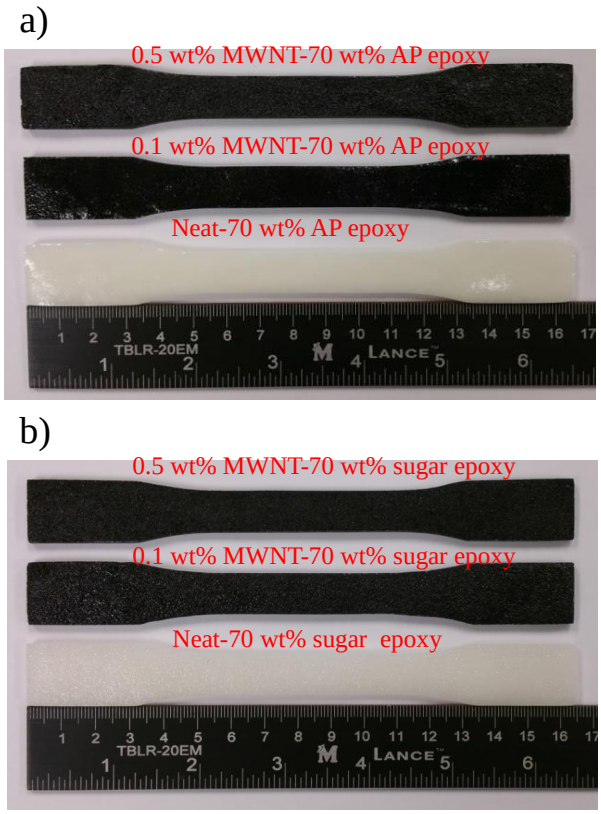

Figure 4.1: As-produced, a) neat AP inert energetic, 0.1 wt% and 0.5 wt% of randomly oriented MWCNTs-AP inert hybrid energetic specimens, b) neat sugar mock energetic, 0.1 wt% and 0.5 wt% of randomly oriented MWCNTs-sugar mock hybrid energetic specimens for quasi-static tensile testing

nanocomposite binder having 0.1 and 0.5 wt% MWCNTs relative to the entire MWCNT-AP-epoxy inert hybrid energetic and MWCNT-sugar-epoxy mock hybrid energetic samples (i.e. corresponding to 0.34 wt% and 1.65 wt% MWCNTs relative to the epoxy, respectively). In preparing hybrid composite samples [92, 93], MWCNTs were added first to a lower viscosity fast evaporating solvent (acetone) and dispersed using bath sonication for one hour. Epoxy precursor was added to predispersed MWCNTs solutions which were resonicated for an additional hour with the same settings to obtain a homogeneous MWCNTs distribution within the epoxy. The solvent was then evaporated from the solutions using a rotary evaporator. The aforementioned curing agent was added to the final mixture and blended thoroughly with lab spoon using mechanical stirring. Subsequent stirring on a stirring plate with mag-

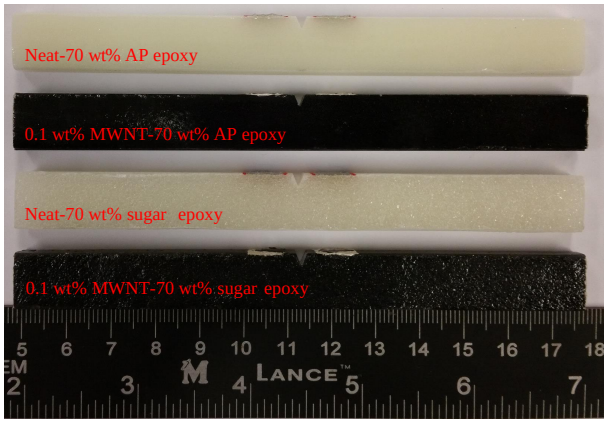

Figure 4.2: As-produced, a) neat AP inert energetic, 0.1 wt% of randomly oriented MWCNTs-AP inert hybrid energetic specimens, b) neat sugar mock energetic, 0.1 wt% of randomly oriented MWCNTs-sugar mock hybrid energetic specimens for low velocity impact testing

netic stir bar was used to obtain more homogeneous nanocomposite solution. 70 wt% AP or sugar crystals were then added to the prepared solution and blended thoroughly with a lab spoon using mechanical stirring to obtain both MWCNT-AP-epoxy inert hybrid energetic and MWCNT-sugar-epoxy mock hybrid energetic mixtures. The prepared mixtures were then casted into silicon molds and cured at room temperature for 24 hours. It is to be noted that epoxy precursor was sonicated with the same settings in the preparation of neat AP-epoxy inert energetics and sugar-epoxy mock energetics in order to have a consistency in sample fabrication. Figure 4.1 shows the resulting neat AP-epoxy inert energetic, MWCNT-AP-epoxy inert hybrid energetic, neat sugar mock energetic and MWCNT-sugar-epoxy mock hybrid energetic specimens prepared for quasi-static tensile testing. All specimens have a gage length of 50 mm corresponding to ASTM standard D638 for specimen type I. Figure 4.2 shows the resulting neat AP-epoxy inert energetic, MWCNT-AP-epoxy inert hybrid energetic, neat sugar mock energetic and MWCNT-sugar-epoxy mock hybrid energetic specimens prepared for low velocity impact testing. All Charpy specimens have dimensions of 127 x 12.7 x ranging from 6.35 to 7.5 mm (L x W x t) with $''V''$ notch (45°) with a radius of 2.54 mm corresponding to ASTM D6110.

4.1.3 Morphological Characterization

AP and sugar crystals were firstly investigated using a combination of benchtop scanning electron microscope (SEM) and a Hirox high magnification(350-7000x) optical microscope to assess the crystal size distribution. A LEO/Zeiss 1550 high-performance Schottky field-emission scanning electron microscope (FE-SEM) was used to conduct fracture surface topography characterization of neat inert, MWCNT inert hybrid energetics, neat mock and MWCNT mock hybrid energetics after mechanical testing.

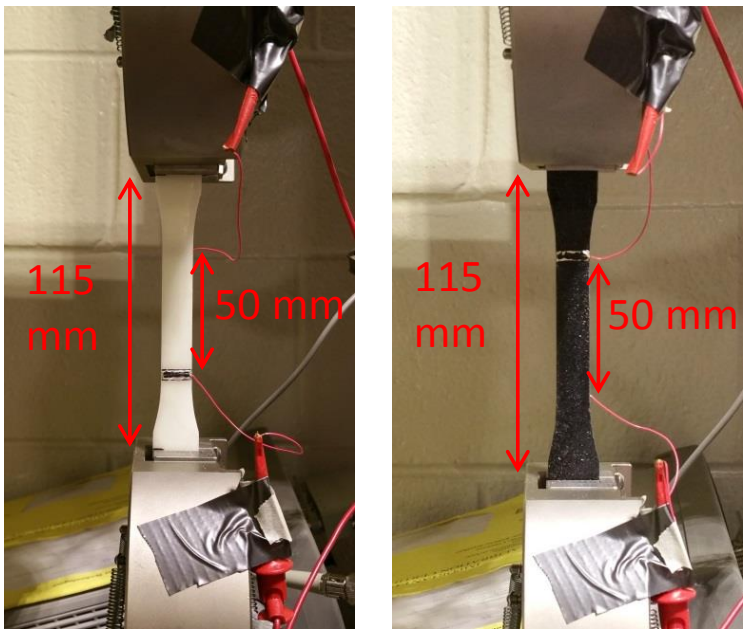

Figure 4.3: Electrode set-up for piezoresistive response under tensile loading

4.1.4 Electrical, Mechanical and Electro-Mechanical-Optical Characterization

The electrical properties of as-produced neat AP-epoxy inert energetic, neat sugar-epoxy mock energetic, randomly oriented MWCNT-AP-epoxy inert hybrid energetic and MWCNT-sugar-epoxy mock hybrid energetic samples were measured using an Agilent Technologies

E4980A Precision LCR Meter via a two terminal method. The 8331 Silver conductive epoxy was applied to the samples to construct electrodes. The piezoresistive behavior of the as-produced hybrid composites were obtained using LCR meter by applying 2 V at 10 kHz in conjunction with mechanical testing. Average resistance readings over eight data points were obtained from LCR meter and correlated to applied strain from crosshead displacement during mechanical loading. The electrode placements for measuring piezoresistive response through instantaneous resistance change ($\Delta R/R_0$, where R_0 is initial resistance) as the specimens undergo deformation were cemented on top and bottom of the gauge section at distance 50 mm apart on alternate sides of the sample to obtain volume resistivity measurements as shown in Fig. 4.3. Tensile tests were conducted in accordance with ASTM D638. The quasi-static monotonic loading was implemented at constant crosshead displacement rate of 0.1 mm/min corresponding to a strain rate of 0.000869 $mm/mm/min$ (1.48 x 10^{-5} s^{-1}). The piezoresistive sensitivity was quantified by the gauge factor as $G = \frac{\Delta R/R_0}{\varepsilon}$.

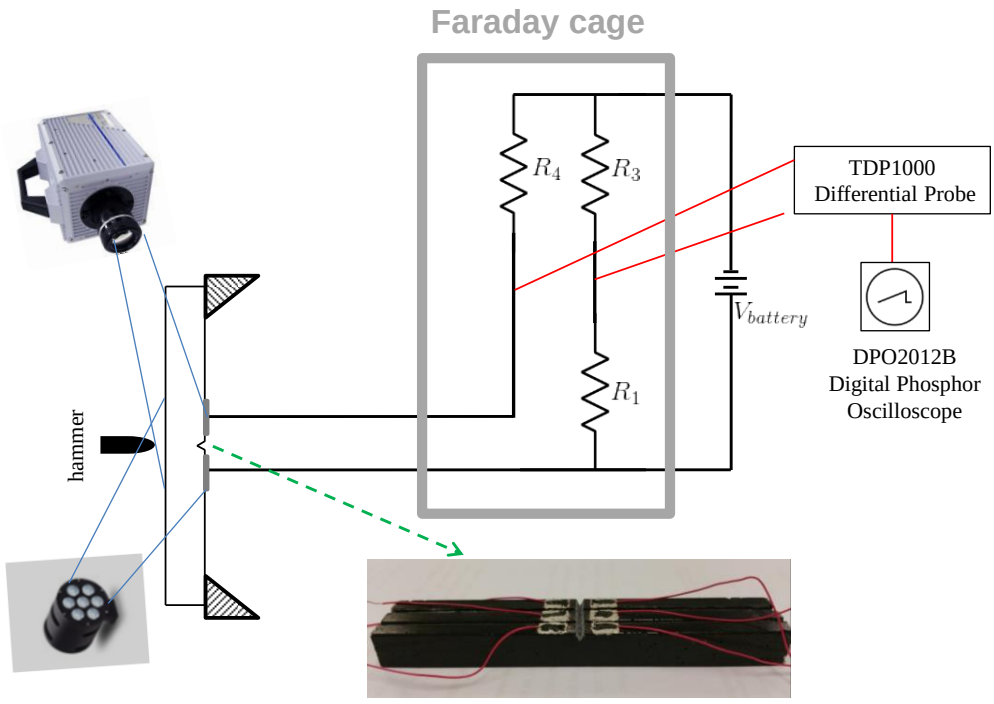

Figure 4.4: Experimental setup used for measuring instanteneous resistance change under low velocity impact experiments

Low velocity impact tests were conducted in accordance with ASTM D6110. Dynamic loading was implemented with an instrumented Charpy hammer with strain gauge load sensor, with 10.8 J potential energy and 3.46 m/s impact velocity, in conjunction with CEAST DAS 64k high speed data acquisition system to record load history. The silver conductive epoxy electrodes were cemented on each sides of the notch as provided in Fig. 4.2 and 4.4 in order to investigate the electrical response of the specimens during impact event. Figure 4.4 shows the schematic of the experimental setup involving in-house built bridge circuitry in order capture the change in voltage difference at the bridge. The change in voltage difference was measured with a differential probe (Tek TDP1000), and recorded with a digital phosphor oscilloscope (Tektronix DPO 2012B). The change in voltage difference (ΔV) was then correlated to the change in resistance of inert and mock energetic specimens under dynamic loading using the derived Eqn. 4.1. It should be noted that the input impedance/resistance of differential voltage probe (R_{probe}) was taken into account while correlating voltage to the resistance. The impact event was also recorded with Photron FASTCAM SA1.1 high speed camera at 250000 fps with a resolution of 128 x 80 (h x v pixels).

$$\Delta R_{specimen} = -\frac{R_4(\Delta V R_1 R_3 + \Delta V(R_1 + R_3)R_{probe} + R_1 R_{probe} V_{battery})}{\Delta V(R_3(R_4 + R_{probe}) + R_1(R_3 + R_4 + R_{probe})) - R_3 R_{probe} V_{battery}} \tag{4.1}$$

4.2 Results and Discussion

4.2.1 Microstructure

Initial characterization of AP and sugar crystals, neat AP-epoxy inert energetic and neat sugar-epoxy mock energetic was obtained using scanning electron microscope as shown in Fig. 4.5. Figure 4.5 c and d clearly show the apparent quality of binder coating/infusion of AP and sugar crystals with small degree of void formation within the binder. The size

distribution of crystals was obtained by counting more than 500 data points. AP and sugar

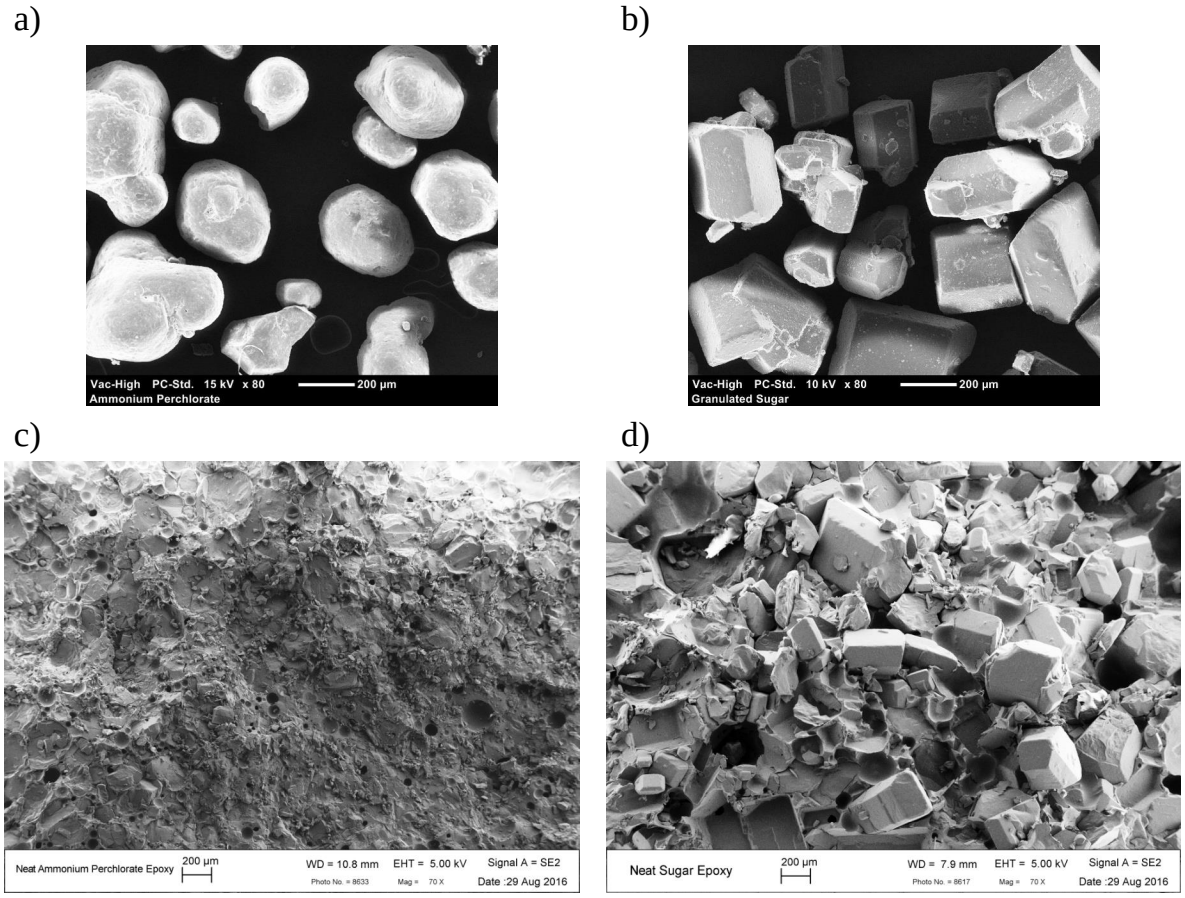

Figure 4.5: SEM micrographs of a) AP crystals, b) sugar crystals, c) neat 70 wt% AP-epoxy inert energetic and d) neat 70 wt% sugar-epoxy mock energetic

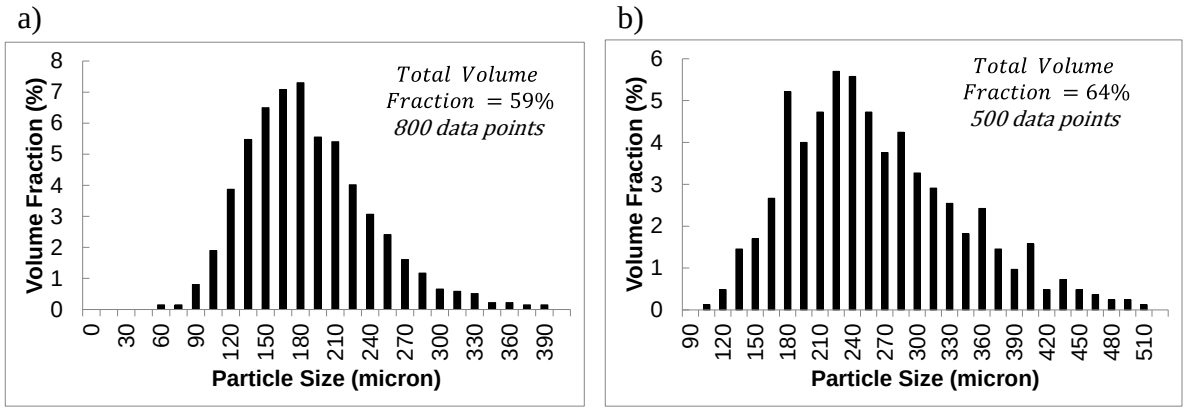

Figure 4.6: Crystal size distribution of a) AP and b) sugar

crystals can be observed with associated average length scales of ∼180μm and ∼230μm, respectively in Fig. 4.6, which are similar size to actual explosive crystals [141, 143, 144, 146, 147].

4.2.2 Electrical Properties

The electrical properties of as-produced neat AP-epoxy inert energetics, neat sugar-epoxy mock energetics, MWCNT-AP-epoxy inert hybrid energetics and MWCNT-sugar-epoxy mock hybrid energetics were measured using an Agilent Technologies E4980A Precision LCR Meter. Figure 4.7 shows the log-log scale plot of the frequency dependence of real part ($Re(\sigma) = \sigma^{'} = \frac{L}{A}(\frac{R}{R^2+X^2})$) and imaginary part ($Im(\sigma) = \sigma^{''} = -\frac{L}{A}(\frac{X}{R^2+X^2})$) of complex AC electrical conductivity ($\sigma = \sigma^{'} + j\sigma^{''}$ where L is the distance between electrodes, A is the area of the electrodes, R is the measured resistance and X is the measured reactance (capacitive reactance)) for as-produced samples. It is to be noted that the data presented in Fig. 4.7 has error bars asscociated with each data point calculated by testing six different samples. Neat epoxy, neat AP inert energetic and neat sugar mock energetic samples' conductivity is plotted to provide a baseline measurement from which to assess the effect of MWCNT concentration on the electrical conductivity. For the neat AP inert energetic and neat sugar mock energetic samples, both crystals, AP and sugar, and the epoxy binder are expected to have low conductivity and thus, these samples display a strong insulator-like behavior, i.e. frequency dependence as a function of input frequency measurement (20 Hz-2MHz). The real component of complex conductivity increases from ∼ 4.5E-10 S/cm and ∼ 7.8E-10 S/cm at low frequency (20 Hz) to 5.8E-8 S/cm and 6.09E-8 S/cm at higher frequency (1 MHz) for neat AP inert energetics and neat sugar mock energetics. It is to be further noted that neat epoxy, neat AP inert energetic and neat sugar mock energetic samples display a high degree of fluctuations because of their extremely low conductivities. With the addition of highly conductive MWCNTs, the real component of complex conductivity of randomly oriented well-dispersed MWCNT AP inert hybrid energetics and sugar mock hybrid energetics

is observed to increase ∼3 and ∼5 orders of magnitude (∼ 1E-7 S/cm and ∼1E-5 S/cm at 20 Hz for 0.1 and 0.5 wt% MWCNTs AP inert hybrid energetics and sugar mock hybrid energetics, respectively) from that of the baseline neat AP inert energetics and neat sugar mock energetics. The increase in effective conductivity is attributed to formation of conductive

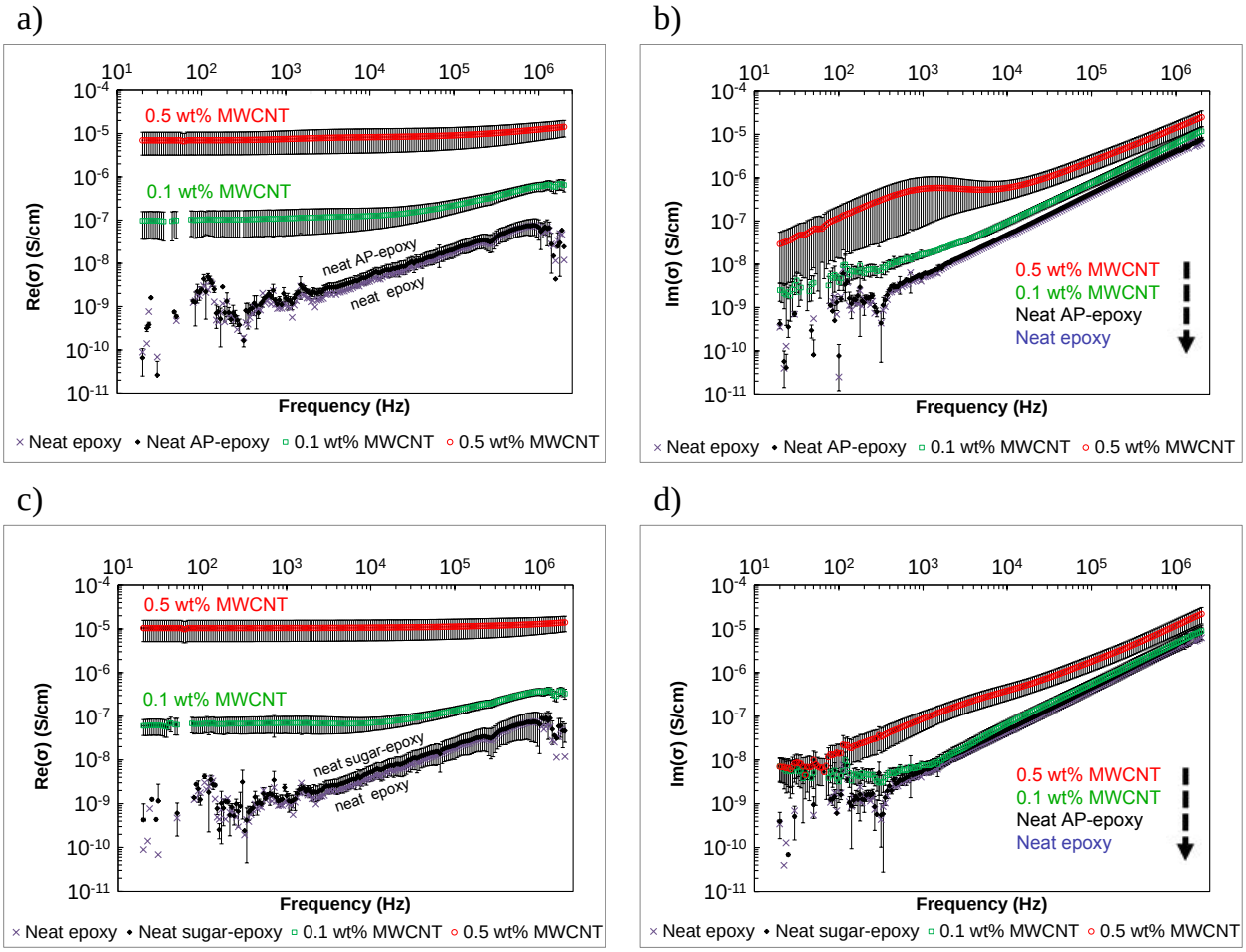

Figure 4.7: Assessment of the complex AC electrical conductivity at various measurement frequencies for (a-b) neat epoxy, neat AP inert energetics and MWCNT AP inert hybrid energetics and (c-d) neat epoxy, neat sugar mock energetics and MWCNT sugar mock hybrid energetics

pathways within the local polymer binder (i.e. nanotube networks) which make the binder more conductive as MWCNT weight concentration is increased. It is clear that the real component of complex AC conductivity for 0.1 wt% MWCNTs AP inert hybrid energetics and sugar mock hybrid energetics remains constant from low frequency (20 Hz) to intermediate

frequency (20 kHz) but starts to increase for higher frequencies which can be atrributed to high frequency dispersion phenomenon. The decrease in frequency dependence as a function of input frequency measurements indicates transitioning towards percolation leading to a more conductive behavior for 0.1 wt% MWCNTs AP inert hybrid energetics and sugar mock hybrid energetics. In comparison, the real component of complex AC conductivity for 0.5 wt% MWCNTs AP inert hybrid energetics and sugar mock hybrid energetics remains constant from low frequencies till high frequencies, which is an indication that system is already percolated leading to even more conductive behavior. For the imaginary component of complex conductivity in Fig. 4.7 b and d, both neat and MWCNT hybrid samples' imaginary part of complex AC conductivity increase with input frequency following a power law. It is clear that the imaginary component of complex AC conductivity for neat epoxy, neat AP inert energetics and neat sugar mock energetics are on the same order of magnitude with the real component of complex AC conductivity and equally frequency dependent, indicating a strong insulator-like behavior. In comparison, for MWCNT AP inert hybrid and sugar mock hybrid energetics, the imaginary component of complex AC conductivity is orders of magnitude less than the real component of complex AC conductivity. In contrast to the real component, imaginary component is frequency dependent due to uniform dispersion of highly conductive MWCNTs which forms many parallel and/or serial microcapacitors connected to each other [179]. It is also obvious that the capacitive reactance of formed microcapacitors decreases with the increase of input frequency. It is to be further noted that percolation concentration mentioned here is for the entire MWCNT AP inert hybrid and sugar mock hybrid energetics which is different from the local MWCNT-epoxy percolation. Local percolation of the MWCNT-epoxy nanocomposite binder is difficult to assess from the macroscale testing performed herein.

4.2.3 Dielectric Properties

Figure 4.8 shows the log-log scale plot of the frequency dependence of dielectric constants for as produced inert and mock energetics. It is to be noted that the data presented in Fig. 4.8 also has error bars asscociated with each data point calculated by testing five different samples. Dielectric constant ($k = \frac{L}{\epsilon_0 A}\frac{1}{2\pi f X}$ where ϵ_0 is the permittivity of free space and f is the input frequency) of neat epoxy, neat AP inert energetics and neat sugar mock energetics is plotted to provide a baseline measurement from which to assess the effect of MWCNT concentration on the dielectric properties. In Fig. 4.8 a and b, it is clear that dielectric constant of neat epoxy, neat AP inert energetics and neat sugar mock energetics are similar to each other, ∼10 at 100 Hz, and are not sensitive to the change of measurement frequency since both mock crystal, ammonium perchlorate and sugar, and epoxy binder has low conductivity and therefore displays a strong insulator-like behavior as provided in electrical conductivity measurements in Fig. 4.7. Incorporating highly conductive MWCNTs,

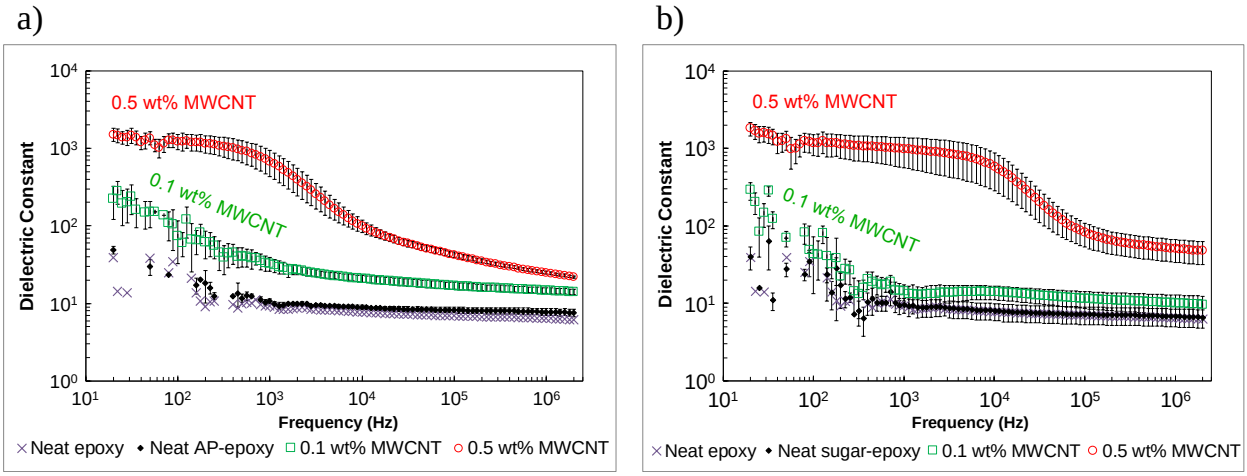

Figure 4.8: Assessment of neat and hybrid composites dielectric constant and dielectric loss at various measurement frequencies associated and at different MWCNT concentrations a-c) for AP inert energetics and b-d) for sugar mock energetics

the dielectric constants of MWCNT AP inert hybrid energetics and MWCNT sugar mock hybrid energetics are closely related to the measurement frequencies, decreasing with the increase of frequency. For 0.1 wt% MWCNTs AP inert hybrid energetics and MWCNTs

sugar mock hybrid energetics at 100 Hz, there is an order of magnitude increase in dielectric constant, ∼100, compared to neat epoxy, neat AP inert energetics and sugar mock energetics. The increase in dielectric constant can be attributed to uniform dispersion of highly conductive MWCNTs which forms many parallel and/or serial microcapacitors connected to each other [179]. The dielectric constant decreases initially from the range of 100 Hz to 1 kHz, indicating that the percolation transition network, disturbed by external input frequency, still remains electrically insulated due to insulating polymer binder and becomes stable at ∼20 with larger frequencies. On the other hand, the attained dielectric constant, ∼1000, for 0.5 wt% MWCNTs AP inert hybrid and sugar mock hybrid energetics is 2 orders of magnitude larger than that of neat energetics at 100 Hz due to having a percolated network as shown in AC conductivity measurements provided in Fig. 4.7a and c. Indeed, the dielectric constant is stable and not getting disturbed by external input frequencies until 1 kHz and 10 kHz for 0.5 wt% MWCNTs AP inert hybrid energetics and sugar mock hybrid energetics, respectively. However, the dielectric constant starts to decrease in the range 1 kHz -10 kHz and 10 kHz -100 kHz for 0.5 wt% MWCNTs AP inert hybrid energetics and sugar mock hybrid energetics, respectively. It is obvious that the capacitive reactance of the formed microcapacitors decreases with the increase of input frequency, resulting a decrease in dielectric constant. Therefore, input frequency is the key driver to tune capacitive reactance ($X = \frac{1}{2\pi fC}$ where $C = \frac{k\epsilon_0 A}{L}$ is the capacitance) and dielectric constant (k). The discrepancy in the induced dielectric relaxation of MWCNT AP inert hybrid energetics and MWCNT sugar mock hybrid energetics may be attributed to the dispersion state of MWCNTs in AP inert hybrid energetics and sugar mock hybrid energetics and can be explained with AC conductivity measurements provided in Fig. 4.7b and d. The imaginary component of complex conductivity is ∼5.59E-7 at 1 kHz and ∼5.89E-7 at 10 kHz for 0.5 wt% MWCNTs AP inert hybrid energetics; however, it is ∼8.82E-8 at 1 kHz and 3.83E-7 at 10 kHz for 0.5 wt% MWCNTs sugar mock hybrid energetics. It is clear that the imaginary component of complex conductivity of 0.5 wt% MWCNTs AP inert hybrid energetics stays constant for the input frequency range from 1 kHz to 10 kHz, thereby capacitive reactance

also remains unchanged. Therefore, the increase at a given frequency leads to a reduction in the capacitance of microcapacitors, leading a decrease in dielectric constant for the input frequency range from 1 kHz to 10 kHz for MWCNT AP inert hybrid energetics.

4.2.4 Mechanical Properties

Tensile tests were conducted to evaluate the mechanical properties of as-produced neat AP inert energetic, neat sugar mock energetic, MWCNTs AP inert hybrid energetic and sugar mock hybrid energetic specimens. Figure 4.9 shows the stress-strain behavior of the as-produced AP-epoxy and sugar-epoxy mock samples in order to compare the results of mechanical testing and to ensure consistency of the experiments. As can be seen in Fig. 4.9 a, the mechanical response of neat AP-epoxy inert energetics and MWCNT-AP-epoxy hybrid energetics demonstrates an initial elastic response followed by a reduction in composite stiffness believed to be associated with the formation of microcracks, and a subsequent abrupt brittle-like failure associated with the formation of macrocracks. In contrast, neat sugar-epoxy mock energetics and MWCNT-sugar-epoxy mock hybrid energetics observed in Fig. 4.9 b undergoe a much smaller initial elastic response, followed by a drastic reduction in composite stiffness and ductile-like extension of the strain to failure believed to be due to the formation of microcracks before final abrupt failure associated with macroscopic crack formation. It is to be noted, as shown in Fig. 4.5, that the AP crystals had rounded edges compared to the sugar crystals. It is believed that the sharp edges of the sugar crystals lead to stress concentrations which cause damage to initiate in a much more distributed fashion in the sugar mock samples and is therefore the main reason for the significant differences in mechanical properties (strength and fracture strain) observed between the AP inert energetics and sugar mock energetics. The resulting values for tensile modulus, tensile strength and fracture strain for as-produced AP inert energetic and sugar mock energetic specimens are provided in Fig. 4.10. The average tensile modulus for neat AP-epoxy inert energetics was measured to be 3.55 ± 0.24 GPa. Incorporation of randomly oriented MWCNTs into epoxy

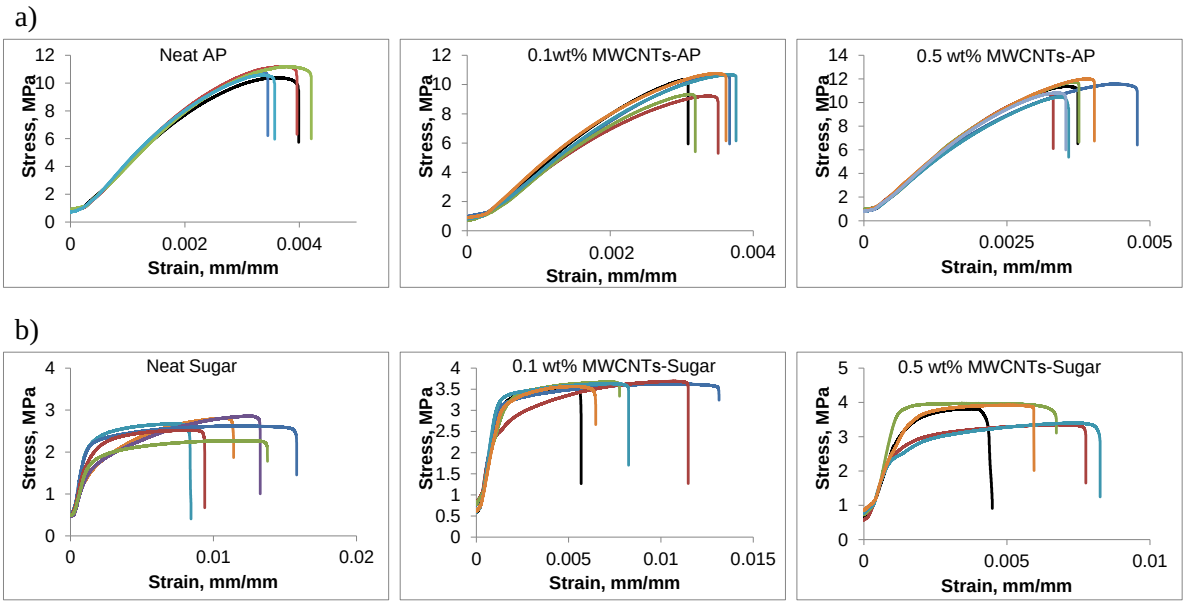

Figure 4.9: Stress-strain curves for a) neat AP inert energetics and MWCNT AP inert hybrid energetics b) neat sugar mock energetics and MWCNT sugar mock hybrid energetics

binder was found to lead to small changes in modulus having about 1.4% (3.60 ± 0.51 GPa) and 15% (4.06 ± 0.21 GPa) increase for 0.1wt% and 0.5 wt% MWCNTs-AP-epoxy hybrid energetics, respectively. The average tensile strength was found to be 10.83 ± 0.32 MPa for neat AP-epoxy, 10.17 ± 0.65 MPa for 0.1 wt% MWCNTs-AP-epoxy hybrid energetics and 11.25 ± 0.53 MPa for 0.5 wt% MWCNTs-AP-epoxy hybrid energetics. Moreover, the average fracture strain was measured to be $0.38 \pm 0.028\%$, $0.35 \pm 0.025\%$ and $0.38 \pm 0.044\%$, respectively. In brief, it was found that incorporating randomly oriented MWCNTs into epoxy polymer binder had no significant improvement in mechanical properties of AP inert energetics studied herein as demonstrated in Fig. 4.10 a.

On the other hand, the mechanical properties of sugar mock energetics were sensitive to MWCNTs incorporation into polymer binder as shown in Fig. 4.10 b. The average tensile modulus for neat sugar-epoxy mock energetics was measured to be 1.7 ± 0.36 GPa. Incorporating MWCNTs into epoxy binder had a substantial effect on the tensile modulus for sugar mock energetics. 0.1 wt% and 0.5 wt% MWCNTs-sugar-epoxy mock hybrid energetics have about 64% and 74% higher tensile modulus (2.79 ± 0.34 GPa and 2.97 ± 0.48 GPa, respec-

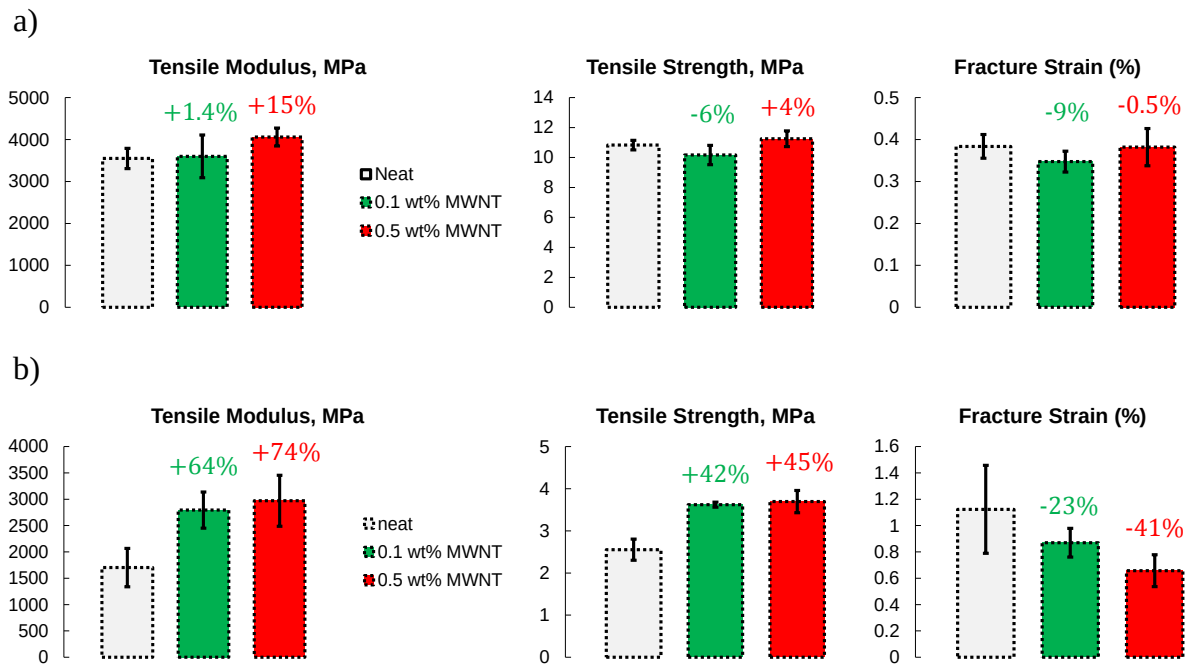

Figure 4.10: The resulting mechanical properties of a) AP inert energetics b) sugar mock energetics: Tensile Modulus, Strength and Fracture Strain

tively) than the neat sugar-epoxy mock energetics. Moreover, the average tensile strength was improved approximately 42% and 45% (3.62 ± 0.06 MPa and 3.69 ± 0.26 MPa, respectively) for 0.1 wt% and 0.5 wt% MWCNTs-sugar-epoxy mock hybrid energetics compared to the neat sugar-epoxy mock energetics (2.55 ± 0.25 GPa). The average fracture strain was measured to be $1.12 \pm 0.33\%$ for neat sugar-epoxy, $0.87 \pm 0.28\%$ for 0.1 wt% MWCNTs-sugar-epoxy mock hybrid energetics and $0.65 \pm 0.12\%$ for 0.5 wt% MWCNTs-sugar-epoxy mock hybrid energetics.

Low velocity Charpy impact tests were conducted to evaluate the load-displacement, load-time and impact absorbed energy-time history of as-produced neat AP inert energetic, neat sugar mock energetic, MWCNTs AP inert hybrid energetic and sugar mock hybrid energetic specimens. Basically, strain gauge load sensor attached to the instrumented striker records a voltage-time response, which is converted to a force (F)-time response through load cell calibration. According to the impulse momentum theorem, the change in momentum of the specimen is equal to the impulse applied to it as defined in Eqn. 4.2, in which the velocity

of the striker (V) during an impact can be inferred with the numerical integration of the measured force to obtain the velocity-time response (where V_0 is the initial impact velocity of the striker and τ is the duration of impact). Equation 4.3 represents the second numerical integration to obtain displacement (d)-time response. These data is then used to construct the force-displacement response. In addition, the impact absorbed energy ($E_{absorbed}$) can be determined through the numerical integration of force-displacement response as defined in Eqn. 4.4.

$$\begin{aligned} \int_0^\tau F dt &= m(V_0 - V) \\ V &= V_0 - \frac{1}{m}\int_0^\tau F dt \end{aligned} \tag{4.2}$$

$$\begin{aligned} d &= \int_0^\tau V dt \\ d &= \int_0^\tau (V_0 - \frac{1}{m}\int_0^\tau F dt) dt \end{aligned} \tag{4.3}$$

$$E_{absorbed} = \int_0^\tau FV dt \tag{4.4}$$

Figure 4.11 and 4.12 show the typical load-displacement curves, load-time curves and impact absorbed energy-time curves of the as-produced AP-epoxy inert energetics and sugar-epoxy mock energetics during the entire impact process. Multiple specimens were tested in order to compare the results of low velocity Charpy impact testing and to ensure consistency of the experiments. Region I in Fig. 4.11 and 4.12 corresponds to initial impact loading with the absence of damage (maximum impact load) (a-d) and the energy required to initiate microdamage fracture (pre-maximum load energy) (e-f) for as-produced neat AP inert energetic, neat sugar mock energetic, 0.1 wt% MWCNTs AP inert hybrid energetic and sugar mock hybrid energetic specimens. Region II in Fig. 4.11 and 4.12 corresponds to reduction

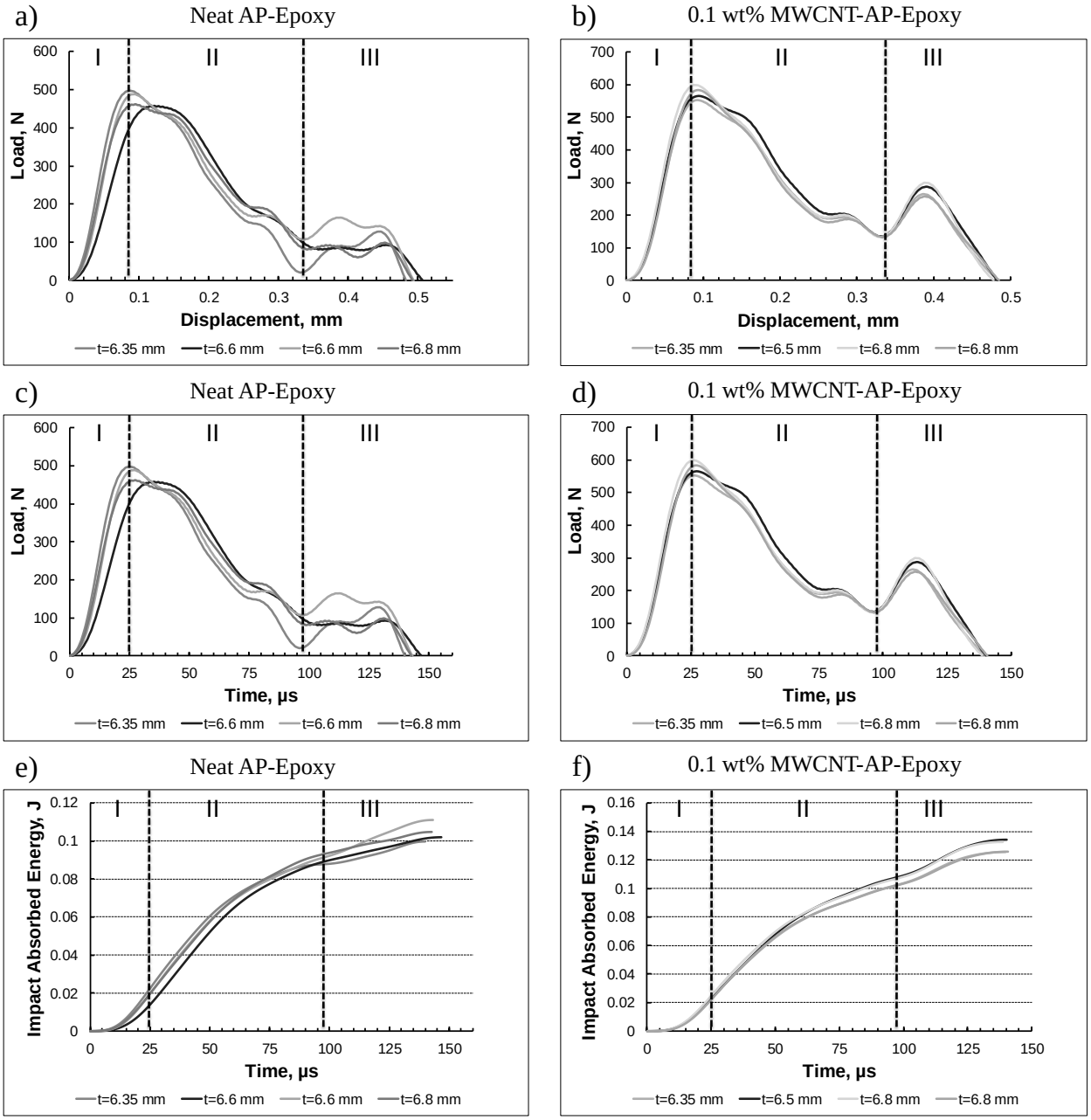

Figure 4.11: Low velocity impact load and impact absorbed energy history of a) neat AP inert energetics and b) MWCNT AP inert hybrid energetics, *t represents specimen thickness

in load carrying capacity due to initiation and propagation of micro and/or macroscale damage (a-d), and the energy required to propagate ductile fracture (post-maximum load energy) (e-f) for as-produced neat AP inert energetic, neat sugar mock energetic, 0.1 wt%

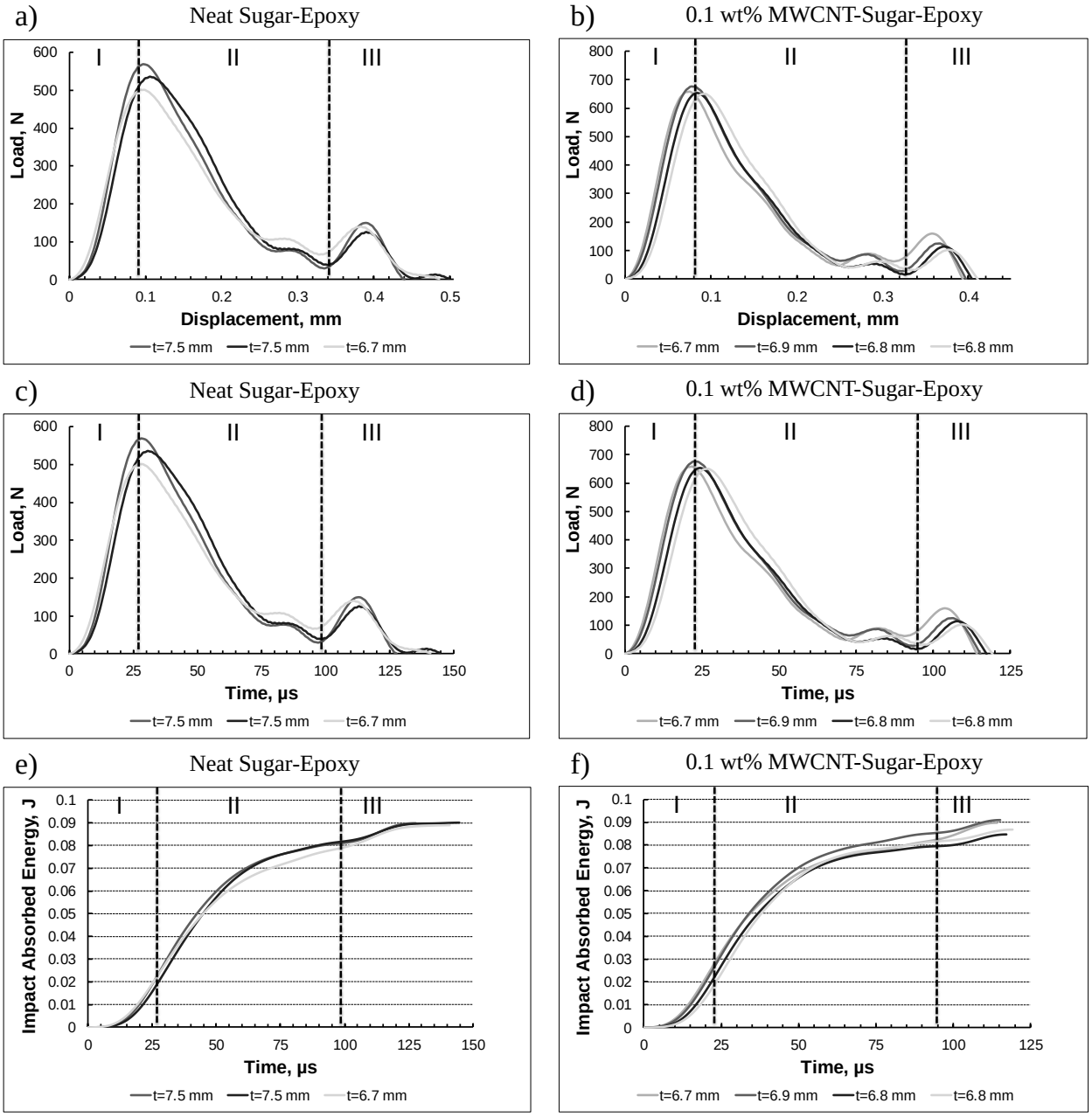

Figure 4.12: Low velocity impact load and impact absorbed energy history of a) neat sugar mock energetics and b) MWCNT sugar mock hybrid energetics, *t represents specimen thickness

MWCNTs AP inert hybrid energetic and sugar mock hybrid energetic specimens. Region III corresponds to the appearance of reloading after the peak impact load is observed for

as-produced neat AP inert energetic, neat sugar mock energetic, 0.1 wt% MWCNTs AP inert hybrid energetic and sugar mock hybrid energetic specimens. Previous studies in the open literature indicated that low frequency fluctuations caused by stored elastic energy and reflected stress waves [180], the influence of the hammer deformation caused by the vibration of the hammer [181], loss of contact and the regaining of contact between the specimen and the hammer, and the specimen and the supporting anvils [182,183] may all result in multiple peaks in load-time or load-displacement curves.

It is believed that reflected stress waves and hammer vibration have minimal contributions in the cases tested herein due to stiffness mismatch between the specimens and the hammer. Rather, the slight rotation of the hammer due to pendulum rigid body rotation [184] may result in asymmetric contact force distribution on top and bottom of the specimen during impact which may induce alternating reloading and unloading. In addition, the high speed recordings revealed that crack propagation resistance of MWCNT-AP inert hybrid energetics, resulting in releasing and restoring of the energy, induces the reloading peak as provided in Fig. 4.21.

It should be noted that the impact absorbed fracture energy is mainly dominated by impact force, fracture deflection and impact time. It is deduced from Fig. 4.11 that the averaged peak impact load for neat AP-epoxy inert energetics was measured to be 476.4 ± 16.97 N. Incorporation of randomly oriented MWCNTs into epoxy binder was found to have substantial effect on the peak impact load having about 21% (577.6 ± 16.5 N) increase for 0.1wt% MWCNTs-AP-epoxy inert hybrid energetics. The maximum fracture deflection (displacement at break) for neat AP-epoxy inert energetics and 0.1wt% MWCNTs-AP-epoxy inert hybrid energetics was indistinguishable and measured to be $\sim 0.5\ mm$. Furthermore, the energy required to propagate ductile fracture (post-maximum load energy) in Region II and the total energy required at failure was improved ∼16% and ∼24% for 0.1 wt% MWCNTs-AP-epoxy inert hybrid energetics compared to the neat AP-epoxy inert energetics. For sugar mock energetics, it is deduced from Fig. 4.12 that the averaged peak impact load for neat sugar-epoxy energetics was measured to be 535.1 ± 27.6 N. Incorporation of randomly ori-

ented MWCNTs into epoxy binder was found to have substantial effect on the peak impact load having about 16% (619.9±79.6 N) increase for 0.1wt% MWCNTs-sugar-epoxy mock hybrid energetics. The maximum fracture deflection, the energy required to propagate ductile fracture (post-maximum load energy) in Region II and the total energy required at failure were indistinguishable for sugar mock energetics studied herein as demonstrated in Fig. 4.12.

4.2.5 Fracture Surface Topography

In order to assess key failure mechanisms of as produced AP inert energetics and sugar mock energetics, their fracture surface topography after quasi-static tensile loading until failure has been examined with FE-SEM as shown in Figs. 4.13 and 4.14. It is to be noted that none of samples fracture surface has been polished after mechanical testing to investigate the raw fracture surface topography. The two possible predominant failure mechanisms that need to be investigated are interfacial seperation between the crystals and the binder, and crack initiation and propagation in the polymer binder. It is known that the stress required to initiate debonding between an inhomogeneity and the matrix is strongly dependent on not only the interfacial adhesion strength between an inhomogeneity and the binder but also the geometry of the inhomogeneity. It would be expected that the particularly sharp edged sugar crystals would lead to higher local stress concentration compared to spherical AP crystals, and therefore enable the initiation of interfacial failure much more readily; making occasional crystal fractures less of a contributing factor to the cause of failure. Figure 4.13 shows the fracture surface microgrpahs for 0.1 wt% MWCNTs AP inert hybrid energetics and sugar mock hybrid energetics. The interfacial debonding between the crystals and the binder was observed for AP inert hybrid energetics and sugar mock hybrid energetics. On further zooming into binder regions between the crystals in Fig. 4.13 a and c, individual MWCNTs forming a local nanotube network are observed in Fig. 4.13 b and d. It should be noted that the local MWCNT networks in the vicinity of microcracks as shown in Fig. 4.13 b and d are what provide microscale strain and damage sensing capability in piezoresistive

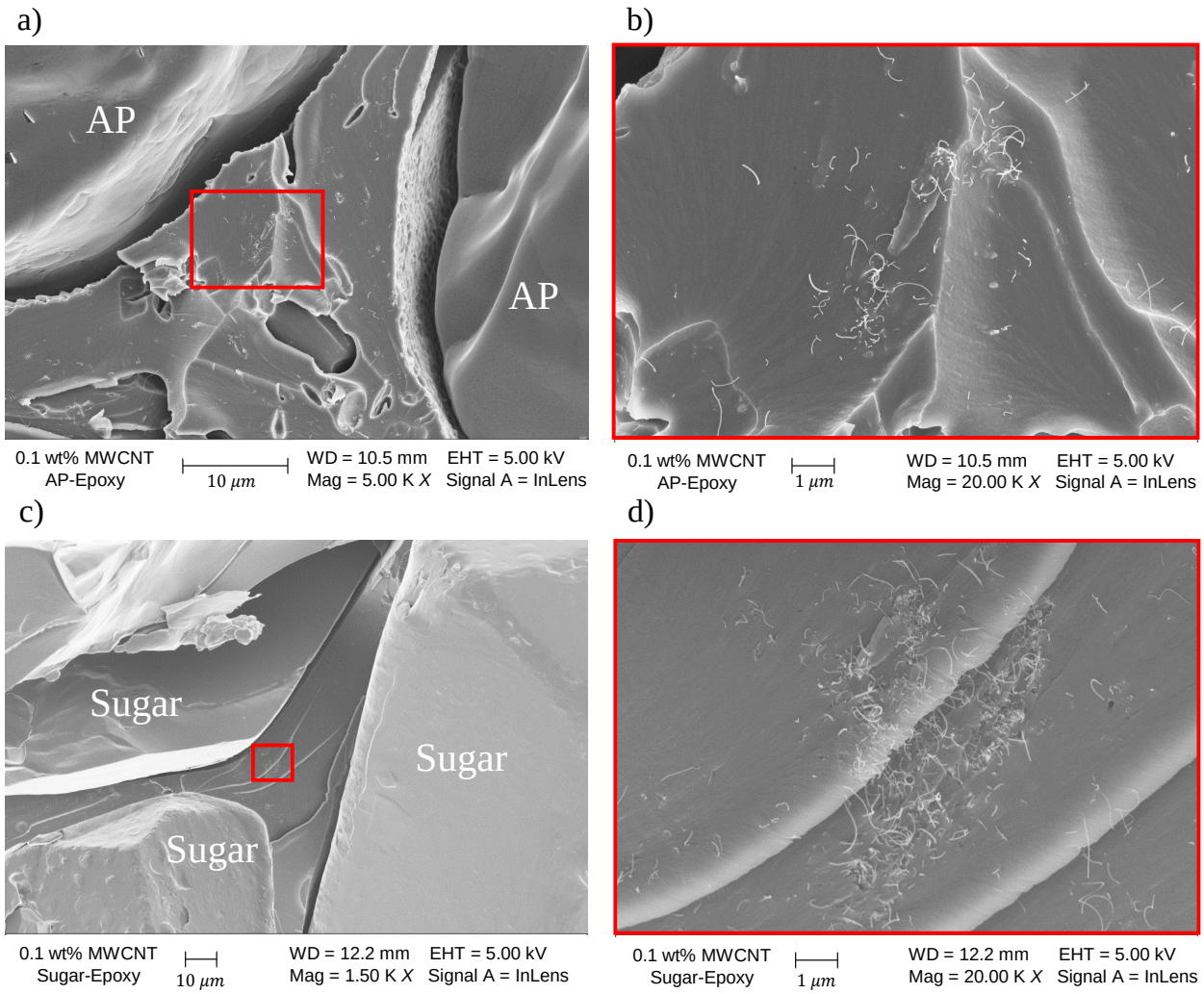

Figure 4.13: Fracture surface of AP inert hybrid energetics (a-b) and sugar mock hybrid energetics (c-d) embedded with 0.1 wt% MWCNTs

measurements. For the 0.5 wt% MWCNTs AP inert hybrid energetics and sugar mock hybrid energetics from Fig. 4.14 a and c, it is clear that there is still interfacial debonding between the crystals and the binder. On further zooming into binder regions between the crystals in Fig. 4.14 a and c, there is an increase in the number of individual MWCNTs forming local nanotube networks which are more unifomly distributed within the binder as observed in Fig. 4.14 b and d.

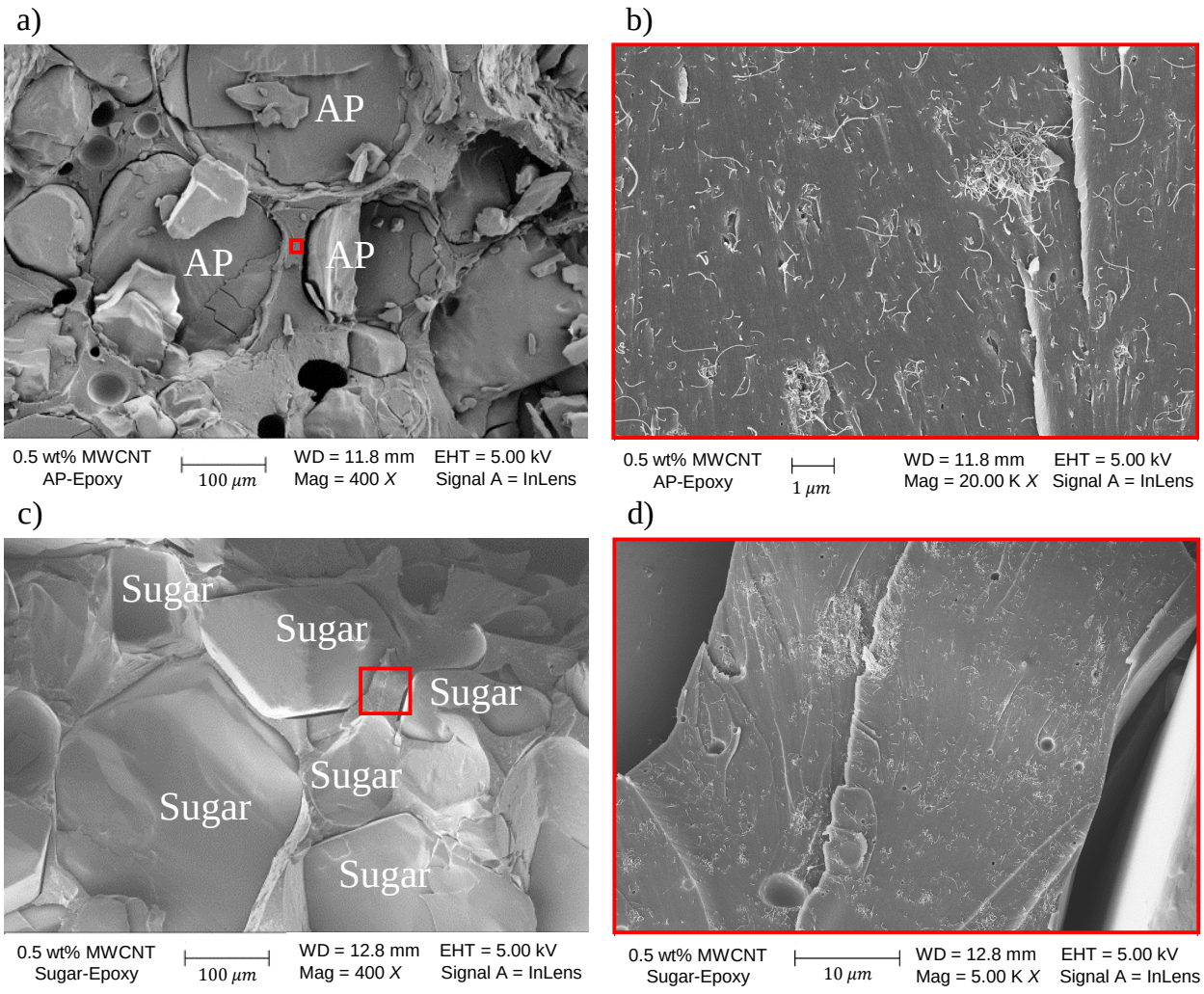

Figure 4.14: Fracture surface of AP inert hybrid energetics (a-b) and sugar mock hybrid energetics (c-d) embedded with 0.5 wt% MWCNTs

4.2.6 Piezoresistive Properties under Quasi-Static Loading

The piezoresistive response is quantitatively and qualitatively evaluated for MWCNT AP inert hybrid energetic and MWCNT sugar mock hybrid energetic specimens under quasi-static loading until failure. Neat AP energetics and sugar mock energetics were also tested to provide a baseline measurement from which to assess the effect of MWCNT incorporation on the piezoresistivity. For the neat AP inert energetic and sugar mock energetic samples, with the AP, sugar and epoxy having low conductivity and no inherent piezoresistivity,

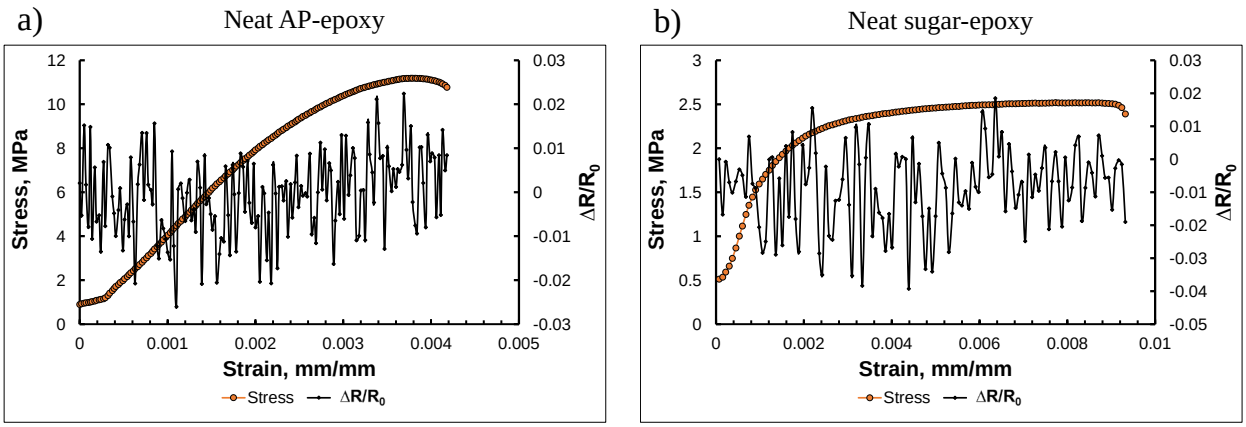

Figure 4.15: Electro–mechanical response of a) AP inert energetic ($R_0 = 3.37\ G\Omega$) and b) sugar mock ($R_0 = 4.98\ G\Omega$) energetic

Table 4.1: Measured gauge factors for AP inert hybrid energetics ($R_0 = 41.89 \pm 11.08\ M\Omega$) and sugar mock hybrid energetics ($R_0 = 72.76 \pm 2.99\ M\Omega$) embedded 0.1 wt% MWCNTs

Averaged Gauge Factors	AP Inert Hybrid Energetics	Sugar Mock Hybrid Energetics
G_I	2.05 ± 0.47	1.96 ± 0.38
G_{II}	2.12 ± 0.34	2.98 ± 0.86
G_{III}	7.52 ± 1.91	7.14 ± 1.03

no piezoresistive response is observed from the neat AP inert energetics and sugar mock energetics as demonstrated in Fig. 4.15. With the incorporation of randomly oriented-well dispersed MWCNTs into the epoxy binder, the MWCNT AP inert hybrid energetic and MWCNT sugar mock hybrid energetic samples indicate a clear and measurable piezoresistive response which correlates well with the stress-strain response as shown in Fig. 4.16. It was found that on addition of randomly oriented 0.1 wt% MWCNTs, a positive effect on the piezoresistive response was observed for MWCNT AP inert hybrid energetic and sugar mock hybrid energetic specimens as provided in Fig. 4.16. It is to be noted that the corresponding gauge factors provided in Table 4.1, measurements of strain and damage sensing sensitivities, are calculated for each data point and averaged within each regions (I, II, III corresponding to elastic, microscale damage and macroscale damage, respectively) and averaged from five specimens each for AP inert hybrid energetic and sugar mock hybrid energetic samples to provide lower and upper limits of sensitivity measurements. In terms of piezoresistive

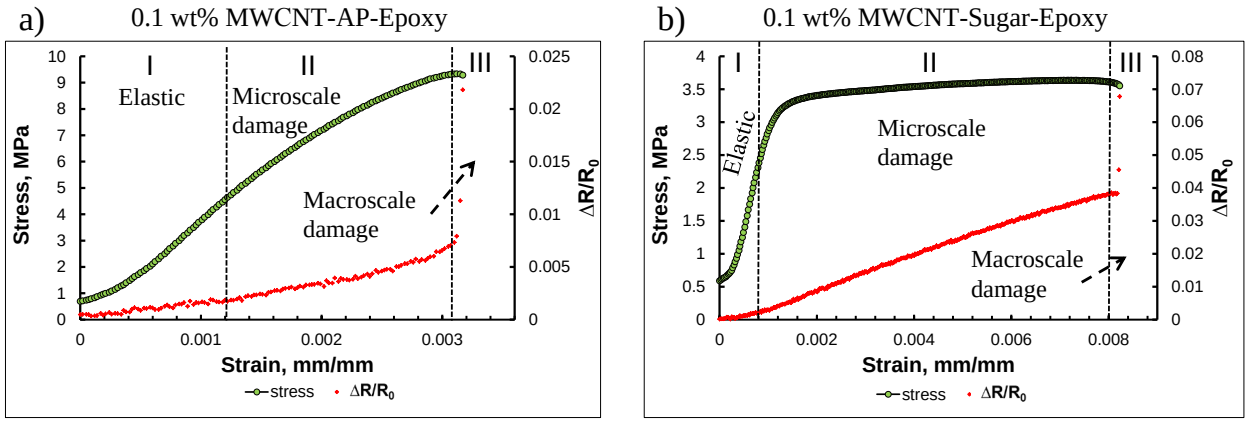

Figure 4.16: Piezoresistive response of a) AP inert hybrid energetic ($R_0 = 43.78\ M\Omega$) and b) sugar mock hybrid energetic ($R_0 = 72.23\ M\Omega$) embedded with 0.1 wt% MWCNTs

response of 0.1 wt% MWCNTs AP inert hybrid energetics in Fig. 4.16 a, the normalized relative change in resistance follows a linear increase in initial elastic region I up to 0.12% applied strain with an averaged gauge factor (G_I) of 2.05 ± 0.47. In terms of piezoresistive response of 0.1 wt% MWCNTs sugar mock hybrid energetics in Fig. 4.16 b, the normalized relative change in resistance also follows a linear increase in initial elastic region I up to 0.08% applied strain with an averaged gauge factor (G_I) of 1.96 ± 0.38. For both MWCNT AP inert hybrid energetics and sugar mock hybrid energetics, the observed relative change in resistance for region I can be attributed to local deformations of inherently piezoresistive MWCNT-epoxy binder in the absence of interfacial damage for the aforementioned low values of applied strains. On the further application of strain, an increase in the rate of change of the normalized relative change in resistance is observed in region II for both MWCNT AP inert hybrid energetics and sugar mock hybrid energetics, with the corresponding averaged gauge factors (G_{II}) of 2.12 ± 0.34 and 2.98 ± 0.86, respectively. The observed gauge factors for region II start to include the effect of local interfacial debonding between crystal and binder interfaces and local microcracks developing within the polymer binder medium as was shown in Fig. 4.13. As observed in the stress-strain response of region II in Fig. 4.16, reduction in hybrid composite stiffness for sugar mock hybrid specimen compared to AP hybrid specimen is drastic due to the formation of extensive interfacial debonding of the

sharp edged sugar crystals from the nanocomposite binder relative to spherical AP crystals, believed to be leading to higher gauge factors for sugar mock hybrid samples. It is also worth noting that the local MWCNT networks in the vicinity of microcracks as shown in Fig. 4.13 b and d induce microscale damage sensing capability in piezoresistive measurements for the observed gauge factors for region II. Finally, development of macrocracks in region III for both MWCNT AP inert hybrid energetics and sugar mock hybrid energetics lead to a non-linear evolution of normalized relative change in resistance which can be closely correlated to corresponding reduction in the stress response until failure, and leads to averaged gauge factors (G_{III}) of 7.52±1.91 and 7.14±1.03, respectively. In short, Table 4.1, measurements of strain and damage sensing sensitivities, includes the data for all MWCNT AP inert hybrid energetics and MWCNT sugar mock energetics which demonstrated final abrupt failure within the gauge section, thereby within the electrodes.

It should be further noted that for such particulate composites with heterogeneous granular microstructure, it is difficult to constrain the local interfacial debonding between crystal and binder interfaces and the developing microcracks to initiate in the gauge section for the dog-bone samples, especially for the sugar mock hybrid energetic specimens tested herein. In some cases, local interfacial debonding and microcracks can develop outside of the gauge section, relaxing the local stresses in the gauge section. Hence, digital image correlation (DIC) was conducted to obtain full displacement and strain fields as the AP inert hybrid energetics and sugar mock hybrid energetics undergo deformation in conjuntion with the piezoresistive testing. A multi-camera stereo DIC was implemented using LaVision E-lite 2M progressive scan CCD cameras, with 1628 x 1236 pixel resolution, 14 frames/sec and 12 bits, which are fixed at a 30° angle to one another. MWCNT AP inert hybrid energetics and MWCNT sugar mock hybrid energetics were speckled patterned before electro-mechanical-optical characterization. Figure 4.17 shows in situ DIC with piezoresistive response of MWCNT AP inert hybrid energetics and MWCNT sugar mock hybrid energetics. The electrodes on the monitored surface is excluded from the input images for the deformation calculation, as shown in Fig. 4.17. The aforementioned observations for piezoresistive response still remains valid for

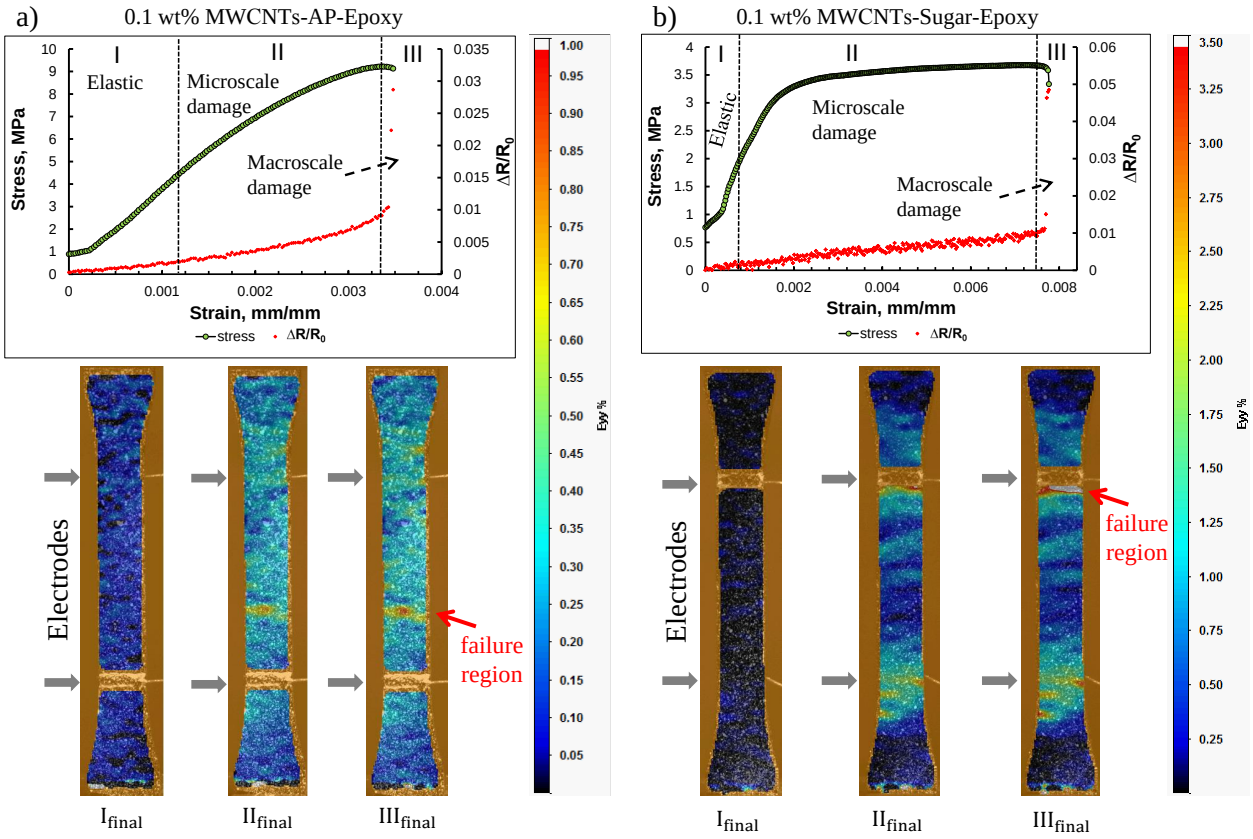

Figure 4.17: Coupled DIC and piezoresistive response of a) AP inert hybrid energetic ($R_0 = 54.44\ M\Omega$) and b) sugar mock hybrid energetic ($R_0 = 70.09\ M\Omega$) embedded with 0.1 wt% MWCNTs

MWCNT AP inert hybrid energetic and MWCNT sugar mock hybrid energetic specimens. Figure 4.17 a clearly indicated that microcracks and macroscale fractures initiate and propagate within the gauge section, within the electrodes, for MWCNT AP inert hybrid energetic due to rounded edges of the AP crystals. On the other hand, debonding of sharp edged sugar crystals have more randomness in terms of where the damage initiates compared to rounded edges of the AP crystals. For some MWCNT sugar mock hybrid energetics, illustrated in Fig. 4.17 b, it is clear that some microcracks are developing outside of the gauge section, outside of the electrodes, leading to a local stress relaxation within the binder in the gauge section which resulted in less increase in the piezoresistive sensitivity in the microscale damage region II. However, the mock hybrid energetic specimen still fails within the gauge

section in the electrodes as shown in Fig. 4.17 b. Such piezoresistive response of sugar mock hybrid energetic specimens have been included to calculate the lower bound of measurement of sensitivities, gauge factors, in the microscale damage region II provided in Table 4.1. It should be noted that electrical impedance tomography via embedding multiple electrodes on a specimen would provide much more detailed information about discerning and sensing the damage location through electrical resistance measurements for in situ real-time SHM applications. However, DIC in conjunction with piezoresistive measurement was still useful approach to discern the damage location initiation and propagation correlated to electrical resistance change for the as-produced AP inert hybrid energetic and sugar mock hybrid energetic samples.

In order to assess the performance of in situ real-time SHM and self-diagnostic functionalities of as-produced MWCNT AP inert hybrid energetics and sugar mock hybrid energetics, one should be aware how an ideal sensor should respond in the absence and presence of damage. Figure 4.18 a and b demonstrate the piezoresistive response and corresponding measurement of sensitivities (gauge factors) of ideal sensors, respectively for strain and damage sensing. In terms of piezoresistive response and corresponding gauge factors of ideal sensors, the normalized relative change in resistance should follow a linear increase, thereby leading to a constant gauge factor in initial elastic region I in the absence of damage for strain sensing. In the presence of microscale damage initiation and propagation, an increase in the rate of change of the normalized relative change in resistance should be observed in terms of piezoresistive response, and lead to a continuous increase in gauge factor as shown in region II. Furthermore, in the presence of macroscale damage initiation and propagation, the rate of change of the normalized relative change in resistance should increase even more in piezoresistive response, leading to further continuous increase in gauge factor as depicted in region III. In order to evaluate the typical performance of as-produced MWCNT AP inert hybrid energetics and sugar mock hybrid energetics, the measurement of sensitivities (gauge factors) have been calculated in each elastic, microscale damage and macroscale damage regions and plotted for two samples each of AP inert hybrid and sugar mock hybrid

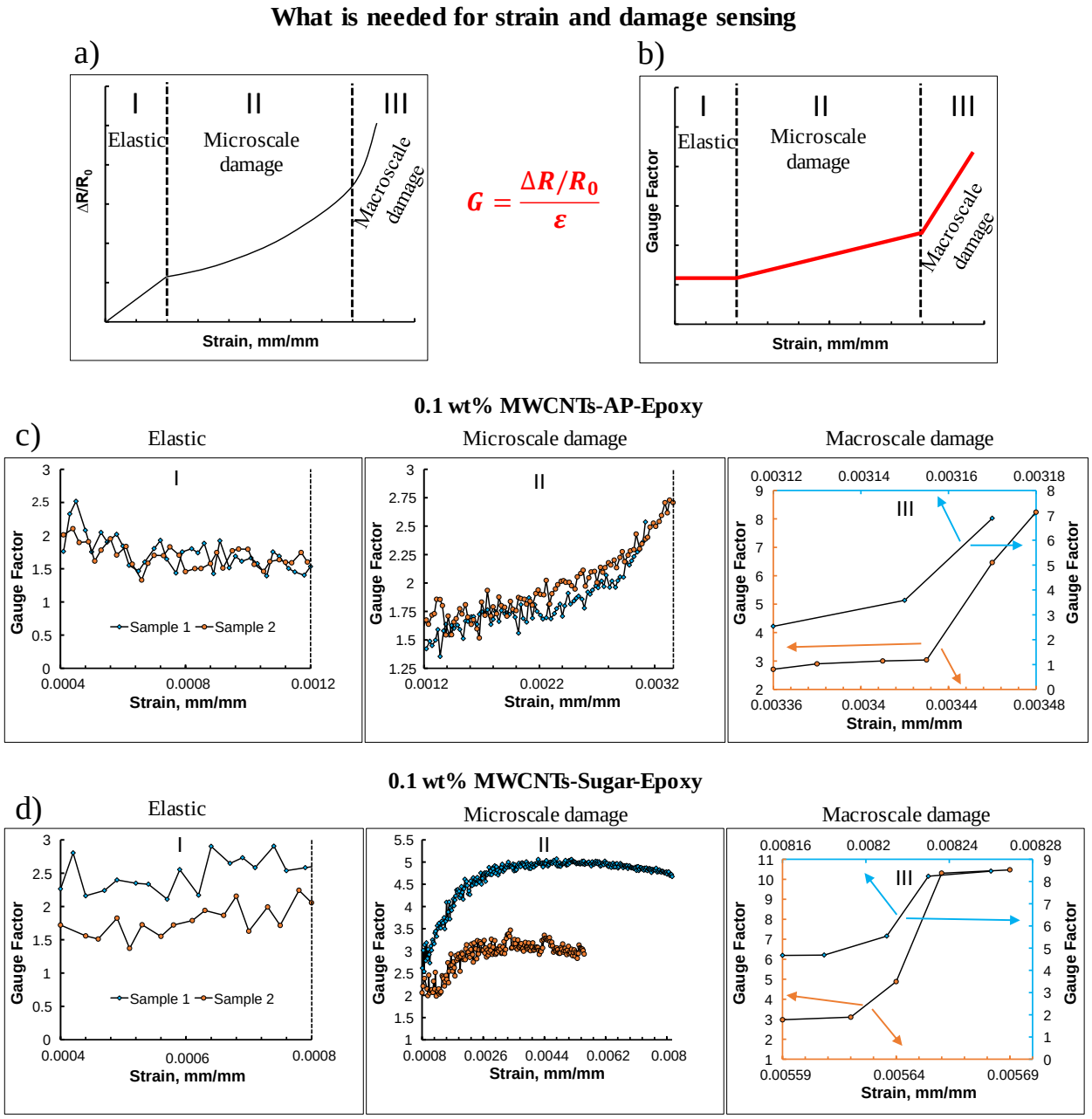

Figure 4.18: a) Piezoresistive response and b) corresponding measurement of sensitivities of ideal sensor for SHM applications and experimental measurement of sensitivities of c) AP inert hybrid and d) sugar mock hybrid energetics embedded with 0.1 wt% MWCNTs

energetics in Fig. 4.18 c and d, respectively. For both MWCNT AP inert hybrid energetics and MWCNT sugar mock hybrid energetics, the calculated gauge factors for each data point

are fairly stable and constant in elastic region I in Fig. 4.18 c and d, which demonstrates the ideal strain sensing performance. For microscale damage region II, it is obvious that the performance of actual MWCNT AP inert hybrid energetics in Fig. 4.18 c clearly indicates a continuous increase in the gauge factor in the presence of microscale damage initiation and propagation, demonstrating an ideal microscale damage sensing capability. On the other hand, MWCNT sugar mock hybrid energetics shows a continuous increase in gauge factors which follows the drastic reduction in stiffness, demonstrating an ideal microscale damage sensing performance and then the gauge factor becomes stable and fairly constant due to ductile-like extension in stress-strain response in region II, as was shown in Fig. 4.16. In terms of macroscale damage region III, both MWCNT AP inert hybrid energetics and MWCNT sugar mock hybrid energetics in Fig. 4.18 c and d clearly show a further increase in gauge factor in the presence of macroscale damage initiation and propagation, illustrating an ideal macroscale damage sensing capability. In short, MWCNT AP inert hybrid energetics and MWCNT sugar mock hybrid energetics clearly demonstrated in situ real-time sensing of deformation, microscale and macroscale damage initiation and propagation as ideal sensors.

4.2.7 Piezoresistive Properties under Low Velocity Impact Loading

The piezoresistive response is quantitatively and qualitatively evaluated for MWCNT AP inert hybrid energetic and MWCNT sugar mock hybrid energetic specimens under low velocity impact loading as described in Fig. 4.4. Neat AP energetics and sugar mock energetics were also tested to provide a baseline measurement from which to assess the effect of MWCNT incorporation on the piezoresistivity. No piezoresistive response is observed from the neat AP inert energetics and sugar mock energetics due to the extreme low conductivities and inherent piezoresistivity capabilities of AP/sugar crystals and polymer binder as demonstrated in Fig. 4.7. Figure 4.19 shows the typical initial resistance data under zero-load conditions for 0.1 wt% MWCNT AP inert hybrid energetic and MWCNT sugar mock hy-

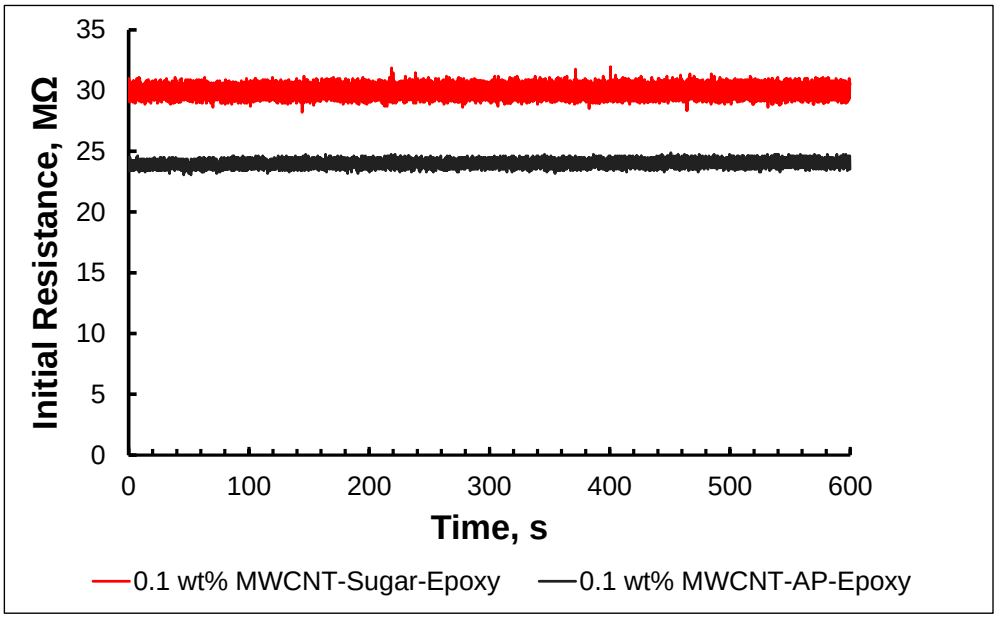

Figure 4.19: Typical initial resistance data for a) AP inert hybrid energetic and b) sugar mock hybrid energetic embedded with 0.1 wt% MWCNTs

brid energetics. The typical initial resistance data under zero loading exhibits no deviation with time. With the incorporation of 0.1 wt% randomly oriented-well dispersed MWCNTs into the epoxy binder, the MWCNT AP inert hybrid energetic and MWCNT sugar mock hybrid energetic samples indicate a clear and measurable piezoresistive response which correlates well with the low velocity impact loading history. In terms of piezoresistive response provided in Figs. 4.20, 4.21 and 4.22, the normalized relative change in resistance starts to increase during initial impact loading, corresponding to tensile strain sensing in the absence of damage in region I, which is an indication of deformation sensing capabilities of 0.1 wt% MWCNTs AP inert hybrid energetics and sugar mock hybrid energetics. For both MWCNT AP inert hybrid energetics and sugar mock hybrid energetics, the observed relative change in resistance within region I can be attributed to local deformations of inherently piezoresistive MWCNT-epoxy binder in the absence of interfacial failure and matrix cracking. On further application of impact loading, the piezoresistive response captures the damage initiation instantaneously. The normalized relative change in resistance continues to increase as load carrying capacity of AP inert hybrid energetics and sugar mock hybrid energetics

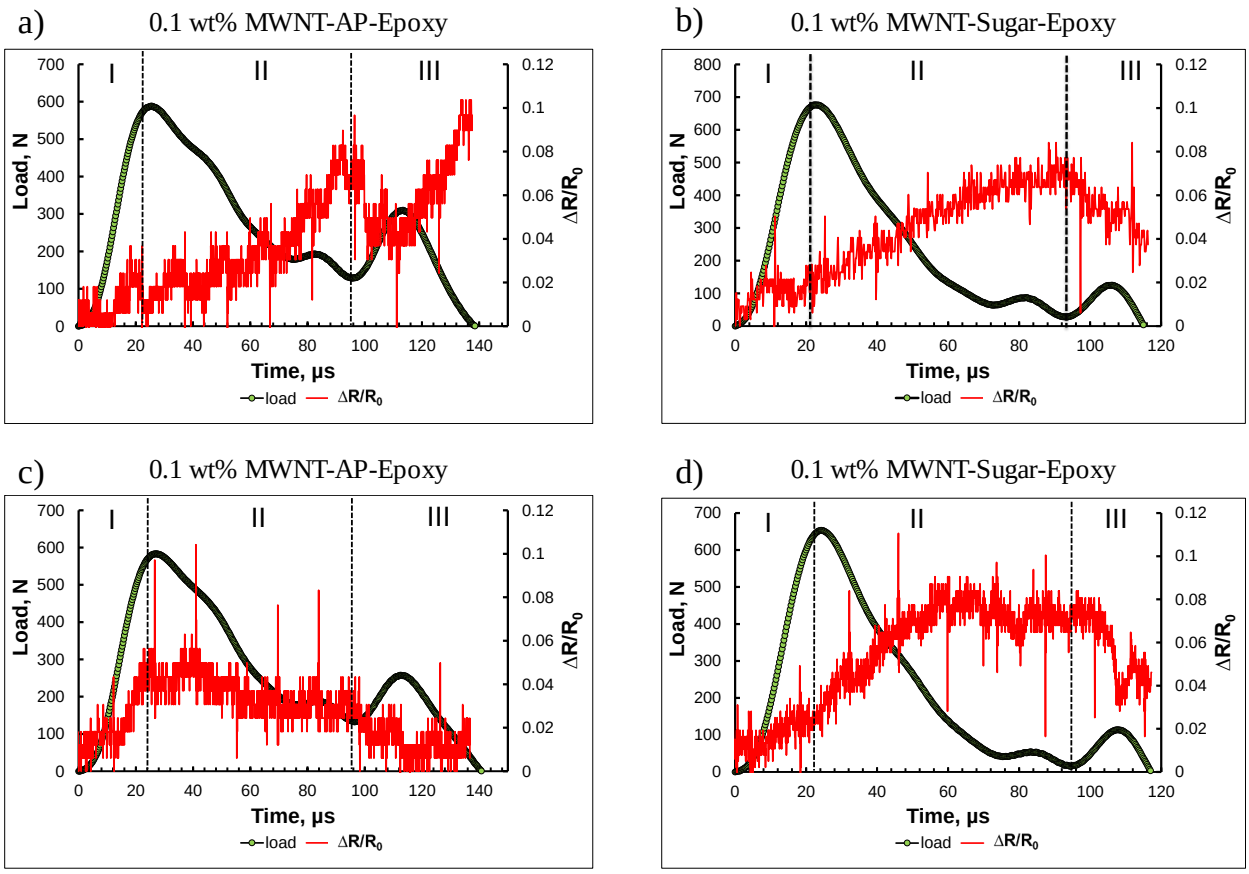

Figure 4.20: Piezoresistive response of a) AP inert hybrid and b) sugar mock hybrid energetics embedded with 0.1 wt% MWCNTs

starts to decrease due to initiation of microscale damage within region II. An increase in the rate of change of the normalized relative change in resistance is observed in region II for both MWCNT AP inert hybrid energetics and sugar mock hybrid energetics, which is an indication of a continuous assessment of damage state between damage initiation events as damage propagates. The following reduction and increase in the normalized relative change in resistance in region III during reloading and unloading can be attributed to the change in the current density within local polymer binder. Thus, the incorporation of MWCNTs into actual and mock energetic materials revealed promising self-diagnostic functionalities for in situ real-time SHM applications under quasi-static and low velocity impact loading for solid rocket propellants, detonators and munitions.

For the videos below, click to start, then click options and click "trust this document one time only" then click on the videos again to play.

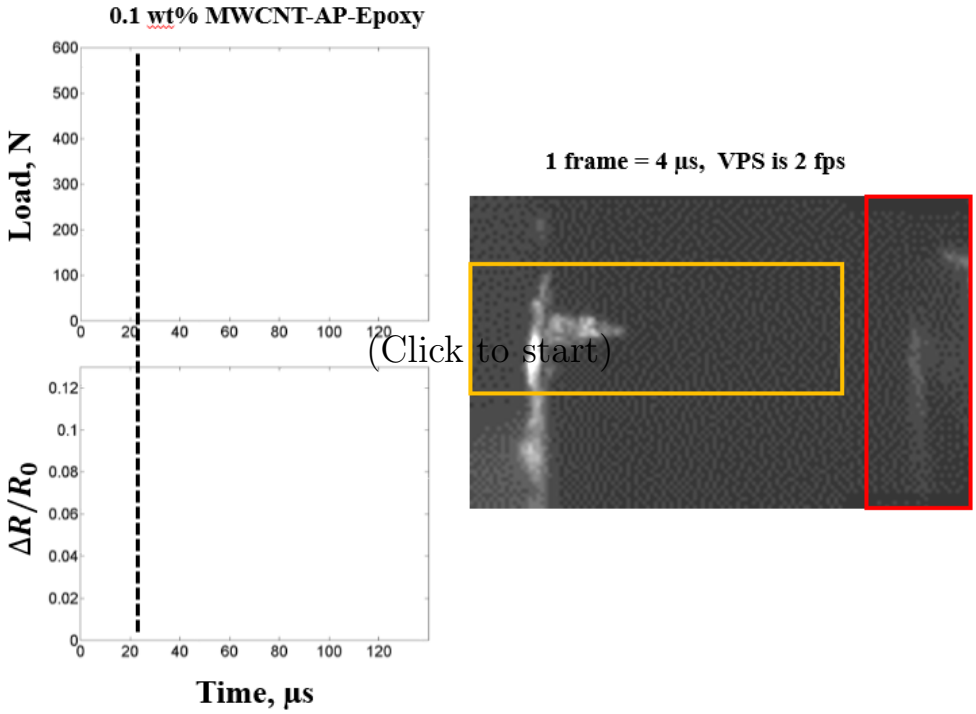

Figure 4.21: Electro-mechanical-optical characterization of AP inert hybrid energetic specimen under low velocity impact loading, see frames in Appendix C

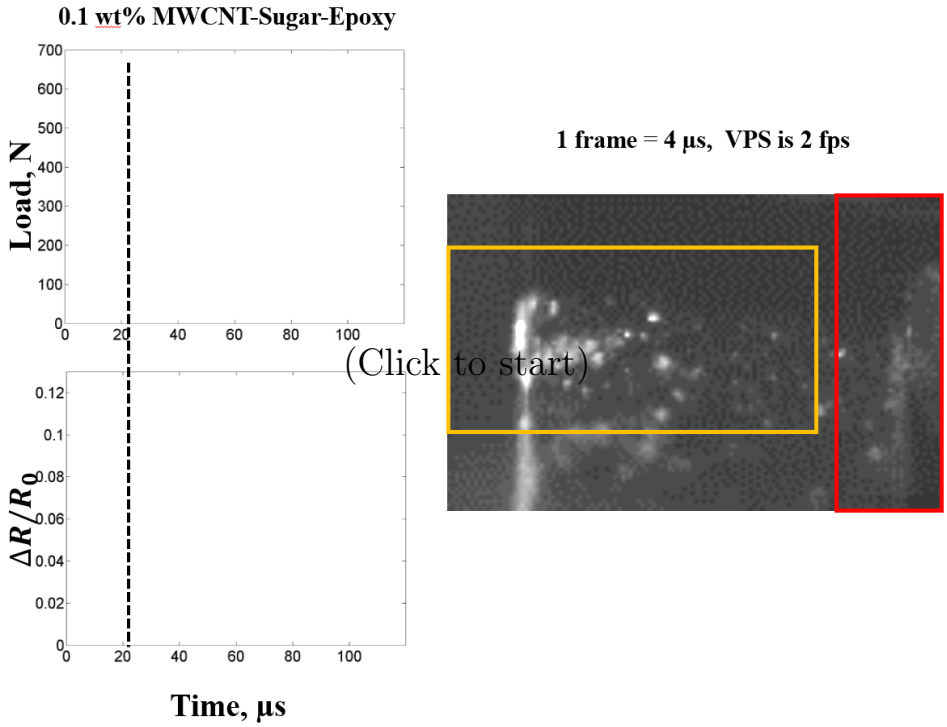

Figure 4.22: Electro-mechanical-optical characterization of sugar mock hybrid energetic specimen under low velocity impact loading, see frames in Appendix C

Chapter 5

Conclusions

This experimental study involves controlling the dispersion of CNTs and orientation of CNT filaments within nanocomposites under dielectrophoresis. Various process parameters, CNT concentration, applied electric field intensity, frequency and exposure time for guiding the design and fabrication process of nanocomposites were investigated. Aligned CNT polymer nanocomposites were scaled up with dielectrophoresis to investigate mechanical, electrical and sensing properties at the structural level. The piezoresistive response at a CNT concentration well below the nomimal percloation threshold demonstrated strain and microdamage sensing, underscoring the importance of orientation and microscale CNT distribution and network formation/disruption in governing the piezoresistive sensitivity. Furthermore, inherently sensing energetics were investigated for real-time embedded sensing of strain and damage through piezoresistive response for structural health monitoring in energetics under quasi-static and low velocity impact loading. Overall, the current work explores processing-structure-property relationships starting from CNT based nanocomposites to particulate hybrid composites to investigate deformation and damage sensing capabilities of inherently sensing materials and structures through piezoresistive response.

Chapter 2 focused on controlling the dispersion and orientation of carbon nanotube filaments within the structure. The formation and orientation of CNT filaments was achieved

by using dielectrophoresis during the manufacturing process. As such, here a phenomenological approach to understanding the CNT alignment and the multi-CNT-filament formation was explored by tuning the applied electric field magnitude, frequency and exposure time. Statistically meaningful distribution functions for morphological features were constructed. Some of the key observations based on the results presented in Chapter 2 are

- Much better dispersion with very few agglomerations was obtained using COOH-SWNTs in acrylate solution compared to pristine SWNTs.
- The filament width and the spacing between filaments of pristine SWNT-acrylate polymer nanocomposites both increase as exposure time to AC electric field and frequency increase.
- Comparatively, the aligned pristine SWCT-filaments were wider compared to the aligned COOH-SWNT-filaments. This indicates that the network for filament formation is much more efficient for pristine SWNT-acrylate solution than that of the COOH-SWNT-acrylate solution.
- Small degrees of misalignment in high aspect ratio CNT filaments led to a network of SWNT filaments that have bridges from one to the other in the transverse direction.
- Increases in exposure time to AC field and the frequency during fabrication resulted in an increase in conductivity in the alignment direction and in the direction transverse for both pristine SWNT and COOH-SWNT-acrylate polymer nanocomposites, which was well correlated with polarized Raman spectroscopy results.
- It was observed that a combination of exposure time to AC electric field and its frequency is the key driver of filament width and spacing and that, in general, the COOH-SWNTs align to a greater extent than the pristine SWNTs, though they do not form filaments that are as wide and contiguous for the exposure times studied herein.

- Changes in the microscale structure led to significant changes in the properties of the material system, and controlling the morphological features helped us to develop an effective empirical model, validate the model and quantify the uncertainty for guiding the design and fabrication process.

In Chapter 3, dielectrophoresis under the application of AC electric fields was used here to obtain long range alignment of CNTs at the structural level within a photopolymerizable monomer blend (urethane dimethacrylate (UDMA) and 1,6-hexanediol dimethacrylate (HDDMA)). The degree of alignment of CNTs within this long range architecture was observed via polarized Raman spectroscopy such that there was good alignment between $+/-$ 30 degrees; however, there was also a noticeable degreee of misalignment in the transverse direction. The influence of CNT alignment was also assessed with electrical conductivity measurements where improvements in electrical conductivity were obtained at a concentration below percolation threshold due to formation of CNT filaments. The increases in effective conductivity in the transverse direction to the alignment was also observed due to the small degrees of misalignment in high aspect ratio CNT filaments leading to a network of CNT filaments that have bridges from one to the other in the transverse direction. CNT-acrylate polymer nanocomposites piezoresistive response was quantitatively and qualitatively assessed for randomly oriented CNTs and both the CNT alignment and transverse to alignment directions under quasi-static monotonic and cyclic loading. Some of the key observations based on the results presented in Chapter 3 are

- The measured instantaneous electrical resistance change helped to both detect axial and transverse strain for the nanocomposites with gauge factors in the axial direction on the order of 2, and 5 fold increase to values on the order of 10 in the transverse direction.

- The change in resistance in the alignment direction under deformation can be attributed to disruption of conductive paths due to the rearrangement of carbon nanotube network in the matrix medium.

- Based on Raman analysis, it was believed the higher sensitivity of the transverse direction is tied to architectural evolution of misaligned bridging structures which connect alignment structures resulting in formation of conductive paths under load due to Poisson's contraction.
- The permanent and larger resistance change in the alignment direction after each subsequent cycle in the unloaded state supported the belief in an increase CNT network disruption inside nanocomposites and microdamage accumulation.
- The obtained results in the present study showed the piezoresistive capabilities at a concentration below percolation threshold for aligned specimens with SWCNTs loading as low as 0.03 wt% to detect strain and microdamage accumulation.
- Control of the CNT network allows for the establishment of percolation paths and piezoresistive response well below the nominal percolation rather than piezoresistive threshold observed for random, so called well-dispersed CNT network distributions.

In Chapter 4, distributing the sensing network throughout the binder phase of inert and mock energetic composites in an effort for real-time embedded sensing of strain and damage in energetic materials through piezoresistive response for SHM in energetic materials was studied to reduce the stochastic nature of safety characterization and help in designing insult tolerant energetic materials. As such, electrical, mechanical, electro-mechanical and electro-mechanical-optical characterization of neat AP inert energetics, neat sugar mock energetics, MWCNT AP inert hybrid and MWCNT sugar mock hybrid energetics was investigated. Some of the key observations based on the results presented in Chapter 4 are

- It was found out that neat AP inert energetic and sugar mock energetic samples are non-conductive and addition of MWCNTs increases the effective conductivity of the hybrid composite by several orders of magnitude.
- Incorporating randomly oriented MWCNTs into polymer binder had no significant improvement in the mechanical properties of AP inert hybrid energetics, whereas the

mechanical properties of sugar mock hybrid energetics were sensitive to MWCNTs incorporation into polymer binder.

- FESEM micrographs revealed that interfacial failure between the crystals and the binder and matrix cracking were the key failure mechanisms for quasi-static experiments.

- The measured instantaneous electrical resistance change for both MWCNT AP inert hybrid energetics and MWCNT sugar mock hybrid energetics helped to detect deformation, microscale damage and macroscale fracture as ideal sensors with gauge factors with values on the order of $\sim$2, $\sim$2.5 and $\sim$7, respectively.

- Piezoresistive measurements under quasi-static loading in conjuntion with DIC helped to sense and discern damage location correlated to the electrical resistance change.

- The measured instantaneous electrical resistance change for both MWCNT AP inert hybrid energetics and MWCNT sugar mock hybrid energetics under low velocity impact loading provided deformation sensing capabilities and a continuous assessment of damage state between damage initiation events as damage propagates with the incorporation of CNTs within local polymer binder of particulate inert and mock energetics.

- The current work demonstrated the electro-mechanical characterization of AP inert hybrid energetic and sugar mock hybrid energetic materials in order to provide the proof of concept for the strain and damage sensing under quasi-static and low velocity impact loading for real-time SHM and self-diagnostic functionalities in energetic materials embedded with CNTs.

Chapter 6

Future Work

Initial proof of concept for the strain and damage sensing under quasi-static and low velocity impact loading for real-time SHM and self-diagnostic functionalities in inert and mock energetics embedded with CNT nanocomposite binder has been demonstrated in Chapter 4. It is essential to investigate the coupled electro-mechanical response of inert, mock and actual energetics with various binder compositions (epoxy, HTPB, PDMS, estane) embedded with CNTs under quasi-static, low velocity impact loading and high strain rate split Hopkinson pressure-bar tests in conjunction with DIC. Further, there are little to no results in the open literature exploring in situ real-time electrical impedance tomography in conjunction with optical characterization of nanocomposite bonded inert, mock and actual energetics under quasi-static and dynamic loading. In addition, it is further needed to conduct thermo-electromechanical testing with thermal cycles in conjunction with electrical measurements to provide thermal induced deformation and damage sensing. Moreover, it is important to simulate hot spot initiation through localized heating with the focused ion laser beam in conjunction with a combination of in-situ real-time electrical measurements, Raman spectroscopy, optical microscopy and thermal imaging to provide localized thermal induced damage sensing. Therefore, in situ real-time SHM in energetics is essential to reduce the large stochasticity in the characterization of the safety and stability of energetic materials.

Bibliography

[1] A. Alivisatos, "Semiconductor clusters, nanocrystals, and quantum dots," *SCIENCE*, vol. 271, no. 5251, pp. 933–937, FEB 16 1996.

[2] X. F. Ningzhong Bao and C. A. Grimes, "Self-organized one-dimensional tio2 nanotube/nanowire array films for use in excitonic solar cells: A review," *Journal of Nanotechnology*, vol. 2012, no. 645931, p. 27, 2012.

[3] A. Kirkeminde, B. A. Ruzicka, R. Wang, S. Puna, H. Zhao, and S. Ren, "Synthesis and Optoelectronic Properties of Two-Dimensional FeS2 Nanoplates," *ACS APPLIED MATERIALS & INTERFACES*, vol. 4, no. 3, pp. 1174–1177, MAR 2012.

[4] S. Jeon, Y.-S. Nam, D. J.-L. Shir, J. A. Rogers, and A. Hamza, "Three dimensional nanoporous density graded materials formed by optical exposures through conformable phase masks," *APPLIED PHYSICS LETTERS*, vol. 89, no. 25, DEC 18 2006.

[5] T. Ozel, A. Gaur, J. Rogers, and M. Shim, "Polymer electrolyte gating of carbon nanotube network transistors," *NANO LETTERS*, vol. 5, no. 5, pp. 905–911, MAY 2005.

[6] A. Javey, J. Guo, Q. Wang, M. Lundstrom, and H. Dai, "Ballistic carbon nanotube field-effect transistors," *NATURE*, vol. 424, no. 6949, pp. 654–657, AUG 7 2003.

[7] M. Winter and R. Brodd, "What are batteries, fuel cells, and supercapacitors?" *CHEMICAL REVIEWS*, vol. 104, no. 10, pp. 4245–4269, OCT 2004.

[8] T. Rueckes, K. Kim, E. Joselevich, G. Tseng, C. Cheung, and C. Lieber, "Carbon nanotube-based nonvolatile random access memory for molecular computing," *SCIENCE*, vol. 289, no. 5476, pp. 94–97, JUL 7 2000.

[9] J. Kong, N. Franklin, C. Zhou, M. Chapline, S. Peng, K. Cho, and H. Dai, "Nanotube molecular wires as chemical sensors," *SCIENCE*, vol. 287, no. 5453, pp. 622–625, JAN 28 2000.

[10] S. Wong, E. Joselevich, A. Woolley, C. Cheung, and C. Lieber, "Covalently functionalized nanotubes as nanometre-sized probes in chemistry and biology," *NATURE*, vol. 394, no. 6688, pp. 52–55, JUL 2 1998.

[11] R. Baughman, A. Zakhidov, and W. de Heer, "Carbon nanotubes - the route toward applications," *SCIENCE*, vol. 297, no. 5582, pp. 787–792, AUG 2 2002.

[12] V. K. Vadlamani, V. B. Chalivendra, A. Shukla, and S. Yang, "Sensing of damage in carbon nanotubes and carbon black-embedded epoxy under tensile loading," *POLYMER COMPOSITES*, vol. 33, no. 10, pp. 1809–1815, OCT 2012.

[13] R. Baughman, C. Cui, A. Zakhidov, Z. Iqbal, J. Barisci, G. Spinks, G. Wallace, A. Mazzoldi, D. De Rossi, A. Rinzler, O. Jaschinski, S. Roth, and M. Kertesz, "Carbon nanotube actuators," *SCIENCE*, vol. 284, no. 5418, pp. 1340–1344, MAY 21 1999.

[14] B. Landi, R. Raffaelle, M. Heben, J. Alleman, W. VanDerveer, and T. Gennett, "Single wall carbon nanotube-Nafion composite actuators," *NANO LETTERS*, vol. 2, no. 11, pp. 1329–1332, NOV 2002.

[15] P. Collins and P. Avouris, "Nanotubes for electronics," *SCIENTIFIC AMERICAN*, vol. 283, no. 6, pp. 62+, DEC 2000.

[16] W. DEHEER, A. CHATELAIN, and D. UGARTE, "A CARBON NANOTUBE FIELD-EMISSION ELECTRON SOURCE," *SCIENCE*, vol. 270, no. 5239, pp. 1179–1180, NOV 17 1995.

[17] R. R. Saito, G. Dresselhaus, M. S. Dresselhaus, and K. (Firm), *Physical properties of carbon nanotubes*. London : Imperial College Press, 1998, includes bibliographical references and index. [Online]. Available: http://app.knovel.com/web/toc.v/cid:kpPPCN0006

[18] G. Yin, N. Hu, Y. Karube, Y. Liu, Y. Li, and H. Fukunaga, "A carbon nanotube/polymer strain sensor with linear and anti-symmetric piezoresistivity," *JOURNAL OF COMPOSITE MATERIALS*, vol. 45, no. 12, pp. 1315–1323, JUN 2011.

[19] L. Gao, T.-W. Chou, E. T. Thostenson, and Z. Zhang, "A comparative study of damage sensing in fiber composites using uniformly and non-uniformly dispersed carbon nanotubes," *Carbon*, vol. 48, no. 13, pp. 3788–3794, 2010.

[20] N. Hu, Y. Karube, M. Arai, T. Watanabe, C. Yan, Y. Li, Y. Liu, and H. Fukunaga, "Investigation on sensitivity of a polymer/carbon nanotube composite strain sensor," *CARBON*, vol. 48, no. 3, pp. 680–687, MAR 2010.

[21] I. H. Paik, N. S. Goo, Y. C. Jung, and J. W. Cho, "Development and application of conducting shape memory polyurethane actuators," *SMART MATERIALS & STRUCTURES*, vol. 15, no. 5, pp. 1476–1482, OCT 2006.

[22] N. G. Sahoo, Y. C. Jung, H. J. Yoo, and J. W. Cho, "Effect of functionalized carbon nanotubes on molecular interaction and properties of polyurethane composites," *MACROMOLECULAR CHEMISTRY AND PHYSICS*, vol. 207, no. 19, pp. 1773–1780, OCT 2 2006.

[23] S. Liu, Y. Liu, H. Cebeci, R. G. de Villoria, J.-H. Lin, B. L. Wardle, and Q. M. Zhang, "High Electromechanical Response of Ionic Polymer Actuators with Controlled-Morphology Aligned Carbon Nanotube/Nafion Nanocomposite Electrodes," *ADVANCED FUNCTIONAL MATERIALS*, vol. 20, no. 19, pp. 3266–3271, OCT 8 2010.

[24] H. Lu, J. Gou, J. Leng, and S. Du, "Magnetically aligned carbon nanotube in nanopaper enabled shape-memory nanocomposite for high speed electrical actuation," *Applied Physics Letters*, vol. 98, no. 17, p. 174105, 2011.

[25] A. Pathak, J. AuBuchon, D. Brei, J. Shaw, J. Luntz, and S. Jin, "Carbon nanotube (cnt) fins for enhanced cooling of shape memory alloy wire," pp. 69 291K–69 291K–8, 2008. [Online]. Available: http://dx.doi.org/10.1117/12.774147

[26] W. P. Lim, K. Yao, and Y. Chen, "Alignment of carbon nanotubes by acoustic manipulation in a fluidic medium," *JOURNAL OF PHYSICAL CHEMISTRY C*, vol. 111, no. 45, pp. 16 802–16 807, NOV 15 2007.

[27] X. H. Kong, C. Deneke, H. Schmidt, D. J. Thurmer, H. X. Ji, M. Bauer, and O. G. Schmidt, "Surface acoustic wave mediated dielectrophoretic alignment of rolled-up microtubes in microfluidic systems," *APPLIED PHYSICS LETTERS*, vol. 96, no. 13, MAR 29 2010.

[28] K. M. Seemann, J. Ebbecke, and A. Wixforth, "Alignment of carbon nanotubes on prestructured silicon by surface acoustic waves," *NANOTECHNOLOGY*, vol. 17, no. 17, pp. 4529–4532, SEP 14 2006.

[29] S. Kumar, T. D. Dang, F. E. Arnold, A. R. Bhattacharyya, B. G. Min, X. Zhang, R. A. Vaia, C. Park, W. W. Adams, R. H. Hauge, R. E. Smalley, S. Ramesh, and P. A. Willis, "Synthesis, structure, and properties of pbo/swnt composites&," *Macromolecules*, vol. 35, no. 24, pp. 9039–9043, 2002.

[30] S. Kumar, T. Dang, F. Arnold, A. Bhattacharyya, B. Min, X. Zhang, R. Vaia, C. Park, W. Adams, R. Hauge, R. Smalley, S. Ramesh, and P. Willis, "Synthesis, structure, and properties of PBO/SWNT composites," *MACROMOLECULES*, vol. 35, no. 24, pp. 9039–9043, NOV 19 2002.

[31] W. Obitayo and T. Liu, "Effect of orientation on the piezoresistivity of mechanically drawn single walled carbon nanotube (swcnt) thin films," *Carbon*, vol. 85, pp. 372 – 382, 2015.

[32] J. Shaver, A. N. G. Parra-Vasquez, S. Hansel, O. Portugall, C. H. Mielke, M. von Ortenberg, R. H. Hauge, M. Pasquali, and J. Kono, "Alignment dynamics of single-walled carbon nanotubes in pulsed ultrahigh magnetic fields," *ACS Nano*, vol. 3, no. 1, pp. 131–138, 2009.

[33] "Magnetic field alignment and electrical properties of solution cast pet-carbon nanotube composite films," *Polymer*, vol. 50, no. 3, pp. 898 – 904, 2009.

[34] E. S. Choi, J. S. Brooks, D. L. Eaton, M. S. Al-Haik, M. Y. Hussaini, H. Garmestani, D. Li, and K. Dahmen, "Enhancement of thermal and electrical properties of carbon nanotube polymer composites by magnetic field processing," *Journal of Applied Physics*, vol. 94, no. 9, 2003.

[35] Y. Miao, Q. Q. Yang, R. Sammynaiken, W. J. Zhang, J. Maley, and G. Schatte, "Influence of aligned carbon nanotube networks on piezoresistive response in carbon nanotube films under in-plane straining," *Applied Physics Letters*, vol. 102, no. 23, 2013.

[36] A. Oliva-Avilés, F. Avilés, and V. Sosa, "Electrical and piezoresistive properties of multi-walled carbon nanotube/polymer composite films aligned by an electric field," *Carbon*, vol. 49, no. 9, pp. 2989 – 2997, 2011.

[37] E. C. Sengezer, G. D. Seidel, and R. J. Bodnar, "Phenomenological characterization of fabrication of aligned pristine-swnt and cooh-swnt nanocomposites via dielectrophoresis under ac electric field," *Polymer Composites*, vol. 36, no. 7, pp. 1266–1279, 2015. [Online]. Available: http://dx.doi.org/10.1002/pc.23031

[38] E. C. Sengezer and G. D. Seidel, ser. 56th AIAA/ASCE/AHS/ASC Structures, Structural Dynamics, and Materials Conference, (AIAA 2015-0126). American Institute of Aeronautics and Astronautics, Jan 2015, ch. Experimental Characterization of Damage Evolution in Carbon Nanotube-Polymer Nanocomposites, 0. [Online]. Available: https://doi.org/10.2514/6.2015-0126

[39] C. Park, J. Wilkinson, S. Banda, Z. Ounaies, K. E. Wise, G. Sauti, P. T. Lillehei, and J. S. Harrison, "Aligned single-wall carbon nanotube polymer composites using an electric field," *Journal of Polymer Science Part B: Polymer Physics*, vol. 44, no. 12, pp. 1751–1762, 2006.

[40] M.-W. Wang, "Alignment of multiwall carbon nanotubes in polymer composites by dielectrophoresis," *Japanese Journal of Applied Physics*, vol. 48, no. 3R, p. 035002, 2009.

[41] C. Ma, W. Zhang, Y. Zhu, L. Ji, R. Zhang, N. Koratkar, and J. Liang, "Alignment and dispersion of functionalized carbon nanotubes in polymer composites induced by an electric field," *Carbon*, vol. 46, no. 4, pp. 706–710, Apr. 2008.

[42] Y.-F. Zhu, C. Ma, W. Zhang, R.-P. Zhang, N. Koratkar, and J. Liang, "Alignment of multiwalled carbon nanotubes in bulk epoxy composites via electric field," *Journal of Applied Physics*, vol. 105, no. 5, 2009. [Online]. Available: http://scitation.aip.org/content/aip/journal/jap/105/5/10.1063/1.3080243

[43] C.-S. Lim, A. J. Rodriguez, M. E. Guzman, J. D. Schaefer, and B. Minaie, "Processing and properties of polymer composites containing aligned functionalized carbon nanofibers," *Carbon*, vol. 49, no. 6, pp. 1873 – 1883, 2011.

[44] S. U. Khan, J. R. Pothnis, and J.-K. Kim, "Effects of carbon nanotube alignment on electrical and mechanical properties of epoxy nanocomposites," *Composites Part A: Applied Science and Manufacturing*, vol. 49, pp. 26 – 34, 2013.

[45] W. Sun, H. Tomita, S. Hasegawa, Y. Kitamura, M. Nakano, and J. Suehiro, "An array of interdigitated parallel wire electrodes for preparing a large-scale nanocomposite film with aligned carbon nanotubes," *Journal of Physics D: Applied Physics*, vol. 44, no. 44, p. 445303, 2011.

[46] J. Shaver, A. N. G. Parra-Vasquez, S. Hansel, O. Portugall, C. H. Mielke, M. von Ortenberg, R. H. Hauge, M. Pasquali, and J. Kono, "Alignment Dynamics of Single-Walled Carbon Nanotubes in Pulsed Ultrahigh Magnetic Fields," *ACS NANO*, vol. 3, no. 1, pp. 131–138, JAN 2009.

[47] B. W. Steinert and D. R. Dean, "Magnetic field alignment and electrical properties of solution cast PET-carbon nanotube composite films," *POLYMER*, vol. 50, no. 3, pp. 898–904, JAN 28 2009.

[48] E. Choi, J. Brooks, D. Eaton, M. Al-Haik, M. Hussaini, H. Garmestani, D. Li, and K. Dahmen, "Enhancement of thermal and electrical properties of carbon nanotube polymer composites by magnetic field processing," *JOURNAL OF APPLIED PHYSICS*, vol. 94, no. 9, pp. 6034–6039, NOV 1 2003.

[49] M. Bryning, M. Islam, J. Kikkawa, and A. Yodh, "Very low conductivity threshold in bulk isotropic single-walled carbon nanotube-epoxy composites," *ADVANCED MATERIALS*, vol. 17, no. 9, pp. 1186+, MAY 2 2005.

[50] A. Moisala, Q. Li, I. A. Kinloch, and A. H. Windle, "Thermal and electrical conductivity of single- and multi-walled carbon nanotube-epoxy composites," *COMPOSITES SCIENCE AND TECHNOLOGY*, vol. 66, no. 10, pp. 1285–1288, AUG 2006.

[51] F. Gojny, M. Wichmann, B. Fiedler, I. Kinloch, W. Bauhofer, A. Windle, and K. Schulte, "Evaluation and identification of electrical and thermal conduction mechanisms in carbon nanotube/epoxy composites," *POLYMER*, vol. 47, no. 6, pp. 2036–2045, MAR 8 2006.

[52] A. Yu, M. E. Itkis, E. Bekyarova, and R. C. Haddon, "Effect of single-walled carbon nanotube purity on the thermal conductivity of carbon nanotube-based composites," *Applied Physics Letters*, vol. 89, no. 13, p. 133102, 2006.

[53] B. Kim, J. Lee, and I. Yu, "Electrical properties of single-wall carbon nanotube and epoxy composites," *JOURNAL OF APPLIED PHYSICS*, vol. 94, no. 10, pp. 6724–6728, NOV 15 2003.

[54] S. Barrau, P. Demont, C. Maraval, A. Bernes, and C. Lacabanne, "Glass transition temperature depression at the percolation threshold in carbon nanotube-epoxy resin and polypyrrole-epoxy resin composites," *MACROMOLECULAR RAPID COMMUNICATIONS*, vol. 26, no. 5, pp. 390–394, MAR 4 2005.

[55] J. Brown, D. Anderson, R. Justice, K. Lafdi, M. Belfor, K. Strong, and D. Schaefer, "Hierarchical morphology of carbon single-walled nanotubes during sonication in an aliphatic diamine," *POLYMER*, vol. 46, no. 24, pp. 10 854–10 865, NOV 21 2005.

[56] M. W. Wang, T. C. Hsu, and C. H. Weng, "Alignment of MWCNTs in polymer composites by dielectrophoresis," *EUROPEAN PHYSICAL JOURNAL-APPLIED PHYSICS*, vol. 42, no. 3, pp. 241–246, JUN 2008.

[57] C. Ma, W. Zhang, Y. Zhu, L. Ji, R. Zhang, N. Koratkar, and J. Liang, "Alignment and dispersion of functionalized carbon nanotubes in polymer composites induced by an electric field," *CARBON*, vol. 46, no. 4, pp. 706–710, APR 2008.

[58] C. Park, J. Wilkinson, S. Banda, Z. Ounaies, K. Wise, G. Sauti, P. Lillehei, and J. Harrison, "Aligned single-wall carbon nanotube polymer composites using an electric field," *JOURNAL*

OF POLYMER SCIENCE PART B-POLYMER PHYSICS, vol. 44, no. 12, pp. 1751–1762, JUN 15 2006.

[59] M. Hughes, "AC electrokinetics: applications for nanotechnology," *NANOTECHNOLOGY*, vol. 11, no. 2, pp. 124–132, JUN 2000, 7th Annual Foresight Conference on Molecular Nanotechnology, SANTA CLARA, CALIFORNIA, OCT 15-17, 1999.

[60] T. Jones, "Basic theory of dielectrophoresis and electrorotation," *IEEE ENGINEERING IN MEDICINE AND BIOLOGY MAGAZINE*, vol. 22, no. 6, pp. 33–42, NOV-DEC 2003.

[61] N. Peng, Q. Zhang, J. Li, and N. Liu, "Influences of ac electric field on the spatial distribution of carbon nanotubes formed between electrodes," *JOURNAL OF APPLIED PHYSICS*, vol. 100, no. 2, JUL 15 2006.

[62] A. K. Srivastava, S. J. Jeong, M.-H. Lee, S. H. Lee, S. H. Jeong, and Y. H. Lee, "Dielectrophoresis force driven dynamics of carbon nanotubes in liquid crystal medium," *Journal of Applied Physics*, vol. 102, no. 4, 2007.

[63] Y. Lu, C. Chen, L. Yang, and Y. Zhang, "Theoretical Simulation on the Assembly of Carbon Nanotubes Between Electrodes by AC Dielectrophoresis," *NANOSCALE RESEARCH LETTERS*, vol. 4, no. 2, pp. 157–164, FEB 2009.

[64] M. Dimaki and P. Boggild, "Dielectrophoresis of carbon nanotubes using microelectrodes: a numerical study," *NANOTECHNOLOGY*, vol. 15, no. 8, pp. 1095–1102, AUG 2004.

[65] H. A. Pohl, *Dielectrophoresis : the behavior of neutral matter in nonuniform electric fields*, 1978, vol. , no. .

[66] W. Xu and M. G. Allen, "Deformable strain sensors based on patterned mwcnts/polydimethylsiloxane composites," *Journal of Polymer Science Part B: Polymer Physics*, vol. 51, no. 20.

[67] X. Song, S. Liu, Z. Gan, Q. Lv, H. Cao, and H. Yan, "Controllable fabrication of carbon nanotube-polymer hybrid thin film for strain sensing," *Microelectronic Engineering*, vol. 86, no. 11, pp. 2330 – 2333, 2009.

[68] S. Luo and T. Liu, "Structurepropertyprocessing relationships of single-wall carbon nanotube thin film piezoresistive sensors," *Carbon*, vol. 59, pp. 315 – 324, 2013.

[69] M. Park, H. Kim, and J. P. Youngblood, "Strain-dependent electrical resistance of multi-walled carbon nanotube/polymer composite films," *Nanotechnology*, vol. 19, no. 5, p. 055705.

[70] I. Kang, Y. Y. Heung, J. H. Kim, J. W. Lee, R. Gollapudi, S. Subramaniam, S. Narasimhadevara, D. Hurd, G. R. Kirikera, V. Shanov, M. J. Schulz, D. Shi, J. Boerio, S. Mall, and M. Ruggles-Wren, "Introduction to carbon nanotube and nanofiber smart materials," *Composites Part B: Engineering*, vol. 37, no. 6, pp. 382 – 394, 2006.

[71] I. Kang, M. J. Schulz, J. H. Kim, V. Shanov, and D. Shi, "A carbon nanotube strain sensor for structural health monitoring," *Smart Materials and Structures*, vol. 15, no. 3, p. 737.

[72] G. Yin, N. Hu, Y. Karube, Y. Liu, Y. Li, and H. Fukunaga, "A carbon nanotube/polymer strain sensor with linear and anti-symmetric piezoresistivity," vol. 45, no. 12, pp. 1315–1323, 2011.

[73] K. Loh, J. Lynch, B. Shim, and N. Kotov, "Tailoring piezoresistive sensitivity of multilayer carbon nanotube composite strain sensors," vol. 19, no. 7, pp. 747–764, 2008.

[74] G. T. Pham, Y.-B. Park, Z. Liang, C. Zhang, and B. Wang, "Processing and modeling of conductive thermoplastic/carbon nanotube films for strain sensing," *Composites Part B: Engineering*, vol. 39, no. 1, pp. 209 – 216, 2008.

[75] J. H. Kang, C. Park, J. A. Scholl, A. H. Brazin, N. M. Holloway, J. W. High, S. E. Lowther, and J. S. Harrison, "Piezoresistive characteristics of single wall carbon nanotube/polyimide nanocomposites," *Journal of Polymer Science Part B: Polymer Physics*, vol. 47, no. 16.

[76] A. de la Vega, J. Sumfleth, H. Wittich, and K. Schulte, "Time and temperature dependent piezoresistance of carbon nanofiller/polymer composites under dynamic load," *Journal of Materials Science*, vol. 47, no. 6, 2012.

[77] S. Luo, W. Obitayo, and T. Liu, "Swcnt-thin-film-enabled fiber sensors for lifelong structural health monitoring of polymeric composites - from manufacturing to utilization to failure," *Carbon*, vol. 76, pp. 321 – 329, 2014.

[78] R. Zhang, H. Deng, R. Valenca, J. Jin, Q. Fu, E. Bilotti, and T. Peijs, "Strain sensing behaviour of elastomeric composite films containing carbon nanotubes under cyclic loading," *Composites Science and Technology*, vol. 74, pp. 1 – 5, 2013.

[79] J. Bautista-Quijano, F. Avils, J. Aguilar, and A. Tapia, "Strain sensing capabilities of a piezoresistive mwcnt-polysulfone film," *Sensors and Actuators A: Physical*, vol. 159, no. 2, pp. 135 – 140, 2010.

[80] M. Rein, O. Breuer, and H. Wagner, "Sensors and sensitivity: Carbon nanotube buckypaper films as strain sensing devices," *Composites Science and Technology*, vol. 71, no. 3, pp. 373 – 381, 2011.

[81] N. Hu, Y. Karube, C. Yan, Z. Masuda, and H. Fukunaga, "Tunneling effect in a polymer/carbon nanotube nanocomposite strain sensor," *Acta Materialia*, vol. 56, no. 13, pp. 2929 – 2936, 2008.

[82] L. Gao, E. T. Thostenson, Z. Zhang, and T.-W. Chou, "Coupled carbon nanotube network and acoustic emission monitoring for sensing of damage development in composites," *Carbon*, vol. 47, no. 5, pp. 1381 – 1388, 2009.

[83] P. Fernberg, G. Nilsson, and R. Joffe, "Piezoresistive performance of long-fiber composites with carbon nanotube doped matrix," *Journal of Intelligent Material Systems and Structures*, vol. 20, no. 9, pp. 1017–1023, 2009. [Online]. Available: http://dx.doi.org/10.1177/1045389X08097387

[84] M. H. G. Wichmann, S. T. Buschhorn, J. Gehrmann, and K. Schulte, "Piezoresistive response of epoxy composites with carbon nanoparticles under tensile load," *Phys. Rev. B*, vol. 80, p. 245437, Dec 2009.

[85] V. K. Vadlamani, V. B. Chalivendra, A. Shukla, and S. Yang, "Sensing of damage in carbon nanotubes and carbon black-embedded epoxy under tensile loading," *Polymer Composites*, vol. 33, no. 10.

[86] E. Thostenson and T.-W. Chou, "Carbon nanotube networks: Sensing of distributed strain and damage for life prediction and self healing," *Advanced Materials*, vol. 18, no. 21.

[87] W. Zhang, J. Suhr, and N. Koratkar, "Carbon nanotube/polycarbonate composites as multifunctional strain sensors," *Journal of Nanoscience and Nanotechnology*, vol. 6, no. 4, pp. 960–964, 2006-04-01T00:00:00.

[88] J. Ku-Herrera and F. Avils, "Cyclic tension and compression piezoresistivity of carbon nanotube/vinyl ester composites in the elastic and plastic regimes," *Carbon*, vol. 50, no. 7, pp. 2592 – 2598, 2012.

[89] L. Bger, M. H. Wichmann, L. O. Meyer, and K. Schulte, "Load and health monitoring in glass fibre reinforced composites with an electrically conductive nanocomposite epoxy matrix," *Composites Science and Technology*, vol. 68, no. 78, pp. 1886 – 1894, 2008.

[90] M. Nofar, S. Hoa, and M. Pugh, "Failure detection and monitoring in polymer matrix composites subjected to static and dynamic loads using carbon nanotube networks," *Composites Science and Technology*, vol. 69, no. 10, pp. 1599 – 1606, 2009, cNT-NET 07 Special Issue with regular papers.

[91] N. Heeder, A. Shukla, V. Chalivendra, S. Yang, and K. Park, "Electrical response of carbon nanotube reinforced nanocomposites under static and dynamic loading," *Experimental Mechanics*, vol. 52, no. 3, 2012.

[92] A. K. Chaurasia, E. C. Sengezer, K. K. Talamadupula, S. Povolny, and G. D. Seidel, "Experimental characterization and computational modeling of deformation and damage sensing through the piezoresistive response of nanocomposite bonded surrogate energetic materials," *Journal of Multifunctional Composites*, vol. 2, no. 4, 2014.

[93] E. C. Sengezer and G. D. Seidel, "Application of piezoresistive nanocomposite binders for real time embedded sensing of strain and damage in energetic materials," in *58th AIAA/ASCE/AHS/ASC Structures, Structural Dynamics, and Materials Conference*, 2017, p. 0122.

[94] E. C. Sengezer, S. Povolny, and G. Seidel, "Real time in-situ sensing of damage evolution in carbon nanotube-polymer nanocomposite bonded surrogate energetics," in *Proceedings of 57th AIAA/ASCE/AHS/ASC Structures, Structural Dynamics, and Materials Conference, San Diego, California, USA*, 2016, pp. 2016–0412.

[95] E. C. Sengezer and G. D. Seidel, "Real time in-situ sensing of damage evolution in nanocomposite bonded surrogate energetic materials," *SPIE Smart Structures and Materials+ Nondestructive Evaluation and Health Monitoring*, p. 98000X, 2016.

[96] E. C. Sengezer, G. D. Seidel, and R. J. Bodnar, "Anisotropic piezoresistivity characteristics of aligned carbon nanotube-polymer nanocomposites," *Smart Materials and Structures*, vol. 26, no. 9, p. 095027, 2017.

[97] E. C. Sengezer and G. D. Seidel, "Structural health monitoring of nanocomposite bonded energetic materials through piezoresistive response," *AIAA Journal*, p. manuscript accepted, 2017-03-J056178.

[98] J. J. Ku-Herrera, F. Avilés, and G. D. Seidel, "Self-sensing of elastic strain, matrix yielding and plasticity in multiwall carbon nanotube/vinyl ester composites," *Smart Materials and Structures*, vol. 22, no. 8, p. 085003.

[99] A. Naghashpour and S. V. Hoa, "A technique for real-time detection, location and quantification of damage in large polymer composite structures made of electrically non-conductive fibers and carbon nanotube networks," *Nanotechnology*, vol. 24, no. 45, p. 455502.

[100] E. T. Thostenson and T.-W. Chou, "Real-time in situ sensing of damage evolution in advanced fiber composites using carbon nanotube networks," *Nanotechnology*, vol. 19, no. 21, p. 215713.

[101] A. K. Chaurasia, X. Ren, and G. D. Seidel, "Computational micromechanics analysis of electron hopping and interfacial damage induced piezoresistive response in carbon nanotube-polymer nanocomposites," *Smart Materials and Structures*, vol. 23, no. 7, p. 075023.

[102] C. Li and T.-W. Chou, "Modeling of damage sensing in fiber composites using carbon nanotube networks," *Composites Science and Technology*, vol. 68, pp. 3373 – 3379, 2008.

[103] T. Theodosiou and D. Saravanos, "Numerical investigation of mechanisms affecting the piezoresistive properties of cnt-doped polymers using multi-scale models," *Composites Science and Technology*, vol. 70, no. 9, pp. 1312 – 1320, 2010.

[104] B. Hu, N. Hu, Y. Li, K. Akagi, W. Yuan, T. Watanabe, and Y. Cai, "Multi-scale numerical simulations on piezoresistivity of cnt/polymer nanocomposites," *Nanoscale Research Letters*, vol. 7, no. 402, pp. 1–11, 2012.

[105] A. K. Chaurasia and G. D. Seidel, "Computational micromechanics analysis of electron hopping induced conductive paths and associated macroscale piezoresistive response in carbon nanotube-polymer nanocomposites," *Journal of Intelligent Material Systems and Structures*.

[106] X. Ren and G. D. Seidel, "Computational micromechanics modeling of inherent piezoresistivity in carbon nanotubepolymer nanocomposites," *Journal of Intelligent Material Systems and Structures*, 2013.

[107] X. Ren, A. K. Chaurasia, A. I. Oliva-Avils, J. J. Ku-Herrera, G. D. Seidel, and F. Avils, "Modeling of mesoscale dispersion effect on the piezoresistivity of carbon nanotube-polymer nanocomposites via 3d computational multiscale micromechanics methods," *Smart Materials and Structures*, vol. 24, no. 6, p. 065031.

[108] C. Li and T.-W. Chou, "Modeling of damage sensing in fiber composites using carbon nanotube networks," *Composites Science and Technology*, vol. 68, pp. 3373–3379, 2008.

[109] F. Du, R. Scogna, W. Zhou, S. Brand, J. Fischer, and K. Winey, "Nanotube networks in polymer nanocomposites: Rheology and electrical conductivity," *Macromolecules*, vol. 37, pp. 9048–9055, 2004.

[110] N. Hua, Y. Karube, C. Yan, Z. Masuda, and H. Fukunaga, "Tunneling effect in a polymer/carbon nanotube nanocomposite strain sensor," *Acta Materialia*, vol. 56, pp. 2929–2936, March 2008.

[111] X. Sun and M. Song, "Highly conductive carbon nanotube/polymer nanocomposites achievable?" *Macromolecular Theory and Simulations*, vol. 18, pp. 155–161, April 2009.

[112] C. Li, E. T. Thostenson, and T.-W. Chou, "Dominant role of tunneling resistance in the electrical conductivity of carbon nanotubebased composites," *Applied Physics Letters*, vol. 91, no. 22, pp. –, 2007.

[113] J. G. Simmons, "Electric tunnel effect between dissimilar electrodes separated by a thin insulating film," *Journal of Applied Physics*, vol. 34, no. 9, 1963.

[114] M. S. Fuhrer, J. Nygrd, L. Shih, M. Forero, Y.-G. Yoon, M. S. C. Mazzoni, H. J. Choi, J. Ihm, S. G. Louie, A. Zettl, and P. L. McEuen, "Crossed nanotube junctions," *Science*, vol. 288, no. 5465, pp. 494–497, 2000.

[115] A. Buldum and J. P. Lu, "Contact resistance between carbon nanotubes," *Phys. Rev. B*, vol. 63, p. 161403, Apr 2001.

[116] C. Li, E. T. Thostenson, and T.-W. Chou, "Effect of nanotube waviness on the electrical conductivity of carbon nanotube-based composites," *Composites Science and Technology*, vol. 68, no. 6, pp. 1445 – 1452, 2008.

[117] Z. Wang and X. Ye, "A numerical investigation on piezoresistive behaviour of carbon nanotube/polymer composites: mechanism and optimizing principle," *Nanotechnology*, vol. 24, no. 26, p. 265704.

[118] R. Rahman and P. Servati, "Effects of inter-tube distance and alignment on tunnelling resistance and strain sensitivity of nanotube/polymer composite films," *Nanotechnology*, vol. 23, no. 5, p. 055703.

[119] T. N. Tallman and K. W. Wang, "The influence of nanofiller alignment on transverse percolation and conductivity," *Nanotechnology*, vol. 26, no. 2, p. 025501.

[120] N. Hu, Y. Karube, M. Arai, T. Watanabe, C. Yan, Y. Li, Y. Liu, and H. Fukunaga, "Investigation on sensitivity of a polymer/carbon nanotube composite strain sensor," *Carbon*, vol. 48, no. 3, pp. 680 – 687, 2010.

[121] T. W. Tombler, C. Zhou, L. Alexseyev, J. Kong, H. Dai, L. Liu, C. S. Jayanthi, M. Tang, and S.-Y. Wu, "Reversible electromechanical characteristics of carbon nanotubes under local-probe manipulation," *Nature*, vol. 405, no. 6788, pp. 769–772, Jun 2000.

[122] J. Cao, Q. Wang, and H. Dai, "Electromechanical properties of metallic, quasimetallic, and semiconducting carbon nanotubes under stretching," *Phys. Rev. Lett.*, vol. 90, p. 157601, Apr 2003.

[123] C. Stampfer, A. Jungen, R. Linderman, D. Obergfell, S. Roth, and C. Hierold, "Nano-electromechanical displacement sensing based on single-walled carbon nanotubes," *Nano Letters*, vol. 6, no. 7, pp. 1449–1453, 2006, pMID: 16834427.

[124] P. Dharap, Z. Li, S. Nagarajaiah, and E. V. Barrera, "Nanotube film based on single-wall carbon nanotubes for strain sensing," *Nanotechnology*, vol. 15, no. 3, p. 379.

[125] A. Rochefort, P. Avouris, F. Lesage, and D. R. Salahub, "Electrical and mechanical properties of distorted carbon nanotubes," *Phys. Rev. B*, vol. 60, pp. 13 824–13 830, Nov 1999.

[126] S. Peng and K. Cho, "Chemical control of nanotube electronics," *Nanotechnology*, vol. 11, no. 2, p. 57.

[127] A. J. Paleo, F. W. J. van Hattum, J. Pereira, J. G. Rocha, J. Silva, V. Sencadas, and S. Lanceros-Mndez, "The piezoresistive effect in polypropylene carbon nanofibre composites obtained by shear extrusion," *Smart Materials and Structures*, vol. 19, no. 6, p. 065013.

[128] F. Avilés, A. May-Pat, G. Canché-Escamilla, O. Rodríguez-Uicab, J. J. Ku-Herrera, S. Duarte-Aranda, J. Uribe-Calderon, P. I. Gonzalez-Chi, L. Arronche, and V. La Saponara, "Influence of carbon nanotube on the piezoresistive behavior of multiwall carbon nanotube/polymer composites," 2014.

[129] K. Parmar, M. Mahmoodi, C. Park, and S. S. Park, "Effect of cnt alignment on the strain sensing capability of carbon nanotube composites," *Smart Materials and Structures*, vol. 22, no. 7, p. 075006.

[130] A. de la Vega, I. Kinloch, R. Young, W. Bauhofer, and K. Schulte, "Simultaneous global and local strain sensing in swcnt-epoxy composites by raman and impedance spectroscopy," *Composites Science and Technology*, vol. 71, no. 2, pp. 160 – 166, 2011.

[131] J. M. Gonzalez-Dominguez, A. Ansón-Casaos, M. T. Martinez, A. Ferreira, F. Vaz, and S. Lanceros-Méndez, "Piezoresistive response of pluronicwrapped single-wall carbon nanotube epoxy composites," 2012.

[132] R. Rizvi, B. Cochrane, E. Biddiss, and H. Naguib, "Piezoresistance characterization of poly(dimethyl-siloxane) and poly(ethylene) carbon nanotube composites," *Smart Materials and Structures*, vol. 20, no. 9, p. 094003.

[133] W. Zhang, J. Suhr, and N. Koratkar, "Carbon nanotube/polycarbonate composites as multifunctional strain sensors," *Journal of Nanoscience and Nanotechnology*, vol. 6, no. 4, pp. 960–964, 2006-04-01.

[134] T. Zhai, D. Li, G. Fei, and H. Xia, "Piezoresistive and compression resistance relaxation behavior of water blown carbon nanotube/polyurethane composite foam," *Composites Part A: Applied Science and Manufacturing*, vol. 72, pp. 108 – 114, 2015.

[135] E. M. Remillard, Q. Zhang, S. Sosina, Z. Branson, T. Dasgupta, and C. D. Vecitis, "Electric-field alignment of aqueous multi-walled carbon nanotubes on microporous substrates," *Carbon*, vol. 100, pp. 578 – 589, 2016.

[136] H. Meeuw, C. Viets, W. Liebig, K. Schulte, and B. Fiedler, "Morphological influence of carbon nanofillers on the piezoresistive response of carbon nanoparticle/epoxy composites under mechanical load," *European Polymer Journal*, vol. 85, pp. 198 – 210, 2016.

[137] D. R. Drodge, D. M. Williamson, S. J. P. Palmer, W. G. Proud, and R. K. Govier, "The mechanical response of a PBX and binder: combining results across the strain-rate and frequency domains," *Journal of Physics D: Applied Physics*, vol. 43, no. 33, p. 335403, 2010.

[138] C. Siviour, P. Laity, W. Proud, J. Field, D. Porter, P. Church, P. Gould, and W. Huntingdon-Thresher, "High strain rate properties of a polymer-bonded sugar: their dependence on applied and internal constraints," *Proceedings of the Royal Society of London A: Mathematical, Physical and Engineering Sciences*, vol. 464, pp. 1229–1255, 2008.

[139] J. T. Hagan and M. M. Chaudhri, "Fracture surface energies of high explosives PETN and RDX," *Journal of Materials Science*, vol. 12, pp. 1055–1058, May 1977.

[140] J. M. Zaug, "Elastic constants of β–HMX and tantalum, equations of state of supercritical fluids and fluid mixtures and thermal transport determinations," *Proc., 11th International Detonation Symposium, Snowmass, Colorado*, pp. 498–509, 1998.

[141] S. J. P. Palmer, J. E. Field, and J. M. Huntley, "Deformation, strengths and strains to failure of polymer bonded explosives," *Proceedings of the Royal Society of London A: Mathematical, Physical and Engineering Sciences*, vol. 440, pp. 399–419, 1993.

[142] F. P. Bowden and A. D. Yoffe, "Initiation and growth of explosion in liquids and solids ," (republ.1985). Cambridge, UK: Cambridge University Press (1952).

[143] P. J. Rae, S. J. P. Palmer, H. T. Goldrein, J. E. Field, and A. L. Lewis, "Quasi–static studies of the deformation and failure of PBX 9501," *Proceedings of the Royal Society of London A: Mathematical, Physical and Engineering Sciences*, vol. 458, pp. 2227–2242, 2002.

[144] P. J. Rae, H. T. Goldrein, S. J. P. Palmer, J. E. Field, and A. L. Lewis, "Quasi–static studies of the deformation and failure of β–HMX based polymer bonded explosives," *Proceedings of the Royal Society of London A: Mathematical, Physical and Engineering Sciences*, vol. 458, pp. 743–762, 2002.

[145] P. Chen, H. Xie, F. Huang, T. Huang, and Y. Ding, "Deformation and failure of polymer bonded explosives under diametric compression test," *Polymer Testing*, vol. 25, pp. 333 – 341, 2006.

[146] C. B. Skidmore, D. S. Phillips, S. F. Son, and B. W. Asay, "Characterization of hmx particles in pbx 9501," *AIP Conference Proceedings*, vol. 429, no. 1, 1998.

[147] D. R. Drodge and D. M. Williamson, "Understanding damage in polymer-bonded explosive composites," *Journal of Materials Science*, vol. 51, no. 2, pp. 668–679, 2016.

[148] J. E. Balzer, C. R. Siviour, S. M. Walley, W. G. Proud, and J. E. Field, "Behaviour of ammonium perchlorate–based propellants and a polymer–bonded explosive under impact loading," *Proceedings of the Royal Society of London A: Mathematical, Physical and Engineering Sciences*, vol. 460, no. 2043, pp. 781–806, 2004.

[149] H. D., "The history of solid–propellant rocketry: What we do and do not know," *35th AIAA, ASME, SAE, ASEE Joint Propulsion Conference and Exhibit*, vol. AIAA Paper 99-2925, no. 6, pp. H–2330, 1999.

[150] G. S. PEARSON and D. SUTTON, "Composite solid propellant ignition - ignition of ammonia and other fuels by perchloric acid vapor." *AIAA Journal*, vol. 5, no. 2, pp. 344–346, Feb 1967. [Online]. Available: https://doi.org/10.2514/3.3968

[151] E. W. PRICE, J. C. HANDLEY, R. PANYAM, R. K. SIGMAN, and A. GHOSH, "Combustion of ammonium perchlorate-polymer sandwiches," *AIAA Journal*, vol. 19, no. 3, pp. 380–386, Mar 1981. [Online]. Available: https://arc.aiaa.org/doi/abs/10.2514/3.7775

[152] M. W. BECKSTEAD, T. L. BOGGS, and R. L. DERR, "Surface structure of ammonium perchlorate composite propellants," *AIAA Journal*, vol. 8, no. 2, pp. 370–372, Feb 1970. [Online]. Available: https://doi.org/10.2514/3.5675

[153] A. D. BAER, J. A. KELLER, and N. W. RYAN, "Ignition of ammonium perchlorate composite propellants by convectiveheating." *AIAA Journal*, vol. 4, no. 8, pp. 1358–1365, Aug 1966. [Online]. Available: https://doi.org/10.2514/3.3678

[154] F. A. HOROWITZ, R. S. MAGEE, I. R. F. MCALEVY, and J. A. WRUBEL, "Flame spreading over the surface of igniting solid rocket propellants and propellant ingredients." *AIAA Journal*, vol. 5, no. 2, pp. 265–271, Feb 1967. [Online]. Available: https://doi.org/10.2514/3.3951

[155] Z. Hu, H. Luo, S. G. Bardenhagen, C. R. Siviour, R. W. Armstrong, and H. Lu, "Internal deformation measurement of polymer bonded sugar in compression by digital volume correlation of in-situ tomography," *Experimental Mechanics*, vol. 55, no. 1, pp. 289–300, 2015.

[156] K. Tan, N. Watanabe, and Y. Iwahori, "X-ray radiography and micro-computed tomography examination of damage characteristics in stitched composites subjected to impact loading," *Composites Part B: Engineering*, vol. 42, no. 4, pp. 874 – 884, 2011.

[157] P. J. Schilling, B. R. Karedla, A. K. Tatiparthi, M. A. Verges, and P. D. Herrington, "X-ray computed microtomography of internal damage in fiber reinforced polymer matrix composites," *Composites Science and Technology*, vol. 65, no. 14, pp. 2071 – 2078, 2005. [Online]. Available: http://www.sciencedirect.com/science/article/pii/S0266353805001879

[158] P. J. de Groot, P. A. Wijnen, and R. B. Janssen, "Real-time frequency determination of acoustic emission for different fracture mechanisms in carbon/epoxy composites," *Composites Science and Technology*, vol. 55, no. 4, pp. 405 – 412, 1995.

[159] C. Meola and G. M. Carlomagno, "Recent advances in the use of infrared thermography," *Measurement Science and Technology*, vol. 15, no. 9, p. R27, 2004. [Online]. Available: http://stacks.iop.org/0957-0233/15/i=9/a=R01

[160] J. L. Rose, *Ultrasonic Guided Waves in Solid Media*. Cambridge University Press, 2014.

[161] V. Giurgiutiu and G. Santoni-Bottai, "Structural health monitoring of composite structures with piezoelectric-wafer active sensors," *AIAA Journal*, vol. 49, no. 3, pp. 565–581, Mar 2011. [Online]. Available: https://doi.org/10.2514/1.J050641

[162] A. Jorio, A. G. Souza Filho, G. Dresselhaus, M. S. Dresselhaus, A. K. Swan, M. S. Ünlü, B. B. Goldberg, M. A. Pimenta, J. H. Hafner, C. M. Lieber, and R. Saito, "g-band resonant raman study of 62 isolated single-wall carbon nanotubes," *Phys. Rev. B*, vol. 65, p. 155412, Mar 2002.

[163] H. Gommans, J. Alldredge, H. Tashiro, J. Park, J. Magnuson, and A. Rinzler, "Fibers of aligned single-walled carbon nanotubes: Polarized Raman spectroscopy," *JOURNAL OF APPLIED PHYSICS*, vol. 88, no. 5, pp. 2509–2514, SEP 1 2000.

[164] M. Kalbac, L. Kavan, and L. Dunsch, "Effect of Bundling on the Tangential Displacement Mode in the Raman Spectra of Semiconducting Single-Walled Carbon Nanotubes during Electrochemical Charging," *JOURNAL OF PHYSICAL CHEMISTRY C*, vol. 113, no. 4, pp. 1340–1345, JAN 29 2009.

[165] C. Su, L. Xu, R.-j. Yan, M.-q. Chen, and C. Zhan, "Electric field induced conductive network formation of MWNTs and MWNTs-COOH in polycarbonate composites," *MATERIALS CHEMISTRY AND PHYSICS*, vol. 133, no. 2-3, pp. 1034–1039, APR 16 2012.

[166] C. Park and R. Robertson, "Crystallization of poly(ethylene oxide) in a photopolymerizable monomer under an electric field," *POLYMER*, vol. 42, no. 6, pp. 2597–2609, MAR 2001.

[167] L. A. Montoro and J. M. Rosolen, "A multi-step treatment to effective purification of single-walled carbon nanotubes," *CARBON*, vol. 44, no. 15, pp. 3293–3301, DEC 2006.

[168] D. Chattopadhyay, I. Galeska, and F. Papadimitrakopoulos, "Complete elimination of metal catalysts from single wall carbon nanotubes," *CARBON*, vol. 40, no. 7, pp. 985–988, 2002.

[169] P. Hou, C. Liu, Y. Tong, S. Xu, M. Liu, and H. Cheng, "Purification of single-walled carbon nanotubes synthesized by the hydrogen arc-discharge method," *JOURNAL OF MATERIALS RESEARCH*, vol. 16, no. 9, pp. 2526–2529, SEP 2001.

[170] T.-J. Park, S. Banerjee, T. Hemraj-Benny, and S. S. Wong, "Purification strategies and purity visualization techniques for single-walled carbon nanotubes," *J. Mater. Chem.*, vol. 16, pp. 141–154, 2006.

[171] A. Pescaglini, U. Emanuele, A. O'Riordan, and D. Iacopino, "Dielectrophoretic Self-Assembly of Au Nanorods for Sensing Applications," in *SENSORS & THEIR APPLICATIONS XVI*, ser. Journal of Physics Conference Series, Kyriacou, PA and O'Riordan, A and McConnell, G, Ed., vol. 307, 2011, 16th Conference in the Biennial Sensors and their Applications, Univ Coll Cork, Tyndall Natl Inst, Cork, IRELAND, SEP 12-14, 2011.

[172] P. Smith, C. Nordquist, T. Jackson, T. Mayer, B. Martin, J. Mbindyo, and T. Mallouk, "Electric-field assisted assembly and alignment of metallic nanowires," *APPLIED PHYSICS LETTERS*, vol. 77, no. 9, pp. 1399–1401, AUG 28 2000.

[173] P. Zijlstra, M. van Stee, N. Verhart, Z. Gu, and M. Orrit, "Rotational diffusion and alignment of short gold nanorods in an external electric field," *PHYSICAL CHEMISTRY CHEMICAL PHYSICS*, vol. 14, no. 13, pp. 4584–4588, 2012.

[174] Z. Yu and L. Brus, "Rayleigh and Raman scattering from individual carbon nanotube bundles," *JOURNAL OF PHYSICAL CHEMISTRY B*, vol. 105, no. 6, pp. 1123–1134, FEB 15 2001.

[175] R. RENKA and A. CLINE, "A TRIANGLE-BASED C-1 INTERPOLATION METHOD," *ROCKY MOUNTAIN JOURNAL OF MATHEMATICS*, vol. 14, no. 1, pp. 223–237, 1984.

[176] M. Dresselhaus, G. Dresselhaus, A. Jorio, A. Souza, and R. Saito, "Raman spectroscopy on isolated single wall carbon nanotubes," *CARBON*, vol. 40, no. 12, pp. 2043–2061, 2002.

[177] J. Fischer, W. Zhou, J. Vavro, M. Llaguno, C. Guthy, R. Haggenmueller, M. Casavant, D. Walters, and R. Smalley, "Magnetically aligned single wall carbon nanotube films: Preferred orientation and anisotropic transport properties," *JOURNAL OF APPLIED PHYSICS*, vol. 93, no. 4, pp. 2157–2163, FEB 15 2003.

[178] H. H. Gommans, J. W. Alldredge, H. Tashiro, J. Park, J. Magnuson, and A. G. Rinzler, "Fibers of aligned single-walled carbon nanotubes: Polarized raman spectroscopy," *Journal of Applied Physics*, vol. 88, no. 5, 2000.

[179] J. Chang, G. Liang, A. Gu, S. Cai, and L. Yuan, "The production of carbon nanotube/epoxy composites with a very high dielectric constant and low dielectric loss by microwave curing," *Carbon*, vol. 50, no. 2, pp. 689 – 698, 2012. [Online]. Available: http://www.sciencedirect.com/science/article/pii/S0008622311007706

[180] A. Savadori, "Impact testing of plastics: Present knowledge," *Polymer Testing*, vol. 5, no. 3, pp. 209 – 241, 1985. [Online]. Available: http://www.sciencedirect.com/science/article/pii/014294188590039X

[181] T. Kobayashi, I. Yamamoto, and M. Niinomi, "On the accuracy of measurement of dynamic elastic-plastic fracture toughness parameters by the instrumented charpy test," *Engineering Fracture Mechanics*, vol. 26, no. 1, pp. 83 – 94, 1987. [Online]. Available: http://www.sciencedirect.com/science/article/pii/0013794487900828

[182] A. J. Kinloch, G. A. Kodokian, and M. B. Jamarani, "Impact properties of epoxy polymers," *Journal of Materials Science*, vol. 22, no. 11, pp. 4111–4120, Nov 1987. [Online]. Available: https://doi.org/10.1007/BF01133366

[183] W. Böhme and J. F. Kalthoff, "The behavior of notched bend specimens in impact testing," *International Journal of Fracture*, vol. 20, no. 4, pp. R139–R143, Dec 1982. [Online]. Available: https://doi.org/10.1007/BF01130620

[184] M. Manahan and R. Stonesifer, "Studies toward optimum instrumented striker designs," *European Structural Integrity Society*, vol. 30, pp. 221 – 228, 2002, from Charpy To Present Impact Testing. [Online]. Available: http://www.sciencedirect.com/science/article/pii/S1566136902800243

[185] S. N. Rocker, W. Pearrell, E. C. Sengezer, and G. D. Seidel, "Electro-thermal response of polymer-bonded explosives for structural health monitoring of energetic materials," in *Proceedings of the ASME 2017 Conference on Smart Materials, Adaptive Structures and Intelligent Systems SMASIS 2017, Snowbird, Utah, USA*, 2017, pp. SMASIS2017–3869.

Appendix A

Curvature Alignment of Multi-CNT-Filament via Dielectrophoresis

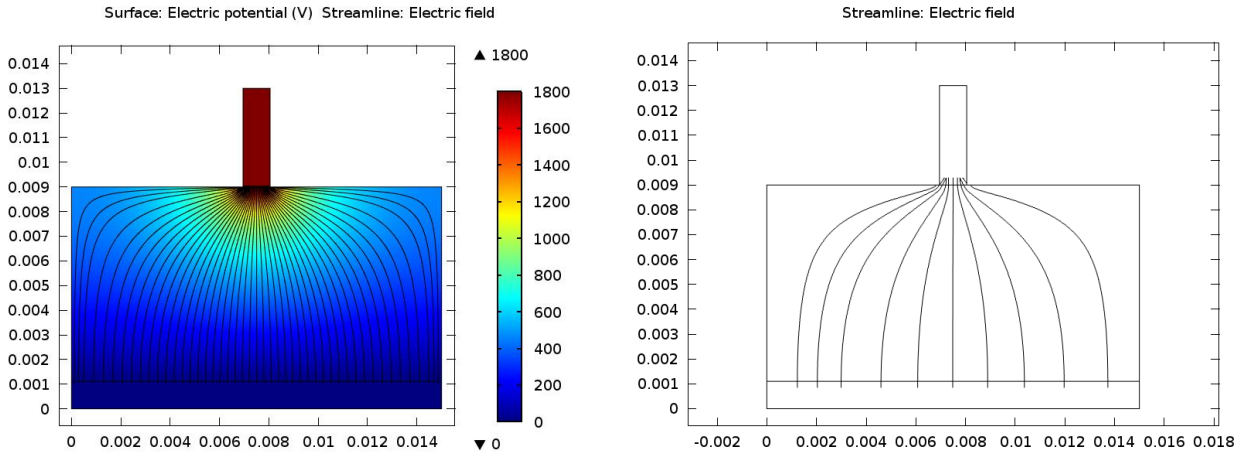

Figure A.1: COMSOL model to demonstrate the electric field within specimen.

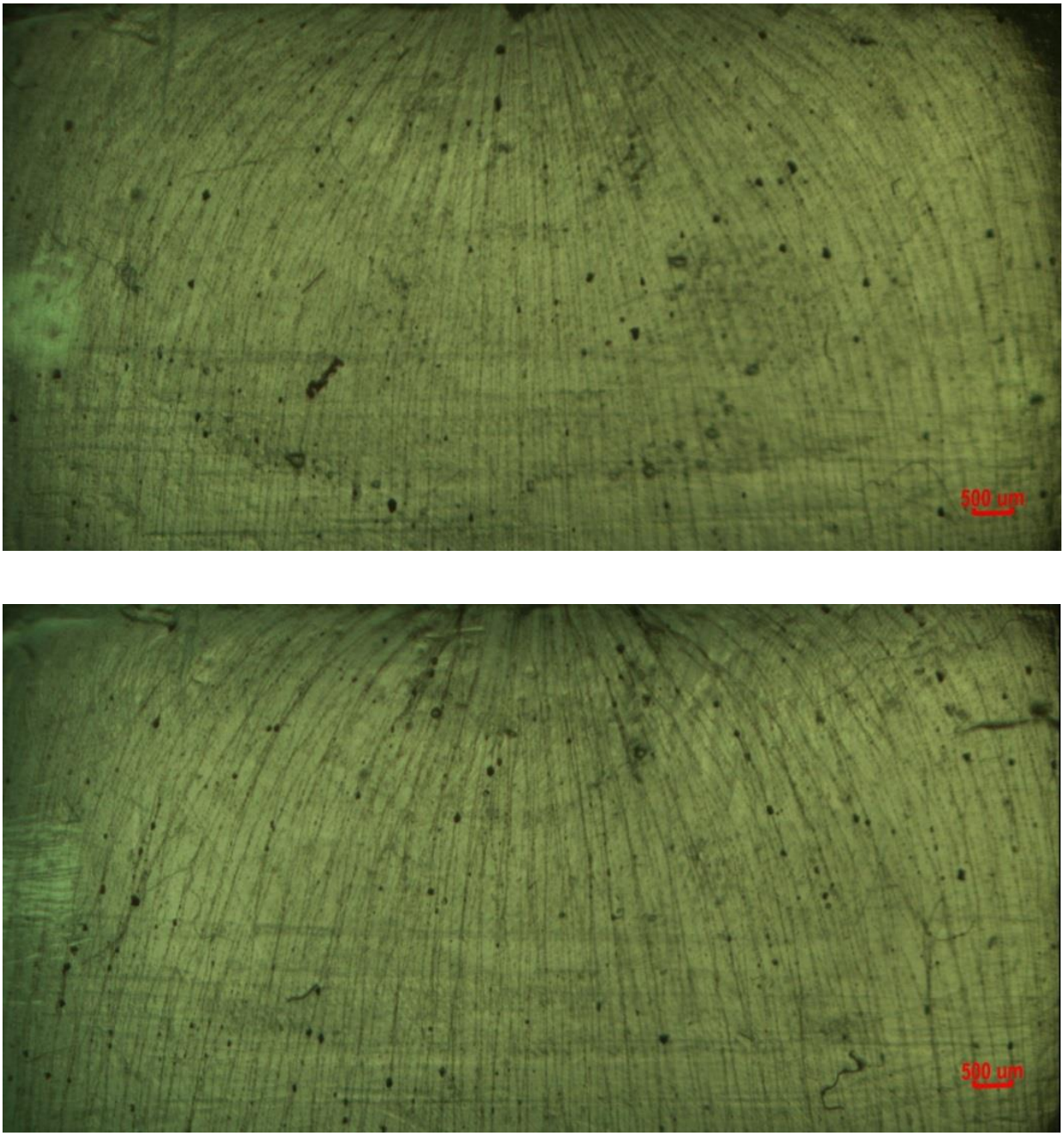

Figure A.2: Transmission optical microscope panoramic images of 0.03 wt% SWNT-COOH-acrylate polymer nanocomposite with curvature aligned CNT-filament formation under AC electric field of 150 $V_{RMS}\ mm^{-1}$ (with 3 kHz and 1 min) and 200 $V_{RMS}\ mm^{-1}$ (with 5 kHz and 1 min), respectively.

Appendix B

Initial Experimental Characterization of Deformation and Damage Sensing of Mock Energetic Materials

This work aims to explore the potential for in situ structural health monitoring in polymer bonded energetic materials through the introduction of carbon nanotubes (CNTs) into the binder phase as a means to establish a significant piezoresistive response through the resulting nanocomposite binder. The experimental effort herein is focused towards electro-mechanical characterization of mock materials in place of actual energetic (explosive) materials in order to provide proof of concept for the strain and damage sensing. The electrical conductivity and the piezoresistive behavior of samples containing randomly oriented, well dispersed MWNTs at concentrations of 0.09-0.6 wt% introduced into the epoxy binder of 70 wt% granulated sugar-epoxy hybrid composites are evaluated. Scanning Electron Microscopy (SEM) of as-produced MWNT-sugar-epoxy hybrid composites is used to obtain crystal and fracture morphology. The in situ real-time electrical resistance measurements under quasi-static tensile loading obtained experimentally demonstrates the strain and damage sensing potential in carbon nanotube infused mock hybrid energetics.

B.1 Experimental Investigation

B.1.1 Fabrication of MWNT-Sugar-Epoxy Hybrid Composites and Microstructural Morphology Assessment

In the present study, MWNTs and granulated sugar have been dispersed in 105 Epoxy Resin/206 Slow Hardener (West System) (being 5 parts 105 epoxy resin and 1 part 206 slow hardener). The epoxy system was selected as the binder for its general coating and bonding applications along with its low viscosity and very long working life at room temperature. The pristine MWNTs (PD15L1-5) (NanoLab) were reported to have a purity of more than 95%. The granulated pure cane sugar (Domino®) was used as a mock material in place of actual explosive materials. Neat sugar-epoxy samples were prepared with a weight ratio of 70/30 (corresponding to 64 vol% sugar) to obtain the neat sugar-epoxy mixture, with this ratio likewise being maintained in the preparation of hybrid binder samples having concentrations of 0.09, 0.15, 0.3 and 0.6 wt% MWNTs relative to the entire sugar-epoxy-MWNT sample (corresponding to 0.3, 0.5, 1 and 2 wt% MWNTs relative to the epoxy, respectively). In preparing hybrid composite samples, varying weight concentrations of MWNTs were added first to the lower viscosity (compared to epoxy) fast evaporating acetone solvent with 2.5 ml acetone used for each 0.01 grams of MWNTs. MWNTs were dispersed in acetone using a bath sonication for one hour with a QsonicaSonicator 4000 operating at 20 kHz and amplitude of 25% in order to obtain a more uniform initial dispersion of MWNTs. 105 Epoxy resin was added to the predispersed MWNTs-acetone solutions and resonicated for an additional hour with the same settings to obtain a homogeneous MWNT distribution within the epoxy. Acetone was evaporated from the solutions using a Buchi Rotavapor RII rotary evaporator with heating bath at 35^oC. The aforementioned curing agent and 70 wt% (64 vol%) mock material (granulated pure cane sugar) was then added to evaporated solution and blended thoroughly using mechanical stirring with tongue depressors. The prepared mixtures were cast into silicon molds and cured at room temperature for 24 hours. Fig. B.1a shows the resulting specimens prepared for quasi-static tensile testing. The neat sugar-epoxy and MWNTs-sugar-epoxy hybrid composite specimens have a gauge length of 11 mm, rescaled from ASTM standard D638 for specimen type IV, with the loading exerted in longitudinal direction at a distance of 28.2 mm between the grips.

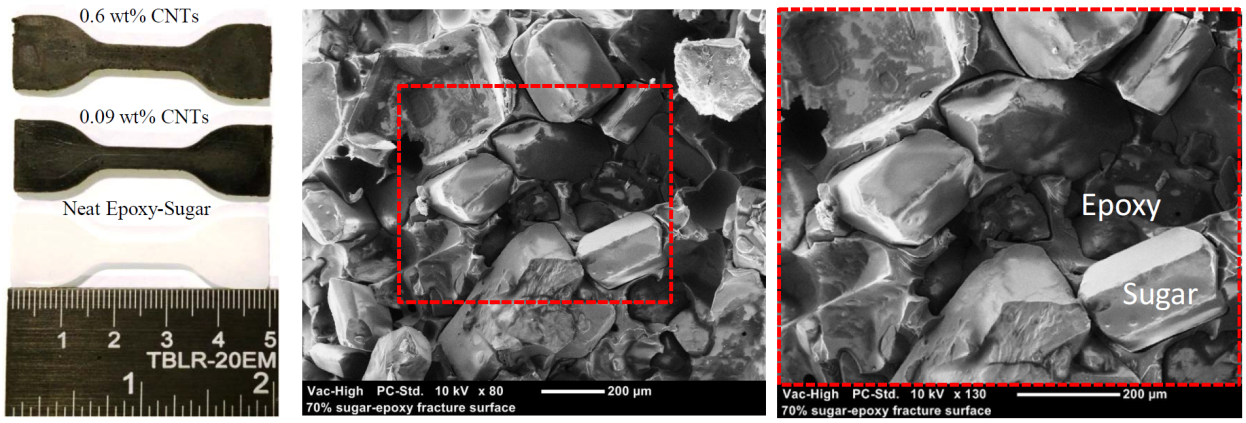

Figure B.1: a) As-produced, randomly oriented 0.6 wt%, 0.09 wt% MWNT-70 wt% sugar-epoxy, neat 70 wt% sugar-epoxy hybrid composites (wt% represents relative to the entire sugar-epoxy-MWNT sample), b) and c) SEM micrographs of neat-64 vol.% sugar-epoxy fracture surface.

Both the neat and hybrid composites have inherently multiscale material architectures with microstructural features ranging the nanoscale (nanotubes) and the mesoscale (nanotube network) in the hybrid material to the microscale (grains) and macroscale of both the neat and hybrid samples. In order to assess key morphological features of the as-produced neat epoxy-sugar and hybrid MWNT-epoxy-sugar composites such as MWNT and sugar crystal distribution, Scanning Electron Microscopy (SEM and FE-SEM) was used. Fig. B.1 provides the SEM micrographs of neat-64 vol.% sugar-epoxy fracture surface where the sugar crystal can be observed with associated length scales of $\sim 200\mu m$. Additionally, regions of crystal pull-outs are observed in contrast to the polymer coated crystal surfaces. The surfaces of these pull-outs appear to have epoxy polymer left behind during the fracture event indicating that the fracture appears to have occurred in the binder phase.

Fig. B.2 shows SEM micrographs taken using NeoScope JCM-5000 Benchtop SEM for 0.6 wt% MWNT (2 wt% relative to epoxy)-hybrid composite fracture surfaces. As with the neat sugar-epoxy samples, sugar crystals, pull-outs and the polymer binder are visible in Fig. B.2a and the zoomed versions Fig. B.2b and B.2c. It is not until the scale is reduced to the order of 5μm in Fig. B.2d that bundles/agglomerations of CNTs are observed in the form of white clouds/specs on the fracture surface in the local binder region. In order to confirm that the observed cloud-like

structures are indeed bundles/agglomerations MWNTs, FE-SEM micrographs were taken using a LEO/Zeiss 1550 high-performance Schottky field-emission SEM as shown in Fig. B.3. Fig. B.3a, B.3c and B.3e are micrographs taken of the fracture surface for the 0.09 wt% MWNT samples while Fig. B.3b, B.3d snd B.3f are taken from the fracture surface of a 0.6 MWNT wt% sample. It is observed that the FE-SEM provides the capability to go to 200nm length scale on the scale bars in Fig. B.3d andB.3e which is much finer resolution (higher magnification) than the SEM pictures

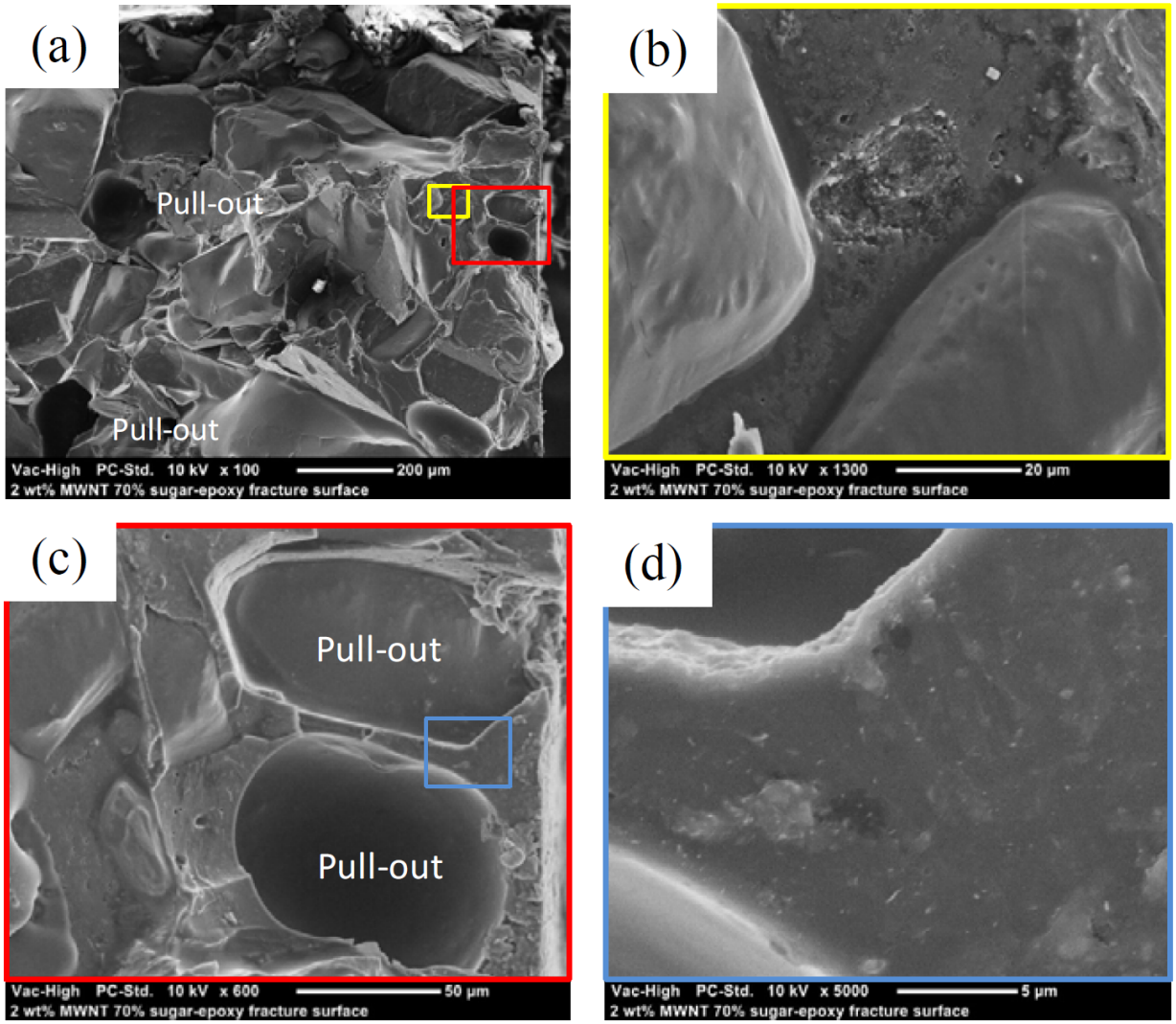

Figure B.2: SEM photographs of hybrid composite fracture surface for 0.6 wt% MWNT (2 wt% relative to epoxy) samples at different zoomed scales. Pull-out refers to the surfaces left behind by sugar crystals pulling out during the fracture event.

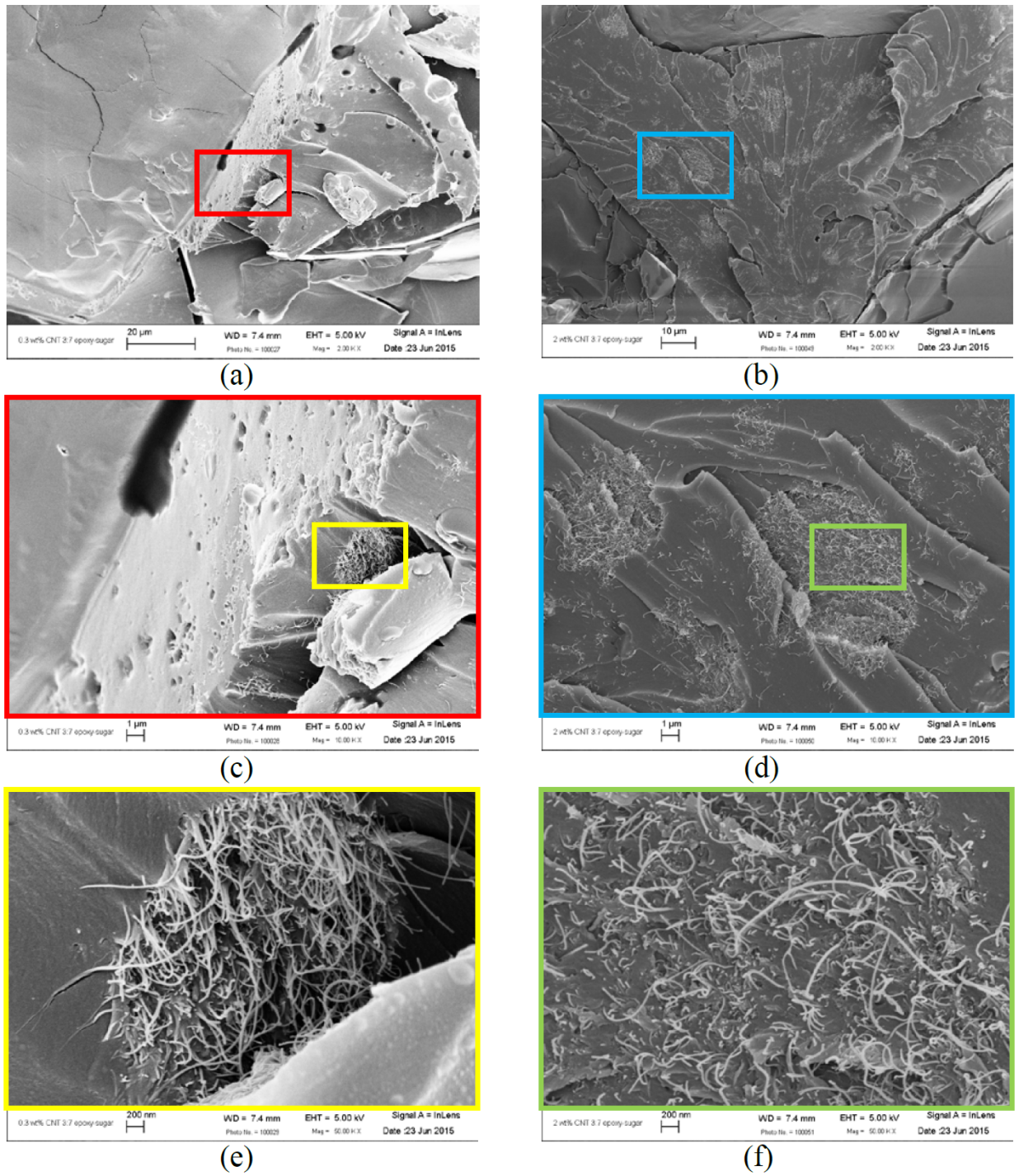

Figure B.3: FE-SEM micrographs of fracture surface for a),c),e) 0.09 wt% MWNT-sugar-epoxy samples, and b),d),f) 0.6 wt% MWNT-sugar-epoxy samples.

presented in Fig. B.2. The white cloud like structures observed in Fig. B.2 are also observed for both 0.09 and 0.6 wt% MWNT samples using the FE-SEM, as shown in Fig. B.3a and Fig. B.3b, respectively. On further zooming in to these clouds, a collection of individual MWNTs is observed where the MWNTs are sticking out of the fracture surface for each of the samples. It is to be noted that the the white clouds comprised of a collection of MWNTs are more difficult to isolate for the 0.09 wt% as compared to the 0.6 MWNT wt% sample because of smaller weight concentration of MWNTs for the 0.09 wt% samples. It is further observed that the MWNTs are bundled/agglomerated in collections (local nanotube networks) within the local polymer binder which will have a significance in the measured macroscale properties of these nanocomposites.

B.1.2 Electrical Characterization of MWNT-Sugar-Epoxy Hybrid Composites

The electrical properties of as-produced neat sugar-epoxy and MWNT-sugar-epoxy hybrid composite samples were measured using an Agilent Technologies E4980A Precision LCR Meter. A conductive epoxy was used to connect the electrodes as shown in Fig. B.4. The conductive epoxy electrodes were cemented on top and bottom of the gauge section at distance 4 mm apart on alternate sides of the sample to obtain volume conductivity measurements. Fig. B.4 shows the log-log scale plot of the frequency dependence (range: 20 Hz-2MHz) of absolute AC conductivity for as-produced hybrid composites. It is to be noted that the data presented in Fig. B.4 has error bars associated with each data point calculated by testing at least 8 different samples for each MWNT weight concentration. Neat sugar-epoxy composite conductivity is plotted to provide a baseline measurement from which to assess the effect of MWNT on the electrical conductivity. For the neat samples, both the epoxy and the sugar crystals have very low conductivity and thus the effective composite displays insulator-like behavior at measured input frequencies (i.e. low absolute conductivity and large frequency dependence).

For the neat sugar-epoxy samples, both the epoxy and the sugar crystals are believed to have very low conductivity and thus the effective composite displays strong insulator behavior, which is frequency dependence as a function of the input measurement frequency (20 Hz-2MHz). The value

increases from ∼2E-9 S/cm at low frequency (20 Hz) to 1E-5 S/cm at high frequency (1MHz). On addition of highly conductive (∼1E3 S/cm) [REF needed] MWNTs, the conductivity of the MWNT-sugar-epoxy composite is observed to increase from that of the baseline sugar-epoxy composite. As an example, at 20 Hz input measurement frequency, the conductivity of the neat, 0.09, 0.15, 0.3 wt% MWNT hybrid composites is observed to be about 2E-9 S/cm, 6E-8 S/cm, 1E-7 S/cm and 4.4E-7 S/cm , respectively. The increase in effective conductivity is attributed to formation of conductive pathways within the local polymer binder (i.e. nanotube networks) which make the binder more conductive as MWNT weight concentration is increased. Yet, large input measurement frequency dependence of the conductivity is still observed, therefore indicating that the as-produced MWNT hybrid composites are still below percolation threshold, remaining as an insulator. On the other hand, the effective conductivity for the 0.6 wt% MWNT hybrid composites at low measurement frequency (20 Hz) showed four orders of magnitude increase, which was observed to be 1E-5 S/cm, with respect to neat sugar-epoxy samples. It is also observed to be less frequency dependent as compared to the neat sugar-epoxy and the other MWNT weight concentration cases, which is an indication that the 0.6 wt% MWNT hybrid composites is in percolation transition region[†].

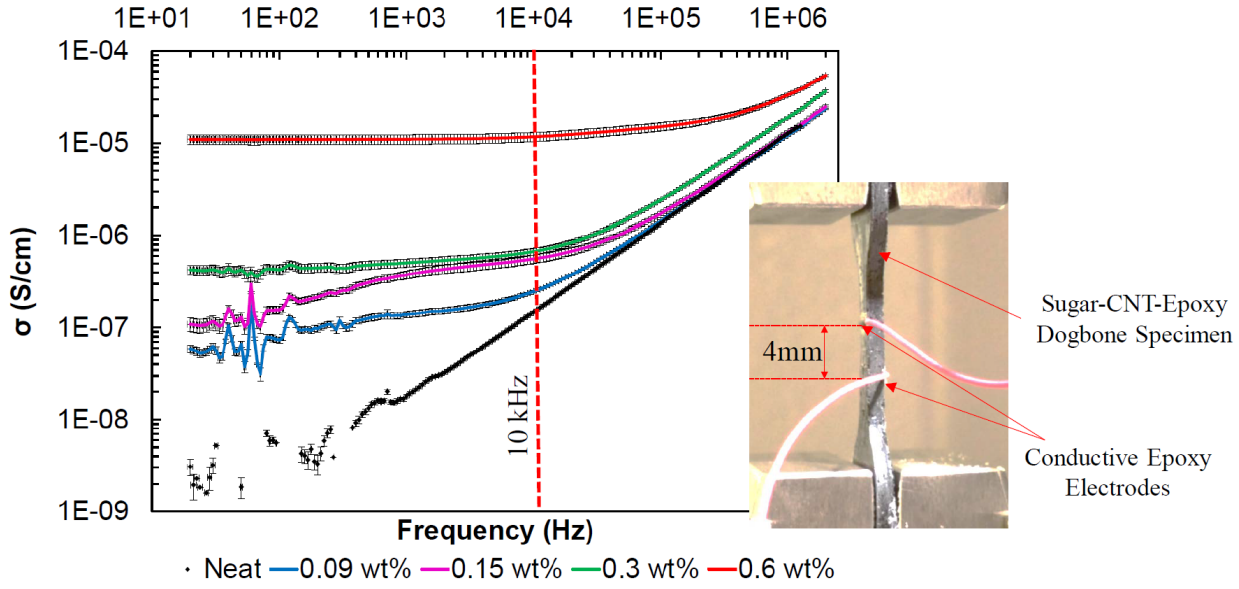

Figure B.4: Assessment of neat and hybrid composite electrical conductivity at various measurement frequencies associated and at different MWNT concentrations. Inset shows conductive epoxy electrodes cemented on top and bottom of the gauge section of the dog-bone specimen at distance 4 mm apart to obtain volume conductivity measurements.

On addition of highly conductive (∼1E3 S/cm) MWNTs, the conductivity of the MWNT-sugar-epoxy nanocomposite is observed to increase from that of the baseline sugar-epoxy composite at any given frequency. It is further observed that addition of larger weight concentration of MWNTs in the polymer binder leads to a higher value of effective conductivity for the samples at a given frequency. As an example, at 1kHz applied frequency, the conductivity of the neat, 0.09, 0.15, 0.3 and 0.6 wt% MWNT concentration samples is observed to be about 1.1E-8 S/cm, 1.05E-7 S/cm, 1.3E-7 S/cm, 1.4E-7 S/cm and 1E-5 S/cm, respectively. The increase in effective conductivity is attributed to formation of conductive pathways within the local polymer binder (i.e. nanotube networks) which make the binder more conductive as MWNT weight concentration is increased. The effective conductivity for the 0.6 wt% MWNT nanocomposites is observed to be less frequency dependent as compared to the neat samples and the smaller weight concentration cases. Additionally, the increase in the effective conductivity is much larger for the 0.6 wt% MWNT case relative to the neat epoxy samples signifying that 0.6 wt% MWNT samples are close to percolation[†].

B.1.3 Piezoresistive Testing of MWNT-Sugar-Epoxy Hybrid Composites

The piezoresistive behavior of MWNT-sugar-epoxy hybrid composites was obtained using a two terminal method (volume resistivity test) applying 1 V at 10 kHz, from an Agilent Technologies E4980A Precision LCR Meter while loading within an Instron testing system controlled by LabVIEW. Specimens were tested for each MWNT weight concentration (0.15, 0.3 and 0.6%) for piezoresistivity measurements. The quasi-static tensile loading was applied at a constant rate of 0.025 mm/min which corresponds to a strain rate of 0.00089 mm/mm/min. An average resistance reading was obtained to detect strain and damage initiation as well as its progression under quasi-static loading. The volume piezoresistivity measurements were recorded in terms of relative resis-

[†]It is to be noted that percolation concentration mentioned here is for the entire MWNT-sugar-epoxy nanocomposite which is different from the local MWNT-epoxy percolation. Local percolation of the nanocomposite binder is difficult to assess from the macroscale testing performed herein. However, the percolation threshold for MWNT-epoxy nanocomposites has been reported in the literature to be in between 0.002wt% to 5wt% depending on the type of MWNT, aspect ratio and dispersion process.

tance change ($\Delta R/R_0$) as the specimens underwent deformation, where R_0 was initial unstrained resistance. The piezoresistive sensitivity of randomly dispersed 0.15, 0.3 and 0.6 wt% MWNT-sugar-epoxy hybrid composites was quantified by defining the gauge factor as $G = (\Delta R/R_0)/\varepsilon$.

Fig. B.5a provides the baseline mechanical stress-strain response of neat sugar-epoxy samples. It is observed that the effective stress follows an initial linear elastic response up to about 0.1% applied strain, depicted by region I. The initial linear elastic stiffness of the neat sugar-epoxy composite is observed to be 2.08±0.55 GPa, where the initial stiffness values errors are calculated by averaging over the initial response of four different samples tested for statistical significance and consistency of the experiments. Thereafter, the effective stress-strain response starts to deviate from the initial linear elastic behavior and the effective stiffness of the composite reduces monotonically in region II. The reduction in effective composite stiffness in region II is attributed to local damage in the polymer binder (microcracks) in response to local deformations on application of tensile strains which reduces the load carrying capacity of the composite. A peak stress of about 5 GPa is observed at about 0.75% applied strain for the test presented here. Over four different samples, the peak stress was observed to be 4.60±0.29 MPa at an applied strain of 0.86±0.26%. Finally, after the peak stress is reached, a sharp decline in effective stress is observed because of macroscale damage (macrocracks) of the composite dog-bone specimen leading to complete failure at about 0.85% applied strain, as observed from region III in Fig. B.5a. The piezoresistive response for the neat epoxy samples could not be obtained because of low conductivity at 10 kHz applied frequency leading to problems with data acquisition. Similar to the neat sample addition of 0.09%wt MWNTs to the polymer binder does not increase the effective conductivity enough for piezoresistive measurements, hence, it is not reported herein.

The effective stress-strain response of nanocomposite samples with addition of 0.15%wt of MWNTs to the epoxy binder are shown in Fig. B.5b. The effective stress-strain response is observed to undergo an initial linear increase in effective stress (region I) on application of less than 0.1% strain. The initial stiffness averaged over four 0.15%wt MWNT samples is observed to be 1.76±0.33 GPa, which is about 18% smaller than the neat polymer samples in comparing the mean values. The stress-strain response undergoes a similar behavior as was observed for the neat polymer samples progressing through a non-linear region (region II) as the sample develops microcracks up to an

average peak stress of about 3.29±0.08 MPa at an average strain of 1.06± 0.10. While the average peak stress for the 0.15%wt MWNT samples is observed to be 40% smaller than that of the neat polymer samples, the strain to failure (region III) is observed to be 1.40% which is 64% larger than that observed for the neat epoxy shown in Fig. B.5a.

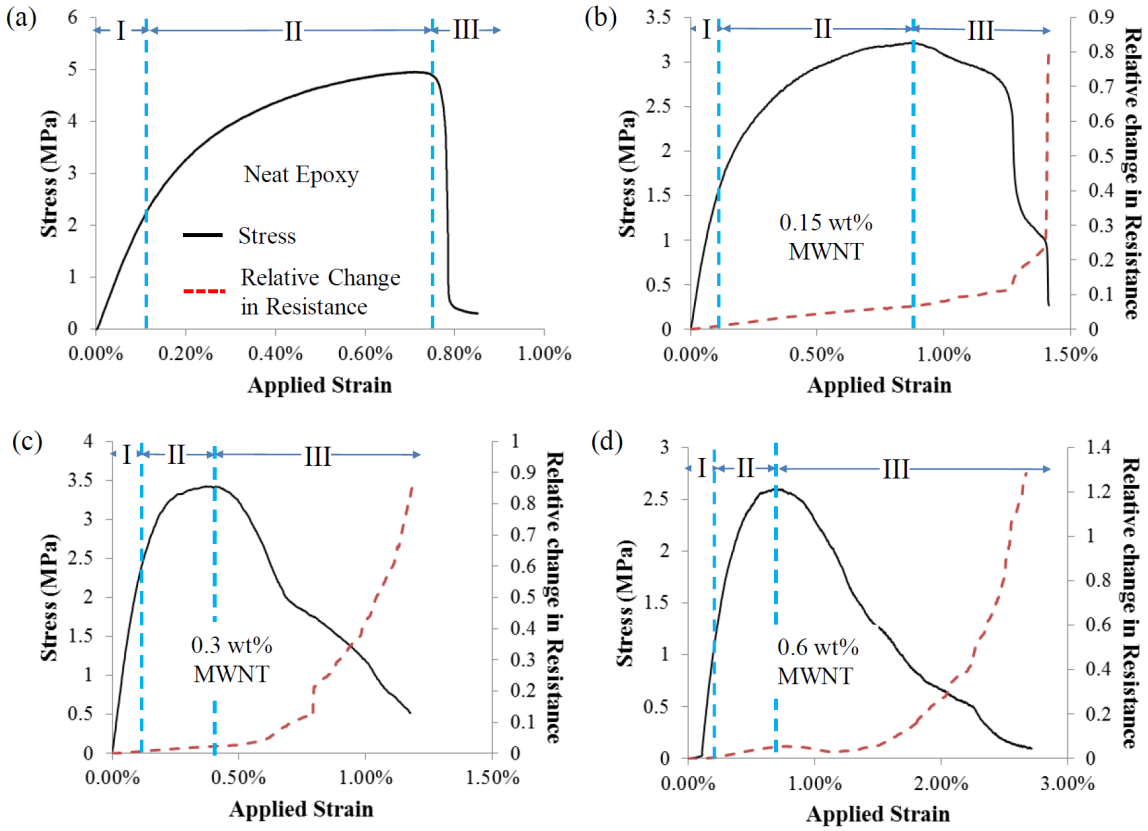

Figure B.5: Stress-strain and relative change in resistance-strain response of as-produced hybrid composites a) Neat sugar-epoxy, b) 0.15 wt% MWNT hybrid composite (0.5 wt% relative to epoxy) $R_0 = 16.53M\Omega$, c) 0.3 wt% MWNT hybrid composite (1 wt% relative to epoxy) $R_0 = 11.7M\Omega$ and d) 0.6 wt% MWNT hybrid composite (2 wt% relative to epoxy) $R_0 = 0.82M\Omega$.

In terms of the piezoresistive response of the 0.15%wt MWNT samples, the relative change in resistance follows a linear increase in initial linear elastic region I with a gauge factor (G^I) of 7.74 calculated at 0.1% applied strain. The observed relative change in resistance for region I can be attributed to the local deformations of the inherently piezoresistive MWNT-epoxy binder in absence of interfacial damage for low values of applied strains. It is to be noted that the

inherent MWNT-polymer polymer piezoresistivity is dependent of several factors including CNT network arrangement/morphology distribution and electron hopping/quantum tunneling. However, isolation of dominant piezoresistive mechanism in the local interfacial binder is difficult based on the macroscale tests conducted herein. On further application of strain, a linear increase in relative change in resistance is observed in region II with the corresponding gauge factor (G^{II}) of 7.49 calculated at the strain corresponding to peak stress (0.9%). The observed gauge factor for region II starts to include the effect of local microcracks developing within the polymer binder medium and at the binder-crystal interfaces. Finally, development of macrocracks in region III leads to a non-linear evolution of relative change in resistance which can be closely correlated to the corresponding changes in the stress-strain response. An effective gauge factor (G^{III}) of 16.19 is observed just before the failure strain (1.4%) indicating large scale damage of the dog-bone specimen.

For the 0.3%wt MWNT samples result stress-strain response regions similar to those observed for to 0.15%wt MWNT case, i.e. linear elastic region I, microcracks based stiffness reduction in region II and macrocracks leading to eventual failure in region III, as shown in Fig. B.5c. The averaged initial stiffness of the 0.3%wt MWNT samples is observed to be 2.50±0.26 GPa, with an averaged peak stress of 3.66±0.33 MPa at an average applied strain of 0.36±0.05 MPa. The change in resistance follows an initial linear increase through regions I and II with effective gauge factors (G^I and G^{II}) of 5.81 and 5.78, respectively, again similar to the 0.15%wt MWNT sample. Finally, in region III, macrocracks develop in the dog-bone sample resulting in loss of load carrying capacity leading to eventual failure at around 1.2% applied strain. The relative change in resistance, in region III, increases non linearly with close correlation to the reduction in effective stress leading to a gauge factor of 71.04 just before failure.

Finally, the 0.6%wt MWNT sample features similar behavior as was observed for the 0.15%wt and 0.3%wt MWNT in the stress-strain and relative change in resistance. One of the key differences in the relative change in resistance for the 0.6%wt MWNT sample is that it exhibits a non-monotonic behavior unlike the other 0.15%wt and 0.3%wt MWNT cases for which the relative change in resistance increases monotonically. For such composites with granular composite microstructure, it is difficult to constrain the developing microcracks to initiate in the gauge section for the dog-bone samples like the ones tested here. In some cases, microcracks can develop outside of the gauge

section which relax the local stresses in the gauge section. While this information is not represented in the effective stress which is calculated from the load cells (i.e. always outside the electrode gauge section), the effective resistance can reduce because of local relaxation of the specimen within the gauge section. Similar piezoresistive responses were observed for a handful of samples in which macrocracks were noted to occur outside of the electrodes, though alternative sources of such behavior can include complex rearrangements of the current carrying pathways as the interfaces separate. More direct correlations for such observations would require in situ monitoring of the microstructure which is beyond the scope of the initial work.

B.1.4 Key Findings

- The neat sugar-epoxy samples are non-conductive and addition of MWNTs increases the effective conductivity of the composite.
- The stress-strain response MWNT-sugar-epoxy hybrid composites undergoes a ductile failure behavior going through the initial linear elastic behavior, formation of microcracks leading to reduction in composite stiffness and finally macrocracks result in eventual failure.
- The relative change in resistance captures the effect of microcracks and macrocracks earlier than the stress strain response.
- It should be noted that neat sugar-epoxy composites and MWNT-sugar-epoxy hybrid composites, rescaled from ASTM D638 with gage length of 11 mm, resulted in very fragile specimens. Specimens were too fragile that it was inevitable not to induce any microscale damage while placing them into tensile grips.
- Due to lack of expertise, it should be also noted that the solvent evaporation during sample fabrication were not fully achieved for these specimens, which resulted in inconsistent specimen fabrication.
- With the knowledge obtained from this initial experimental work, a detailed study on AP inert energetics and sugar mock energetics was conducted with greater consistency as presented in Chapter 4.

Appendix C

Electro-mechanical-optical Characterization of Inert and Mock Hybrid Energetics

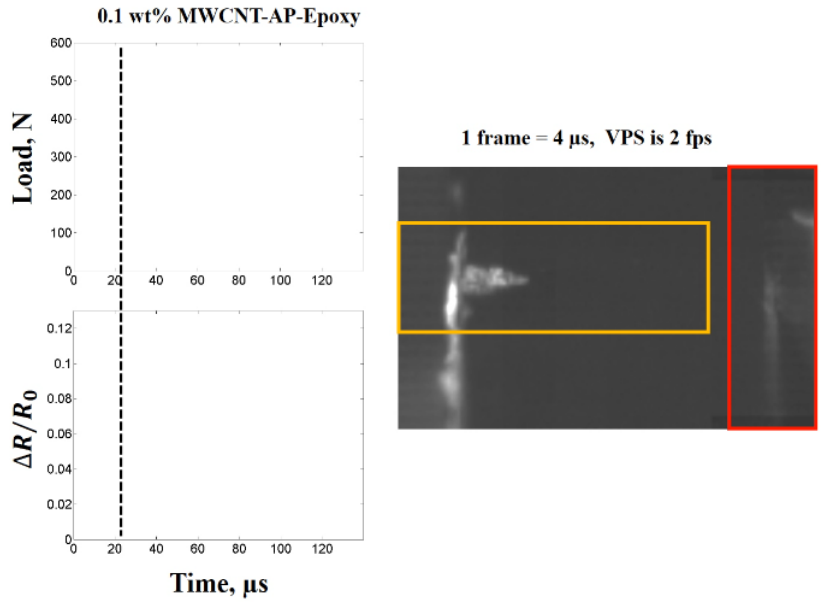

Figure C.1: Electro-mechanical-optical characterization of AP inert hybrid energetic specimen under low velocity impact loading at rest

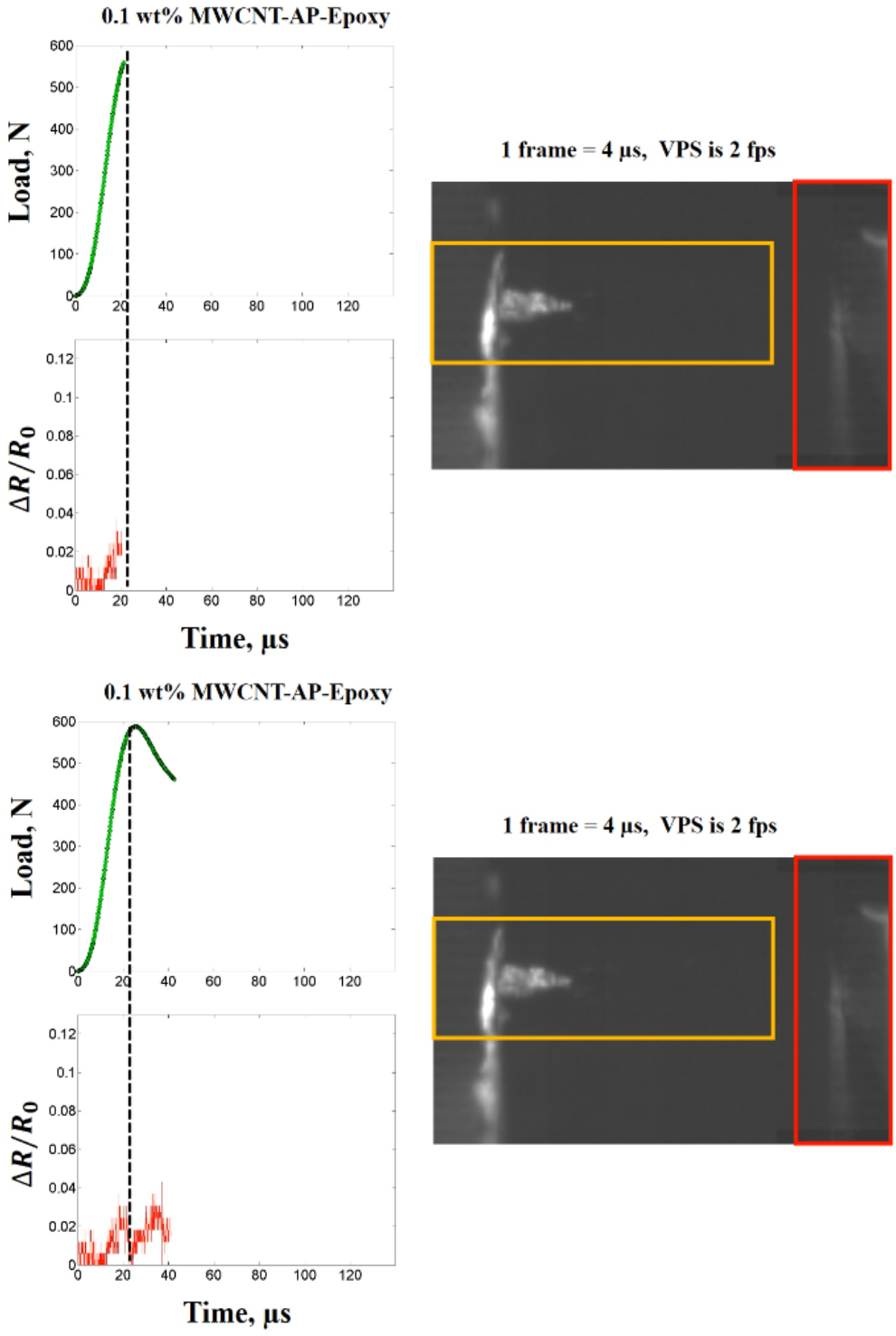

Figure C.2: Electro-mechanical-optical characterization of AP inert hybrid energetic specimen under low velocity impact loading at t=20 μs and t=40 μs

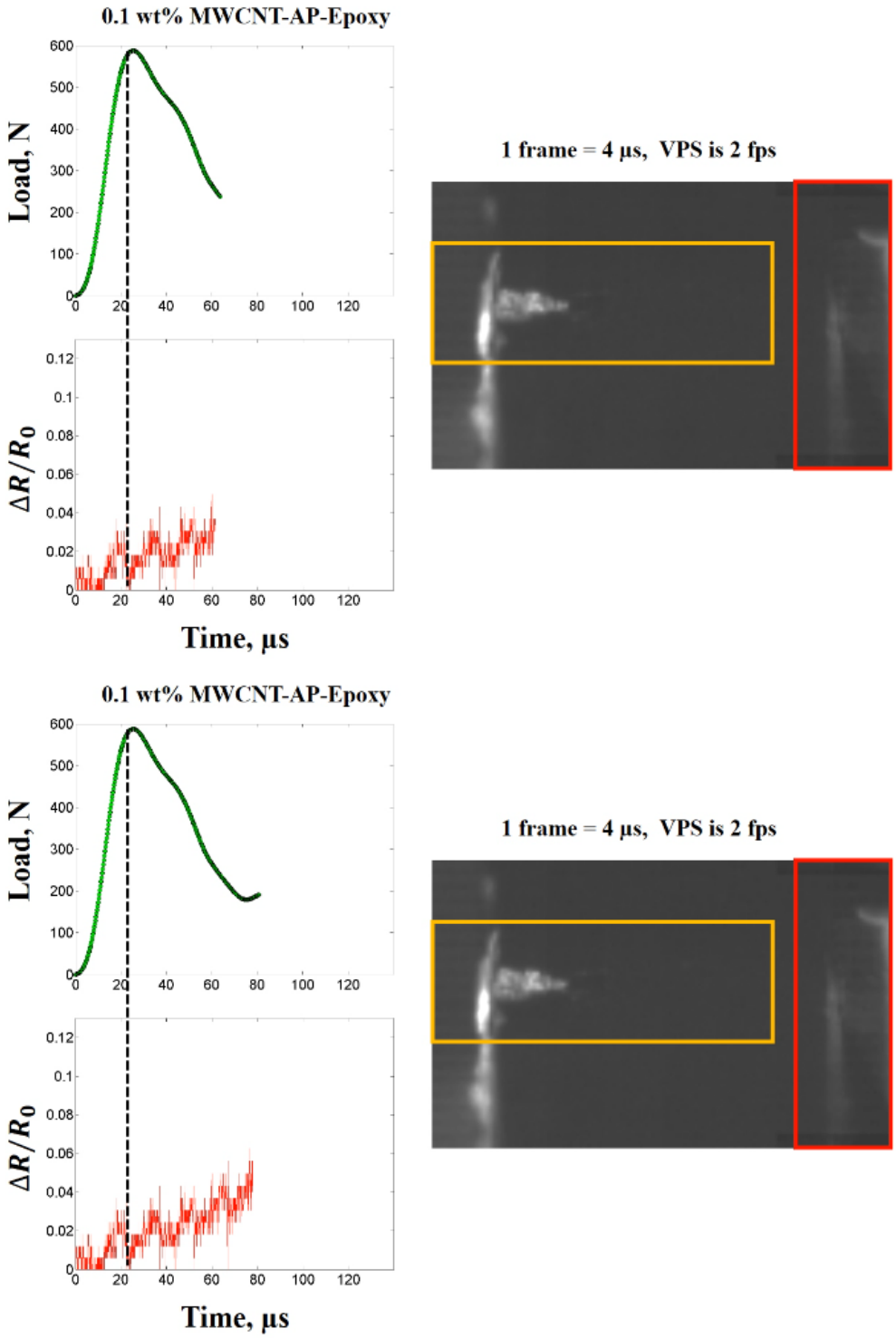

Figure C.3: Electro-mechanical-optical characterization of AP inert hybrid energetic specimen under low velocity impact loading at t=60 μs and t=80 μs

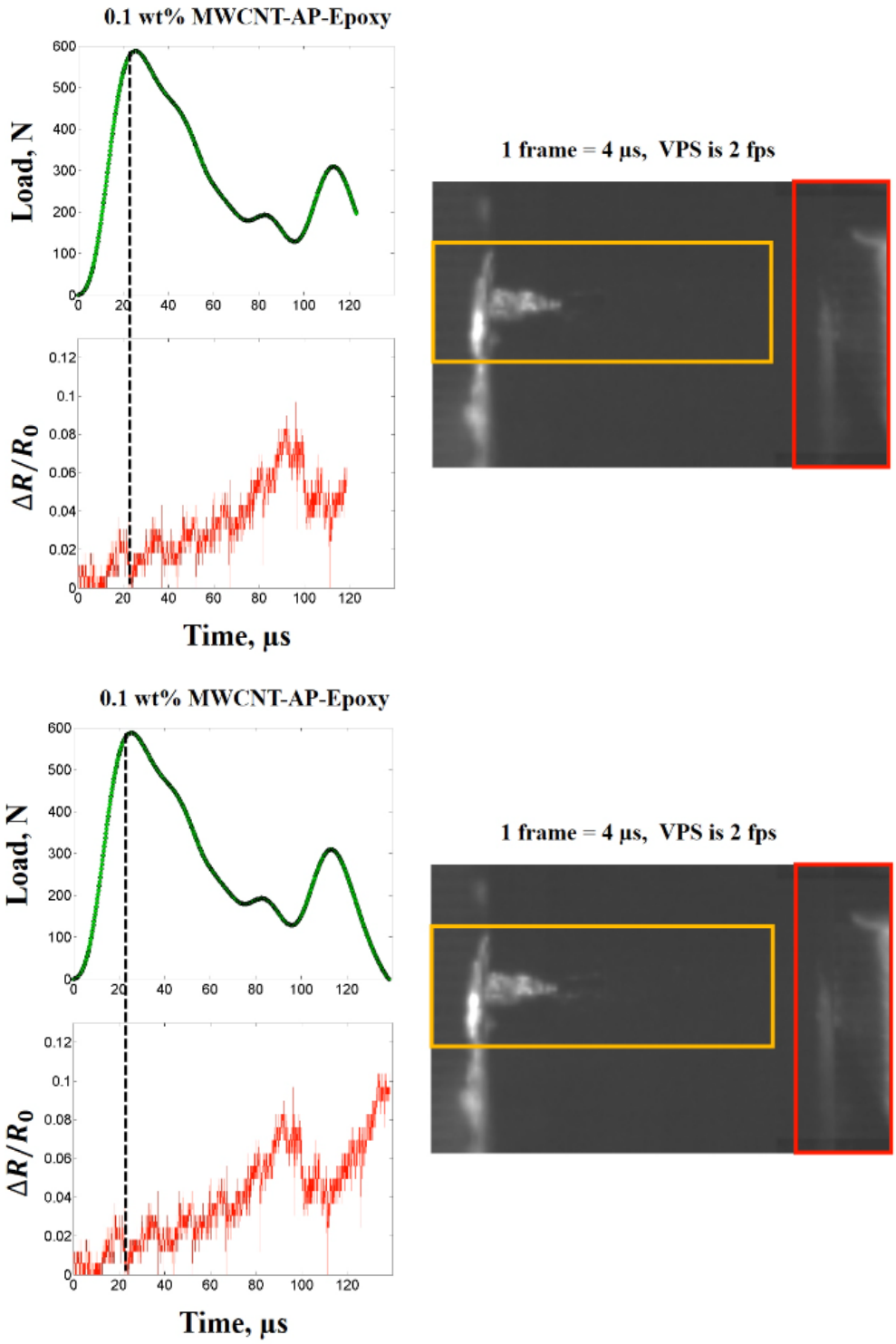

Figure C.4: Electro-mechanical-optical characterization of AP inert hybrid energetic specimen under low velocity impact loading at t=120 μs and t_{final}

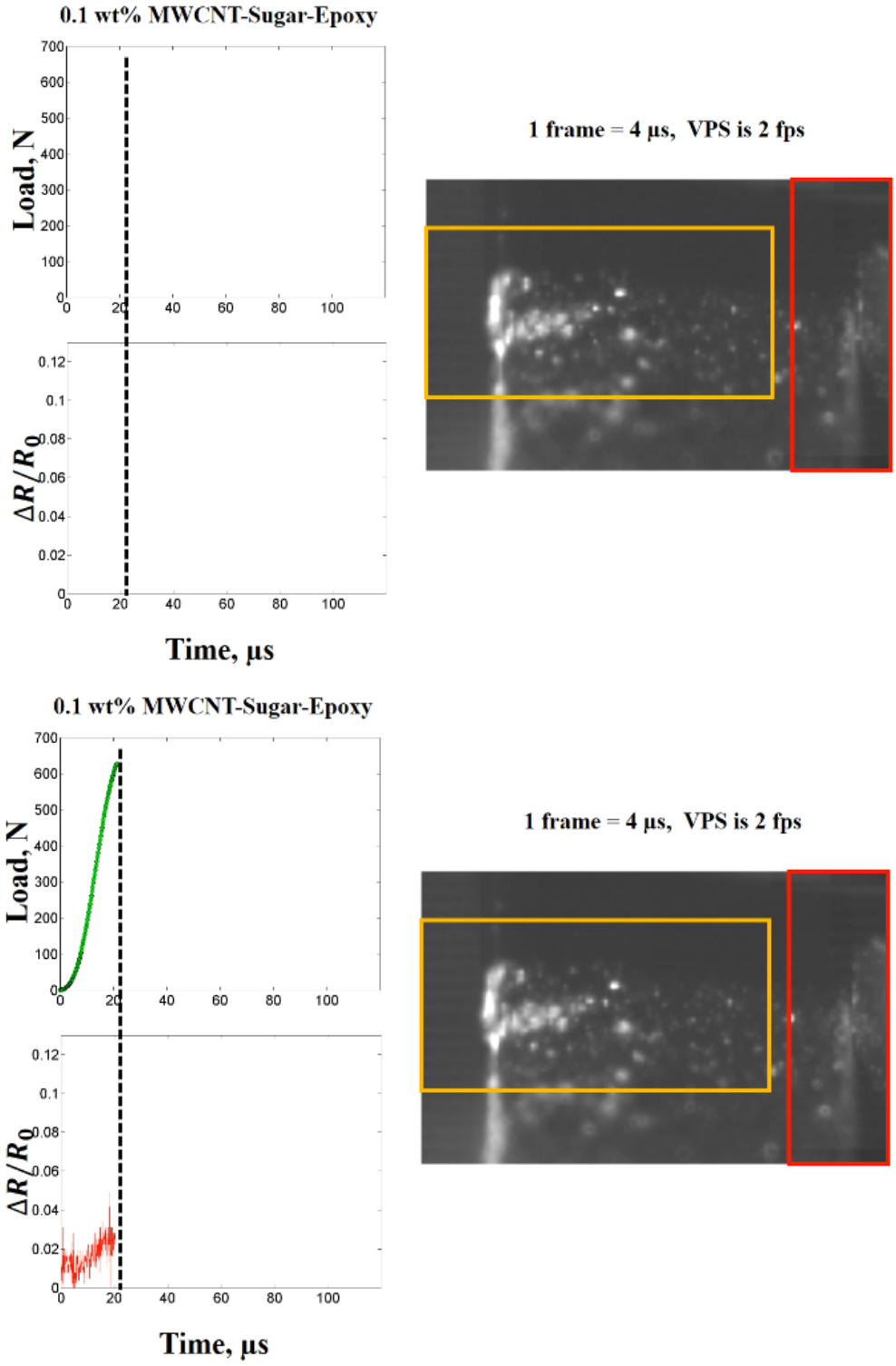

Figure C.5: Electro-mechanical-optical characterization of sugar mock hybrid energetic specimen under low velocity impact loading at rest and t=20 μs

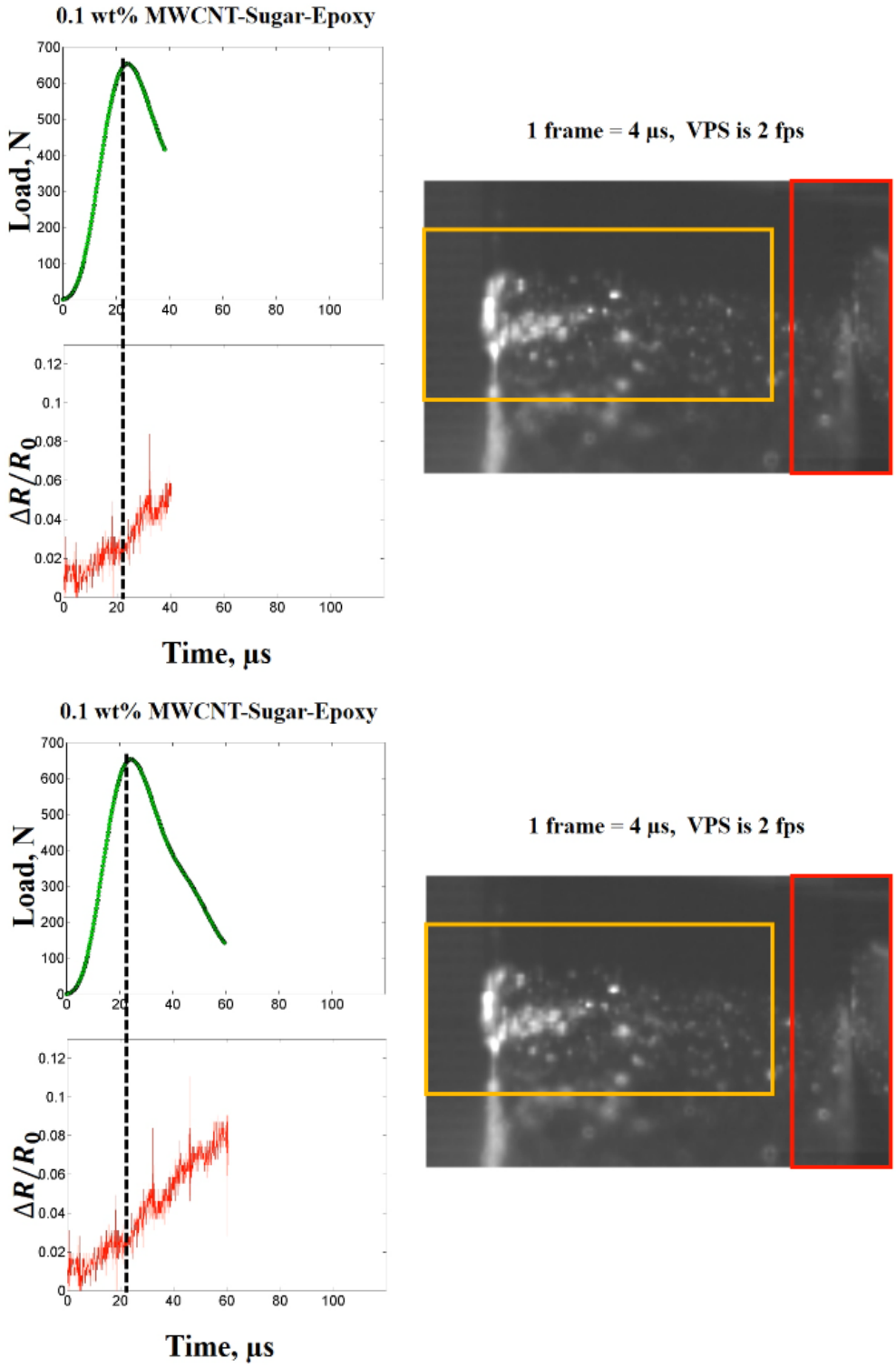

Figure C.6: Electro-mechanical-optical characterization of sugar mock hybrid energetic specimen under low velocity impact loading at t=40 μs and t=60 μs

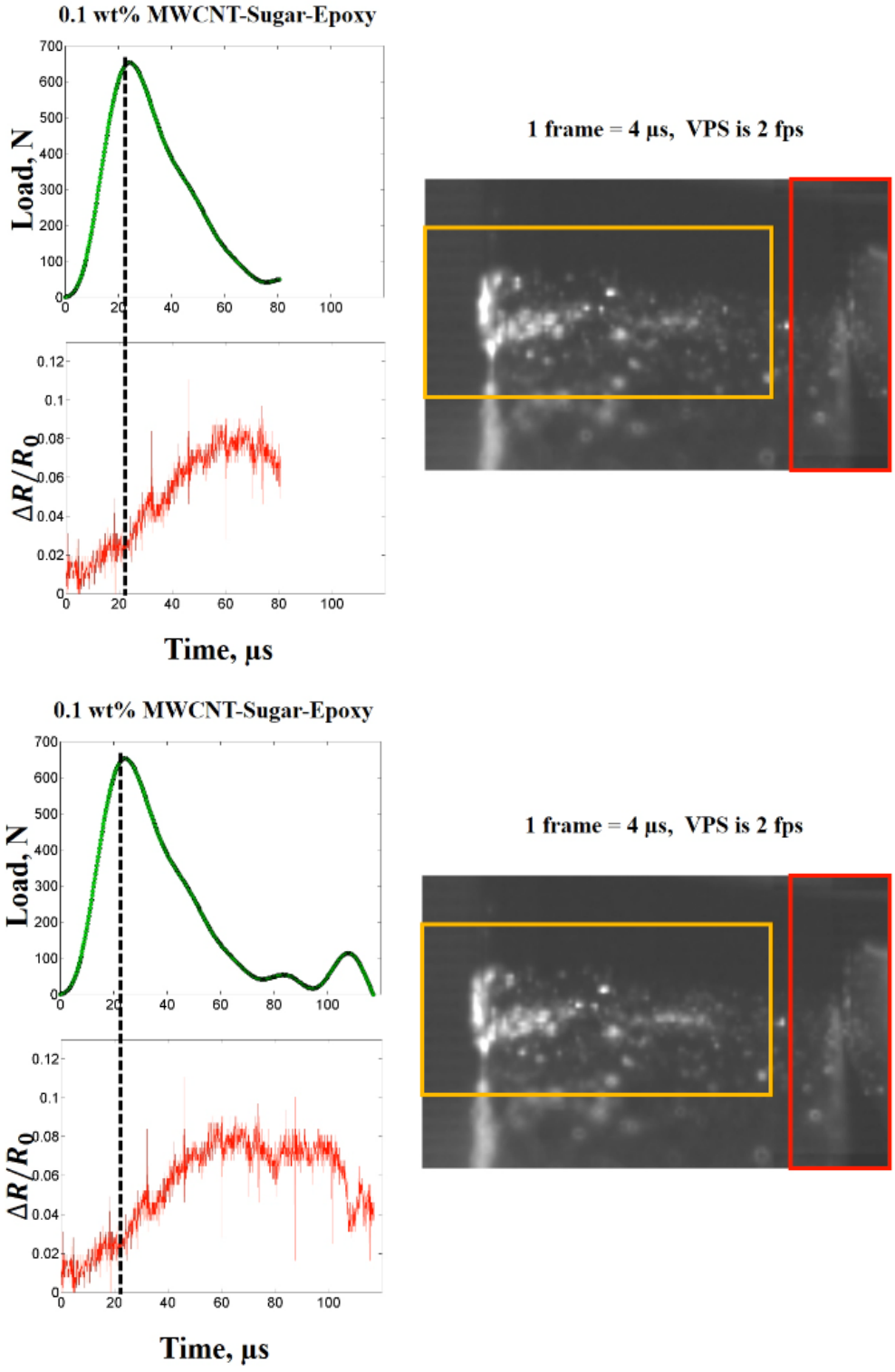

Figure C.7: Electro-mechanical-optical characterization of sugar mock hybrid energetic specimen under low velocity impact loading at t=80 μs and t_{final}

Appendix D

Initial Experimental Characterization of Thermoresistive Response of AP Inert Hybrid Energetics through Localized Heating

This experimental study [185] was conducted by Samantha N. Rocker and T. Wade Pearrell under supervision of Engin C. Sengezer and Gary D. Seidel.

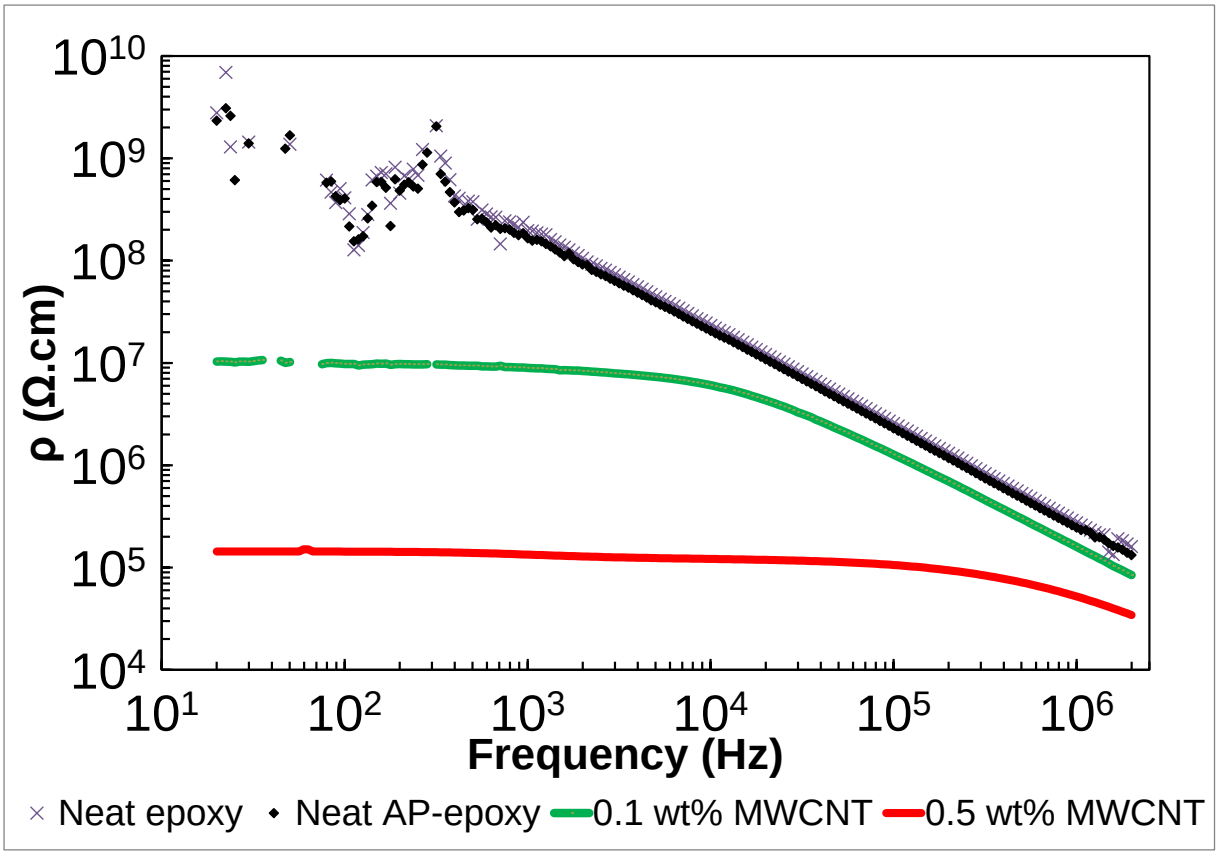

Figure D.1: Assessment of absolute complex AC electrical resistivity for neat epoxy, neat AP inert energetics and MWCNT AP inert hybrid energetics

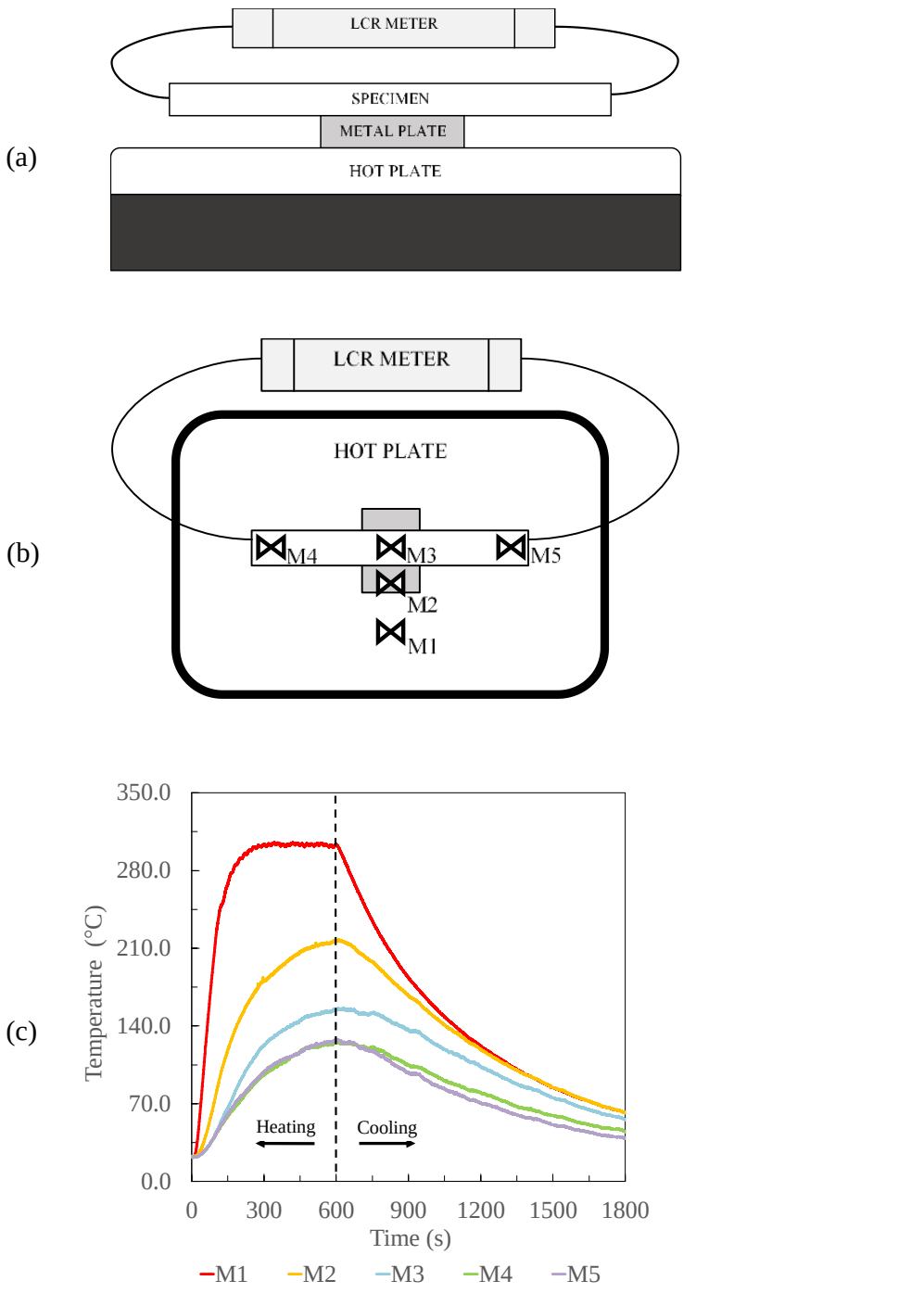

Figure D.2: Experimental setup. (a) Side view (b) Top view (c) Temperature profile of MWCNT AP inert hybrid energetic at measurement points in (b)

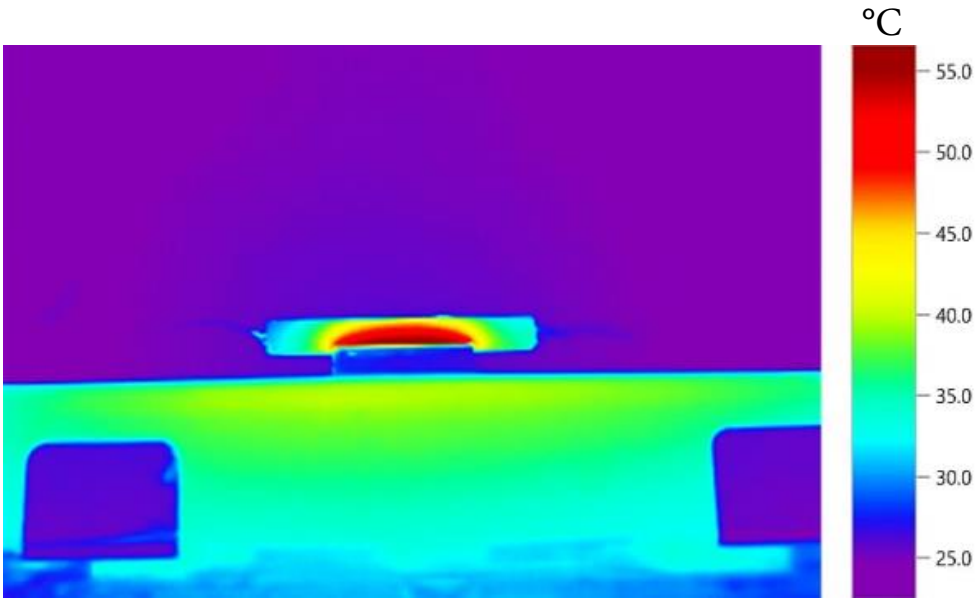

Figure D.3: Thermal Image: Side view of neat AP inert energetics during initial heating

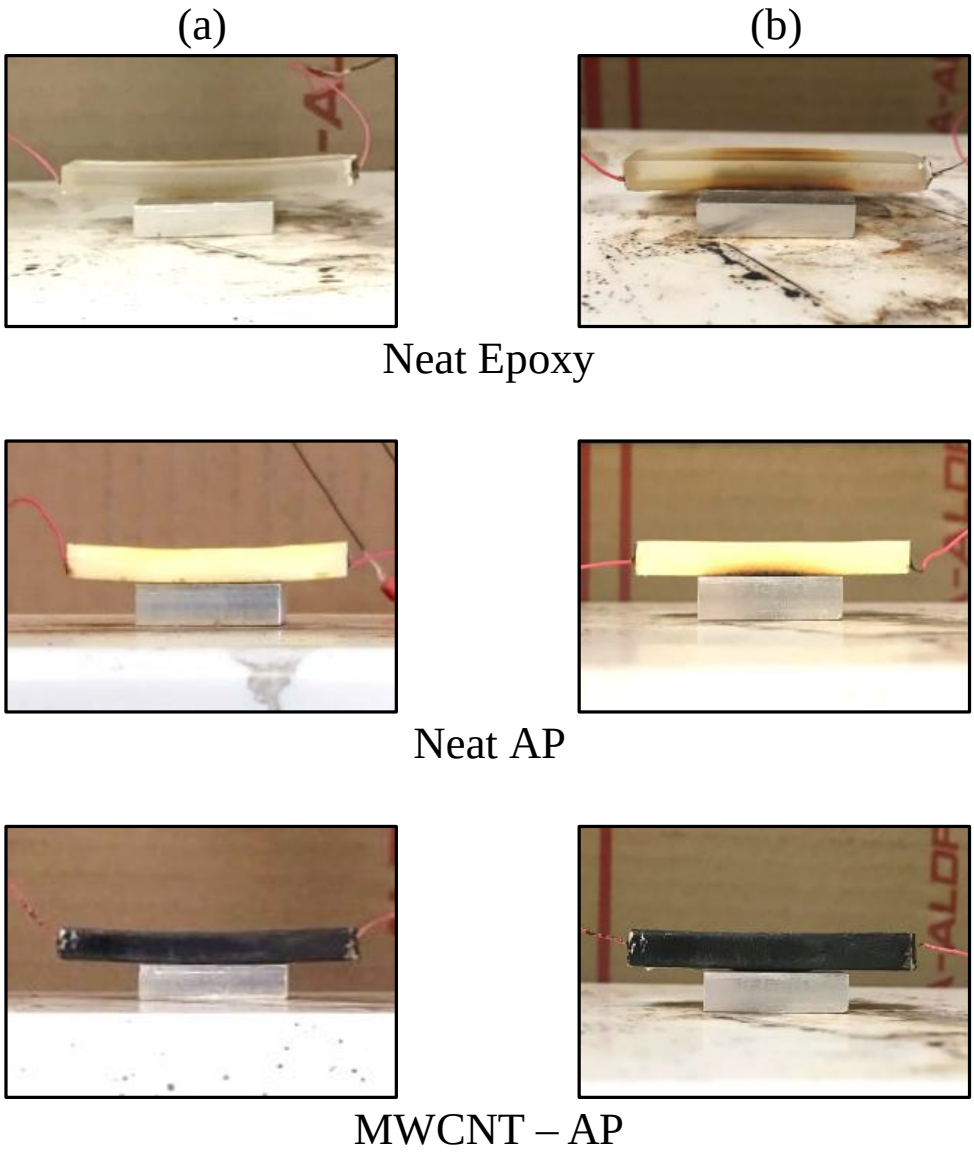

Figure D.4: Types of test specimen in thermal loading phases: (a) heating (thermal expansion) (b) cooling (recovery)

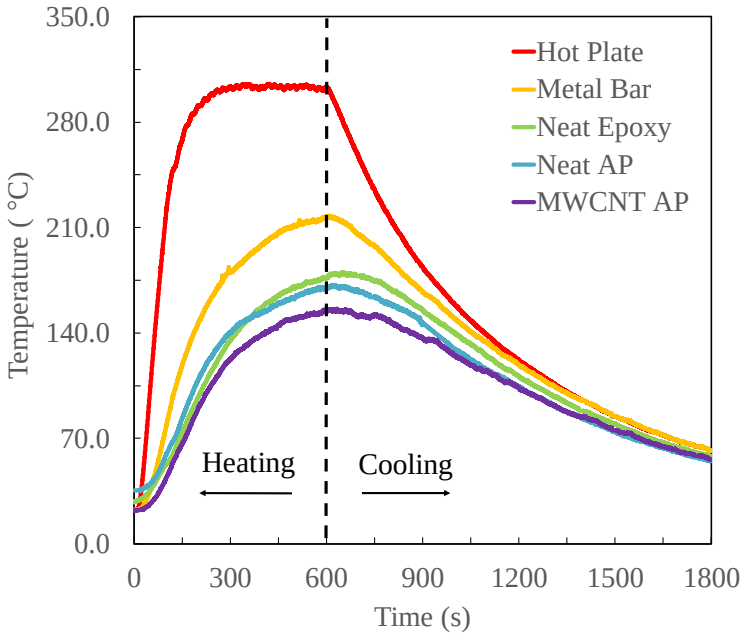

Figure D.5: Temperature profile for inert energetics tested with 10 kHz input frequency (neat epoxy, neat AP inert energetic, and MWCNT AP inert hybrid energetic)

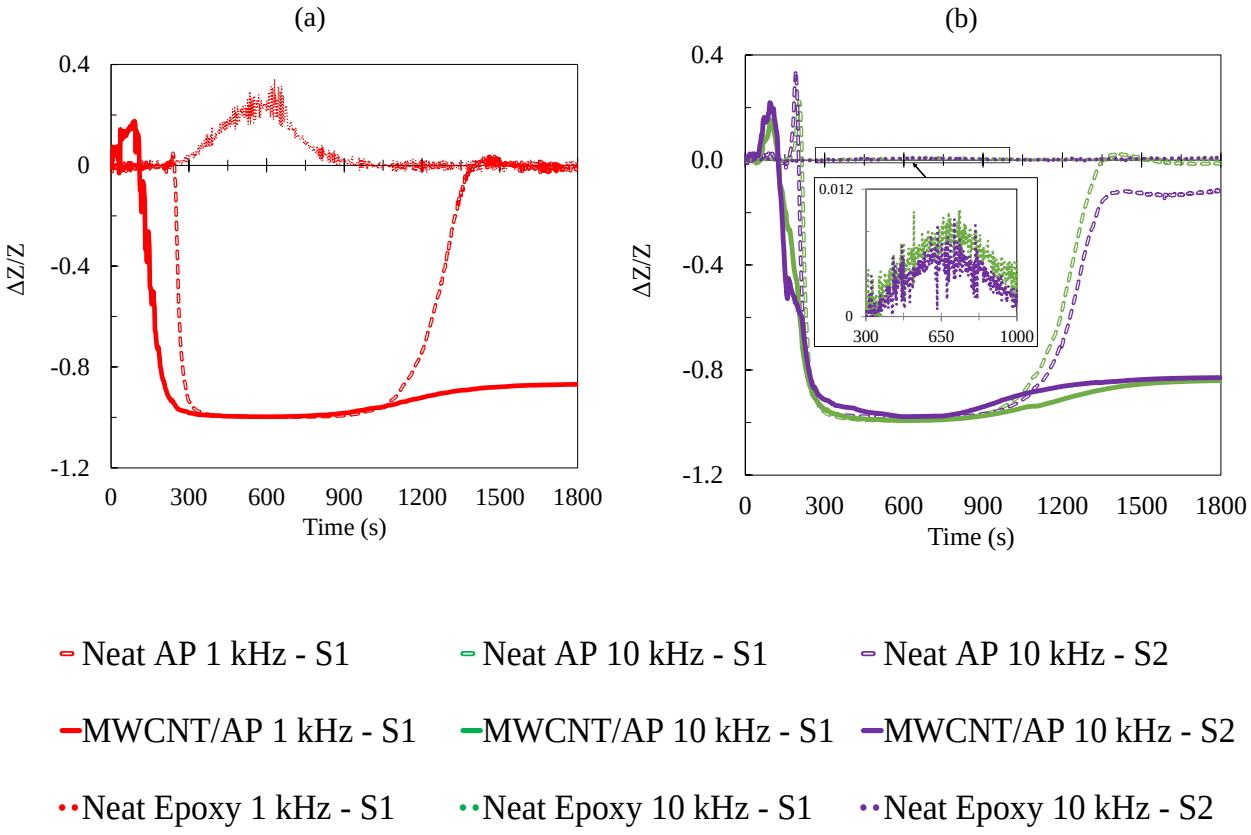

Figure D.6: Impedance results from thermal loading on neat epoxy, neat AP inert energetic, and MWCNT AP inert hybrid energetics at input frequencies: (a) 1 kHz (b)10 kHz (two samples)

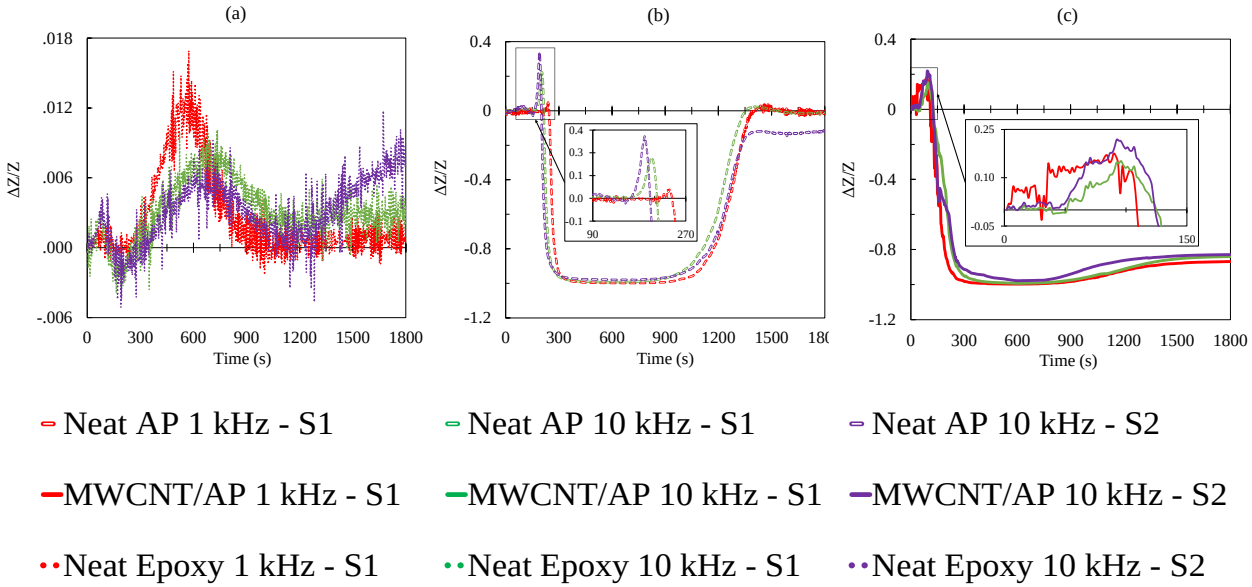

Figure D.7: Impedance results from thermal loading at multiple input frequencies for each material: (a) neat Epoxy (b)Neat AP inert energetic (c) MWCNT AP inert hybrid energetic